

**SEMI-EMPIRICAL STUDY OF STARVATION
IN MIXED ELASTOHYDRODYNAMIC LUBRICATION
OF A POINT CONTACT**

**ÉTUDE SEMI-EMPIRIQUE DE LA CARENCE EN
RÉGIME DE LUBRIFICATION ÉLASTO-
HYDRODYNAMIQUE MIXTE D'UN CONTACT
PONCTUEL**

A Thesis Submitted to the Division of Graduate Studies
of the Royal Military College of Canada
by

Augustine Wai-Hong Wong

In partial Fulfillment of the Requirements for the Degree of
Doctor of Philosophy

June, 2016

© This thesis may be used within the Department of National Defence but
copyright for open publication remains the property of the author.

ABSTRACT

The aim of this research was to investigate the behaviour of a starved lubricating film in mixed elasto-hydrodynamic regime, for the case of point contact. The literature defines starvation in lubrication as the condition that creates an appreciable decrease of the film thickness when the relative speed of the surfaces in contact is increased. The conditions of starvation for the mixed regime were studied experimentally and computationally. The film thickness was modelled through a combination of a numerical solution of Reynolds equation, applied to the contact geometry which induces an important variation of the viscosity of the lubricant with pressure, and the elastic deformation predicted by Hertz's theory. In mixed lubrication the load supported by the bearing area is shared between the asperities and the lubricating film. A new iterative approach was developed for predicting the load distribution as function of the total shearing load at the contact zone produced by the relative motion. The Eyring stress model was used to predict the rheological behaviour of the lubricant under high pressure and shear.

Starvation was studied experimentally using a ball-on-rotating cylinder lubricity tester that allowed the measurement of the friction at the point contact under different operating conditions; using three oils with different viscosities. The rheological properties of these oils were assessed at various temperatures using a commercial rheometer. Several conditions of loading and surface roughness were explored at various relative speeds. It was found that operating conditions influenced significantly the occurrence and severity of starvation, which consequently affected the film thickness. On the other hand, the onset of starvation was delayed with increasing surface roughness, implying its beneficial effect of acting as a reservoir. The concept of meniscus formation at the inlet of the contact zone in starved condition, was considered for the interpretation of these results. A criterion predicting the condition of starvation has been developed.

RÉSUMÉ

Le but de cette recherche était d'investiguer le comportement d'un film de lubrification sous carence en régime élasto-hydrodynamique mixte d'un contact ponctuel. La littérature définit la condition de carence en lubrification par la diminution notable de l'épaisseur du film quand la vitesse relative des surfaces en contact accroît. Les conditions de carence pour le cas du régime mixte ont été étudiées expérimentalement et par méthode computationnelle. L'épaisseur du film a été modélisée par une combinaison de la solution numérique de l'équation de Reynolds, appliquée à la géométrie de ce contact qui produit une variation importante de la viscosité du lubrifiant avec la pression, et la déformation élastique prédite par la théorie de Hertz. En régime de lubrification mixte, la charge supportée par la surface d'appui est distribuée parmi les aspérités et le film de lubrification. Un processus itératif nouveau a été développé pour la prédiction de cette distribution en fonction de la charge de cisaillement au niveau du contact; produite par le mouvement relatif. Le modèle de la contrainte de Eyring a été utilisé pour prédire le comportement rhéologique du lubrifiant.

La carence de lubrification a été étudiée expérimentalement à l'aide d'un tribomètre du type sphère sur cylindre tournant, simulant un contact ponctuel, permettant l'évaluation du frottement au niveau de l'interface à diverses conditions d'opération; pour le cas de trois huiles de viscosités différentes. Les propriétés rhéologiques de ces huiles ont été déterminées à différentes températures à l'aide d'un rhéomètre commercial. Différentes conditions de chargement, et rugosités de surface ont été examinées à diverses vitesses relatives de glissement. Il a été conclu que les conditions d'opération influencent grandement l'apparition de la carence de lubrification qui par conséquent affecte l'épaisseur du film ainsi que son comportement. Par ailleurs la carence est retardée dans le cas des surfaces rugueuses suggérant que les creux de la rugosité servent de réservoir de lubrifiant. Le concept de formation de ménisque à l'entrée de la zone de contact, a été considéré pour l'interprétation de ces résultats. Un critère de prédiction de la condition de carence a été proposé.

STATEMENT OF CONTRIBUTIONS

- Due to modern requirements for reducing weight of mechanical equipment, and higher performance; bearing systems are becoming very sophisticated to be able to function under starvation. Studies have emerged with the goal of understanding the behaviour of the lubricating film in this condition. However, due to the extreme difficulty of the experimental or simulation modeling of this phenomenon, which profoundly affects the performance, the research is still not firmly conclusive. The case of rudimentary contact models such as curved surface with relative motion on a flat surface; the latter most of the time transparent to permit film thickness quantification, have been explored for the case of hydrodynamic regime. This study is interested in an even more challenging aspect of this subject:
 - 1) The development of an experimental model and conditions simulating an actual ball bearing operating in harsh situation of relative sliding motion.
 - 2) The modelling of the elastic behaviour of the bearing elements operating in the condition of partial contact through the asperities.
 - 3) The effect of the operating conditions as well as surface roughness on starvation in mixed elasto-hydrodynamic lubrication (EHL) regime.
- Developed innovative and precise experimental procedures to determine the shear loading in two extreme conditions of fully separated contacting surfaces and boundary lubrication, necessary for the study of the starved mixed regime.
- Developed a comprehensive iterative process predicting the film thickness in starved condition from measurements of the friction force at the contact zone.
- Conducted thorough analysis of the results to develop new conclusions on the effect of the operating conditions including surface roughness on starvation; among them:
 - a) Approximating the friction component at the asperities contact by Coulomb law produces erroneous modelling of the actual behaviour. The friction-load ratio concept is suggested for a more accurate representation.
 - b) The roughness of the contacting surface delays the occurrence of starvation and decreases its severity independently of the supplied amount of lubricant.
 - c) The assessment of starvation expressed by the ratio of the thicknesses of inlet and the central of the contact in fully flooded condition films, as function of the operating conditions represented by $\sqrt{M/L}$

constitutes a powerful technique permitting the development of tangible conclusions on the mechanisms governing this important phenomenon.

- Proposed an empirical relationship for the prediction, with reasonable confidence, of the minimum inlet distance as function of the operating conditions; which would generate fully flooded mixed EHL.

The present thesis contributed to the enhancement and refinement of an existing empirical model developed to fit data obtained under simplified and idealized conditions, to predict the onset of starvation based on a more realistic contact model involving the surface roughness.

I would like to dedicate this work to my wonderful wife Durante.

ACKNOWLEDGEMENTS

I would like to express my sincere gratitude to my advisor Dr. S.H. Benabdallah of the Department of Mechanical and Aerospace Engineering, Royal Military College of Canada, for his continuous guidance and support throughout this research, for his patience, motivation and immense knowledge.

In addition to my advisor, I would like to thank Dr. D.F. James of the Department of Mechanical and Industrial Engineering, University of Toronto, for the use of his rheology laboratory and his insightful suggestions and comments with regard to the rheological experiment.

I would also like to thank Dr. A. Asghar and Dr. L. Momayez of the Department of Mechanical and Aerospace Engineering, Royal Military College of Canada, for their many helpful suggestions on the instrumentation of the tribological experiment.

I take this opportunity to express gratitude to the laboratory technicians of the Department of Mechanical and Aerospace Engineering and the Department of Electrical and Computer Engineering, Royal Military College of Canada, for their essential information and help relating to the preparation of the tribological experiment.

Thanks are also extended to LCol. (ret'd) T. Loveridge, Writing Centre of the Royal Military College of Canada for his suggestions on the preparation of this thesis.

TABLE OF CONTENTS

ABSTRACT.....	ii
RÉSUMÉ.....	iii
STATEMENT OF CONTRIBUTIONS	iv
DEDICATION.....	vi
ACKNOWLEDGEMENTS.....	vii
TABLE OF CONTENTS.....	viii
LIST OF FIGURES	xi
LIST OF TABLES.....	xv
NOMENCLATURE	xix
1. INTRODUCTION	1
1.1 Point Contact	3
1.2 Surface texture.....	9
1.3 Lubrication Regimes.....	12
2. LITERATURE REVIEW	15
3. ELASTOHYDRODYNAMIC THEORY AND FILM THICKNESS IN MIXED LUBRICATION	30
3.1 Elastohydrodynamic Film Thickness Theory	31
3.1.1 Reynolds Equation	31
3.1.2 Elastic Deformation	35
3.1.3 Viscosity-Pressure and Density-Pressure Relationship of Lubricant	38
3.1.4 Elastohydrodynamic Film Thickness Solution	39

3.2	Film Thickness and Friction Estimation in Mixed Lubrication.....	47
3.2.1	Load Sharing Concept and Film Thickness Equation for Mixed Lubrication.....	48
3.2.2	Greenwood and Williamson Asperity Contact Model	50
3.2.3	Friction at Contact Interface.....	56
3.2.4	Procedure for Evaluating Central Film Thickness in Mixed Lubrication.....	62
4.	OIL RHEOLOGICAL TESTS AND RESULTS.....	68
4.1	Tested Oils.....	68
4.2	Viscosity Tests.....	69
4.2.1	Viscosity Measurements	69
4.2.2	Viscosity of Tested Oils	71
4.2.3	Pressure-Viscosity Coefficient and Viscosity-Pressure Index of Tested Oils.....	75
4.3	Oil Surface Tension Measurements.....	77
5.	FRICITION EXPERIMENT.....	79
5.1	Friction Test Apparatus	79
5.2	Test Ball and Cylinder.....	81
5.3	Friction Test Procedures	84
6.	RESULTS AND DISCUSSION.....	88
6.1	Eyring Stress of Tested Oils	88
6.2	Asperity and Lubricant Friction-Load Ratio in Full Flooded Mixed Lubrication	93
6.3	Friction Force in Starved Film Condition.....	102
6.4	Central Film Thickness in Starved Mixed Lubrication.....	107
6.5	Inlet Condition.....	119
6.6	Starvation Degree (SD)	129
7.	CONCLUSIONS AND RECOMMENDATIONS	134
7.1	Conclusions	134
7.2	Recommendations	136
	REFERENCES	137

APPENDIX A	DEVRIVATION OF FILM THICKNESS EQUATION FOR MIXED LUBRICATION	150
APPENDIX B	EQUIPMENT SPECIFICATIONS	155
APPENDIX C	PERFORMACE TEST FOR AR2000 RHEOMETER	159
APPENDIX D.	DATA FOR RHEOLOGICAL TEST AND SURFACE TENSION MEASUREMENTS OF TEST OILS	161
APPENDIX E	CONVERSION OF KINEMATICS TO DYNAMIC VISCOSITY OF TESTED OILS IN ACCORDANCE WITH OIL MANUFACTURERS SPECIFICATIONS.....	167
	E.1 Kinematic Viscosity of Tested Oil at 25 °C.....	168
	E.2 Conversion from Kinematics to Dynamic Viscosity.....	169
APPENDIX F	APPARENT DEPENDENCE OF VISCOSITY AND SURFACE TENSION OF TESTED OILS.....	170
APPENDIX G	REFERENCE TEST FOR BALL-ON-CYLINDER LUBRICITY TESTER.....	172
APPENDIX H	DATA FOR TEST CYLINDER AND TEST BALL DIAMETER AND SURFACE PARAMETERS.....	175
APPENDIX I	DATA FOR FRICTION TEST.....	186

LIST OF FIGURES

Figure 1.1 Schematic diagram of the contacts in a ball bearing	4
Figure 1.2 Schematic diagram of two elastic solids in contact	4
Figure 1.3 Model of a contact between an equivalent ellipsoidal and a rigid plane.....	5
Figure 1.4 Elliptical contact area and the generated normal stress distribution.....	7
Figure 1.5 Schematic diagram of components of surface texture.....	10
Figure 1.6 Schematic diagram for the description of average surface roughness (R_a)	11
Figure 1.7 A typical Stribeck curve showing different lubrication regimes In fluid lubrication	13
Figure 1.8 Schematic diagram of lubrication regimes, (a) Boundary lubrication, (b) EHL mixed lubrication and (c) Hydrodynamic (full film) lubrication	14
Figure 2.1 Measured film thickness as a function of speed in starvation study.....	15
Figure 2.2 Schematic illustration of Grubin's EHL contact model	16
Figure 2.3 Interferometric image illustrating the meniscus (air-oil boundary) at the EHL inlet in starved condition of an oil lubricated ball-on-glass disc configuration	17
Figure 2.4 Model for the condition of starvation	21
Figure 2.5 Measured film thickness as a function of operating speed for different contact dimensions, oil viscosities and oil volumes	24
Figure 2.6 Schematic diagram of film thickness across the rolling track	26
Figure 3.1 Schematic illustration of the modelling of the effects occurring at a loaded lubricated contact interface.....	31
Figure 3.2 Fluid element in static equilibrium.....	32
Figure 3.3 Continuity of flow in an element.....	34
Figure 3.4 (a) Schematic diagram of a small rectangular area in the contact zone under uniform pressure p	36
Figure 3.4 (b) Schematic diagram of the coordinate system of a small rectangular area in the contact zone under uniform pressure p	36
Figure 3.5 Schematic model of the EHL film thickness	38
Figure 3.6 Map of EHL lubrication regimes with ellipticity parameter $k = 3$	42
Figure 3.7 Calculated values of the dimensionless central film thickness as a function of dimensionless parameter M and L	45
Figure 3.8 Dimensionless central film thickness as a function of M and L	46
Figure 3.9 Schematic diagram of the contact between a rigid nominally flat smooth surface and an equivalent rough surface	51

Figure 3.10	Flow chart for determining film thickness in fully flooded mixed lubrication	64
Figure 3.11	Flow chart for determining the asperity friction-load ratio in mixed fully flooded lubrication	65
Figure 3.12 (a)	Flow chart for determining the film thickness in starved mixed lubrication (part 1)	66
Figure 3.12 (b)	Flow chart for determining the film thickness in starved mixed lubrication (part 2)	67
Figure 4.1	Schematic diagram of the oil rheological experiment	70
Figure 4.2	Photographs of (a) TA Instrument AR2000 rheometer	70
	(b) An oil sample under test	70
Figure 4.3 (a)	Viscosity versus shear rate of tested oil #1	71
Figure 4.3 (b)	Viscosity versus shear rate of tested oil #2	72
Figure 4.3 (c)	Viscosity versus shear rate of tested oil #3	72
Figure 4.4	Effect of temperature on viscosity of tested oils	74
Figure 4.5	Photographs of (a) Fisher surface tensiometer Model 20	78
	(b) An oil sample under test	78
Figure 5.1	Photograph of the ball-on-cylinder tester for friction test	80
Figure 5.2	Schematic diagram of the friction tests experiment setup	80
Figure 5.3	Photograph of tested cylinder and ball	81
Figure 5.4 (a)	Surface profile and surface profile height amplitude distribution histogram of smooth cylinder	83
Figure 5.4 (b)	Surface profile and surface profile height amplitude distribution histogram of sanded cylinder	83
Figure 5.4 (c)	Surface profile and surface profile height amplitude distribution histogram of rough cylinder	84
Figure 5.4 (d)	Surface profile and surface profile height amplitude distribution histogram of test ball	84
Figure 5.5	Photograph of a typical distributed oil layer on test cylinder	85
Figure 5.6	Schematic diagram of the temperature assessments with Thermocouple (a) Side view ; (b) Bottom view	87
Figure 5.7	Test ball surface temperature variation in friction test (with 9.82 N applied load, rough cylinder surface and 60 μ l oil amount)	87
Figure 6.1	Friction coefficient versus Hersey number in thick film lubrication....	88
Figure 6.2	Shear stress of tested oils versus shear rate	90
Figure 6.3	Shear stress of tested oils and various fluids versus shear rate.....	91
Figure 6.4	Viscosity and surface tension versus Eyring stress of tested oils at 25°C	92
Figure 6.5	Friction contact model for mixed lubrication regime	93
Figure 6.6 (a)	Friction force versus rotation speed for mixed fully flooded Lubrication using rough cylinder	94
Figure 6.6 (b)	Friction force versus rotation speed for mixed fully flooded Lubrication using sanded cylinder	95

Figure 6.7 (a) Asperity friction-load ratio of oil #1	97
Figure 6.7 (b) Asperity friction-load ratio of oil #2.....	97
Figure 6.7 (c) Asperity friction-load ratio of oil #3	98
Figure 6.8 Asperity normal load and friction force components versus rotational speed for oil #1 with rough cylinder and 9.82 N applied total load	99
Figure 6.9 Lubricant normal load and friction force components versus rotational speed for oil #1 with rough cylinder and 9.82 N applied total load	99
Figure 6.10 (a) Lubricant friction-load ratio of oil #1	100
Figure 6.10 (b) Lubricant friction-load ratio of oil #2	101
Figure 6.10 (c) Lubricant friction-load ratio of oil #3	101
Figure 6.11 Superposition of asperity and lubricant friction-load ratios for rough contact lubricated with oil #2 and loaded at 9.82 N	102
Figure 6.12 Friction force versus rotation speed of oil #1 for rough cylinder	104
Figure 6.13 Friction force versus rotation speed of oil #1 for sanded cylinder ...	105
Figure 6.14 Friction force versus rotation speed of oil #2 for rough cylinder	105
Figure 6.15 Friction force versus rotation speed of oil #2 for sanded cylinder ...	106
Figure 6.16 Friction force versus rotation speed of oil #3 for rough cylinder	106
Figure 6.17 Friction force versus rotation speed of oil #3 for sanded cylinder ...	107
Figure 6.18 Normal and friction forces for 100 ml of oil #1, rough cylinder, total applied load 9.82 N.....	108
Figure 6.19 Estimated central film thickness versus rotation speed fully flooded contact for rough and sanded (empty markers) cylinders, $N = 5.88$ N.....	109
Figure 6.20 Estimated central film thickness versus rotation speed fully flooded contact for rough cylinders, $N = 5.88$ N and $N = 9.82$ N (empty markers).....	110
Figure 6.21 Estimated central film thickness versus rotation speed for rough cylinder, $N = 5.88$ N, fully flooded and starved 60 μ l (empty markers).....	111
Figure 6.22 Estimated central film thickness versus rotation speed for starved 60 μ l, $N = 5.88$ N, for rough and sanded (empty markers) cylinders	112
Figure 6.23 Estimated central film thickness versus rotation speed for starved 60 μ l, rough surface, $N = 5.88$ N and $N = 9.82$ N (empty markers).....	113
Figure 6.24 Estimated central film thickness versus rotation speed, rough surface, $N = 5.88$ N for starved contacts 60 μ l and 100 μ l (empty markers).....	114

Figure 6.25	Estimated central film thickness versus rotation speed, sanded surface, $N = 5.88$ N for starved contacts 60 μ l and 100 μ l (empty markers).....	115
Figure 6.26	Relative film thickness for oil #1, rough surface.....	116
Figure 6.27	Relative film thickness for oil #1, sanded surface.....	116
Figure 6.28	Minimum relative film thickness and critical transition speed, all loads and amounts.....	117
Figure 6.29	Minimum relative film thickness and critical transition speed, all loads and 60 μ l.....	118
Figure 6.30	Minimum relative film thickness and critical transition speed, all loads and 100 μ l.....	118
Figure 6.31	Linear variation of γ as function of $\sqrt{M/L}$	120
Figure 6.32	$\left(\frac{h_{cs}}{h_{cff}}\right)$ representing the condition of starvation as function of $\frac{h_{in}}{\bar{\rho}_{max} h_{cff}}$	120
Figure 6.33	Assessment of h_{in}/h_{cff} and γ with respect to $\sqrt{M/L}$ for oil #1, dotted lines represent 60 μ l supply, solid lines are for 100 μ l supply.....	122
Figure 6.34	Assessment of h_{in}/h_{cff} and γ with respect to $\sqrt{M/L}$ for oil #2, dotted lines represent 60 μ l supply, solid lines are for 100 μ l supply.....	123
Figure 6.35	Assessment of h_{in}/h_{cff} and γ with respect to $\sqrt{M/L}$ for oil #3, dotted lines represent 60 μ l supply, solid lines are for 100 μ l supply.....	124
Figure 6.36	s_{ff}/b as function of $\sqrt{M/L}$ for rough surface, fully flooded contact, effect of loading dotted lines for $N = 5.88$ N.....	126
Figure 6.37	s/b as function of $\sqrt{M/L}$ for rough surface, starved contact 60 μ l, effect of loading empty markers for $N = 5.88$ N.....	127
Figure 6.38	s/b as function of $\sqrt{M/L}$, $N = 9.82$ N, starved contact 60 μ l, effect of roughness, solid marker for rough surface.....	128
Figure 6.39	s/s_{ff} as function of $\sqrt{M/L}$, rough surface, starved contact 60 μ l, effect loading, solid marker $N = 9.82$ N.....	129
Figure 6.40	h_{cs}/h_{cff} as function of SD for all oils and conditions.....	132
Figure 6.41	h_{cs}/h_{cff} as function of SD' for all oils and conditions.....	133
Figure B.1	Circuit diagram of the voltage doubler.....	157
Figure C.1	Viscosity versus shear rate of reference test fluid.....	160
Figure F.1	Surface tension versus viscosity of tested oils at 25°C.....	171
Figure G.1	Lower portion of test cylinder submerged into Isopar M fluid in BOCLT reference test.....	173

LIST OF TABLES

Table 4.1 Measured dynamic viscosities	73
Table 4.2 Tested oils specifications provided by the manufacturers	75
Table 4.3 (a) Estimated pressure-viscosity coefficient at 25°C	76
Table 4.3 (b) Pressure-viscosity coefficient of various lubrication oils at 30°C	77
Table 4.4 Liquid-air surface tension measurement results	78
Table 5.1 Measured surface parameters of test cylinders and balls	82
Table 5.2 Experimental conditions for friction tests	86
Table 6.1 Eyring stress of tested oils	92
Table 6.2 Experimental conditions expressed by $\sqrt{M/L}$	122
Table 6.3 Critical starvation conditions expressed by $\sqrt{M/L}$ and h_{in}/h_{eff}	125
Table 6.4 Oil layer width and reservoir height	131
Table D.1 Measured viscosity of oil #1 at 25°C	162
Table D.2 Measured viscosity of oil #1 at 40°C	162
Table D.3 Measured viscosity of oil #1 at 100°C	163
Table D.4 Measured viscosity of oil #2 at 25°C	163
Table D.5 Measured viscosity of oil #2 at 40°C	164
Table D.6 Measured viscosity of oil #2 at 100°C	164
Table D.7 Measured viscosity of oil #3 at 25°C	165
Table D.8 Measured viscosity of oil #3 at 40°C	165
Table D.9 Measured viscosity of oil #3 at 100°C	166
Table D.10 Measured surface tension of test oils at 25°C	166
Table E.1 Estimated kinematic viscosity of tested oils at 25°C	168
Table E.2 Estimated tested oils density	169
Table G.1 Results of BOCTL reference test	174
Table H.1 Measured smooth cylinder diameter	176
Table H.2 Measured sanded cylinder diameter	176
Table H.3 Measured rough cylinder diameter	177
Table H.4 Measured test ball diameter	177
Table H.5 Measured smooth cylinder surface centre line roughness	178
Table H.6 Measured sanded cylinder surface centre line roughness	178
Table H.7 Measured rough cylinder surface centre line roughness	179
Table H.8 Measured test ball surface centre line roughness	179
Table H.9 Measured smooth cylinder surface root mean square roughness	180
Table H.10 Measured sanded cylinder surface root mean square roughness	180
Table H.11 Measured rough cylinder surface root mean square roughness	181
Table H.12 Measured test ball surface root mean square roughness	181
Table H.13 Measured sanded cylinder surface asperity average slope	182
Table H.14 Measured rough cylinder surface asperity average slope	182
Table H.15 Measured test ball surface asperity average slope	183

Table H.16	Measured sanded cylinder surface high spot counts in transverse direction	183
Table H.17	Measured rough cylinder surface high spot counts in transverse direction	184
Table H.18	Measured sanded cylinder surface high spot counts in rolling direction.....	184
Table H.19	Measured rough cylinder surface high spot counts in rolling direction.....	185
Table H.20	Measured test ball surface high spot counts.....	185
Table I.1	Measured friction force and calculated friction coefficient of oil #1 with 5.88 N applied load, sanded cylinder and continuous oil supply	187
Table I.2	Measured friction force and calculated friction coefficient of oil #1 with 5.88 N applied load, sanded cylinder and 60 μ l oil supply	187
Table I.3	Measured friction force and calculated friction coefficient of oil #1 with 5.88 N applied load, sanded cylinder and 100 μ l oil supply	187
Table I.4	Measured friction force and calculated friction coefficient of oil #1 with 9.82 N applied load, sanded cylinder and continuous oil supply	188
Table I.5	Measured friction force and calculated friction coefficient of oil #1 with 9.82 N applied load, sanded cylinder and 60 μ l oil supply	188
Table I.6	Measured friction force and calculated friction coefficient of oil #1 with 9.82 N applied load, sanded cylinder and 100 μ l oil supply	188
Table I.7	Measured friction force and calculated friction coefficient of oil #1 with 5.88 N applied load, rough cylinder and continuous μ l oil supply.....	189
Table I.8	Measured friction force and calculated friction coefficient of oil #1 with 5.88 N applied load, rough cylinder and 60 μ l oil supply	189
Table I.9	Measured friction force and calculated friction coefficient of oil #1 with 5.88 N applied load, rough cylinder and 100 μ l oil supply	189
Table I.10	Measured friction force and calculated friction coefficient of oil #1 with 9.82 N applied load, rough cylinder and continuous oil supply	190
Table I.11	Measured friction force and calculated friction coefficient of oil #1 with 9.82 N applied load, rough cylinder and 60 μ l oil supply	190

Table I.12	Measured friction force and calculated friction coefficient of oil #1 with 9.82 N applied load, rough cylinder and 100 μl oil supply	190
Table I.13	Measured friction force and calculated friction coefficient of oil #2 with 5.88 N applied load, sanded cylinder and continuous oil supply	191
Table I.14	Measured friction force and calculated friction coefficient of oil #2 with 5.88 N applied load, sanded cylinder and 60 μl oil supply	191
Table I.15	Measured friction force and calculated friction coefficient of oil #2 with 5.88 N applied load, sanded cylinder and 100 μl oil supply	191
Table I.16	Measured friction force and calculated friction coefficient of oil #2 with 9.82 N applied load, sanded cylinder and continuous oil supply	192
Table I.17	Measured friction force and calculated friction coefficient of oil #2 with 9.82 N applied load, sanded cylinder and 60 μl oil supply	192
Table I.18	Measured friction force and calculated friction coefficient of oil #2 with 9.82 N applied load, sanded cylinder and 100 μl oil supply	192
Table I.19	Measured friction force and calculated friction coefficient of oil #2 with 5.88 N applied load, rough cylinder and continuous oil supply	193
Table I.20	Measured friction force and calculated friction coefficient of oil #2 with 5.88 N applied load, rough cylinder and 60 μl oil supply	193
Table I.21	Measured friction force and calculated friction coefficient of oil #2 with 5.88 N applied load, rough cylinder and 100 μl oil supply	193
Table I.22	Measured friction force and calculated friction coefficient of oil #2 with 9.82 N applied load, rough cylinder and continuous oil supply	194
Table I.23	Measured friction force and calculated friction coefficient of oil #2 with 9.82 N applied load, rough cylinder and 60 μl oil supply	194
Table I.24	Measured friction force and calculated friction coefficient of oil #2 with 9.82 N applied load, rough cylinder and 100 μl oil supply	194
Table I.25	Measured friction force and calculated friction coefficient of oil #3 with 5.88 N applied load, sanded cylinder and continuous oil supply	195

Table I.26	Measured friction force and calculated friction coefficient of oil #3 with 5.88 N applied load, sanded cylinder and 60 μl oil supply	195
Table I.27	Measured friction force and calculated friction coefficient of oil #3 with 5.88 N applied load, sanded cylinder and 100 μl oil supply	195
Table I.28	Measured friction force and calculated friction coefficient of oil #3 with 9.82 N applied load, sanded cylinder and continuous oil supply	196
Table I.29	Measured friction force and calculated friction coefficient of oil #3 with 9.82 N applied load, sanded cylinder and 60 μl oil supply	196
Table I.30	Measured friction force and calculated friction coefficient of oil #3 with 9.82 N applied load, sanded cylinder and 100 μl oil supply	196
Table I.31	Measured friction force and calculated friction coefficient of oil #3 with 5.88 N applied load, rough cylinder and continuous oil supply	197
Table I.32	Measured friction force and calculated friction coefficient of oil #3 with 5.88 N applied load, rough cylinder and 60 μl oil supply	197
Table I.33	Measured friction force and calculated friction coefficient of oil #3 with 5.88 N applied load, rough cylinder and 100 μl oil supply	197
Table I.34	Measured friction force and calculated friction coefficient of oil #3 with 9.82 N applied load, rough cylinder and continuous oil supply	198
Table I.35	Measured friction force and calculated friction coefficient of oil #3 with 9.82 N applied load, rough cylinder and 60 μl oil supply	198
Table I.36	Measured friction force and calculated friction coefficient of oil #3 with 9.82 N applied load, rough cylinder and 100 μl oil supply	198

NOMENCLATURE

English Notations:

- a = semi-major axis length of contact ellipse
 \bar{a} = half-length of rectangular area in contact zone
 A_a = asperity (solid) contact area at the interface
 A_{Hertz} = nominal Hertzian contact area
 A_L = area of lubricant at contact
 b = semi-minor axis length of contact ellipse
 \bar{b} = half-width of rectangular area in contact zone
 c_1, c_2 = arbitrary constants of integration
 c_p = constant = 1.96×10^8 Ns/m²
 C = constant = $2^{-1.5} 3^{-1.25} \pi^2 (1/\sqrt{k})$
 d = separation between the smooth surface and the equivalent rough surface
 d_d = characteristic distance of the surface topography = $0.82R_q'$
 d_R = travelled distance
 \hat{d} = dimensionless separation
 D = ratio of the equivalent radii = r_x/r_y
 E_1 = elastic modulus of body 1
 E_2 = elastic modulus of body 2
 E' = equivalent modulus of elasticity
 f = total friction coefficient
 f_a = asperity friction-load ratio
 f_L = lubricant friction-load ratio
 F_a = friction force due to asperity interaction
 F_f = friction force
 F_L = friction force due to shearing of lubricant
 F_T = total friction force at contact = $F_a + F_L$
 $F_1(\hat{d})$ = parabolic cylinder function (with power index equals 1)
 $F_{3/2}(\hat{d})$ = parabolic cylinder function (with power index equals 3/2)
 F' = ellipse integral of the first kind
 g_E = dimensionless elastic parameter
 g_v = dimensionless viscosity parameter
 G = dimensionless parameter for material
 $h, h(x,y)$ = height of gap between two surfaces
 h_o = separation between the equivalent ellipsoidal solid and the rigid flat
 h_c = central film thickness
 $h_{c,mix}$ = central film thickness for mixed lubrication
 $h_{c,mix,s}$ = starved central film thickness for mixed lubrication
 $h_{c,ff}$ = central film thickness in fully flooded condition

h_{cs} = film thickness in starved condition
 h_{in} = inlet film thickness
 h_{oil} = oil reservoir height
 $h_{oil\infty}$ = oil reservoir height
 H_{00} = dimensionless parameter for smooth transition between the four asymptotic solutions for the film thickness
 H_{40}, H_{100} = constants for evaluating the viscosity-pressure index
 H_c = dimensionless central film thickness
 $H_{c,mix}$ = dimensionless central film thickness for mixed lubrication
 $H_{c,El}$ = dimensionless central film thickness in elastic-isoviscous regime
 $H_{c,El,mix}$ = dimensionless central film thickness in elastic-isoviscous regime for mixed lubrication
 $H_{c,EV}$ = dimensionless central film thickness in elastic-viscous regime
 $H_{c,EV,mix}$ = dimensionless central film thickness in elastic-viscous regime for mixed lubrication
 $H_{c,RI}$ = dimensionless central film thickness in rigid-isoviscous regime
 $H_{c,RI,mix}$ = dimensionless central film thickness in rigid-isoviscous regime for mixed lubrication
 $H_{c,RV}$ = dimensionless central film thickness in rigid-isoviscous regime
 $H_{c,RV,mix}$ = dimensionless central film thickness in rigid-isoviscous regime for mixed lubrication
 H_s = Hersey number
 HSC_r = high spot count of surface in transverse direction
 HSC_t = high spot count of surface in transverse direction
 k = ellipticity parameter of the Hertzian contact
 K_A, K_B = constants for evaluating viscosity of lubricant at different temperature
 L = Moes dimensionless material parameter
 L_{mix} = Moes dimensionless material parameter for mixed lubrication
 \tilde{L} = assessment length
 m = asperity average slope
 M = Moes dimensionless load parameter
 M_{mix} = Moes dimensionless load parameter for mixed lubrication
 n = power index that implements different limiting shear stress models
 n' = equivalent density of asperity summits per unit area
 N = applied normal load
 N_a = load carried by asperities at the contact
 N_L = load carried by lubricant at the contact
 p_a = pressure supported by asperities with respect to separation
 $p_{as\gamma}$ = shared pressure on asperities
 $p, p(x,y)$ = pressure
 p_{app} = apparent contact pressure
 p_{ave} = average contact pressure
 p_G = pressure in GPa

p_L = pressure acting on lubricant
 p_{max} = maximum contact pressure
 q_x = volume flow rate in x-direction
 q_y = volume flow rate in y-direction
 r = equivalent radius
 r'_p = equivalent average radius of the asperity tips
 r_{p1} = average radius of the asperity tips of surface 1
 r_{p2} = average radius of the asperity tips of surface 2
 $r_r = h_{in}/(\bar{\rho}_{max} h_{eff})$ (dimensionless parameter)
 r_x = equivalent radius in rolling (x) direction
 r_{x1} = radius of curvature of body 1 in rolling (x) direction
 r_{x2} = radius of curvature of body 2 in rolling (x) direction
 r_y = equivalent radius in transverse (y) direction
 r_{y1} = radius of curvature of body 1 in transverse (y) direction
 r_{y2} = radius of curvature of body 2 in transverse (y) direction
 \bar{r} = length of the vector joining points (\bar{x}_1, \bar{y}_1) and (\bar{x}, \bar{y}) on the contact zone
 \mathcal{R} = relative film thickness = h_{cs}/h_{eff}
 R_a = centre line average (CLA) roughness
 R_{a1} = centre line average roughness of body 1
 R_{a2} = centre line average roughness of body 2
 R'_a = equivalent centre line average roughness
 R_q = root mean square roughness
 R_{q1} = root mean square roughness of body 1
 R_{q2} = root mean square roughness of body 2
 R'_q = equivalent root mean square roughness
 \bar{R}_q = dimensionless root mean square roughness
 s = inlet meniscus distance
 s_{ff} = inlet meniscus distance in fully flooded condition
 \hat{s} = dimensionless parameter for smooth transition between the four asymptotic solution in film thickness equation
 \hat{s}_{mix} = dimensionless parameter for smooth transition between the four asymptotic solution in film thickness equation for mixed lubrication
 \bar{s} = dummy variable for integration
 \bar{s}_{ff} = dimensionless inlet meniscus distance
 $S(x,y)$ = geometry of the equivalent ellipsoidal solid
 S' = elliptic integral of the second kind
 SD = starvation degree
 SD' = modified starvation degree
 t = time
 t_o = reference temperature

t_c = cycle time
 t_r = replenishment time
 t_i = a given temperature
 u, u_x = velocity in x-direction
 u_1 = velocity of surface 1 in x-direction
 u_2 = velocity of surface 2 in x-direction
 u_s = sum velocity
 \bar{u} = entrainment velocity (average velocity)
 U = dimensionless parameter for speed
 v = velocity in y-direction
 v_1 = velocity of surface 1 in y-direction
 v_2 = velocity of surface 2 in y-direction
 V = volume of oil applied
 VI = viscosity index
 w = velocity in z-direction
 w_o = velocity of the “floor” of fluid column in z-direction
 w_h = velocity of the “roof” of fluid column in z-direction
 w_{oil} = initial oil layer width of test cylinder
 W = dimensionless parameter for load
 x = rolling direction
 x_{in} = distance between the Hertzian contact centre and the free air-oil boundary
 \tilde{x} = reference axis
 (\bar{x}, \bar{y}) = location of an arbitrary point on the rectangular area in contact zone
 (\bar{x}_1, \bar{y}_1) = location of the pressure on the rectangular area in contact zone
 y = transverse direction
 z = through thickness direction
 $\tilde{z}, \tilde{z}(\tilde{x})$ = height variations of the surface profile
 Z_I = viscosity-pressure index

Greek Notations:

$\delta, \delta(x,y)$ = elastic deformation
 β = volumetric expansion coefficient
 β_m = shear stress-pressure coefficient
 γ = dimensionless film reduction parameter
 γ_1 = load sharing factor for lubricant
 γ_2 = load sharing factor for asperities
 $\dot{\gamma}$ = shear rate
 Γ = curvature difference of the equivalent body
 η = viscosity at ambient

η^* = viscosity under pressure
 η_{40}, η_{100} = absolute viscosities, in centipoise (cP) at 40°C and 100°C, respectively
 η_∞ = constant = 6.31×10^{-5} Ns/m²
 θ = starvation coefficient
 μ = coefficient of friction
 ν_1 = Poisson's ratio of body 1
 ν_2 = Poisson's ratio of body 2
 $\nu_{25}, \nu_{40}, \nu_{100}$ = kinematic viscosities at 25°C, 40°C and 100°C, respectively
 ν_H = kinematic viscosities of the 100 VI oil at 40°C
 ν_k = kinematic viscosity
 ν_L = kinematic viscosities of the 0 VI oil at 40°C
 ν_U = kinematic viscosities of the sample oil at 40°C
 ξ = pressure-viscosity coefficient
 ρ = density
 ρ_o = density at ambient pressure
 ρ_{oo} = density at reference temperature
 ρ_t = density at a given temperature
 ρ^* = density of pressurised fluid
 $\bar{\rho}_{max}$ = dimensionless density with respect to the maximum contact pressure
 σ'_p = equivalent standard deviation of the peak height
 σ'_{p1} = standard deviation of the peak height of body 1
 σ'_{p2} = standard deviation of the peak height of body 2
 σ_s = surface tension of the liquid-air interface
 τ_o = Eyring stress
 τ_L = shear stress in lubricant
 τ_m = limiting shear stress
 τ_{mo} = limiting shear stress at atmospheric pressure
 τ_{xy} = shear stress acting on a fluid element in x-direction
 φ = auxiliary angle for the integration
 $\phi(\bar{s})$ = probability distribution function of \bar{s}
 $\phi(\tilde{z})$ = probability distribution function of surface height
 ω = rotation speed

1. INTRODUCTION

There are billions of bearings in use in machinery with rotating parts. These bearing sizes vary from small enough to run miniature motors to huge bearings used to support parts in hydroelectric power plants [Mathias, 1996 ; Cann and Lubrecht, 1999]. Lubrication plays a vital role in the performance and life of bearings [AST Bearings LLC, 2010]. Some leading bearing companies have stated that 80% of bearing failures in industrial application are related to lubrication problems; nearly half of these are attributed to poor or inadequate lubrication conditions [Snyder, 2005 ; Koyo, 2009 ; Radu, 2010]. In the case of a non-conformal contact within a ball bearing, because the contact area is extremely small, the pressure may become in the order of giga-pascals (GPa) even under relatively low normal loading. Lubricants provide a film at the contact point that separates parts in relative motion and serve as medium for friction heat dissipation. The prevention of solid contact minimises friction and prevents wear. Proper lubrication is essential for reliable operation of optimized power transmission. The thickness of the film at the contact; influenced by the operating conditions and the type of lubricant is the key factor affecting the performance of a bearing.

In ideal operating conditions generating elasto-hydrodynamic lubrication (EHL) regime the friction surfaces are fully separated by the lubrication film whose thickness is predicted by classical lubrication theories for fully flooded contact. At higher operating velocities, an appreciable decrease of the thickness occurs signaling the onset of a phenomenon researchers have called starvation [Cann *et al.*, 2004 ; Pepper, 2008 ; Svoboda *et al.*, 2013]. The relationship expressing this drop of thickness has been the objective of numerous studies. Surfaces of contacting machine elements in relative motion are never perfectly smooth but contain asperities even at microscopic scales resulting from the manufacturing processes. When the lubrication film thickness is comparable to the asperities height, mixed lubrication regime is prevalent [Gelinck, 1999 ; Bhushan, 2002 ; Wang *et al.*, 2007]. It has been determined that mixed lubrication regime is typical in bearings operating at conditions of high speed and loading encountered in automotive and aerospace applications. Depending on the amount of lubricant supplied to the contact zone, a starved film state may be generated; negatively influencing the bearing service life with adverse economic impact. The phenomenon of the development of an EHL film in fully flooded condition, when sufficient lubricant is supplied, is well understood and the thickness of such film can be predicted with good accuracy [Wedeven *et al.*, 1971]. A statistical analysis of the numerical prediction results showed that the experimental values of minimum film thickness were about 23% greater than the corresponding predictions given by Hamrock and Dowson [1977a]. However, this conventional analysis is not applicable to starved contacts, which has triggered an increasing

awareness of the importance of the influence of starvation on EHL behaviour. The understanding of this complex relationship is still at the evolving stage despite considerable effort and thus, further investigation and modelling of this type of lubrication process are sought. The studies of starvation in EHL have revealed that the degree of starvation is influenced by the operating parameters and lubricant properties such as the viscosity [Cann *et al.*, 2004 ; Berthe *et al.*, 2014]. More importantly, the understanding of the conditions expressing the transition from fully flooded to starved contact provides the basis for a more informed choice in bearing design [Cann *et al.*, 2004]. The quantifying of the lubricant film thickness at the contact and its variations with the degree of starvation is the most challenging aspect of these studies [Wedeven *et al.*, 1971 ; Chiu, 1974 ; Chevalier *et al.*, 1998 ; Damiens *et al.*, 2004 ; Svoboda *et al.*, 2013]. The majority of film thickness measurements were carried out using optical interferometry techniques requiring one of the contacting surfaces to be flat and transparent and under thick film lubrication without solid contact. Mostly metal ball on glass plate contact configurations were used in these studies, which is not ideal for simulating contact behaviour in actual ball bearings. In the case of the non-conformal contact geometries applicable to ball bearings; mixed lubrication is more likely to occur [Faraon and Schipper, 2006; 2007 ; Svoboda *et al.*, 2013].

The main goal of this research is to study the starvation phenomenon for the case of point contact under elasto-hydrodynamic mixed lubrication. It will investigate the influence of the operating parameters, including rotation speed, applied load, and surface roughness for the case of different high performance commercially available oils. The experimental model simulating a critical condition of seized ball in a bearing will be used to assess the behaviour of the lubricating film under these conditions.

The available theory for film thickness prediction in ideal cases of fully flooded lubrication will be coupled with results of measurements of the total shearing force generated at the contact zone by relative sliding to determine the central film thickness. The inlet oil supply in terms of the oil meniscus distance; a parameter necessary for the analysis will be based on Hamrock and Dowson [1977b] numerical analysis. The validity of the starvation degree parameter proposed by Cann *et al.* [2004] will be evaluated.

In mixed lubrication, the onset of starvation, because of the reduction in film thickness, has been associated with significant friction increase in comparison to fully flooded condition [Berthe *et al.*, 2014]. Analytical models have been developed to evaluate the friction in the mixed lubrication of point contact configuration as function of the film thickness [Liu *et al.*, 2009 ; Sojoudi and Khonsari, 2010 ; Gasni, 2013]. This model is based on the concept of “Stribeck friction” [Ramezani and Ripin, 2009], which considers that the total applied load to

the bearing is supported by the hydrodynamic pressure that develops at the contact zone and the asperities interacting reaction force. Greenwood and Williamson [1966] elastic contact model predicts the number of asperities participating in the formation of the contact area based on the amount of elastic deformation generated by the loading.

This thesis is prepared in seven chapters with the first chapter being an introduction followed by the definitions of point contact and the surface topography. A literature review on starvation studies since the early 1970s is provided in Chapter 2. Chapter 3 presents the classical EHL theory for evaluating lubricant film thickness for point contact geometry, based on the Reynolds equation, elastic deformation of surfaces and viscosity-pressure relationship of lubricant. It is then followed by a description of the methodology for evaluating the oil film thickness and friction at the contact in mixed lubrication, which is based on the load sharing concept, the statistical asperity elastic contact model and the modified film thickness model. The rheological test for the determination of the variation of viscosity with shear rate of the oils considered in this study is described in Chapter 4. In Chapter 5, descriptions of the friction experiment procedures are given in detail. The results of measurements and the numerical analysis are discussed in Chapter 6. The influence of the operation parameters on the friction and film thickness at the contact, the inlet condition and the onset of starvation under the configuration considered in this study are examined. Chapter 7 presents the conclusions drawn from this study. Recommendations on further research that can extend the work of this study are also presented in this chapter.

1.1 Point Contact

A schematic diagram of the contacts between a ball and the races in a ball bearing is shown in Fig. 1.1 [Hamrock and Dowson, 1981]. As shown, such contacts are in elliptical shape and, hence, they are referred to elliptical contact. The size and shape of these contacts depend on the applied load, the elastic properties of the materials and the geometry of the surfaces. Since this kind of contact initiates from the touching of two surfaces at a point then expands to an area, it is also commonly referred to as point contact.

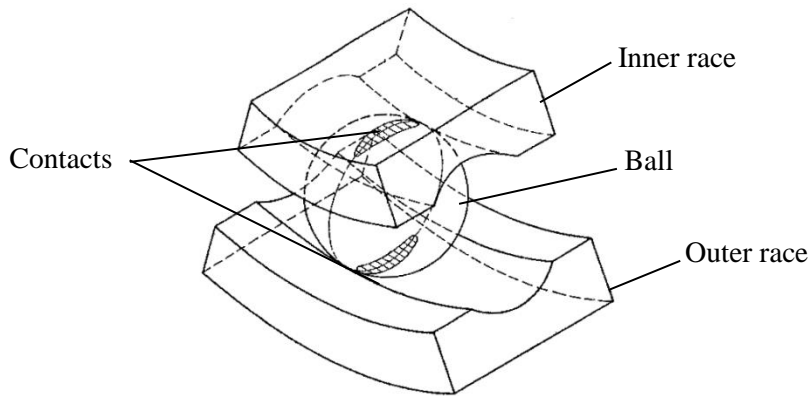


Figure 1.1 Schematic diagram of the contacts in a ball bearing [Hamrock and Dowson, 1981]

Hertz [1896] developed the theory of contact of two surfaces at a point by applying the classical theory of elasticity to two smooth, ellipsoidal and homogeneous elastic bodies in frictionless contact [Johnson, 1985], as shown in Fig. 1.2 [Hamrock and Brewe, 1983].

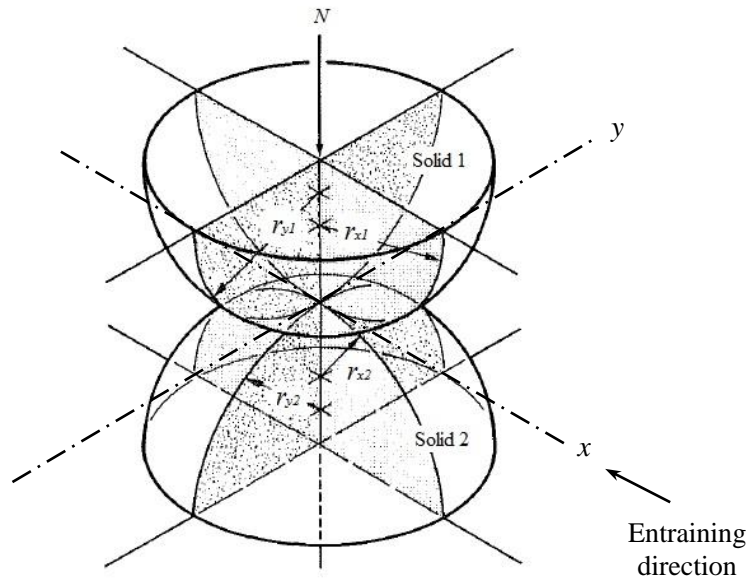


Figure 1.2 Schematic diagram of two elastic solids in contact [Hamrock and Brewe, 1983]

The two solids, solid 1 and solid 2, with different radii of curvature make contact at a single point under an applied load N . The reference direction of entraining motion is x -direction; the transverse is y -direction. The radii of curvature of solid 1 in the x - and y -directions are denoted as r_{x1} and r_{y1} , respectively. Similarly, r_{x2} and r_{y2} are the radii of curvature of solid 2. For ease of analytical treatment, this actual geometry is transformed into an equivalent ellipsoidal solid of radii of curvature r_x and r_y in contact with a rigid flat, as shown in Fig. 1.3. The principle of this transformation is to model the contact of two elastic curved surfaces as an equivalent contact between a rigid plane and the new ellipsoidal solid that possesses equivalent elastic properties and geometric shape. With this transformation, it is no longer necessary to be concerned with evaluating the elastic deflections on each of the original surfaces, for the new equivalent solid experiences and equivalent total elastic deflection [Blahey, 1985]. The equivalent radii r_x and r_y are defined below:

$$\frac{1}{r_x} = \frac{1}{r_{x1}} + \frac{1}{r_{x2}} \quad (1.1a)$$

$$\frac{1}{r_y} = \frac{1}{r_{y1}} + \frac{1}{r_{y2}} \quad (1.1b)$$

Convex surfaces and concave surfaces exhibit positive curvature or negative curvature, respectively. Flat surfaces are considered to have infinite radius of curvature.

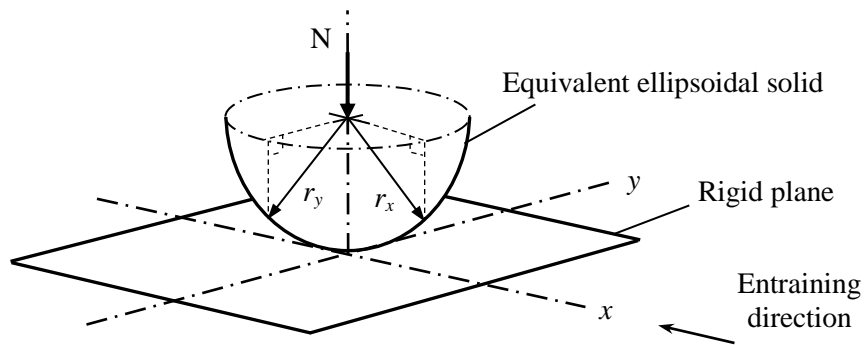


Figure 1.3 Model of a contact between an equivalent ellipsoidal and a rigid plane

The mechanical properties of the materials are expressed by the equivalent modulus of elasticity E' , which generates the same total deformation on the reduced equivalent ellipsoidal solid (in Fig. 1.3) as the cumulated deformation on the original solid 1 and solid 2 (in Fig. 1.2) with moduli E_1 and E_2 , respectively. This equivalent modulus of elasticity is:

$$\frac{1}{E'} = \frac{1}{2} \left[\frac{(1 - \nu_1^2)}{E_1} + \frac{(1 - \nu_2^2)}{E_2} \right] \quad (1.2)$$

Where E_1 = modulus of elasticity of solid 1,
 E_2 = modulus of elasticity of solid 2,
 ν_1 = Poisson's ratio of solid 1,
 ν_2 = Poisson's ratio of solid 2.

The calculation of the elastic surface deformations resulting from a continuous pressure distribution between two curved surfaces at the contact interface in the EHL analysis is based upon this equivalent contact.

Hertz [1896] considered the stresses and deformations in two perfectly smooth, ellipsoidal, contacting elastic solids as shown in Fig. 1.2. The application of the classical theory of elasticity to this problem forms the basis of stress calculation for machine elements such as ball and roller bearings, gears, seals, and cams. The following assumptions were imposed to obtain a simplified but realistic solution [Hamrock and Dowson, 1981]:

- The materials are homogeneous, isotropic and their yield strength is not exceeded.
- No tangential reaction is induced at the interface between the solids.
- Contact is limited to a small portion of the surface, such that the characteristic dimensions of the contact area are small compared with the radii of the ellipsoids.
- The solids are at rest and in equilibrium (steady state).

The following equation describing the normal stress distribution on an elliptical contact area, also called pressure, has been derived. A schematic of such pressure distribution generated by the loading N is shown in Fig. 1.4 [Hamrock and Dowson, 1981].

$$p(x, y) = p_{max} \sqrt{1 - \left(\frac{x}{b}\right)^2 - \left(\frac{y}{a}\right)^2} \quad (1.3)$$

where p_{max} = the maximum contact pressure,
 a = the length of the semi-major axis,
 b = the length of the semi-minor axis.

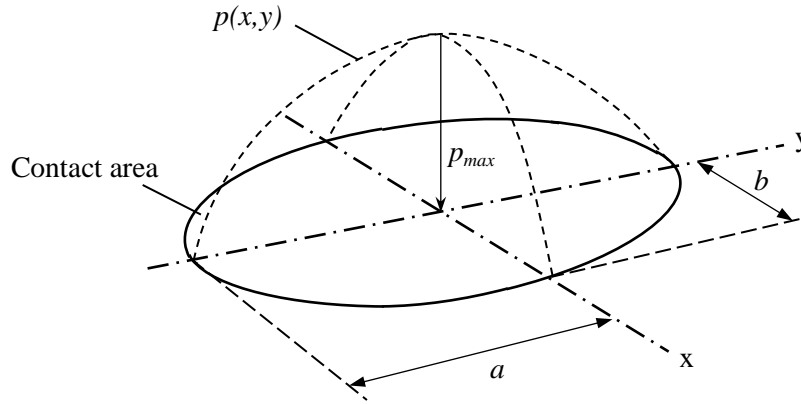


Figure 1.4 Elliptical contact area and the generated normal stress distribution [Hamrock and Dowson, 1981]

Considering the entire contact pressure distribution, it peaks at the centroid of the area of contact ($x=0, y=0$) and decays to zero along its perimeter. The maximum contact pressure p_{max} and average contact pressure p_{ave} are expressed by the following equations:

$$p_{max} = \frac{3N}{2\pi ab} \quad (1.4)$$

$$p_{ave} = \frac{N}{\pi ab} \quad (1.5)$$

where N = applied load

The Hertzian solution for this contact problem permits one to determine the semi-major and semi-minor widths defining the elliptical shape by the following equations:

$$a = \left(\frac{6 k^2 S' r N}{\pi E'} \right)^{\frac{1}{3}} \quad (1.6)$$

$$b = \left(\frac{6 S' r N}{\pi k E'} \right)^{\frac{1}{3}} \quad (1.7)$$

where N = applied load,

r = equivalent radius = $1/(1/r_x + 1/r_y)$,

k = ellipticity parameter of the Hertzian contact (will be defined below),

S' = elliptic integral of the second kind,

E' = equivalent modulus of elasticity.

Harris [1966] has shown that the ellipticity parameter k can be written as a transcendental equation, as shown in Eq. (1.8), relating to the curvature difference expressed $\Gamma = r (1/r_x - 1/r_y)$ and the elliptic integrals of the first F' and second kind S' . The elliptic integrals are the generalizations of the inverse trigonometric elliptic functions and provide solutions to a wide class of problems of giving the arc length of an ellipse. In general, integrals in this form cannot be expressed in terms of elementary functions. For instance, while the arc length of a circle is given as a simple function of the parameter, however, computing the arc length of an ellipse requires the elliptic integrals. The elliptic integrals of the first and second kinds are the canonical forms of the integrals arising from the arc length calculations through the appropriate transformations and reductions, and they are shown in Eqs (1.9) and (1.10), respectively.

$$k = \left[\frac{2F' - S'(I + \Gamma)}{S'(I - \Gamma)} \right]^{\frac{1}{2}} \quad (1.8)$$

in which:

$$F' = \int_0^{\pi/2} \left[1 - \left(1 - \frac{1}{k^2} \right) \sin^2 \varphi \right]^{-1/2} d\varphi \quad (1.9)$$

and,

$$S' = \int_0^{\pi/2} \left[1 - \left(1 - \frac{1}{k^2} \right) \sin^2 \varphi \right]^{1/2} d\varphi \quad (1.10)$$

where φ = auxiliary angle for the integration.

The above equations are usually solved by an iterative numerical procedure described by Hamrock and Anderson [1973], or with the aid of charts, as shown by Jones [1946]. Brewe and Hamrock [1977] used a linear regression by the method of least squares to obtain the simplified solutions for F' and S' reproduced hereafter:

$$F' = \frac{\pi}{2} + \left(\frac{\pi}{2} - 1 \right) \ln \left(\frac{r_y}{r_x} \right) \quad (1.11)$$

$$S' = 1 + \frac{(\pi/2) - 1}{r_y/r_x} \quad (1.12)$$

At the same time, a numerical evaluation of the effect of the variation of the ratio r_x/r_y on the ellipticity parameter has yielded the following relationship, which can be used for a direct evaluation avoiding the tedious step of solving the elliptic integrals (Eqs 1.9 and 1.10):

$$k = \left(\frac{r_y}{r_x} \right)^{2/\pi} \quad (1.13)$$

1.2 Surface texture

Surfaces of machine elements are never perfectly smooth. Asperities, the peaks of surface undulations, are the result of the fabrication of the elements on the surfaces. According to the American National Standards Institute [ANSI, 1978], surface texture is composed of the repetitive or random deviation from the nominal surface which forms the three dimensional topography of the surface. Surface texture components include lay, waviness and roughness. These components are illustrated schematically in Fig. 1.5.

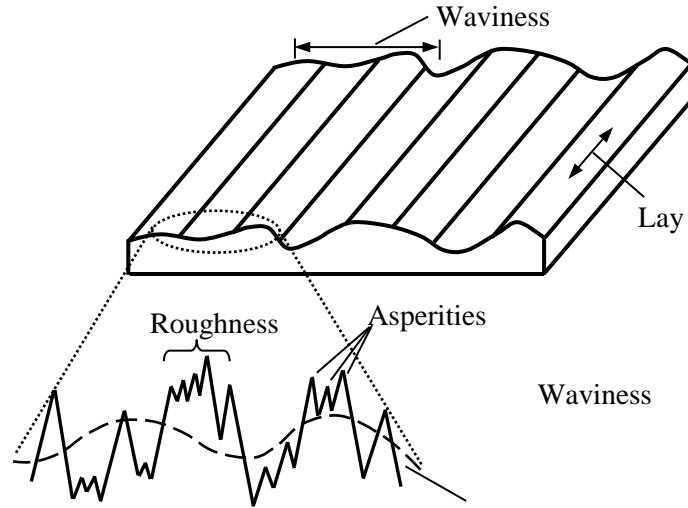


Figure 1.5 Schematic diagram of components of surface texture

Lay refers to the machine feed marks left on the surface by a cutting tool. A surface may have more than one lay direction created by a number of passes in different directions by the cutting tool. Waviness is the long wavelength of the surface. Roughness is the finer irregularities of the surface texture, usually resulting from the inherent action of the manufacturing process.

A common parameter for characterising roughness is the average roughness R_a , also called the arithmetic mean or centre line average (CLA) roughness, of the surface profile. The average roughness is the arithmetic mean of the absolute value of the height variation on the surface. Mathematically it can be expressed as:

$$R_a = \frac{1}{\tilde{L}} \int_0^{\tilde{L}} |\tilde{z}(\tilde{x})| d\tilde{x} \quad (1.14)$$

where \tilde{L} = assessment length,

\tilde{x} = reference axis,

$\tilde{z}(\tilde{x})$ = height variation of the surface profile (with respect to the reference axis).

The average roughness is graphically described as shown in Fig. 1.6 [Khonsari and Booser, 2008]. The centre line divides the surface profile into 'upper' and 'lower' portions such that the total area enclosed by the profile and the centre

line above the centre line (total shaded area) equals that below the centre line (total area of the valleys). This line serves as reference axis for the vertical coordinates of the points defining the profile. A reference sampling length is considered for this assessment.

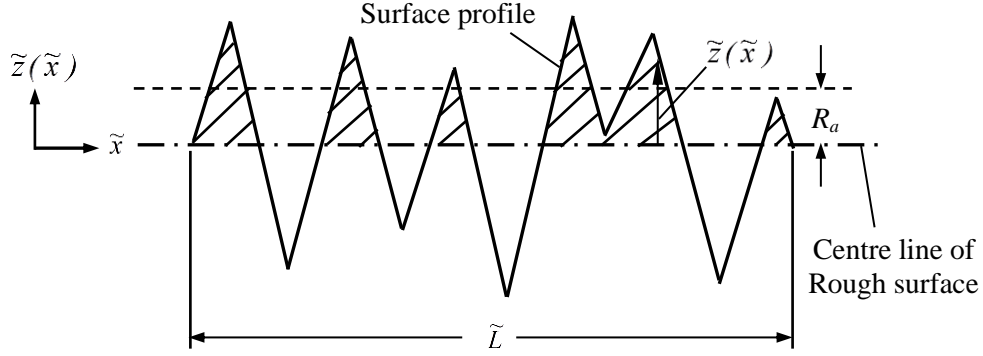


Figure 1.6 Schematic diagram for the description of average surface roughness (R_a) [Khonsari and Booser, 2008]

Another commonly used surface roughness parameter is the root mean square roughness R_q . It is the root mean square average height of the surface profile. The root mean square roughness is more sensitive to the occasional high and low points on the surface than the average roughness. The root mean square roughness is mathematically expressed as:

$$R_q = \sqrt{\frac{1}{\tilde{L}} \int_0^{\tilde{L}} [\tilde{z}(\tilde{x})]^2 d\tilde{x}} \quad (1.15)$$

Equivalent average roughness R_a' and equivalent root mean square roughness R_q' have been derived to account for the interaction between two surfaces in contact:

$$R_a' = \sqrt{R_{a1}^2 + R_{a2}^2} \quad (1.16)$$

where R_{a1} = average roughness of surface 1,
 R_{a2} = average roughness of surface 2.

$$R_q' = \sqrt{R_{q1}^2 + R_{q2}^2} \quad (1.17)$$

where R_{q1} = root mean square roughness of surface 1,
 R_{q2} = root mean square roughness of surface 2.

1.3 Lubrication Regimes

Interactions between asperities on the surfaces of machine components in contact with relative motion cause adhesion and deformation, which creates friction. Friction is not a material property; it is a system response. If there are neither chemical films nor adsorbents intercalated between two solid surfaces, high friction occurs. Lubricant provides a coherent film that separates the direct contact between the asperities. The majority of bearings operate under high loads and high speeds. The maximum contact pressure may be in the order of a giga-pascal (GPa) [Engineering Edge, 2010] due to the extremely small area of contact. The combination of severe loading and high velocity creates harsh lubrication conditions hindering the development of ideal fully flooded contact with thick film. These bearings operate under thin film, boundary or starved lubrication regimes.

According to tribologists, the performance of bearings in continuous use in machinery depends highly on the lubrication regime under which they operate [Williams, 1994 ; Cann and Lubrecht, 2005]. Stribeck performance curve is the most common tool used to illustrate the regimes of lubrication in bearings by relating the friction coefficient μ to a dimensionless parameter expressing the operating conditions, generally called Hersey number, H_s . These two parameters are defined as shown in Eq. (1.18) and Eq. (1.19).

$$\mu = \frac{F_f}{N} \quad (1.18)$$

where F_f = friction force,
 N = applied normal load.

$$H_s = \frac{\eta \omega}{p_{ave}} \quad (1.19)$$

where η = lubricant viscosity at ambient,
 ω = rotation speed,
 p_{ave} = average contact pressure.

If the applied load and the lubricant viscosity remain constant in operation, the frictional performance curve is directly related to the speed. A typical performance plot, referred to Stribeck curve, presents the friction behaviour for a hypothetical fluid-lubricated bearing system in terms of the friction coefficient as a function of the Hersey number that illustrates standard lubrication regimes variation is shown in Fig. 1.7 [Bhushan, 2002]. This plot also includes the friction behaviour of dry contact between clean surfaces, as illustrated in the extremely low Hersey number; however, it is not the interest of the present study.

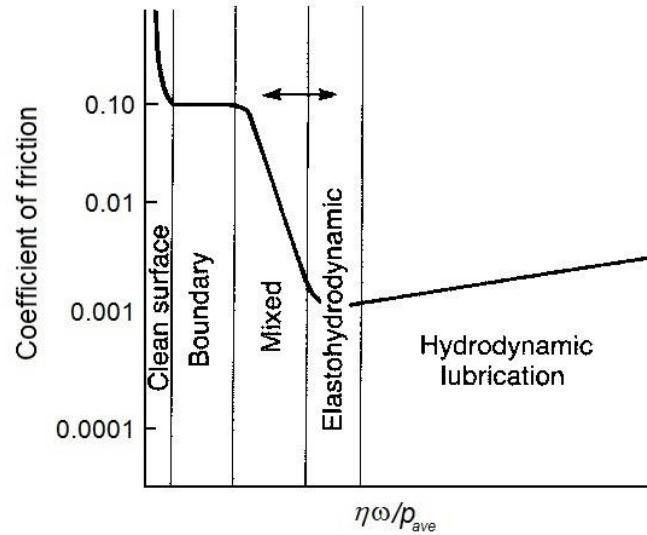


Figure 1.7 A typical Stribeck curve showing different lubrication regimes in fluid lubrication [Bhushan, 2002]

At low Hersey number (low speed), the lubricant film does not build-up and only a very thin layer of lubricant, a few molecules thick remains on the surfaces. This lubricant layer is unable to separate the surfaces and direct contact between the asperities plays a predominant role at the contact interface. A schematic diagram modelling this lubrication regime is shown in Fig. 1.8 (a). This situation most commonly occurs at start-up and shut-down during which acceleration and deceleration phases take place. The corresponding lubrication regime is referred to as boundary lubrication and results high friction at the contact. This high friction value is persistent with increasing Hersey number until a first threshold value is reached. As the Hersey number increases, a noticeable and rapid decrease in friction values is emerged. This is explained by the buildup of EHL film and shared load support between the surface asperities and the pressurised liquid lubricant present at the contact interface. The lubrication film is further built up as the Hersey number increases so that there are fewer asperities in contact and, hence, friction decreases. In this regime, because the lubrication film is thin and is penetrated by the asperities so that some contacts take place between the asperities. The friction at the contact interface is contributed by two lubrication mechanisms: the lubricated asperity interactions and the shearing of the EHL film and it is referred to mixed lubrication regime. Fig. 1.8 (b) illustrates the contact interface of the mixed lubrication. In this

regime, wildly varying friction values can be measured and are strongly dependent on operating conditions. With a further increase in Hersey number, friction reaches a lower plateau values, corresponding to the surfaces are just no longer in contact and they are effectively separated by the full film EHL. This indicates the onset of the hydrodynamic lubrication, at which asperity contact has negligible effect on load support and friction. The resistance to motion (friction) originates from the shearing of the film. A schematic model of the contact interface operating under this regime is shown in Fig. 1.8 (c). A slight increase of friction with the Hersey number following the establishment of the hydrodynamic lubrication may happen. This increase in friction can be attributed to increase in shear stress in the lubricant film, which increases the redundant work in the system; hence, negatively affecting the performance of the bearing [Hamrock *et al.*, 2004]. In addition, Hersey numbers pertaining to the borders between different lubrication regimes are not universal as this parameter is sensitive to the operating condition and the viscosity of the lubricant.

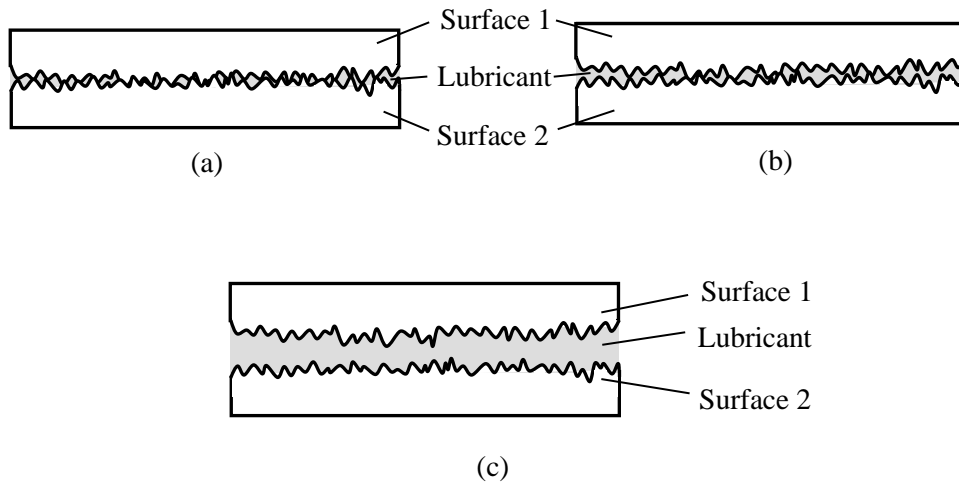


Figure 1.8 Schematic diagrams of lubrication regimes, (a) Boundary lubrication, (b) EHL mixed lubrication and (c) Hydrodynamic (full film) lubrication

2. LITERATURE REVIEW

The increase of film thickness with the speed, interpreted from the friction performance, in a fully flooded EHL regime has been verified analytically [Cann *et al.*, 2004 ; Pepper, 2008 ; Svoboda *et al.*, 2013]. In contrast, insufficient lubrication may trigger a decrease in the film thickness at a critical speed signaling the onset of starved condition [Guangteng *et al.*, 1992 ; Cann *et al.*, 2004 ; Berthe *et al.*, 2014]. Fig. 2.1 [Cann *et al.*, 2004] shows published experimental results of measured film thickness at the contact of a ball-on-disc model as a function of speed. The film thickness increases initially with speed, in agreement with the classical relationship for fully flooded condition which predicts a power law variation. An exponent equivalent to 0.67 has been reported by [Damiens *et al.*, 2004]. The occurrence of starvation affects the film thickness, which decreases with speed and research shows that in this case a power index of -1 is applicable.

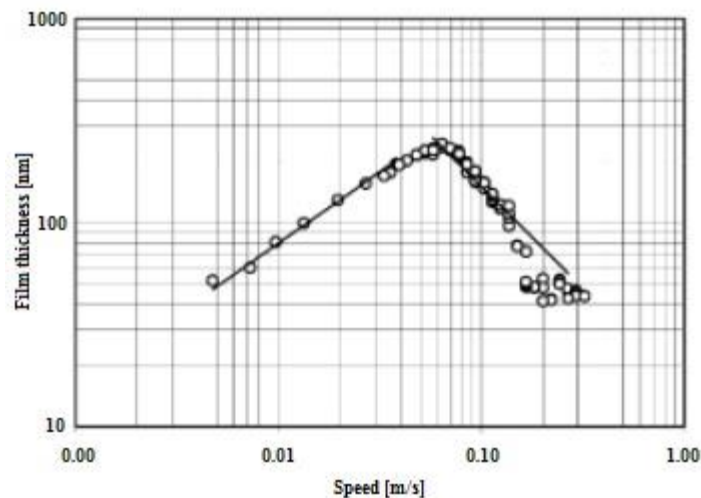


Figure 2.1 Measured film thickness as a function of speed in starvation study [Cann *et al.*, 2004]

The phenomenon of side leak may also affect starvation in the case of non-replenishment of lubricant [Cann *et al.*, 2004]. Chevalier *et al.* [1998], Cann *et al.* [2004], Ali and Hartl [2012], Svoboda *et al.* [2013] and Berthe *et al.* [2014] have concluded that starvation is accentuated for the case of lubricants exhibiting high nominal viscosity, which negatively influences the replenishment mechanism; based on their work on high-speed bearings lubricated with grease. Much attention has been paid to the understanding of starvation in lubricated systems operating under conditions that, although perceived as generating, ideal lubrication regime, do not permit the build-up of thick film. In such cases mixed lubrication starved regime is

more likely to occur [Faraon and Schipper, 2006 ; 2007]. The perception that fully flooded contacts prevailed; assuming the inlet was in all cases supplied with sufficient lubricant was questioned when it was recognised that some machine elements suffered from lubricant starvation [Hamrock and Dowson, 1981]. The findings of the initial studies interested in the starvation phenomenon pointed out the importance of the volume of lubricant supplied to the inlet of the bearing.

Gurbin theory [Grubin and Vinogradova, 1949] stipulates that in EHL regime, the central film thickness h_c build-up process is primarily initiated far in advance upstream of the border of the Hertzian contact area generated by the loading. Fig 2.2 [Errichello, 2015] depicts a schematic illustration of this model, with h as the height of the gap between two surfaces. The literature reported convincing evidence, in agreement with the theory, to demonstrate that the film thickness in the active zone of a bearing is controlled by the conditions governing the inlet region; specifically the inlet film thickness h_{in} , which defines in a way the supply of lubricant. However, the classical EHL theory is based on the condition of continuity of flow. In this ideal situation, the pressure buildup in the lubricant starts far away from contact area edge at almost zero pressure gradients. This pressure increase produces viscosity rise contributing greatly to the conditions for load bearing capacity.

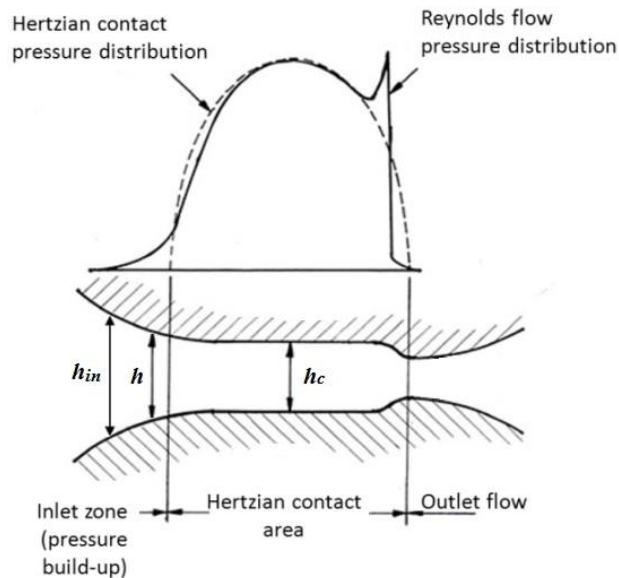


Figure 2.2 Schematic illustration of Grubin's EHL contact model [Errichello, 2015]

The discovery of starvation created by limiting the supply of lubricant at the inlet has prompted researchers to develop new models to describe starved films. In

practical applications, starvation is typical for bearings operating with less than ideal supplies of lubricant. This occurs in an environment that does not allow adequate replenishment in between over-rolling actions. In this case, the thickness and shape of the film at the inlet are influenced by body forces acting on it and the loading on the bearing but also the amount of lubricant supplied and the efficiency of replenishment action. In starved condition, the inlet boundary of the pressurized zone is free. The distance between this air-oil boundary, called the meniscus as shown in Fig. 2.3 [Ali and Hartl, 2012], and the edge of the Hertzian contact area, denoted as the inlet meniscus distance, was also found to be an important physical parameter for quantifying starvation. Closer location implies shorter inlet distance for pressure build-up, with the consequence of less than ideal film thickness and simultaneous increase of starvation severity. Accordingly, the onset of starvation has been defined by the condition that produces a shift of the inlet boundary to the location where the pressure build-up in the lubricant is initiated. Wedeven *et al.*, [1971] proposed that a good approximation of that location can be obtained from the maximum pressure gradient along the entraining direction. It was found that, according to the classical EHL theory, this pressure gradient reaches a maximum when the ratio between the local film thickness, along the entraining direction, and the central film thickness $h/h_c = 1.5$ and diminishes approaching zero in the upstream direction. An experimental assessment of this ratio by Wedeven *et al.* suggested an onset of starvation at $h_{in}/h_c \leq 9$ independently of the loading. However, it was concluded that starvation cannot be very well defined by this ratio.

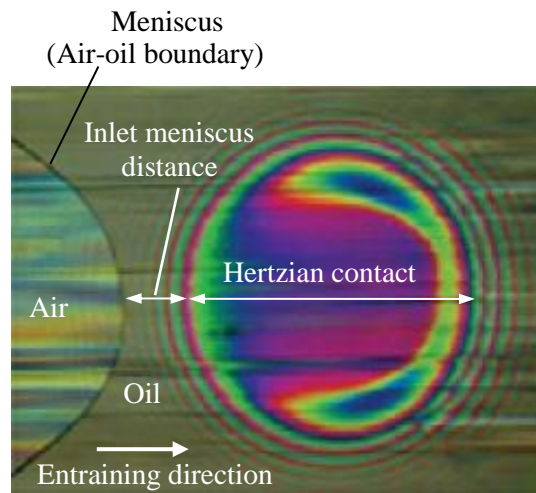


Figure 2.3 Interferometric image for illustrating the meniscus (air-oil boundary) at the EHL inlet in starved condition of oil lubricated ball-on-glass disc configuration [Ali and Hartl, 2012]

Wolveridge *et al.* [1971] extended Grubin's approach for the EHL film thickness [Grubin and Vinogradova, 1949] to propose a semi-analytical solution expressing the effect of the variation of the position of the inlet boundary (meniscus) of the lubricant film on the loading capacity of bearing rollers displaying line contact geometry. Subsequent studies were interested in the relationship between the relative film thickness reduction compared to fully flooded and the inlet boundary distance [Castle and Dowson, 1972]. However, it was realized that the proposed solution was less satisfactory when applied to point contact. Other studies such as Chiu [1974] also confirmed experimentally the significant reduction in film thickness at contact at high operation speeds after reaching a maximum value. In this study, it was supposed that some of the lubricant is pushed to the sides to form, in the case of a ball on raceway or flat, two ridges on either side of the track flows back into the track, driven by surface tension, and that the lubricant which thus returns provides the required inlet reservoir. Other authors did not acknowledge the importance of restricted oil supply on starvation in comparison with the combination of high speed and high viscosity. Hamrock and Dowson [1977b] developed a mathematical model describing the inlet meniscus position dependence on the film thickness in the starved EHL of point contact. The numerical finite difference iteration of Reynolds equation for evaluating the central film thickness in point contact configuration was modified to account for the influence of starvation. In their study, the location of the inlet boundary was moved closer to the Hertzian region to simulate the reduction of the inlet meniscus distance. The influence of partial filling, simulated by different starting positions of the inlet meniscus, on pressure and film thickness was explored theoretically. The conclusions were in agreement with the results obtained in the study by Wedeven *et al.* [1971].

Kingsbury [1973] proposed that the degree of starvation is linked to the balance between the amount of oil ejected from the rolling track and replenishment at the inlet. Pemberton and Cameron [1976], using aerated oil, observed of the direction of flow around an EHL contact formed between a glass plate and steel ball. Replenishment of the inlet region from lubricant side bands was perceived within the inlet meniscus.

The parched lubrication concept was proposed by Kingsbury [1985]. It was suggested that the surfaces remain separated by a thin film even when there is effectively no lubricant resupply. Because of severe starvation in this case, the film thickness ceases to decrease. This concept was experimentally verified using oil films of 80 nm and 200 nm thick deposited on ball bearing surfaces. It was shown that the bearings operated smoothly for considerable period without further resupply of lubricant. Parched lubrication concept was also verified by Guangteng *et al.* [1992] by performing film thickness measurements in the heavily starved condition. Ultra-thin film interferometry combining IR reflection-absorption

spectroscopy and optical techniques served to measure thin oil films at and on the out-of-contact locations. It was observed that when there was no measurable meniscus beyond a certain speed. A film 10 nm to 30 nm thick remained at the contact interface to separate the surfaces. It was concluded that as the inlet meniscus approaches the edge of the Hertzian contact area, the balance between the loss and the in-flow of oil creates an equilibrium state of the film thickness. It was suggested that this mechanism is typical in high speed bearings and systems with limited oil supply. Jacod *et al.* [1998] proposed an additional replenishment mechanism: out-of-flow reflow, which takes place remotely from the contact, during the time between over-rolling. However, it was shown that this replenishment mechanism was ineffective to play an important role when dealing with thin layers of lubricants. On the contrary, rapid flow was detected occurring at the vicinity of the contact area which was attributed to in-contact reflow mechanism. Numerical simulation results showed similar flow pattern to the experimental observation. However, the theoretical prediction showed much milder decreases in film thickness than those observed experimentally. Therefore an additional unknown oil loss mechanism may be responsible of eliminating oil from the track at higher speed.

A practical model to describe starved lubrication was put forward later by Chevalier *et al* [1998]. In their investigation, the Elrod [1981] algorithm for cavitation analysis to EHL problems was applied and showed that if the thickness of oil layers present on the surfaces (“initial film thickness”, a parameter representing the amount of oil) is known, the inlet meniscus can be obtained numerically. They investigated the film thickness decay rate due to side leakage by repeatedly using the outlet film thickness behind the contact as the initial film thickness. Accordingly, the condition of starvation is related to the ratio between the thickness of the lubricant layer at the inlet h_{in} and the gap height predicted by the theory (Reynolds equation). Further research done on this subject revealed good correlation between this ratio and the relative film thickness with respect to the fully flooded state; according to the following relationship; in which γ is the dimensionless film reduction parameter introduced to characterize the EHL contact behaviour in starvation regime. The dimensionless film reduction parameter is based on defining the amount of oil that is removed from the over-rolled track every time the rolling elements pass through the contact. This parameter depends on the operating conditions which influence the behaviour of the actual contact zone with respect to the flowing characteristics of the lubricant. It can be considered as a resistance to side-flow, hence, $\gamma = \infty$ means no side flow. Setting the condition of starvation as the relative film thickness \mathcal{R} , which is the ratio between the reduced central film thickness in the starved condition h_{cs} and the central film thickness in the fully flooded condition h_{cff} :

$$\mathcal{R} = \left(\frac{h_{cs}}{h_{cff}} \right) \quad (2.1)$$

The influence of the inlet film thickness h_{in} on the starvation is according to the following model [Chevalier *et al.*, 1998]:

$$\frac{\left(\frac{h_{in}}{h_{cff}} \right)}{\sqrt[\gamma]{1 + \left(\frac{h_{in}}{\bar{\rho}_{max} h_{cff}} \right)^\gamma}} = \mathcal{R} \quad (2.2)$$

It is to note that $\bar{\rho}_{max}$ is the dimensionless density parameter, which will be discussed in section 3.1.3, with respect to the maximum Hertzian pressure. A generalized graphical solution of the relative film thickness \mathcal{R} ; characterising the condition of starvation, as function of $(h_{in}/\bar{\rho}_{max} h_{cff})$ for $\gamma=1, 2, 3$ and 4 , taken as examples, is depicted in Fig. 2.4. It serves to illustrate the severity of starvation which may occur when a bearing, required to operate under certain conditions, is lubricated by a layer of oil that generates an inlet film thickness h_{in} . The solution is constrained by two asymptotes: the 45° line models the starved condition with no excess flow of lubricant around the contact zone. The second asymptote corresponding to increasing $(h_{in}/\bar{\rho}_{max} h_{cff})$ which would reduce the severity of starvation; converging toward $(h_{cs}/h_{cff}) = 1$ depending on γ . Operating under conditions generating higher γ which implies less resistance of the contact to the lubricant would prevent starvation when $(h_{in}/\bar{\rho}_{max} h_{cff}) > 1$. According to this concept, fully flooded film takes place when γ is very high and $h_{in} = \bar{\rho}_{max} h_{cff}$.

The above starvation criterion was used to estimate h_{in} in the present study, from Eq. 2.2, which gives:

$$h_{in} = \frac{\bar{\rho}_{max} h_{cff}}{\sqrt[\gamma]{\left(\frac{h_{cff}}{h_{cs}} \right)^\gamma - 1}} \quad (2.3)$$

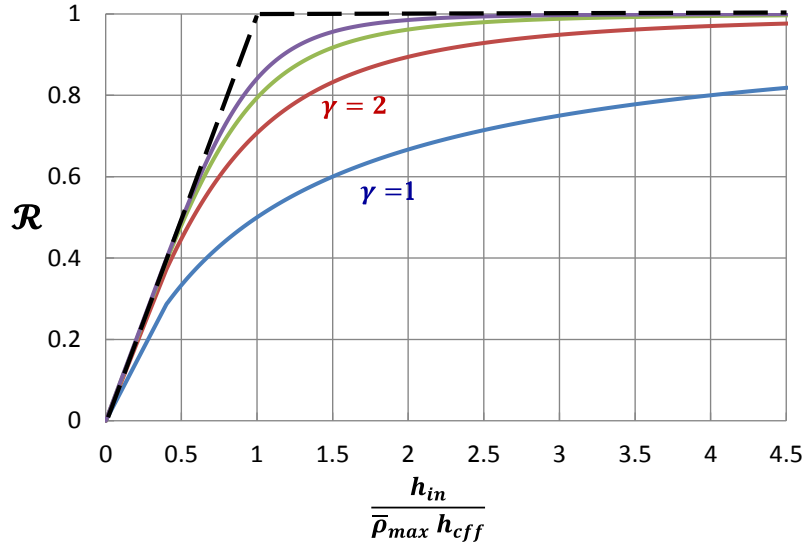


Figure 2.4 Model for the condition of starvation [Chevalier *et al.*, 1998]

In an effort to develop quantitative modeling of the degree of starvation, exploration of the significance of the location of the free boundary of the lubricating film at the inlet of the contact zone became the focus of many researchers. Important findings followed suit in the prediction of its location from the edge of the Hertzian contour of the area of contact taken as reference. This part of the whole lubricating film constitutes the meniscus. The notion of meniscus distance was introduced for defining the location of the free boundary with the objective of using this parameter to quantify the degree of starvation. The inlet meniscus distance s is then:

$$s = x_{in} - b \quad (2.4)$$

where x_{in} = distance between the Hertzian contact centre and the free air-oil boundary,

b = semi (minor) axis length along the entraining direction of the Hertzian contact ellipse.

Making reasonable assumption that x_{in}/b should be small; between 2 to 3, Wedeven *et al.*, [1971] have obtained the following relationship which estimates s as function of h_{in} and h_c with at least 93 % confidence.

$$s = \left(\frac{h_{in}/h_c - 1}{1.21} \right)^{\frac{2}{3}} \frac{(r_x h_c)^{\frac{2}{3}}}{b^{\frac{1}{3}}} \quad (2.5)$$

EHL theory as well as the extensive experimental work done in this field, reveal the very efficient use of the available lubricant at the inlet of these contacts. Even small amounts of lubricant are sufficient to generate a “healthy” film. However, if h_{in} is not sufficient, the hydrodynamic pressure initiation is delayed downstream closer to the Hertzian contact zone and in this situation the film thickness converges toward $h_{in}/\bar{\rho}_{max} h_{eff}$; almost equivalent to h_{in} with a small correction for compressibility effects. In starved contact, the close location of the meniscus to the Hertzian causes very sharp pressure and viscosity gradients. In this situation Reynolds equation predicts a constraint on the lubricant to flow straight across the active zone. The dimensionless parameter γ , introduced earlier, is a function of the length of the pressure buildup zone upstream from the Hertzian area. A short inlet length s implies $\mathcal{R} < 1$ and a relatively higher value of γ , simulating a sudden increase of the bulk modulus of the lubricant preventing it from “escaping”. When operating with larger inlet length reaching s_{ff} ; the threshold of fully flooded state, a gentler pressure build-up occurs far away from the highly stressed area. Based on this model, Damiens *et al.*, [2004] have proposed the following equation for the estimation of s_{ff} depending on the geometry of the contact zone, the shape of the surfaces and the operating conditions which include the viscosity.

$$\bar{s}_{ff} = \frac{s_{ff}}{b} = C \sqrt{\frac{S'}{k (1 + r_x/r_y)}} \sqrt{\frac{L}{M}} \quad (2.6)$$

where S' = elliptic integral of the second kind

k = ellipticity parameter

r_x = equivalent radius in rolling (x) direction

r_y = equivalent radius in transverse (y) direction

For elliptical contact the constant C is equivalent to [Damiens, 2003]:

$$C = 2^{-1.5} 3^{-1.25} \pi^2 \frac{1}{\sqrt{k}} \quad (2.7)$$

M is the Moes [1992] dimensionless load parameter and L the dimensionless material parameter, representing the materials properties, operating conditions and lubricant properties and shown by Eqs (2.8) and (2.9), respectively:

$$M = \frac{N}{E' r_x^2} \left(\frac{\eta u_s}{E' r_x} \right)^{-3/4} \quad (2.8)$$

$$L = \xi E' \left(\frac{\eta u_s}{E' r_x} \right)^{1/4} \quad (2.9)$$

where N = applied load,

E' = equivalent elastic modulus,

r_x = equivalent radius in rolling (x) direction,

η = viscosity at ambient,

u_s = sum (combined) velocity of the entraining surfaces,

ξ = pressure-viscosity coefficient.

The dimensionless ratio s/s_{ff} represents the importance of Poiseuille's component of the flow modeled by Reynolds equation. Higher is this component more significant is the side flow removing the lubricant from the track. According to the concepts describing the flow, introduced earlier, this situation is represented by high γ and $\mathcal{R} \gg 1$; allowing h_{cs}/h_{eff} to converge toward 1. It is to note that this constitutes the ideal situation in a sense that increasing h_{in} further would not generate any additional benefit.

A quantitative model predicting the starved film thickness from the amount of oil available at the inlet zone was developed in more recent studies. The oil loss and replenishment mechanisms were considered to provide a model capable of predicting the onset of starvation. Damiens *et al.* [2004] described the creation of a lubricating film in starved condition as the function of the lubricant volume, contact conditions and geometry. The ratio between the dimensionless load and material parameters [Moes, 1992] appears to be the decisive factor in predicting the flow of lubricant in the contact. A dimensionless parameter of starvation was derived and used to characterise starvation under various lubrication conditions by relating to the ratio between the dimensionless load and material parameters.

Cann *et al.* [2004] modified the more classical replenishment model proposed by Damiens *et al.* [2001], which considered the starvation to be governed by speed, oil viscosity and applied load, by assuming that replenishment is driven by surface tension effect in the vicinity of the contact. Both studies pointed out that the replenishment flow is inversely proportional to the base oil viscosity, the

rolling track width and the velocity. Further investigations on starvation were carried out by studying the relationship between the film thickness, the properties of the lubricant and various parameters, such as lubricant volume, operation speed, applied load and lubricant viscosity. Fig. 2.5 [Cann and Lubrecht, 2007] shows the measured film thickness as a function of operating relative speed for different contact dimensions, oil viscosities and lubricant volumes in a typical starvation study. These results show a wide range of starvation critical speeds strongly depending on the operating conditions. The role of the product of lubricant viscosity and sliding speed [Chiu, 1974 ; Cann *et al.*, 2004] and the influence of the lubricant volume [Guangteng *et al.*, 1992] were examined. At the same time, Chevalier *et al.* [1998] related the lubricant film thickness at the interface to the amount of oil in the track of rolling, which depends on the amount of oil present in the vicinity of the rolling track. Cann *et al.* [2004] modified a more classical replenishment model proposed by Guangteng *et al.* [1992], considered that the replenishment out of contact is very slow and that rapid flow only occurs in the vicinity of the contact [Jacod *et al.*, 1998]. The fundamental assumption of the model is that oil will be pushed toward the sides of the contact; however, part of this oil flows back into the contact by reflow. This would have a beneficial effect on the film thickness formation between the surfaces in contact [Gershuni *et al.*, 2008]. In the Cann *et al.* study, the influences of combined parameters such as speed-viscosity and speed-load on film thickness were investigated. It was also noticed that the volume of oil played no role so long as the lubrication was in the fully flooded condition. Many of the above mentioned conclusions were also verified in another recent study [Svoboda *et al.*, 2014].

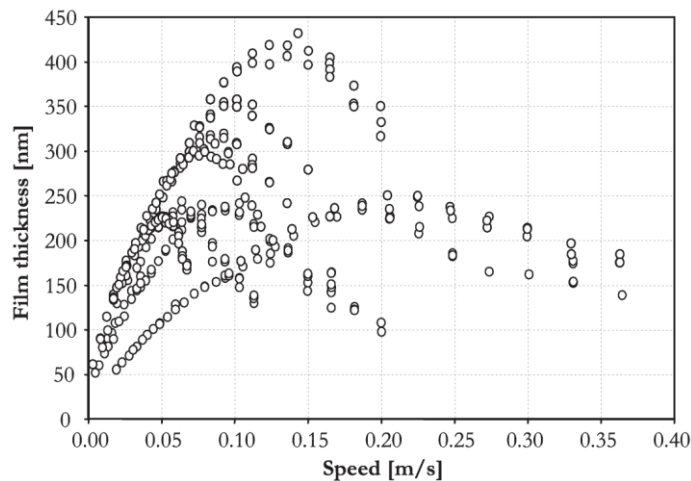


Figure 2.5 Measured film thickness as a function of operating speed for different contact dimensions, oil viscosities and oil volumes [Cann and Lubrecht, 2007]

Practically starvation could arise when replenishment becomes insufficient. This phenomenon occurs more often than it can be foreseen. Damiens *et al.* [2001] have simulated the loss and replenishment mechanisms at the contact zone in an effort to offer insights on the effects of replenishment on starvation. The model used supposed that lubricant replenishment occurs between over-rollings with the fundamental assumption that the amount of oil in the rolling track which generates h_{in} depends on the amount of oil supplied. This amount has been modeled in term of a fictive film called oil reservoir having a height $h_{oil\infty}$. In a steady EHL regime, the displaced lubricant redistributes itself to form equilibrium between loss and replenishment amounts. This process was modelled by the introduction of two characteristic time constants. The first represents the cycle time t_c , which represents the time available for replenishment and is defined by the travelling time of the lubricant between two over-rollings. It is the ratio of the travelled distance d_R and the relative sliding speed u .

$$t_c = \frac{d_R}{u} \quad (2.10)$$

The second time constant is the replenishment time t_r , which was determined by many researchers to be dependent on the lubricant properties which affect its side flow through the contact area half width in the transverse direction a . This was found to be proportional to the viscosity η and inversely proportional to the lubricant air surface tension σ_s [Guangteng *et al.*, 1992 ; Jacod *et al.*, 1998]; shown by the following equation:

$$t_r = \frac{\eta a}{\sigma_s} \quad (2.11)$$

The concept of starvation degree (SD) consisting of the ratio of both time constants was then introduced to quantify starvation. Accordingly, starvation is triggered at conditions that produce an unbalance of between loss and replenishment.

$$SD = \frac{t_r}{t_c} = \frac{\eta u a}{d_R \sigma_s} \quad (2.12)$$

Various experimental evaluations of this concept have determined some weaknesses in accurately representing starvation phenomenon. Cann *et al.* [2004] modified the proposed model, based on the assumption the replenishment is driven by surface tension effect in the vicinity of the contact. Their tests demonstrated that the volume of oil supplied influences SD linearly. Also, Baly *et al.* [2006] experiments concluded that d_R is not an important parameter. Therefore, it was

replaced by reservoir height $h_{oil\infty}$. This parameter was chosen as a characteristic of the volume of oil supplied, assuming a uniformly distributed layer. The amended version of this parameter is shown below:

$$SD = \frac{\eta u a}{h_{oil\infty} \sigma_s} \quad (2.13)$$

The film thickness $h_{oil\infty}$ and the contact area half width in the transverse direction, a , determined by the Hertzian contact solution according to the loading, are represented schematically in Fig. 2.6.

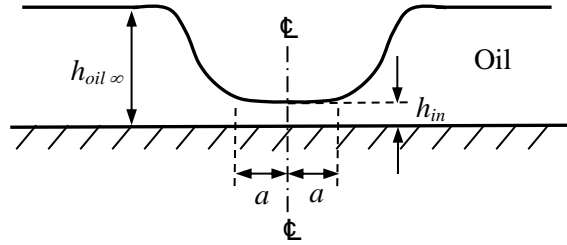


Figure 2.6 Schematic diagram of film thickness across the rolling track [Cann *et al.*, 2004]

The inlet film thickness h_{in} depends on the amount of oil available at the inlet of the track $h_{oil\infty}$ also known as the reservoir height. In this model, it is assumed that the replenishment process is influenced by surface tension of the liquid-air interface of the lubrication σ_s , in the vicinity of the contact; found earlier [Chiu, 1974]. The flow, hence, is proportional to the surface tension and the amount of oil, which is depicted by the reservoir height. The replenishment flow is also dependant on the oil viscosity, η , and the sliding velocity, u . SD was then proposed as criterion expressing the fully flooded to starved transition for the case of oil-lubricated point contact. A certain spread in the SD threshold values was usually observed interpreted by the thermal effects; influencing the lubricant properties, as well as the effects of oil migration at high speeds. Despite this uncertainty, the authors have put forward a threshold value of approximately 2 to indicate a deficit in the replenishment flow yielding starvation. On the contrary, when SD is lower than 1; interpreted by reflow that exceeds the removal, fully flooded condition prevails and the central film thickness can be predicted analytically. From this concept, the minimum quantity of lubricant to adequately lubricate a contact under given operating conditions can be predicted.

Pepper [2008] extended Cann *et al.* study into ultra-starvation. Experimental work by using spiral orbit tribometer, carried out in fully flooded lubrication as well as condition of only a few nano-liters of lubricant, was performed. It was shown that, in contrast to earlier suggested assumptions, lubricant remained on the rolling track in the form of monolayer and on the ball as liquid available for lubrication; not totally ejected from the contact zone. It was then concluded that lubricating fluid film may be established even heavily starved conditions. Berthe *et al.* [2014] carried out further investigation on the onset of starvation by means of friction experiments. Increasing friction was noted when the oil film became thinner increasing solid contact. The influence of oil volume, operation speed and load on the onset of starvation was examined by using a mini traction machine with ball-on-disc configuration. The onset of starvation in this study was found to occur at a range of starvation degree parameter varying between 1.5 and 4.0. It was also concluded that stepwise speed increase while monitoring the friction generated is an effective way of assessing the transition between fully flooded and starved lubrication.

So *et al.* [1987] conducted a theoretical study on the influence of surface roughness on starvation for the case of the rigid point contact; based on Padir and Cheng's [1978 ; 1979] flow model. The combined effect of speed and surface roughness was studied. Results showed that the effects of surface roughness may improve the lubrication to a small extent. Experiments were also performed in this study by using a steel ball on glass disc apparatus. Photo-microscope observations revealed that although the film was thin at low speeds, the inlet provided continuous oil supply to the contact zone creating the conditions of fully flooded lubrication. Inlet meniscus of oil appeared at higher speeds and moved closer to the contact area when the quantity of supplied oil decreased or in the case of increased speed. It was concluded that the relative surface speed was the most dominant parameter affecting the starvation. Svoboda *et al.* [2013] also studied the influence of surface texturing on the contact film thickness experimentally. Optical observations on the oil film thickness at contact by using a steel ball and glass disc tester lubricated in fully flooded and starved condition were performed. Steel ball surfaces were modified to contain micro-dents. It was found that the modification of surfaces affects the lubricant film thickness at the contact. Results showed that the passage of the shallow micro dents, of about 0.16 μm deep, through the contact positively affected the film thickness in starved condition. Moreover, the shallow micro-dents contributed, although slightly, to the increase of film thickness in fully flooded condition; in contrast deeper micro-dents of about 1.49 μm triggered a decrease.

Starvation in high speed ball bearings with complex ball-race contact geometry has been investigated by Olaru and Gafitanu [1993]. An analytical replenishment model correlating to oil viscosity, surface tension and thermal effect

was developed. The reduction of film thickness was computed with respect to the oil meniscus based on Hamrock and Dowson [1977b] proposed model. Correlation between the theoretical and experimental results provided information on the onset of starvation and film thickness reduction. The variation in the degree of replenishment as function of the bearing rotation speed for different oil layer thickness on the rolling track was also discussed. The effect of starvation on the traction and film thickness in EHL line contact was examined by Kumar and Khonsari [2008]. Carreau model, expressing the rheological behaviour of the lubricant, was considered to take shear-thinning effects encountered in EHL. Starved lubrication was simulated by shifting the inlet boundary toward the Hertzian contact area. Equations for estimating the increase of the friction coefficient, also called traction coefficient in rheology, and the film thickness decrease as a function of the degree of starvation were developed based on the simulation results. It was suggested to use the obtained factors to correct the friction coefficient and central film thickness predicted for fully flooded conditions. On the other hand, Hili *et al.* [2010] suggested that the effect that best describes the behaviour of film thickness at very high speeds is inlet shear heating. In their study the major factors that could influence film thickness of EHL contacts at very high speeds were investigated. The EHL film thickness in ball-on-disc fully flooded condition under high speed up to 20 m/s were measured by using optical interferometry technique. The results showed that, when the entrainment speed is increased above a few meter per second, the film thickness falls below those predicted by the Hamrock and Dowson [1977a] equations. It was found that the thermal correction factor predicts the trends of the film thickness behaviour well for the experimental measurements. Most recently, Masjedi and Khonsari [2015] investigated the modelling for the starved EHL film thickness with interaction between surface asperities for line and point contacts that allows studying the effect of starvation in EHL of rough surfaces. The modelling is based on the simultaneous solution to the modified Reynolds equation by Patir and Cheng [1978], deformation of the surfaces, load balance and asperity micro-contact equations suggested by Zhao *et al.* [2000]. In this approach, the degree of starvation is defined by the reduced mass flow rate at the contact centre, which is implemented by moving the inlet location toward the centre of the contact. The starved film thickness is predicted with respect to the operating condition, contact geometry, surface roughness and material properties. By relating the starvation to the reduced mass flow rate, the changes in the pressure distribution, effect of surface roughness and the film thickness were investigated. The simulation results show that, in general, the effect of starvation on the central film thickness is more pronounced compared to the minimum film thickness. In addition, it was found that the reduction in the film thickness is only a function of the fractional reduction in the lubricant mass flow rate in line contact; while in point contact the film thickness reduction is also a function of the ellipticity.

The effects of surface tension of the oil, non-uniformity of the inlet and inlet meniscus length were also taken into account in Nogi's [2015] numerical analysis of EHL starved point contact. It was found that the inlet distance is strongly depended on the amount of oil replenished from the side bands to the inlet. The importance of lubricant viscosity and inlet supply on starvation was emphasized by studies that considered grease as lubricant. It was reported that in a grease lubricated systems, local replenishment process plays a more important role than the bulk rheological properties [Åström *et al.*, 1992 ; Cann and Spikes, 1992 ; Cann *et al.*, 1992 ; Cann and Lubrecht, 1999 ; Venner *et al.*, 2008]. Moreover, it was determined that the design of the bearing; reflecting its geometry and size, significantly impacts the resupply of grease to the contact zone [Cann and Lubrecht, 2007]. The analysis of starvation in the case of grease lubrication is more complex than that in the case of oil [Cann *et al.*, 1996 ; Gershuni *et al.*, 2008]. The findings on this topic implied that the conclusions drawn for oil lubrication starvation are not applicable to very high viscosity lubricants such as grease.

The above review indicates that the film thickness measurements, for starvation studies, were performed in the majority of cases using optical techniques. Although this procedure provides the possibility of direct quantification, it requires one of the contacting surfaces to be flat and transparent; such as glass or clear plastic, and under thick film lubrication condition, without solid contact between the two elements of the bearing.

3. ELASTOHYDRODYNAMIC THEORY AND FILM THICKNESS IN MIXED LUBRICATION

A lubricant is injected between surfaces in contact with relative motion to reduce friction by providing a coherent film that allows the asperities to be separated. In fully flooded lubrication, the resistance to motion is only due to the shearing action of the viscous fluid while the applied load is still able to be carried by the pressure generated within the lubricant at the contact zone. In the case of the non-conformal contact of a ball bearing, it was initially believed that the lubricant would be entirely squeezed out. However, this high pressure produces an increase of viscosity and local elastic deformation of the surfaces. Both outcomes contribute to the process of film generation and increase of its thickness; preventing it from being entirely squeezed out of the contact and therefore at least a thin film is maintained. Fig. 3.1 illustrates schematically a proposed model that represents the three main parameters significantly impacting the behaviour of the lubricating film. The evaluation of the central film thickness requires finding a solution of the Reynolds equation that satisfies at the same time the elastic deformation equation and the viscosity-pressure relationship. These governing equations are generally solved using finite difference iterative process by means of high-speed computers. This numerical method yields estimations of the film thickness for fully flooded EHL regime as well as the pressure distribution in the flow at the contact zone.

Results generated based on the model above have revealed the significant impact of normal load applied to the bearing on the film thickness. In the mixed lubrication, in which contact between asperities of the surfaces take place, Johnson's statistical model describing the mode of interaction between asperities in a dry contact situation [Johnson *et al.* 1972] can be used to evaluate the extent of the solid to solid contact zone. A load shearing concept is introduced to account for the portion of the load supported by the hydrodynamic lifting force of the lubricant which affects the interaction mechanism predicted by Johnson's model. Relevant scaling factors were developed to account for this phenomenon in the evaluation of the resulting film thickness [Nijenbanning *et al.*, 1994]. In this chapter, the theories governing the classical hydrodynamic lubrication, the elastic deformation of bodies in contact and the relationship viscosity-pressure are presented. The results of their combination yielding a method for evaluating the film thickness in ideal case of fully flooded, very smooth contact operating under EHL regime.

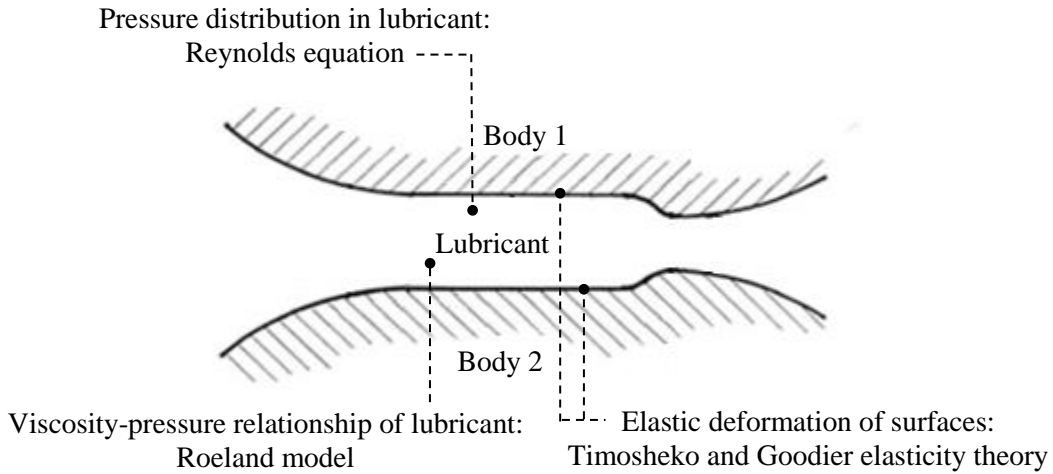


Figure 3.1 Schematic illustration of the modelling of the effects occurring at a loaded lubricated contact interface (contact geometry adopted from [Errichello, 2015])

3.1 Elastohydrodynamic Film Thickness Theory

3.1.1 Reynolds Equation

The first equation derived by Osborne Reynolds in 1886 predicts the relationship between the pressure distribution and the film thickness for an incompressible fluid transported in a converging opening by a relative movement of one surface. The effects of compressibility and dynamic loading were later added to this analysis [Harrison, 1913]. The generalised Reynolds equation was established from the conditions of equilibrium of forces acting on the fluid and the continuity of flow; assuming negligible inertia and body forces.

The equilibrium condition is applied to arbitrary volume element dx , dy and dz at a location in the fluid away from boundaries and moving at velocities u , v and w in x , y and z directions, respectively; as shown in Fig. 3.2. The height of the gap between the two surfaces at that location is h . The surfaces forming the opening move at relative speeds u_1 and u_2 . For simplicity, only two-dimensional case is considered.

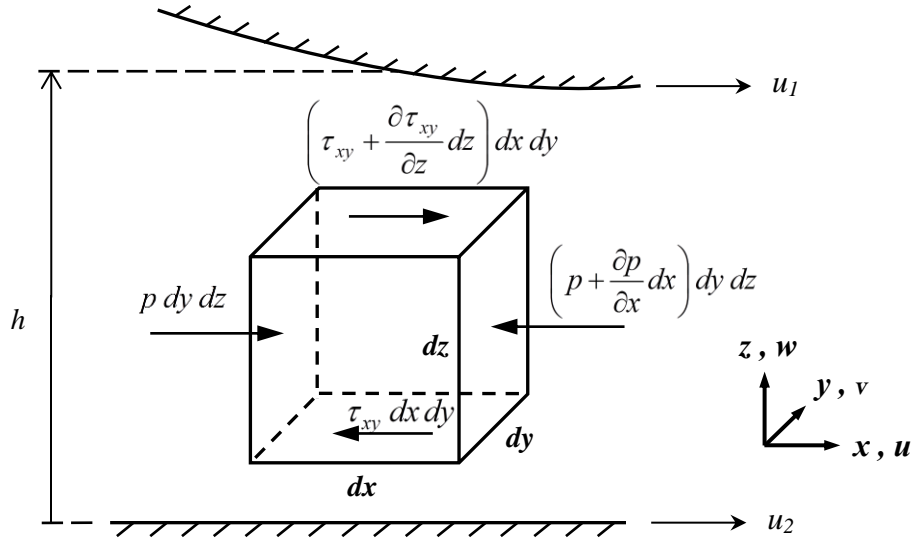


Figure 3.2 Fluid element in static equilibrium

Increments of pressure ($\partial p/\partial x$) along the x -axis and shear stress ($\partial \tau_{xy}/\partial z$) along the vertical axis are considered. The condition of equilibrium of loading on the element about the x is described by the following expression:

$$p \, dy \, dz - \left(p + \frac{\partial p}{\partial x} dx \right) dy \, dz - \tau_{xy} \, dx \, dy + \left(\tau_{xy} + \frac{\partial \tau_{xy}}{\partial z} dz \right) dx \, dy = 0 \quad (3.1)$$

After expanding and cancelling terms, Eq. (3.1) reduces to:

$$\frac{\partial p}{\partial x} = \frac{\partial \tau_{xy}}{\partial z} \quad (3.2)$$

The stressing developed in Newtonian fluids is proportional to the imposed shearing rate level. The proportionality constant is equivalent to the viscosity as shown by the following relationship:

$$\tau_{xy} = \eta \frac{\partial u}{\partial z} \quad (3.3)$$

where η = dynamic viscosity of the fluid,

$\frac{\partial u}{\partial z}$ = velocity gradient in the z -direction; equivalent to shear rate.

Substituting Eq. (3.3) into Eq. (3.2):

$$\frac{\partial p}{\partial x} = \frac{\partial}{\partial z} \left(\eta \frac{\partial u}{\partial z} \right) \quad (3.4)$$

Integrating twice with respect to z yields the following:

$$\frac{\partial p}{\partial x} z + c_1 = \eta \frac{\partial u}{\partial z} \quad (3.5a)$$

$$\frac{z^2}{2} \frac{\partial p}{\partial x} + c_1 z + c_2 = \eta u \quad (3.5b)$$

Applying the boundary conditions of relative motion of the two surfaces: $u = u_2$ at $z = 0$ and $u = u_1$ at $z = h$; permits to evaluate the integration constants:

$$c_1 = \eta \frac{(u_1 - u_2)}{h} - \frac{h}{2} \frac{\partial p}{\partial x} \quad \text{and} \quad c_2 = \eta u_2$$

Substituting c_1 and c_2 into Eq. (3.6) and rearranging; the expression predicting the velocity in the x -direction (u_x) of a fluid particle belonging to the film at the contact is:

$$u_x = \frac{1}{2\eta} \frac{\partial p}{\partial x} (z^2 - zh) + (u_1 - u_2) \frac{z}{h} + u_2 \quad (3.6)$$

The volumetric flow rate along x -direction, considering a unit width d_y , is given by:

$$q_x = \int_0^h u_x dz \quad (3.7)$$

Replacing u_x by Eq. (3.7) and integrating with respect to z :

$$q_x = \left[\frac{1}{2\eta} \frac{\partial p}{\partial x} \left(\frac{z^3}{3} - \frac{z^2 h}{2} \right) + (u_1 - u_2) \frac{z^2}{2h} + u_2 z \right]_0^h = \frac{-h^3}{12\eta} \frac{\partial p}{\partial x} + (u_1 + u_2) \frac{h}{2} \quad (3.8)$$

Similarly, the volume flow rate along y-direction, per unit width dx :

$$q_y = \frac{-h^3}{12\eta} \frac{\partial p}{\partial y} + (v_1 + v_2) \frac{h}{2} \quad (3.9)$$

Also, $\frac{\partial p}{\partial z} = 0$; assuming no pressure gradient through the film thickness.

Fig. 3.3 shows the variation of volume flow rate in all three directions in steady state condition; applied to an element of fluid of height h and base $dx \times dy$.

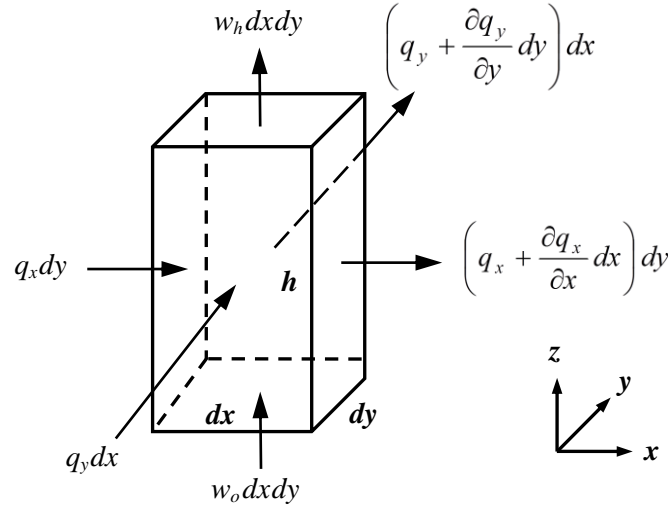


Figure 3.3 Continuity of flow in an element

The condition of continuity can be written as follow:

$$q_x dy + q_y dx + w_o dx dy = \left(q_x + \frac{\partial q_x}{\partial x} dx \right) dy + \left(q_y + \frac{\partial q_y}{\partial y} dy \right) dx + w_h dx dy \quad (3.10)$$

where w_o = velocity of the “floor” of fluid column in z-direction
 w_h = velocity of the “roof” of fluid column in z-direction

After simplification:

$$\frac{\partial q_x}{\partial x} + \frac{\partial q_y}{\partial y} + (w_h - w_o) = 0 \quad (3.11)$$

In steady state condition, the density of the fluid, ρ , is constant and when introduced in the equation of continuity it yields the condition of equilibrium of the mass flow rate:

$$\frac{\partial(\rho q_x)}{\partial x} + \frac{\partial(\rho q_y)}{\partial y} + \rho(w_h - w_o) = 0 \quad (3.12)$$

The generalised Reynolds equation in three-dimensions is obtained by substituting Eqs (3.8) and (3.9) into (3.12) and replacing $(w_h - w_o)$ by $\frac{\partial h}{\partial t}$; t being the time variable, into Eq. (3.12):

$$\begin{aligned} \frac{\partial}{\partial x} \left(\frac{\rho h^3}{12\eta} \frac{\partial p}{\partial x} \right) + \frac{\partial}{\partial y} \left(\frac{\rho h^3}{12\eta} \frac{\partial p}{\partial y} \right) = \\ \frac{\partial}{\partial x} \left[\frac{\rho(u_1 + u_2)h}{2} \right] + \frac{\partial}{\partial y} \left[\frac{\rho(v_1 + v_2)}{2} \right] + \frac{\partial}{\partial t} (\rho h) \end{aligned} \quad (3.13)$$

In the steady state condition with no side flow, Reynolds equation reduces to [Arnell *et al.*, 1991]:

$$\frac{\partial}{\partial x} \left(\frac{\rho h^3}{\eta} \frac{\partial p}{\partial x} \right) + \frac{\partial}{\partial y} \left(\frac{\rho h^3}{\eta} \frac{\partial p}{\partial y} \right) = 12\bar{u} \frac{\partial(\rho h)}{\partial x} \quad (3.14)$$

In which, \bar{u} is the average velocity of the surfaces in contact: $\bar{u} = (u_1 + u_2)/2$, which will be later referred to as the entrainment velocity.

3.1.2 Elastic Deformation

The parameters defining the general geometry of two ellipsoidal solids in elastic contact were described in Chapter 1. The elastic deformation at each point of the contacting surface, in the direction of the normal loading, can be considered to be equivalent to the total deformation of two ellipsoids having elastic constants E_1 , ν_1 and E_2 , ν_2 . This total displacement can be obtained using the force-

displacement relationship developed by Timoshenko and Goodier [1951]. The elastic deformation, $d\delta$ at a point (\bar{x}, \bar{y}) of a semi-infinite solid subject to a pressure p at the point (\bar{x}_1, \bar{y}_1) can be written as:

$$d\delta = \frac{2p d\bar{x}_1 d\bar{y}_1}{\pi E' \bar{r}} \quad (3.15)$$

where \bar{r} is the length of 2D vector joining points (\bar{x}_1, \bar{y}_1) and (\bar{x}, \bar{y}) ; which is equivalent to $\sqrt{(\bar{x} - \bar{x}_1)^2 + (\bar{y} - \bar{y}_1)^2}$.

Considering a uniform pressure p acting on an element of the contacting surface as shown in Figs 3.4 (a) [Gohar, 2001] and 3.4 (b) [Hamrock and Dowson, 1981], the elastic deformation, δ at a point (\bar{x}, \bar{y}) generated by a uniform pressure acting on a rectangular element of the contact surface of dimensions $(2\bar{a} \times 2\bar{b})$ can be written as:

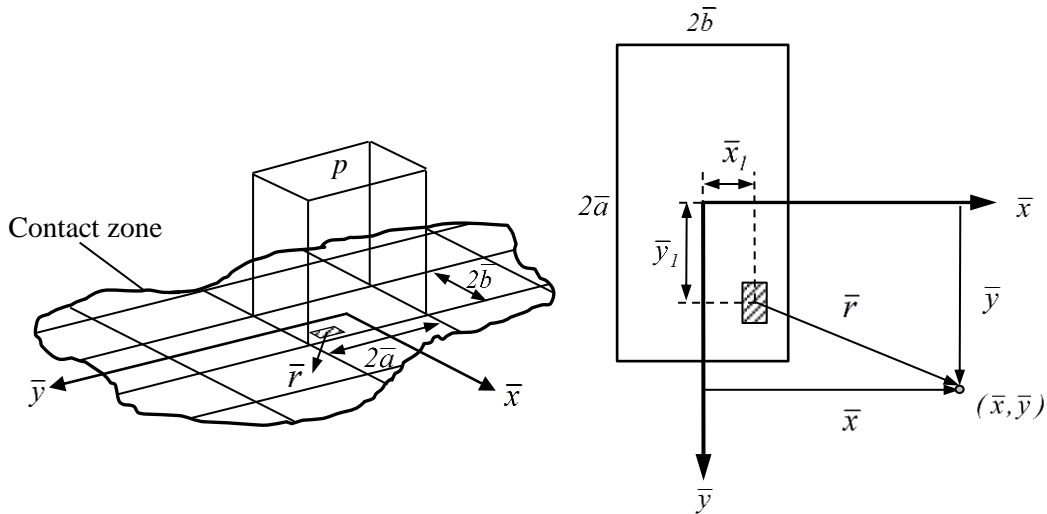


Fig. 3.4 (a) Schematic diagram of a small rectangular area in the contact zone under uniform pressure p [Gohar, 2001]

Fig. 3.4 (b) Schematic diagram of the coordinate system of a small rectangular area in the contact zone under uniform pressure p [Hamrock and Dowson, 1981]

$$\delta = \frac{2p}{\pi E'} \int_{-\bar{a}}^{\bar{a}} \int_{-\bar{b}}^{\bar{b}} \frac{d\bar{x}_l d\bar{y}_l}{\sqrt{(\bar{x} - \bar{x}_l)^2 + (\bar{y} - \bar{y}_l)^2}} \quad (3.16)$$

The displacement equation is generally solved analytically considering constant pressure acting on a surface element. The superposition of all effects of elements of pressure surrounding the point of interest permits the evaluation of contact deflections.

The EHL regime establishes from the combination of hydrodynamic state linked to the build-up of pressure at the contact zone and its engendered elastic deformation allowing the formation of a thick film preventing contact between lubricated surfaces in relative motion. This deformation is dependent on the pressure; particularly the pressure distribution across the whole Hertzian contact zone [Goodyer, 2001]. For point contact configuration, the contact of the two undeformed ellipsoidal solids, as shown in Fig. 1.2, can be described by an equivalent ellipsoidal solid near a plane. This provides a convenient way of viewing the contact, where the geometric surface separations and elastic surface deformation from both surfaces are summed together to act on this equivalent surface [Hamrock and Dowson, 1981 ; Blahey, 1985]. The model simulating the film thickness $h(x,y)$ is shown schematically in Fig. 3.5. It is equivalent to the separation inherent to the geometry of the equivalent ellipsoidal solid, described by the function $S(x,y)$, considered rigid and separated from the flat surface by a film of central thickness h_o , and the elastic deformation $\delta(x,y)$. This is mathematically expressed as follow:

$$h(x, y) = h_o + S(x, y) + \delta(x, y) \quad (3.17)$$

The function representing the geometry of the ellipsoid is:

$$S(x, y) = \frac{x^2}{2r_x} + \frac{y^2}{2r_y} \quad (3.18)$$

The solution of an EHL problem requires calculating the pressure distribution at the contact using Reynolds equation and at the same time account for its effects on the properties of the fluid and on the geometry of the elastic solids. The viscosity and density of lubricant vary with the pressure. If applied to different points forming the contacting area, the lubricant film shape can be estimated [Hamrock and Dowson, 1981].

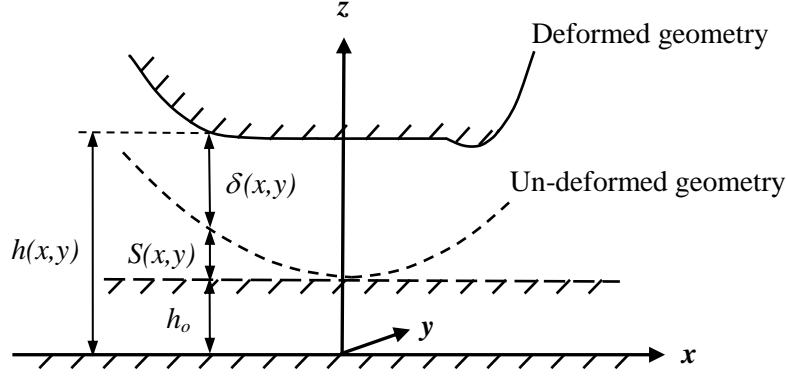


Figure 3.5 Schematic model of the EHL film thickness

3.1.3 Viscosity-Pressure and Density-Pressure Relationships of Lubricant

The behaviour of lubricants under high pressure encountered EHL is extremely important because of the resulting piezo-viscous properties. The increase of the viscosity of lubricants with the pressure is instrumental in forming a high performance film at the contact; when the isothermal condition is considered. When a lubricant is subjected to high pressure, the intermolecular forces increase and so does consequently viscosity [Gohar, 2001 ; Bhushan, 2002]. One of the approaches, which is also considered in the present study, was developed by Roelands [1966], who undertook a wide-ranging study of the effect of pressure on the viscosity of various lubricants. For isothermal condition, the Roelands viscosity-pressure model can be written as follows [Hamrock and Dowson, 1981]:

$$\eta^* = \eta \left(\frac{\eta_\infty}{\eta} \right)^{[1-(1+p/c_p)^{Z_1}]} \quad (3.19)$$

where η^* = viscosity under pressure,
 η = viscosity at ambient pressure,
 η_∞ = constant = 6.31×10^{-5} Ns/m²,
 p = pressure,
 c_p = constant = 1.96×10^8 Ns/m²,
 Z_1 = viscosity-pressure index.

The literature reveals superior experimental data fit by Roelands viscosity-pressure model compared to the initial relationship proposed by Barus [1893], which

predicts unrealistically high viscosities for high pressures encountered EHL. Furthermore, a comprehensive correlative expression, albeit at the cost of some algebraic complexity, for lubricant viscosity that includes the simultaneous effects of temperature and pressure has been further development by Houpert [1985] based on Roelands model. This modified model consists of experimentally determined extra parameters expressing the lubricant characteristics. Nevertheless viscosity variations due to thermal effects in the film of lubricant are generally neglected. This is particular because the temperature variations over the thickness of the film are dominating and these variations have systematically been neglected when deriving the Reynolds equation [Moes, 2000].

The effect of the pressure on viscosity is more marked in comparison to density. However, very high pressures trigger dependence of the density on pressure. This variation of density may be linear then increases at lower rate with pressure [Hamrock and Dowson, 1981]. The limit of the compression of mineral oils is 25%, for a maximum density increase of about 33%. Dowson and Higginson [1966] density-pressure relationship; below, reflects the diminishing compressibility as pressure is increased from atmospheric until the oil solidifies [Hamrock *et al.*, 2004 ; Khonsar and Booser, 2008]:

$$\rho^* = \rho_o \left(1 + \frac{0.6 p_G}{1 + 1.7 p_G} \right) \quad (3.20)$$

where ρ^* = density of pressurised fluid,

ρ_o = density at ambient,

p_G = pressure in GPa.

3.1.4 Elastohydrodynamic Film Thickness Solution

To elucidate the EHL of point contact under rolling, the film shape dictated by the initial geometry of the contacting bodies, the central film thickness as predicted by Reynolds equation considering the flow of lubricant between two rigid bodies in relative motion in addition to the elastic deformation of the surfaces induced by the hydrodynamic pressure distribution need to be considered. To study the behaviour of the film, it is necessary to solve the Reynolds equation, the elastic film shape and the lubricant state equations namely viscosity-pressure and density-pressure relationships. The numerical solution procedure is initiated by finding the footprint geometrical characteristics of the Hertzian elasto-static dry contact, then the corresponding pressure distribution is used as initial guess in the lubricant state equations as well as the Reynolds equation. The elastic deformation is then taken

into account in the evaluation of the film shape. The iterative process continues until convergence of the pressure distribution and film shape for a given load and speed of entraining motion.

Simplifying assumptions made in the past have produced very good approximated solutions starting in 1949 as reported by Ertel [Grubin and Vinogradova, 1949] and other studies [Petrusevich, 1951 ; Weber and Saalfeld, 1954]. More accurate solutions required the use of computers; work pioneered by Dowson and Higginson in 1959. Hamrock and Dowson [1976a ; 1976b ; 1977a] developed a Gauss-Seidel iterative method, based on a finite difference approximation of the Reynolds equation incorporating Vogelpohl pressure transformation and including surface meshing method for the evaluation of the elastic deformation. Wide ranges of operating conditions, which are common to engineering applications, were examined. Although there are more advanced computational methods, such as the non-uniformly spaced grid [Evans and Snidle, 1982], inverse solution procedure [Evens and Snidle, 1981] and multigrid method [Lubrecht, 1987], developed to speed-up the computational process; Hamrock and Dowson's work represents the analysis that is commonly accepted and used by engineering industry. It also serves as benchmark for comparison of results generated using other methods.

The type of lubrication taking place in non-conformal EHL contact is influenced by two major physical effects: the elastic deformation of the surfaces under an applied load and the increases in fluid viscosity with pressure. Although the contacting surfaces are considered undergo elastic deformation and the lubricant is considered to have piezoviscous behaviour at an EHL contact interface, this is not always the case. In fact, there are intermediate conditions that can occur. For example, in highly loaded contacts lubricated by common oils both effects are present. However, at light loads and high speeds, the elastic deformation may be negligible, unless with low modulus solid such as polymer or rubber, changes in viscosity of the lubricant are usually small. Therefore, it is possible to encounter four main EHL regimes of fluid-film lubrication, determined by the operating conditions and the properties of the material, which are qualitatively different [Johnson, 1970 ; Hamrock and Dowson, 1981 ; Gohar, 2001 ; Hamrock *et al.*, 2004]. The four EHL regimes are:

Rigid-isoviscous (RI) – in this regime, the pressure is not high enough to cause considerable elastic deformation of the surfaces in contact so that the elastic deformation effect can be neglected; concurrently, the pressure at the contact interface is too low to cause significant viscosity change in the lubricant. This form of lubrication can be found in lightly loaded roller bearings.

Elastic-isoviscous (EI) – in this regime, there is considerable elastic deformation of the surfaces at the contact, however, the pressure is not sufficiently high to cause any substantial increase in the lubricant viscosity. This situation arises with materials of low elastic modulus such as seals, human joints and elastomeric-material machine elements.

Rigid-piezoviscous (RV) – in this regime, the pressure at the contact is sufficiently high to substantially increase the viscosity of the lubricant at the interface. In this situation, it is necessary to consider the pressure-viscosity characteristics of the lubricant while assuming that the surfaces remain rigid. This form of lubrication may be found in the contacts in moderately loaded cylindrical tapered rollers, and between some piston rings and cylinder liners.

Elastic-piezoviscous (EV) – this is the fully developed EHL regime, in which the elastic deformation of the surfaces plays a significant role of the buildup of the film at the contact to separate the surfaces. At the same time, the pressure at the contact is high enough to cause a significant increase in the viscosity of the lubricant. This form of lubrication is typically encountered in ball and roller bearings, bears, and cams.

Archard [1968] recognised the difference between these regimes and distinguished between them as function of the pressure. The recognition of these regimes was further developed by Johnson [1970] using dimensionless group parameters that readily associate with the contact interface behaviour: dimensionless viscosity parameter g_v and the dimensionless elasticity parameter g_E .

$$g_v = \frac{GW^3}{U^2} \quad (3.21)$$

$$g_E = \frac{W^{8/3}}{U^2} \quad (3.22)$$

with the dimensionless parameters for load W , speed U and material G defined as follow:

$$W = \frac{N}{E' r_x} \quad (3.23)$$

$$U = \frac{\eta \bar{u}}{E' r_x} \quad (3.24)$$

$$G = \xi E' \quad (3.25)$$

Mappings of the EHL lubrication regimes were also performed with film thickness contours presented on a log-log scale chart; sometimes referred to Johnson chart, of the viscosity and elasticity parameters for different ellipticity parameters k . As an example, the map of EHL lubrication regimes for ellipticity parameter $k = 3$ is presented in Fig 3.6 [Hamrock *et al.*, 2004]. The appropriate EHL regime can be determined using the relevant chart. The horizontal axis is the criterion for elastic deformation represented by g_E and the vertical axis is the criterion g_V modelling the viscosity increase. The position of the operating point on the map defines uniquely the property of the EHL contact [Williams, 1994].

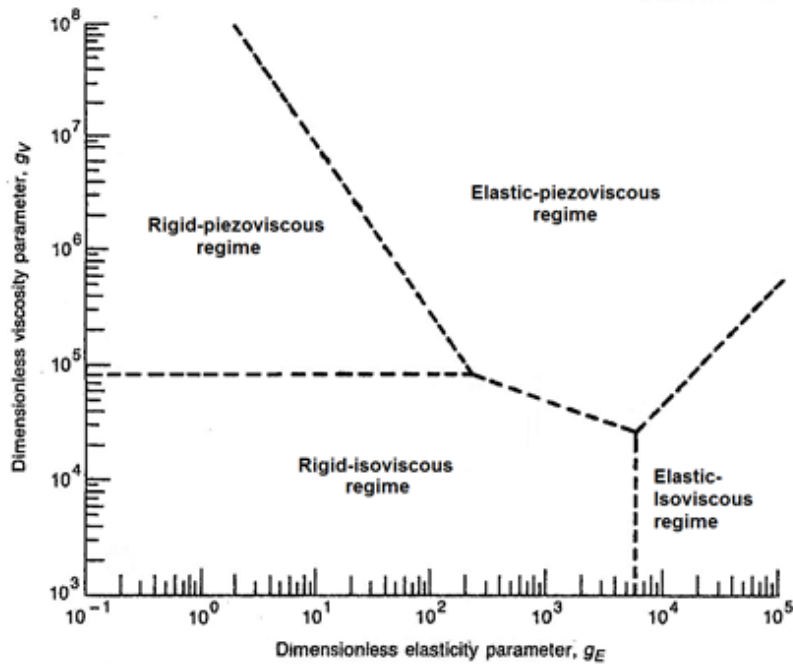


Figure 3.6 Map of EHL lubrication regimes with ellipticity parameter $k = 3$ [Hamrock *et al.*, 2004]

Several researchers have contributed in developing solutions for the EHL film thickness of elliptical contacts, from circular to rectangular, in the four EHL regimes: Brewe *et al.* [1979] investigated and developed the film thickness equation for the rigid-iso-viscous regime. Jeng *et al.* [1987] modified Blok [1952] work for the film thickness equation in the rigid-piezoviscous regime. Hamrock

and Dowson [1978 ; 1979] proposed film thickness equations for elastic-isoviscous and full EHL (elastic-piezoviscous) regime. These equations are the results of fitting an algebraic expression to a large number of computed results. Such equation only applies to the particular range of results from which it was derived and must not be extrapolated into widely different areas (regimes). In order to determine the appropriate equation to be used with respect to the EHL regime, it is necessary to evaluate the dimensionless groups for referring to the EHL regime map, such as that presented in Fig. 3.6.

The multilevel algorithm for the numerical solution of circular contact introduced by Venner [1991] was extended to elliptical contact EHL problem. The variation of the film thickness with the operating conditions and contact geometry were investigated using this algorithm. Venner [1991] and Moes [1992] constructed a film thickness formula, and further developed by Nijebanning *et al.*, [1994], by performing a function fit using solutions for the four asymptotic regimes, derived using Moes dimensionless parameters, as building blocks and further developed by Nijebanning *et al.* [1994]. The four asymptotic solutions: rigid-isoviscous (RI), rigid-piezoviscous (RI), elastic-isoviscous (EI) and elastic-piezoviscous (EV) for the film thickness in an elliptical contact are described below.

The expression for the dimensionless central film thickness , $H_{c,RI}$, in the rigid iso-viscous regime based on the work of Kapitze [1955] and Brewe *et al.* [1979] who proposed the following numerical solutions:

$$H_{c,RI} = 145 \left(1 + 0.796 D^{14/15}\right)^{-15/7} D^{-1} M^{-2} \quad (3.26)$$

The solution for the dimensionless central film thickness in the elastic iso-viscous regime, $H_{c,EI}$, is based on the work of Hamrock and Dowson [1978] and Crook [1961] is:

$$H_{c,EI} = 3.18 \left(1 + 0.006 \ln D + 0.63 D^{4/7}\right)^{-14/25} D^{-1/15} M^{-2/15} \quad (3.27)$$

The dimensionless central film thickness for the rigid piezo-viscous regime, $H_{c,RV}$, and elastic piezo-viscous , $H_{c,EV}$, were derived according to Grubin's work [Grubin and Vinogradova, 1949] are shown in Eq. (3.28) and Eq. (3.29), respectively.

$$H_{c,RV} = 1.29 \left(1 + 0.691 D\right)^{-2/3} L^{2/3} \quad (3.28)$$

$$H_{c,EV} = 1.48 \left(1 + 0.006 \ln D + 0.63 D^{4/7} \right)^{-7/20} D^{-1/24} M^{-1/12} L^{3/4} \quad (3.29)$$

D is the ratio of the equivalent radii; $D = r_x/r_y$, where r_x and r_y are the equivalent radii in rolling and transverse directions, respectively. M is the Moes [1992] dimensionless load parameter and L the dimensionless material parameter, representing the materials properties, operating conditions and lubricant properties described in Chapter 2:

$$M = \frac{N}{E' r_x^2} \left(\frac{\eta u_s}{E' r_x} \right)^{-3/4} \quad (2.8)$$

$$L = \xi E' \left(\frac{\eta u_s}{E' r_x} \right)^{1/4} \quad (2.9)$$

where N = applied load,

E' = equivalent elastic modulus,

r_x = equivalent radius in rolling (x) direction,

η = viscosity at ambient,

u_s = sum (combined) velocity of the entraining surfaces,

ξ = pressure-viscosity coefficient.

Fig. 3.7 [Venner, 1991] illustrates the dimensionless film thickness H_c obtained by direct computational calculations for a wide range of dimensionless parameters M and L . As an example to illustrate different EHL regimes, the rigid-iso-viscous (RI) regime asymptote (Eq. 3.26) and the elastic-iso-viscous (EI) asymptote (Eq. 3.27) are presented as the dotted line on the left and on the bottom, respectively. An accurate film thickness formula that is applicable over the entire parameter range can be obtained if all the four asymptotic solutions are taken into account and merged into one expression, with extra parameters to serve for smooth transitions in the intermediate region between the regimes.

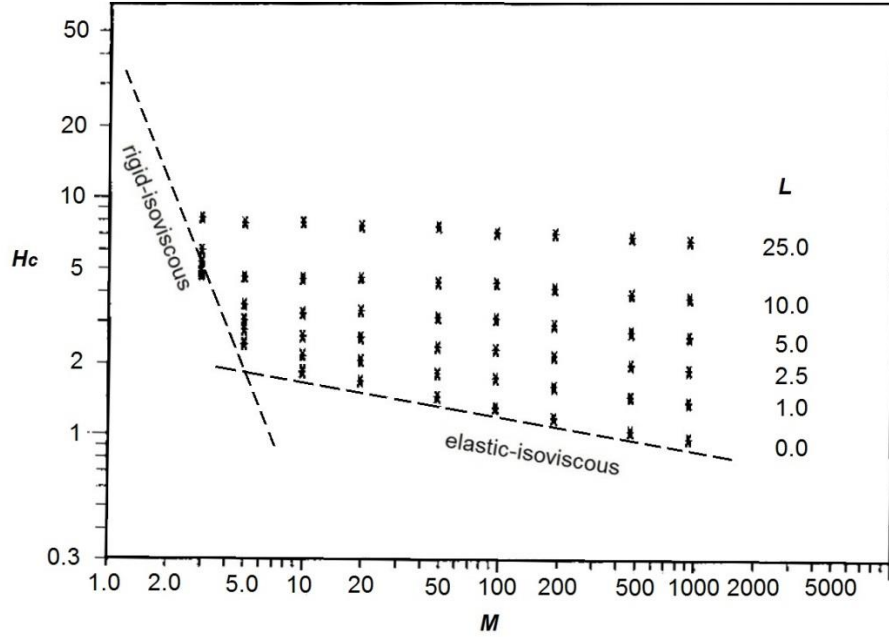


Figure 3.7 Calculated values of the dimensionless central film thickness as a function of dimensionless parameters M and L [Venner, 1991]

The superposition of all four asymptotic solutions predicted for all regimes yielding $H_{c,RI}$, $H_{c,EI}$, $H_{c,RP}$ and $H_{c,EP}$ film thicknesses from Eqs (3.26) to (3.29), respectively, the following expression which fits these results is used for the prediction of the dimensionless central film thickness [Nijenbanning *et al.*, 1994]:

$$H_c = \left\{ \left[H_{c,RI}^{3/2} + \left(H_{c,EI}^{-4} + H_{00}^{-4} \right)^{-3/8} \right]^{2\hat{s}/3} + \left(H_{c,RV}^{-8} + H_{c,EV}^{-8} \right)^{-\hat{s}/8} \right\}^{1/\hat{s}} \quad (3.30)$$

$$\text{with } \hat{s} = 1.5 \left[1 + e^{-1.2(H_{c,EI}/H_{c,RI})} \right] \quad (3.31)$$

$$\text{and } H_{00} = 1.8 D^{-1} \quad (3.32)$$

The parameters \hat{s} and H_{00} are the dimensionless relationships permitting smooth continuity between the four asymptotic solutions. This straight-forward formulation allows simple and efficient calculation process for computer programming.

The dimensional central film thickness, h_c , can be determined as follow [Sojoudi and Khonsari, 2010]:

$$h_c = H_c r_x \left(\frac{\eta u_s}{E' r_x} \right)^{1/2} \quad (3.33)$$

Figure 3.8 [Venner and Lubrecht, 2000] presents the dimensionless central film thickness H_c as a function of M and L , with the four asymptotic EHL regimes also indicated. The markers depict the results obtained directly from the computational numerical solution while the solid lines depicts the solutions obtained by using Nijenbanning *et al.* film thickness equation (Eq. 3.30). Good agreement between these two solutions was obtained. This film thickness equation accurately predicts the computed central film thickness over the entire parameter range values. The dotted lines indicate the predictions of the formula for the central film thickness presented by Hamrock and Dowson [1977a]. Hamrock and Dowson equation for elastic-piezoviscous regime yields comparable results with those obtained from direction computational numerical solution and from Nijenbanning *et al.* equation for $M > 10$ and $2.5 \leq L \leq 25$, However, for small values of M and L the prediction yields values which are much too low as the regime has been shifted from elastic-piezoviscous to the others due to different operating conditions.

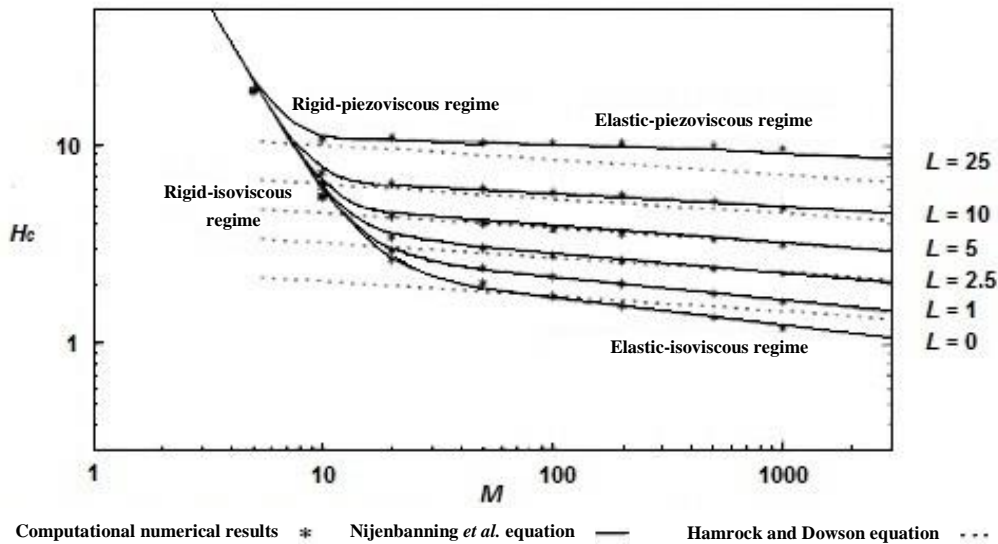


Figure 3.8 Dimensionless central film thickness as a function of M and L [Venner and Lubrecht, 2000]

3.2 Film Thickness and Friction Estimation in Mixed Lubrication

In mixed lubrication, the applied contact load is supported by the hydrodynamic lifting force of the lubricant and asperities interacting force at the contact. The starvation phenomenon in mixed lubrication of elliptical contact is studied by the modelling of the lubricant film thickness at the centre of the contact interface and the shear load at the contact zone. Because this regimes entails solid partial to solid contact trough the asperities combined with total separation by the lubricating film; an iterative procedure was developed to quantify the load shearing between the two load supporting mediums. Convergence is reached when the superposition of the corresponding solid friction and fluid traction forces balances the measured total shear load at different operating conditions and surface roughness. The resulting film thickness is representative of mixed lubrication conditions.

Gelinck and Schipper [2000] first proposed a model to describe the line contact problem in mixed lubrication using the load sharing concept proposed by Johnson *et al.* [1972] together with Greenwood and Williamson's [1966] elastic contact model developed in term of the Hertzian contact pressure to describe the asperities contact. This idea for line loading mixed lubrication model was then expanded by Liu *et al.* [2002] for point contact configuration. The equations for evaluating oil film thickness presented earlier [Hamrock and Dowson, 1981 ; Moes, 1992 ; Nijebanning *et al.*, 1994]; were established for fully flooded and separated surfaces without lubrication starvation. As reported earlier, most of the recent efforts for evaluating lubricant film thickness and friction, in concentrated contact interface under mixed lubrication, require solving the Reynolds equation, the elastic deformation equation and lubricant state equations until load balancing is reached. This uses an iterative procedure that is generally time consuming and often exhibits computational sensitivity [Sojoudi and Khonsari, 2010]. A model and a solution algorithm has been developed for line and point contacts. This model is simple and realistic, provides rapid convergence and requires less computational time [Gelinck and Schipper, 2000 ; Lu *et al.*, 2006 ; Faraon and Schipper, 2006 ; Liu *et al.*, 2009 ; Sojoudi and Khonsari, 2010]. Relevant scaling factors for the load sharing are introduced and an iterative process verifies the compatibility of the obtained film thickness until convergence is reached. The contact pressure on the asperities was evaluated using the asperity elastic contact statistical model proposed by Greenwood and Williamson [1966], based on the separation between the surfaces in contact which depends on the calculated central film thickness film thickness. This iteration process takes place until the condition of equality between the Hertzian contact pressure, due to the portion of load on asperities, and the one determined by the estimated central film thickness is satisfied. A starvation coefficient was used to adjust the calculated film thickness to a thinner starved condition until the calculated total friction concurred with the

experimental measurements. The friction arising from asperity interaction was measured experimentally in the non-starved mixed lubrication regime. Eyring stress model, based on data obtained from friction tests under fully separated and non-starved condition, was used to evaluate to determine the traction of the lubricant at different operating conditions.

3.2.1 Load Sharing Concept and Film Thickness Equation for Mixed Lubrication

In ideal lubrication conditions, the lubricant film is thick enough to fully separate the surfaces. The entire applied load is supported by the lubricant film at the interface and the resistance to motion arises only from shearing action of the film. In mixed and boundary lubrication regimes, the total load is carried by both; the lubricant film and the asperities in contact according to Johnson's load-sharing concept [Johnson *et al.*, 1972]. The distribution of the total applied load, N , can be expressed as:

$$N = N_L + N_a \quad (3.34)$$

where N_L = load carried on the lubricant at the contact interface,
 N_a = load carried on the asperities at the contact interface.

In order to apply the load-sharing concept, load sharing factors for the lubricant, γ_1 , and the asperity, γ_2 , are introduced, so that:

$$N_L = \frac{N}{\gamma_1} \quad (3.35a)$$

$$N_a = \frac{N}{\gamma_2} \quad (3.35b)$$

The relationship between the load sharing factors γ_1 and γ_2 is:

$$\frac{1}{\gamma_1} + \frac{1}{\gamma_2} = 1 \quad (3.36)$$

The total applied load can, hence, be written as:

$$N = \frac{N}{\gamma_1} + \frac{N}{\gamma_2} \quad (3.37)$$

Johnson *et al.* [1972] assumed that the pressure at the contact zone is scaled everywhere by the same factor. This scaled pressure produces a contact zone of the same size as that predicted by the classical Hertzian contact theory, only if the equivalent elastic modulus of the bulk material is reduced by the same factor. Substituting the reduced load (N/γ_i) and equivalent elastic modulus (E'/γ_i) into the established EHL film thickness formula would offer a convenient way to predict the film thickness; applicable to the load-sharing mixed lubrication situation [Liu *et al.*, 2009]. Replacing the total applied load N with N/γ_1 and the equivalent elastic modulus E' with E'/γ_1 , in Eqs (2.8) and (2.9), yields the following dimensionless central film thickness for the mixed lubrication, $H_{c,mix}$, in the case of point contact geometry:

$$H_{c,mix} = \left\{ \left[H_{c,RI}^{3/2} \gamma_1^{9/4} + \left(H_{c,EI}^{-4} \gamma_1^{-2/5} + H_{00}^{-4} \right)^{-3/8} \right]^{2\hat{s}_{mix}/3} + \dots \right. \\ \left. \dots + \left(H_{c,RV}^{-8} \gamma_1^4 + H_{c,EV}^{-8} \gamma_1^4 \right)^{-\hat{s}_{mix}/8} \right\}^{1/\hat{s}_{mix}} \quad (3.38)$$

$$\text{where } \hat{s}_{mix} = 1.5 \left(1 + e^{-1.2\gamma_1^{-7/5}(H_{c,EI}/H_{c,RI})} \right) \quad (3.39)$$

The subscript "mix" designates the mixed lubrication condition. The parameters $H_{c,RI}$, $H_{c,EI}$, $H_{c,RV}$, $H_{c,EI}$ and H_{00} remain the same as presented in Eqs (3.26) to (3.29) and Eq. (3.32), respectively. The dimensional central film thickness for mixed lubrication, $h_{c,mix}$ is:

$$h_{c,mix} = H_{c,mix} \gamma_1^{1/2} r_x \left(\frac{\eta u_s}{E' r_x} \right)^{1/2} \quad (3.40)$$

It was not possible to trace back in the literature the development process that leads to Eqs (3.38) to (3.40), therefore, it was felt important to verify their accuracy. This verification is reported in Appendix A.

A scalar variable θ less than unity, called starvation coefficient, is introduced to account for film thickness reduction due to starvation. Current research efforts have not yet developed a universal model which could be applied to estimate the central film thickness for the starved condition. For the cases in the present study,

this coefficient will be determined for each operating condition. The central film thickness $h_{c,mix,s}$ in mixed lubrication under starved conditions is therefore:

$$h_{c,mix,s} = \theta h_{c,mix} \quad (3.41)$$

3.2.2 Greenwood and Williamson Asperity Contact Model

This modeling is based on a statistical analysis of the surface roughness expressed by a function of amplitude distribution coupled with the classical Hertzian theory which predicts the bearing area. Contact geometry at small scale, between sliding surfaces, has so far been approximated by very smooth surfaces. Assuming Gaussian distribution of asperities height this model is applicable to contacts involving any type of deformation (elastic or plastic), asperities shape and surface roughness (only one surface has roughness or both). Because of the mentioned universal relevance, this model, gained vast popularity in the for the analysis of EHL contacts in mixed lubrication regime as recently pointed out by [Panayi and Schock, 2008 ; Jedynek and Gilewicz, 2013].

Based on Greenwood and Williamson analysis, the contact mechanism between two rough surfaces can simulated by a simpler equivalent model representing the contact between a rigid nominally flat and smooth surface and an equivalent rough surface; as shown in Fig. 3.9 [Johnson *et al.*, 1972]. This is based on the assumptions that each rough surface is covered with a large number of asperities with spherical tips of constant radius and the profile of its roughness satisfying a probability density function $\phi(z)$ with respect to the centre-line of the equivalent rough surface. Greenwood and Tripp [1970-71] have handled the contact of two rough surfaces instead of the one of rough against a flat surfaces treated by Greenwood and Williamson. In the case of two rough surfaces in contact, the pairs of asperities will not be aligned and the usual contact will be between the shoulders of the two hills. Based on this, it was found that as long as peak-height distribution is Gaussian, the questions of asperity shape and whether the asperities are on one or both surfaces are unimportant. Therefore, the contact of two rough surfaces can be reduced to an equivalent, single, rough surface with a plane.

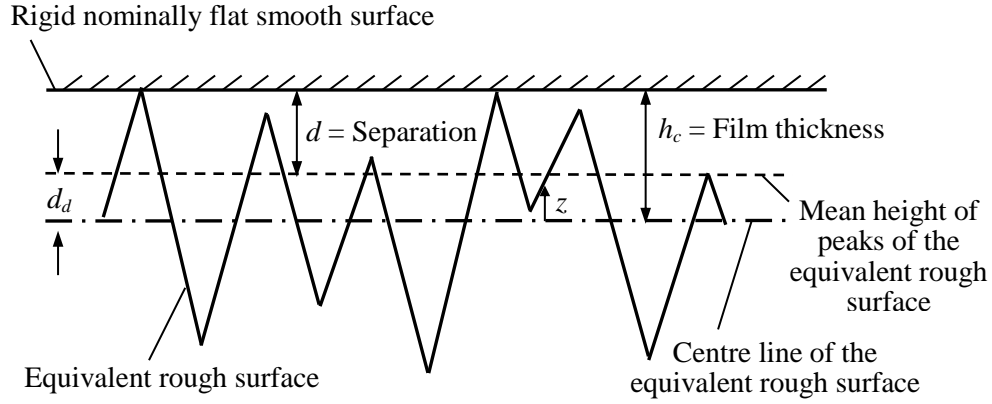


Figure 3.9 Schematic diagram of the contact between a rigid nominally flat smooth surface and an equivalent rough surface [Johnson *et al.*, 1972]

The geometrical model shown in Fig. 3.9 has been used to study the behaviour of the film in the case of mixed EHL [Johnson *et al.*, 1972]. The film thickness h_c is represented by the distance between the centre line of equivalent rough surface and the smooth surface. For the cases of fully flooded and starved conditions in mixed lubrication, h_c becomes $h_{c,mix}$ and $h_{c,mix,s}$, respectively. The separation d of the asperity contact component is defined by the distance between the smooth surface and the plane through the mean height of peaks of the equivalent rough surface [Gelinck, 1999].

Chapter 1 introduced the Hertzian contact characteristics as far as average contact pressure and dimensions of the contact area for perfectly smooth, dry point contact geometry. Knowing the basic dimensions of the elliptical shape from Eqs (1.6) and (1.7) the nominal Hertzian contact area can be determined analytically. However, in a contact situation involving rough surfaces the real contact area would represent the actual footprint constituted by the flattened spots of the roughness profile. Work done on this subject by Bhushan [2002] has permitted to develop a model for predicting this area depending on the loading N the materials elastic constants and the roughness characteristics; for a certain hypothetical separation as shown in Fig. 3.9:

$$A_d = \frac{3\pi}{2} \frac{N}{E' \sqrt{\sigma_p' / r_p'}} \frac{F_1(\hat{d})}{F_{3/2}(\hat{d})} \quad (3.42)$$

where r_p' = equivalent radius of the asperity tips of the two rough surfaces in contact,

σ_p' = equivalent standard deviation of the peak height,

$F_1(\hat{d})$ = parabolic cylinder function (with power index of 1),

$F_{3/2}(\hat{d})$ = parabolic cylinder function (with power index of 3/2),

\hat{d} = dimensionless separation.

The equivalent average radius of the asperity tips r_p' and the parabolic cylinder functions $F_{3/2}(\hat{d})$ and $F_1(\hat{d})$ will be described below.

The equivalent standard deviation of the peak heights σ_p' of the two surfaces, can be evaluated by the expression following general equation reported in Bhushan [2002]:

$$\sigma_p' = \sqrt{\sigma_{p1}^2 + \sigma_{p2}^2} \quad (3.43)$$

where σ_{p1} , σ_{p2} = standard deviation of the peak heights of surface 1 and surface 2, respectively.

Whitehouse and Archard [1970] have proposed a surface heights model from the examination of large number of surface topography. Information obtained from digital analysis profile-meter outputs have shown that for many engineering surfaces the distribution of heights is very closed to Gaussian. Using discrete-random-process analysis, it was concluded that a random type surface profile of tribological importance can be defined by two characteristics: height distribution and the autocorrelation function. It was shown that such a representation can be transformed into a model, appropriate for the study of surface contact, consisting of an array of asperities having a statistical distribution of both heights and curvatures. The standard deviation of the peak height was found to be proportional to the root mean square roughness of the surfaces as shown in Eq. (3.44a). In addition, this model is widely used in the theory of random processes as well as to represent surfaces in studies of the scattering of electromagnetic radiation.

$$\sigma_p' = 0.71R_q' \quad (3.44a)$$

$$\text{Therefore; } \sigma_{p1} = 0.71R_{q1} \text{ and } \sigma_{p2} = 0.71R_{q2} . \quad (3.44b)$$

The equivalent radius of the asperity tips of the two rough surfaces in contact r_p' is [Bhushan, 2002]:

$$r_p' = \left(\frac{1}{r_{p1}} + \frac{1}{r_{p2}} \right)^{-1} \quad (3.45)$$

where r_{p1} , r_{p2} = average radii of the asperity tips for surface 1 and surface 2, respectively.

It was demonstrated [Khonsari and Booser, 2008] that $(\sigma_{p1}/r_{p1})^{1/2}$ and $(\sigma_{p2}/r_{p2})^{1/2}$ can be used to approximate the average slopes of asperities profile. These geometrical characteristics of the roughness can be measured experimentally using a surface profilometer. Using Khonsari and Booser's suggested approximation, the average radius of the peaks tip can therefore be analytically determined.

Greenwood and Williamson [1966], Johnson *et al.*, [1972] and Bhushan [2002] have determined a function relating an apparent contact pressure called p_{app} to the separation under the condition that it is equivalent to an average Hertzian pressure p_{avg} produced by a loading N ; the same loading that would generate p_{app}

$$p_{app} = \frac{2}{3} n' r_p'^{1/2} E' \int_d^\infty (\tilde{z} - d)^{3/2} \phi(\tilde{z}) dz \quad (3.46a)$$

where n' = equivalent density of asperity summits per unit area,

r_p' = equivalent average radius of asperity,

E' = equivalent modulus of elasticity,

d = separation between the smooth surface and the equivalent rough surface,

\tilde{z} = surface profile height,

$\phi(\tilde{z})$ = probability density function of peak heights.

For a Gaussian distribution of the peak heights, with an equivalent standard deviation σ_p' Eq. (3.46a) transforms to the following [Johnson *et al.*, 1972; Bhushan, 2002]. The different roughness considered in this study fall within this category. Different models have been developed and reported by the same author for other distributions such as exponential type.

$$p_{app} = \frac{2}{3} n' r_p' \sigma_p' E' \sqrt{\frac{\sigma_p'}{r_p'}} F_{3/2}(\hat{d}) \quad (3.46b)$$

where r_p' = equivalent average radius of asperity,

σ_p' = equivalent standard deviation of the peak height,

$F_{3/2}(\hat{d})$ = parabolic cylinder function (with power index 3/2),

\hat{d} = dimensionless separation.

The concept of equivalent density of asperities n' is not very well defined due to its complexity. In their study, Greenwood and Tripp [1970-71] suggested to approximate this parameter by the one pertaining to one surface when the surfaces have similar roughness. As for the other cases the trend is: when one surface is rougher; the density of that surface is taken. If the difference in roughness is relatively small the best approximation is to take the density of the roughest surface.

The parabolic cylinder function, $F_{3/2}(\hat{d})$ (special function defined as solution to the differential equation when the technique of separation of variables is used on Laplace equation when expressed in parabolic cylindrical coordinates) is given by [Greenwood and Tripp, 1970-71]:

$$F_{3/2}(\hat{d}) = \int_{\hat{d}}^{\infty} (\bar{s} - \hat{d})^{3/2} \phi(\bar{s}) d\bar{s} \quad (3.47)$$

where \bar{s} is an arbitrary variable for the integration.

For the case that the peak heights distribution is Gaussian, the function $\phi(\bar{s})$ can be expressed by [Greenwood and Tripp, 1970-71]:

$$\phi(\bar{s}) = \frac{e^{-\frac{\bar{s}^2}{2}}}{\sqrt{2\pi}} \quad (3.48)$$

Combining Eqs (3.47) and (3.48) we obtain:

$$F_{3/2}(\hat{d}) = \frac{1}{\sqrt{2\pi}} \int_{\hat{d}}^{\infty} (\bar{s} - \hat{d})^{2/3} e^{-\frac{\bar{s}^2}{2}} d\bar{s} \quad (3.49a)$$

Similarly,

$$F_1(\hat{d}) = \frac{1}{\sqrt{2\pi}} \int_{\hat{d}}^{\infty} (\bar{s} - \hat{d}) e^{-\frac{\bar{s}^2}{2}} d\bar{s} \quad (3.49b)$$

The parabolic cylinder functions $F_{3/2}(\hat{d})$ and $F_1(\hat{d})$ can be evaluated by performing a numerical integration noting that the dimensionless separation \hat{d} is the normalized separation with respect to the equivalent standard deviation of the peak heights σ_p' [Bhushan, 2002] as expressed below:

$$\hat{d} = \frac{d}{\sigma_p'} \quad (3.50)$$

In mixed lubrication in which the total loading is supported partly by the asperities and partly by the film, it is the film thickness in operation that would define the above referred to separation. Johnson *et al.* [1972] proposed the relation between the separation and the film thickness as:

$$\frac{d}{\sigma_p'} \approx \frac{h_c}{R_q'} \quad (3.51)$$

According to Eq. (3.44a) the dimensionless separation, based on to Johnson *et al.* model, is:

$$\hat{d} = \frac{0.71 h_c}{\sigma_p'} \quad (3.52)$$

The dimensionless separation in the above equation can never become negative because the film thickness h_c is always positive. The Johnson *et al.* model of separation was considered to be over simplified in sense that it does not allow any negative value of the dimensionless separation parameter to occur at high applied load.

Gelinck [1999] extended Johnson *et al.* separation model, which was considered to be over simplified in a sense that it does not allow any separation to occur at high applied load. In the proposed Gelinck's model the separation d_d is defined by the distance between the centre line and the plane of the mean height of the peaks of equivalent rough surface, as indicated in Fig. 3.9. This correction is represented by the following expression:

$$d = h_c - d_d \quad (3.53)$$

This separation model has been commonly considered in mixed EHL studies [Gelinck, 1999 ; Gelinck and Schipper 2000 ; Faranon and Schipper, 2007 ; Lu and Khonsari, 2007 ; Wiśniewska-Weinert,, 2011 ; Gasni, 2013].

Based on the surface topography model of Whitehouse and Archard [1970], d_d is proportional to the equivalent root mean square roughness R_q' as expressed below:

$$d_d = 0.82 R_q' \quad (3.54)$$

Using Eq. (3.44a), the dimensionless separation, as defined by Gelinck [1999] model can be written as:

$$\hat{d} = \frac{h_c - 1.155\sigma_p'}{\sigma_p'} = \frac{h_c}{\sigma_p'} - 1.155 \quad (3.55)$$

At the same time, as mentioned earlier, due to the sharing principle of the total loading the apparent contact pressure becomes equivalent to that supported by the asperities p_a expressed as follow:

$$p_a = \frac{2}{3} n' r_p' \sigma_p' E' \sqrt{\frac{\sigma_p'}{r_p'}} F_{3/2} \left(\frac{h_c}{\sigma_p'} - 1.155 \right) \quad (3.56)$$

The present study defines convergence of the iterative process to obtain the actual film thickness by the condition when the difference between the pressure on the asperities determined using Eq. (3.56) and the average Hertzian contact pressure (solid contact) generated by the applicable loading determined according to the sharing model becomes negligible (lower than 0.5%):

$$p_{a,\gamma_2} = \frac{N}{\gamma_2 A_{Hertz}} \quad (3.57)$$

where p_{a,γ_2} = shared pressure on the asperities,

N = total applied normal load,

γ_2 = load sharing factor pertaining to solid (asperity) component of the contact zone,

A_{Hertz} = nominal Hertzian contact area.

The film thickness governs the lubricant breakdown phenomenon initiated at the highest peaks locations. This has direct effect on the friction which affects the performance of the bearing.

3.2.3 Friction at Contact Interface

The literature discloses two main models of estimation of the friction in mixed lubrication regime: theory based EHL methods applied to rough surfaces and load sharing approach. The results obtained according to the first are strongly

dependant on the condition of the film breakdown benchmark. As alluded to earlier, the second model is robust and has proven to generate reliable results. It is based on the simple principal of share effort, between the interacting asperities, to support the applied normal load. Therefore, the total friction force F_T at the contact interface comes from the resistance to the relative motion due to shearing effects of the lubricant F_L as well as the solid contact formed by the interaction between the asperities F_a [Lu *et al.*, 2006 ; Faraon and Schipper, 2007] as expressed by the following equation:

$$F_T = F_L + F_a \quad (3.58)$$

The coefficient of friction is defined by the ratio of the total friction force (also known as tangential force) and the normal force:

$$f = \frac{F_T}{N} \quad (3.59a)$$

Replacing the friction force by its components we obtain:

$$f = \frac{F_L + F_a}{N} = \frac{f_L \frac{N}{\gamma_1} + f_a \frac{N}{\gamma_2}}{N} \quad (3.59b)$$

Therefore:

$$f = \frac{f_L}{\gamma_1} + \frac{f_a}{\gamma_2} \quad (3.59c)$$

The analytical evaluation of the coefficient of friction has focussed mostly on the proper application of the load sharing concept to obtain reasonable predictions of F_L and F_a . However the validity of the resulting total friction coefficient f is also linked to the precision with which f_a and f_L can be determined. For the purpose of simplicity, in the last decades, Amonton's second law of friction was assumed to govern the mechanism of asperity friction [Faraon and Schipper, 2006 ; 2007 ; Liu *et al.*, 2009 ; Sojoudi and Khonsari, 2010 ; Gasni, 2013]. In other cases, f_a was approximated by Coulomb friction coefficient measured using basic lubricated bearing operating at very low speed to avoid hydrodynamic effects [Liu *et al.*, 2009]. This rough approximation of the ratio of the frictional force to normal force was used in the modelling of the friction in mixed lubrication. It was also noted that the sliding velocity affects the deformation process of the asperities which impacts the EHL behaviour of the contact zone [Sojoudi and Khonsari, 2010]. In addition, basic rheological models have been suggested for the estimation

of the traction force in the lubricant generating f_L , although these do not represent adequately the film behaviour when subjected to high shear rate and high loading; operating conditions often found in EHL lubrication.

In order to create and maintain relative motion between surfaces, a shear force in the direction of movement is required to overcome the asperity junction; which is assumed, in this study, equivalent to the friction force at the solid contact. Also, for clarity, f_a is called asperity friction-load ratio and defined by the following equation:

$$f_a = \frac{F_a}{\left(\frac{N}{\gamma_2}\right)} = \frac{F_a}{N_a} \quad (3.60)$$

The studies in the field of tribology have clearly demonstrated that the friction coefficient is not a property of the material but a complex function of the state of the interface and the operating conditions. Therefore, in the present study, a specifically designed experimental procedure will be used to determine the asperity friction-load; precisely for the conditions of interest in the assessment of starvation. This parameter will be indirectly determined, for different applied loads, speeds and surface conditions with different lubricants, from friction tests performed in mixed lubrication under fully flooded condition. The developed relationships are considered to be more accurate models representing the friction behaviour of the solid contact arising from the asperities interaction. This will be used to study the behaviour of the starved film.

The second component involved in the friction mechanism in mixed regime is the reaction force of the shearing process to which the lubricant film is subjected. Under EHL condition this reaction, commonly called traction, is given by the following relationship, as reported by Faraon and Schipper [2007], Sojoudi and Khonsari [2010] and Gasni [2013]:

$$F_L = \tau_L A_L \quad (3.61)$$

where τ_L = shear stress developed in the lubricant,
 A_L = area of lubricant at contact.

According to Newton's law of viscosity, the shear stress τ_L induced in a fluid is proportional to the imposed shear rate $\dot{\gamma}$; expressed by the following:

$$\tau_L = \eta \dot{\gamma} \quad (3.62)$$

where the constant of proportionality is the dynamic viscosity.

Assuming constant velocity gradient throughout the thickness of the fluid film, the shear rate is the ratio of the relative velocity (u_s) and the central film thickness (h_c):

$$\dot{\gamma} = \frac{u_s}{h_c} \quad (3.63)$$

In the case of a lightly loaded film under atmospheric pressure, Newton's law describes well the rheological behaviour of many lubricating oils. At high pressure; typical in EHL contacts, the viscosity increases by many orders of magnitude. On the other hand, the shear strength of most lubricants only increases slightly when subjected to high pressure. Therefore, at high shear rates or high pressures with only moderate shear rates, Newton's law would predict unreasonably high shear stress; which the lubricant is unable to withstand.

Limiting shear stress behaviour is one of the rheological models to describe the shear stress in a lubricant in EHL analysis. Studies [Bair and Winer, 1979 ; Jacobson, 1985 ; Höglund and Jacobson, 1986] have shown that at a given pressure there is a critical shear stress at which the lubricant will shear plastically with no further increase in shear stress with increasing shear rate. The limiting shear stress concept was, hence, proposed to impose the lubricant does not experience shear stress exceeding this limit. The limiting shear stress behaviour has been described in different rheological models by several researchers. A generalised form of the model is [Elsharkawy and Hamrock, 1996]:

$$\dot{\gamma} = \left(\frac{\tau_m}{\eta} \right) \ln \left(1 - \frac{\tau_L}{\tau_m} \right)^{-1/n} \quad (3.64)$$

where $\dot{\gamma}$ = shear rate,

τ_m = limiting shear stress,

η = viscosity,

τ_L = shear stress in lubricant.

In which n is a power index that implements different models : $n = 2$ gives the circle model proposed by Lee and Hamrock [1990], $n = 1.8$ approximates the logarithmic model of Bair and Winer [1979] and $n = 1$ gives Iivonen and Hamrock's [1991] linear model. Moreover, the \tanh^{-1} model was proposed by Gecim and Winer [1981] as:

$$\dot{\gamma} = \left(\frac{\tau_m}{\eta} \right) \tanh^{-1} \left(\frac{\tau_L}{\tau_m} \right) \quad (3.65)$$

The limiting shear stress τ_m was found to be a linear function of pressure p , according to experimental results, and is expressed as:

$$\tau_m = \tau_{mo} + \beta_m p \quad (3.66)$$

where τ_{mo} = limiting shear stress at atmospheric pressure,
 β_m = shear stress-pressure coefficient.

In a typical EHL contact with high pressure at the contact interface, the pressure-dependent part in Eq. (3.66), $\beta_m p$, becomes dominant.

In the early studies, the limiting shear stress of various lubricants at a certain EHL pressure ranges were measured by using the self-constructed high pressure rheometers [Bair and Winer, 1979 ; Höglund and Jacobson, 1986]. However, due to the difficulties in constructing and operating of the high pressure rheometers, impacting ball apparatus was constructed by Jacobson [1985], and then later developed by Höglund [1989], to measure the shear stress-pressure coefficient. In this measurement, a high speed image processing system is required for the analysis of the rotation and the translator motion of a steel ball after impact on a lubricated surface. The limiting shear stress-pressure coefficient β_m can be calculated from the angular velocity of the ball and the maximum height the ball reaches after the impact [Jacobson, 1991].

The literature suggests to use Eyring stress model as reported by Faraon and Schipper [2006 ; 2007], Liu *et al.* [2009] and Wiśniewska-Weinert [2011]. In contrast to the limiting shear stress, the parameter Eyring stress τ_o that determines the linearity limit of a lubricant can be experimentally obtained by using an apparatus capable of generating high shear rates on the film. For this study, the same tribometer used to study the starvation is used to determine Eyring stress of the tested oils under similar conditions including material, geometry and loading. This rheological model expresses the relationship between the shear stress in a fluid τ_L and the shear rate $\dot{\gamma}$ when subjected to high pressure and shear rate. As elucidated by Eq. (3.67), the shear stress-shear rate relation is an inverse hyperbolic sine law with a limiting shear stress called Eyring stress.

$$\tau_L = \tau_o \sinh^{-1} \left(\frac{\eta^* \dot{\gamma}}{\tau_o} \right) \quad (3.67)$$

where τ_o = Eyring stress,
 η^* = viscosity of lubricant under pressure.

Coming back to the traction force evaluation in mixed lubrication, the pressure acting on the lubricant p_L ; generated by the portion of the loading supported by the lubricant film can be evaluated as follow:

$$p_L = \frac{N_L}{A_L} \quad (3.68)$$

A_L is the portion of the nominal Hertzian contact area A_{Hertz} supported by the lubricant; the remaining been that pertaining to the solid contact A_a :

$$A_L = A_{Hertz} - A_a = \left[\pi a b - \frac{3\pi}{2} \frac{\left(\frac{N}{\gamma_2} \right)}{E' \sqrt{\sigma_p' / r_p'}} \frac{F_1(\hat{d})}{F_{3/2}(\hat{d})} \right] \quad (3.69)$$

A_a is function of the separation and can be evaluated by [Johnson *et al.*, 1972 ; Bhushan, 2002]:

$$A_a = \frac{3\pi}{2} \frac{\left(\frac{N}{\gamma_2} \right)}{E' \sqrt{\sigma_p' / r_p'}} \frac{F_1(\hat{d})}{F_{3/2}(\hat{d})} \quad (3.70)$$

The traction force in the lubricant film can then be determined as follow:

$$F_L = \tau_L A_L = \tau_o \left[\sinh^{-1} \left(\frac{\eta^* \dot{\gamma}}{\tau_o} \right) \right] \left[\pi a b - \frac{3\pi}{2} \frac{\left(\frac{N}{\gamma_2} \right)}{E' \sqrt{\sigma_p' / r_p'}} \frac{F_1(\hat{d})}{F_{3/2}(\hat{d})} \right] \quad (3.71)$$

The computing procedures for evaluating central film thickness at the contact interface will be described in the next section.

3.2.4 Procedure for Evaluating Central Film Thickness in Mixed Lubrication

The mixed lubrication modelling described in the previous section permits to numerically evaluate the central film thickness at the contact interface as well as the friction for fully flooded conditions; according to Eqs (3.40) and (3.59c), respectively. However, this evaluation requires the knowledge of the load sharing factors. To circumvent this problem, this study is proposing an indirect way of estimating the film thickness by means of a precise measurement of the total friction force at the interface. This iterative process is based on the conclusions of the studies performed by Gelinck and Schipper [1999 ; 2000], Liu *et al.* [2009], Sojoudi and Khonsari [2010] and Gasni [2013]. For a given operating condition, contact geometry and material and lubricant properties, an initial guessed γ_2 greater than unity is assumed. The load sharing factor of lubricant γ_1 is obtained according to the load sharing concept Eq. (3.36). The dimensionless central film thickness is estimated using Eq. (3.38). The pressure acting on the asperities for a separation equivalent to the estimated film thickness is determined using Eq. (3.56). Thus iterative process continues until compatibility between this pressure and the equivalent Hertzian pressure; Eq. (3.57). Convergence was set at a specified tolerance value of 0.005 (0.5%). This procedure scheme is depicted by the flowchart in Fig. 3.10.

The asperity friction-load ratio necessary for the study of the lubricating film behaviour in starved condition, for which there is no model available for film thickness evaluation, has been determined from the measured total friction force in the mixed lubrication under fully flooded state. The initially unknown friction force at the asperities junctions (solid contact) is obtained from the balancing model of the total friction force knowing the traction force of the lubricant film. This procedure is described by the flowchart in Fig. 3.11.

In starved lubrication, the film thickness at the contact interface is reduced, in comparison to the fully flooded lubrication; a condition which generates thick film. Starved film is the result of an insufficient amount of lubricant supplied to the contact inlet. On the other hand, high relative speed may affect the rheological properties of the lubricant inhibiting ideal lubrication. It was demonstrated that the available models for film thickness estimation in mixed lubrication regime cannot be used when starvation occurs. Therefore, in this study, it is proposed to use the information resulting from the assessment of the friction mechanisms according to experiments conducted under fully flooded mixed lubrication regime to estimate the film thickness in starved state. This is a reasonable assumption for the fact that the same experimental model, procedure and operating conditions were used for both assessments. The flowcharts of Figs. 3.12 (a) and (b) containing many elements similar to those introduced earlier are proposed for the computational evaluation of the film thickness in mixed lubrication starved regime.

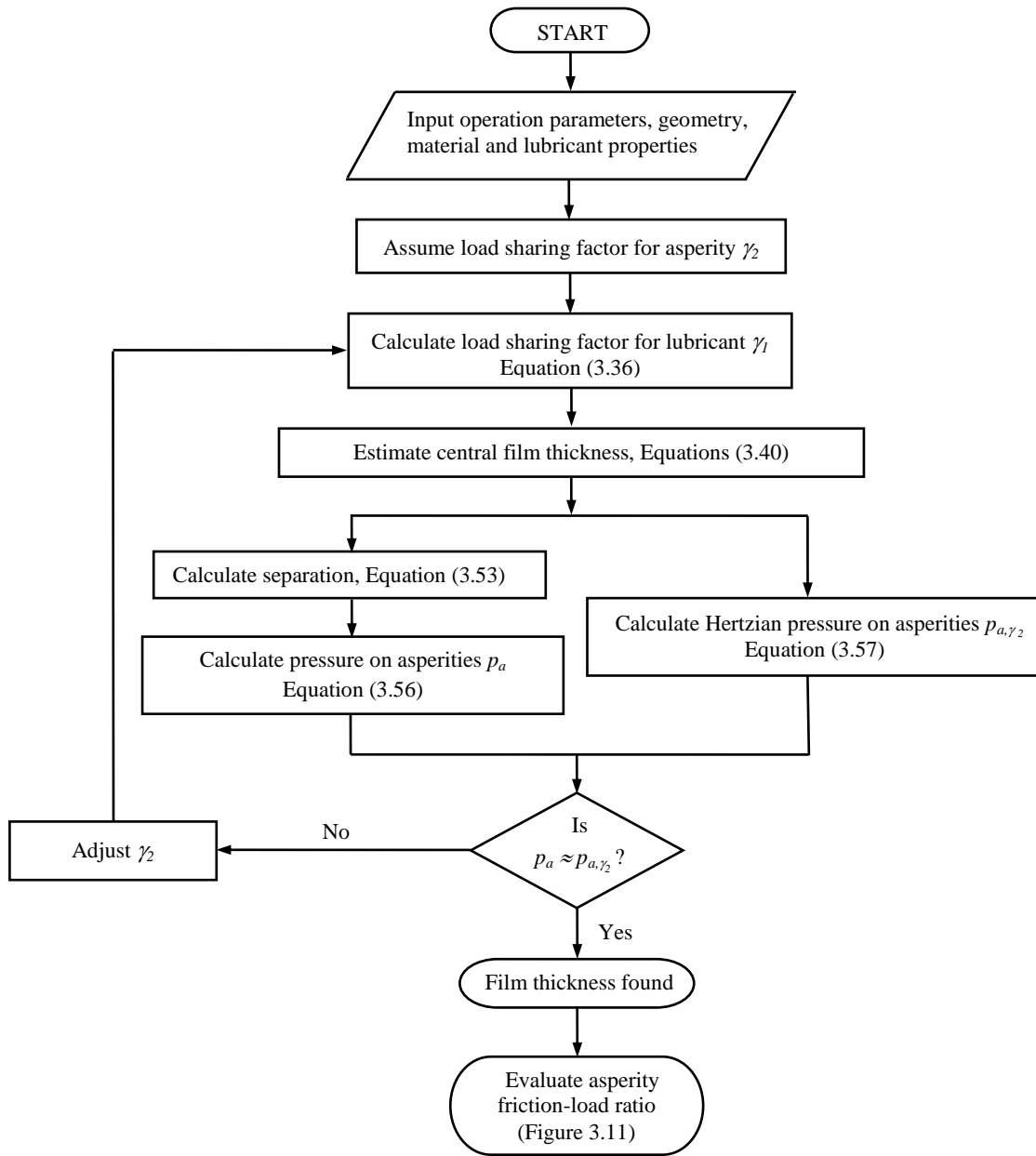


Figure 3.10 Flow chart for determining film thickness in fully flooded mixed lubrication

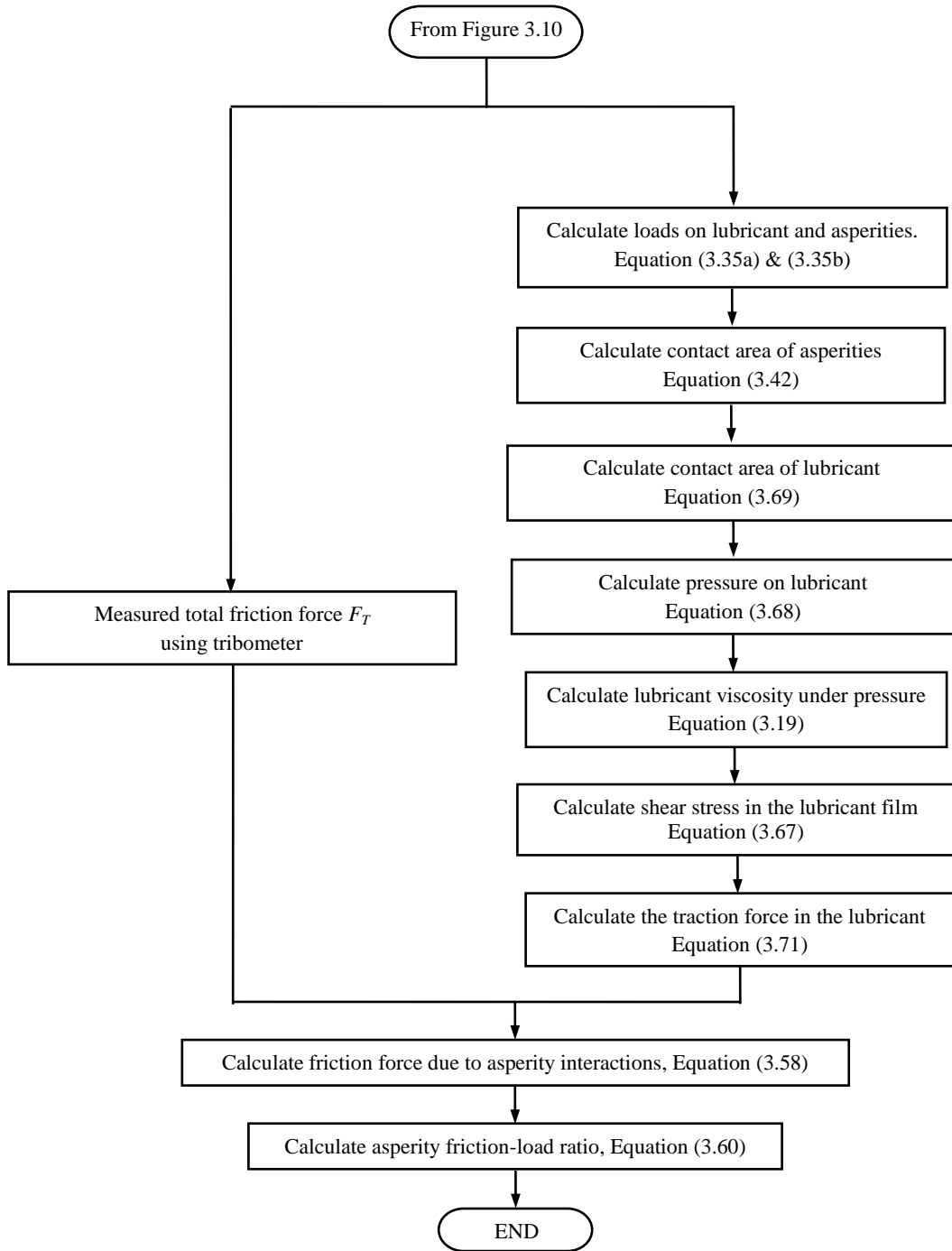


Figure 3.11 Flow chart for determining the asperity friction-load ratio in mixed fully flooded lubrication

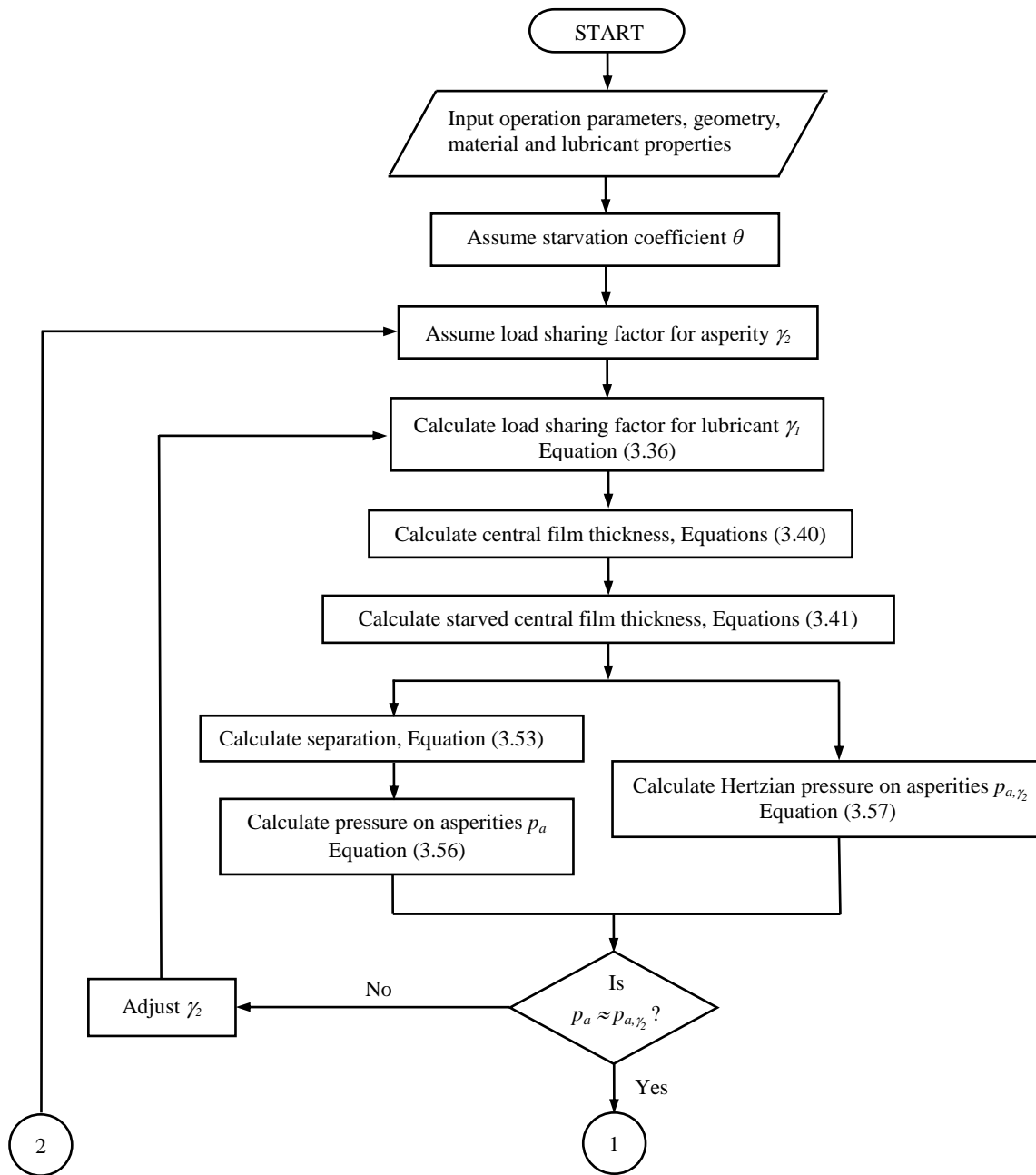


Figure 3.12 (a) Flow chart for determining the film thickness in starved mixed lubrication (part 1)

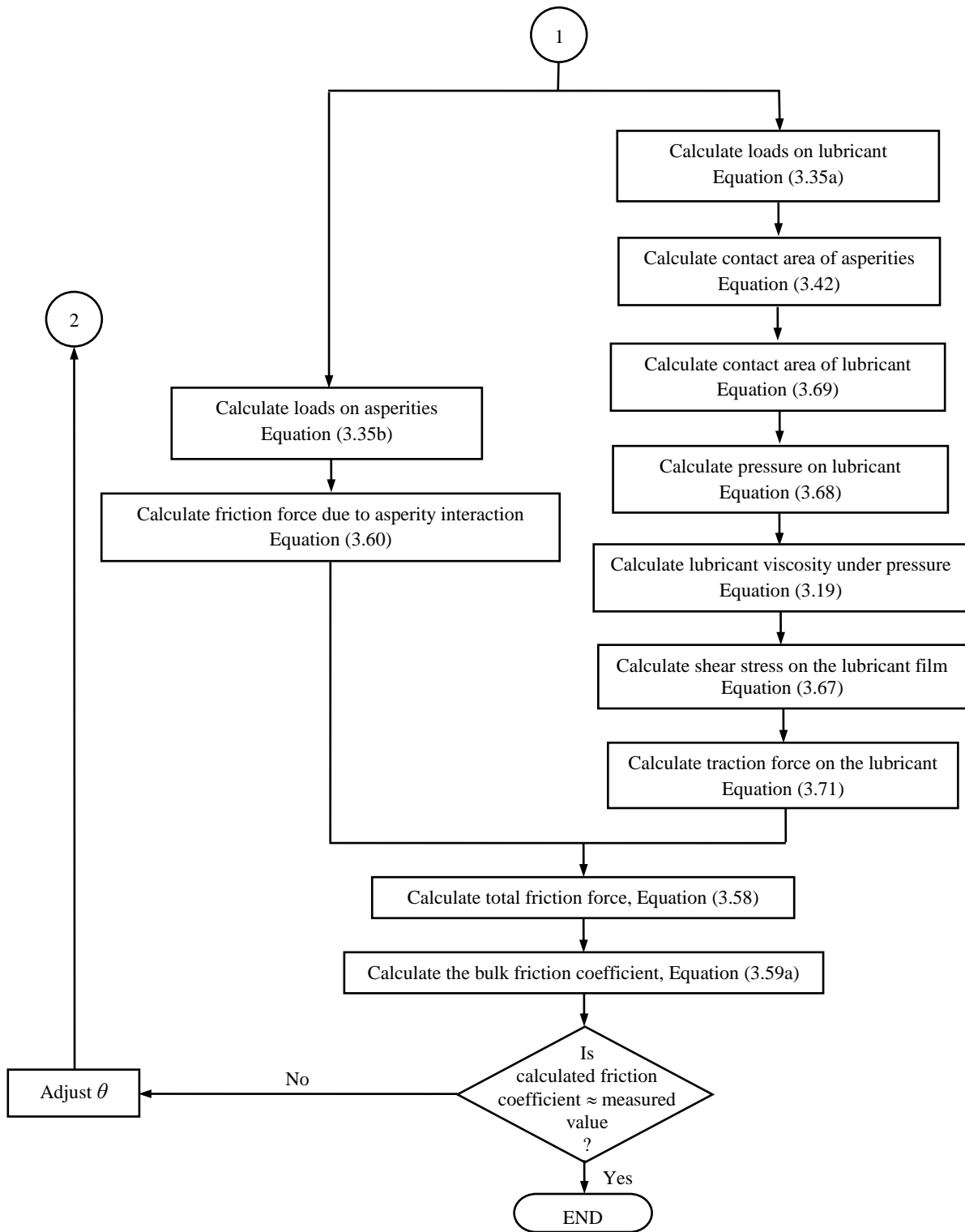


Figure 3.12 (b) Flow chart for determining the film thickness in starved mixed lubrication (part 2)

4. OIL RHEOLOGICAL TESTS AND RESULTS

The behaviour of a lubricant in operation depends on its rheological properties determined according to standard methods. The viscosity is the main parameter influencing the development of the film. Although these properties can be used to define the state of the lubricant at the inlet; the conditions defining the EHL regime in a bearing, specifically the high loading, high viscosity, and high shear rate affect them significantly. The parameter pressure-viscosity coefficient of a lubricant is needed to predict the viscosity-pressure relationship according to available models. This study has considered three different oils: one gear oil and two polyalkylene glycol (PAG) oils. The relationships of the shear stress-shear rate were obtained experimentally at relevant ambient temperatures; which permitted to examine the viscosity variation with shear rate and temperature. These experiments have also served to evaluate the pressure-viscosity coefficient according to ASTM Standard D341-09 [ASTM, 2009]. In addition, the liquid-air surface tension of these oils was measured to enable a precise evaluation of the starvation degree (SD).

4.1 Tested Oils

Three different lubricating oils were considered in this study: Oil #1 is extreme-pressure (EP) gear oil, oils #2 and #3 consist of base oil blended with soluble synthetic PAG polymer additive. Oil #1 was selected because of its high viscosity at ambient temperature, which makes it susceptible to easily develop starved lubrication conditions; a good candidate for this study. Oils #2 and #3 were developed specifically to lubricate the compressor bearings of recent vehicle air-conditioning systems using R134a refrigerant. It was determined that the performance of the compressor; specifically its failure, was heavily linked to a wrong prediction at the specific operating condition.

It is common that the specifications of a lubrication oil provided by its manufacturer states the kinematic viscosities at 40 °C and 100 °C instead of the engineering dynamic (absolute) viscosity. In this study, however, it is required the knowledge of the dynamic viscosities of the tested oils at 25 °C, 40 °C and 100 °C. It is because 25 °C is the temperature for performing the tribological friction test in this study. The evaluation of the pressure-viscosity coefficient of the tested oils requires the dynamic viscosities at 40 °C and 100 °C. In order to obtain these dynamic viscosities, the kinematic viscosity of the tested oils at 25 °C can be first estimated according to the ASTM Standard D341-09 [ASTM, 2009] based on the kinematic viscosities at 40 °C and 100 °C given by the manufactures. The kinematics viscosities of the tested oils at the three temperatures were then converted to the dynamic viscosities. On the other hand, a more practical approach

to obtain the dynamic viscosities at the three temperatures is to perform direct rheological measurements. Furthermore, the Newtonian behaviour of the tested oils can be examined by the measurements.

4.2 Viscosity Tests

4.2.1 Viscosity Measurements

A TA Instrument AR2000 rheometer with a cone-and-plate fixture was used to perform the viscosity measurements. A schematic diagram displaying the main its main components appears in Fig. 4.1. The cone has a radius of 20 mm and the angle between the cone and plate is 1° . Liquid samples can be subjected to controlled shear rates ranging from 1.0 s^{-1} to 15000 s^{-1} , under ambient temperatures equivalent to 25°C , 40°C or 100°C . A data acquisition system measures the induced torque to shear the lubricant film, from which the shear stress in the fluid is evaluated. The temperature of 25°C is often chosen to be representative of the ambient operating conditions of the tribological tests; the results obtained at 40°C and 100°C were used to determine the pressure-viscosity coefficient according to [Hamrock *et al.*, 2004]. The oil sample was placed in the aperture between the rotational cone and stationary plate. Care was taken to ensure that sufficient oil volume is always present. The shear rate is evaluated from the known aperture shape and dimensions which imposes the thickness of the tested fluid, and the rotation speed. A controller maintains the plate at the specified test temperature and the test rig as well as oil samples are required to reach thermal equilibrium before starting the test. Signals were transmitted to the controller unit, which was interfaced to a PC computer for data acquisition. The data recording interval was 5 data points per one decade (in log scale) in shear rate basis. All tests were triplicated each time using new oil sample. Photographs of the AR2000 rheometer and an oil sample being tested are shown in Figs 4.2 (a) and (b), respectively. Additional technical specifications of the AR2000 rheometer are reported in Appendix B.

The calibration of the instrument was verified by performing tests with reference fluid B500; with a known constant viscosity of $0.50 \text{ Pa}\cdot\text{s}$ at 25°C . A difference in viscosity equivalent to $+0.001 \text{ Pa}\cdot\text{s}$ with maximum uncertainty of $\pm 0.0031 \text{ Pa}\cdot\text{s}$ were found. The details of the testing procedure to perform this verification are described in Appendix C.

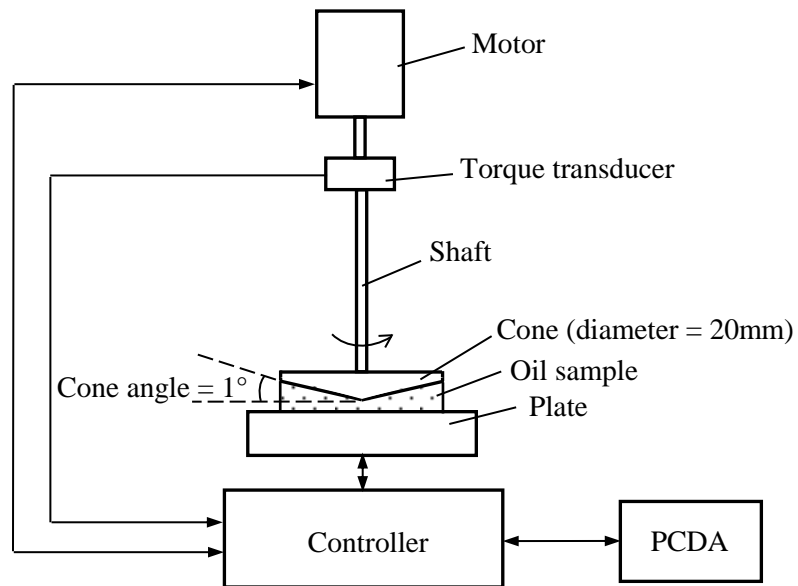


Figure 4.1 Schematic diagram of the oil rheological experiment



(a)



(b)

Figure 4.2 Photographs of (a) TA Instrument AR2000 rheometer;
(b) An oil sample under test

The rheometer permits the measurement of the dynamic viscosity. Unfortunately it was not possible to use the full shear rate range capability of the rheometer due to substantial migration of the tested oil generated by high centrifugal forces at rates higher than 6310 s^{-1} . The data points depicted in the following Figs (4.3 (a) to (c)) representing the variation of viscosity with shear rate at different temperatures, for each oil, are average values from 3 consecutive tests with new oil samples. Deviations of $\pm 0.0035 \text{ Pa}\cdot\text{s}$, $\pm 0.0050 \text{ Pa}\cdot\text{s}$ and $\pm 0.0045 \text{ Pa}\cdot\text{s}$ were found for the case of oils #1, #2 and #3, respectively. These slight deviations demonstrate precision of the measurements. The raw data are shown in Appendix D.

4.2.2 Viscosity of Tested Oils

In general, the viscosity is a measure of the fluid's resistance to flow. It describes the internal friction between its molecules when the fluid is subjected to motion. Practically, it quantifies the resistance to steady deformation by shearing or tension. The instantaneous dynamic (shear, or absolute) viscosity is equivalent to the ratio of the induced shear stress to the corresponding imposed shear rate. On the other hand, the kinematic viscosity (momentum diffusivity) in which no force is involved is the ratio of the dynamic viscosity to density.

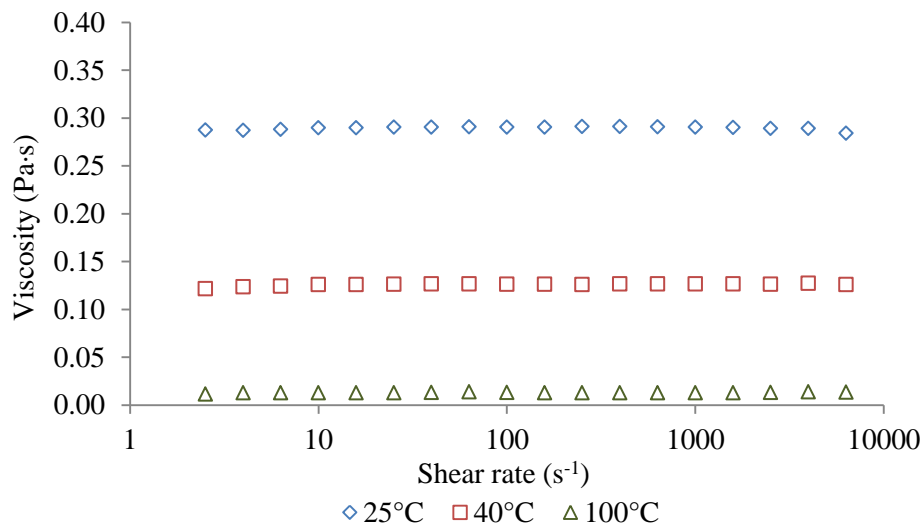


Figure 4.3 (a) Viscosity versus shear rate of tested oil #1

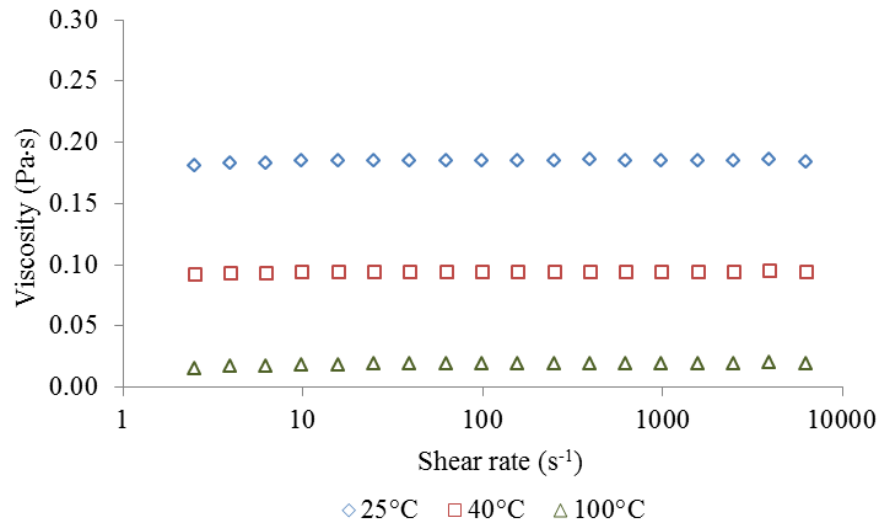


Figure 4.3 (b) Viscosity versus with shear rate of tested oil #2

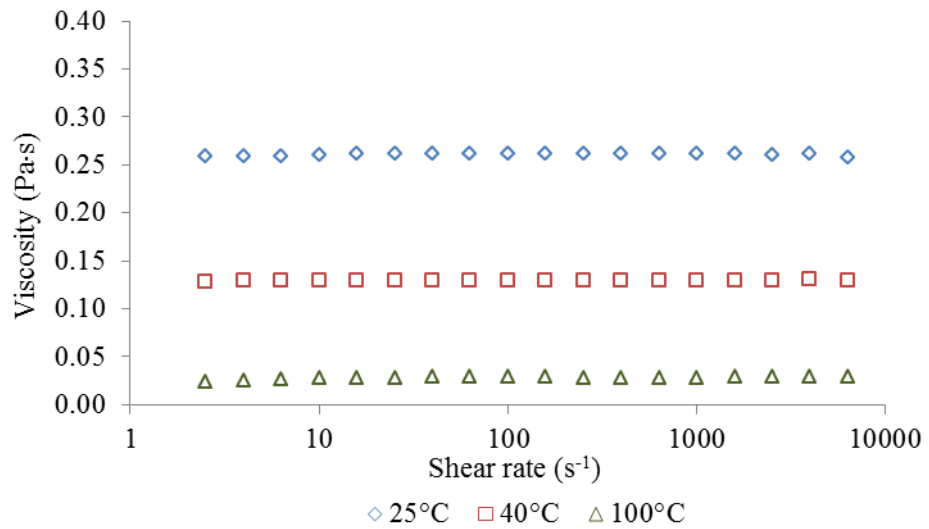


Figure 4.3 (c) Viscosity versus with shear rate of tested oil #3

These data indicate uniformity in dynamic viscosity substantiated by almost no variation with the shear rate; it shows that these oils behave as Newtonian fluids within the tested shear rate range. It is believed that the additives, chemical compounds that improve the lubricant performance, in these oils enhance their shear stability. It was therefore concluded that it is appropriate to use average values of the viscosity, considering all data obtained for the range of shear rate experimented, in this study. These data are shown in Table 4.1. At 100 °C their shear thickening effect is apparent; however, in this study average values are considered for the estimation of the pressure-viscosity coefficient.

Table 4.1 Measured dynamic viscosities

Oil #	Dynamic viscosity (Pa·s)		
	25 °C	40 °C	100°C
1	0.290 ± 0.0018	0.126 ± 0.0013	0.013 ± 0.0005
2	0.185 ± 0.0011	0.093 ± 0.0006	0.019 ± 0.0011
3	0.261 ± 0.0011	0.130 ± 0.0004	0.028 ± 0.0015

Fig. 4.4 illustrates the variation, in logarithmic scale, of the viscosity with temperature. The results clearly indicate notable dependence of the viscosity on the temperature; with variations as expected. The shown trend lines reveal power law relationships. All oils exhibit viscosity reduction with rising temperature. Lubricants are generally classified according to the degree of deviation of their viscosity with temperature effects. This variation is generally quantified by an empirical measure called Viscosity Index (VI), which is commonly used to indicate the relative decrease in viscosity with increasing temperature. The VI scale was set up by the Society of Automotive Engineers (SAE). It relates the change in viscosity of a lubricant at two temperatures, 40 °C and 100 °C, to two reference oils. At the time of it was introduced, the natural mineral oils that showed the least variation of viscosity with temperature came from the Pennsylvania oil fields in the United States and was given a VI of 100. On the other hand, the oil that suffered the greatest decrease of viscosity with temperature came from the coast line of Gulf of Mexico a VI of 0. For calculations of the VI, kinematic viscosities of the two reference oils and the sample oil are assumed to be equal at 100 °C, while they are different at 40 °C and these values are used in the calculations for the VI of the sample oil by the relationship $VI = 100 (v_L - v_U) / (v_L - v_H)$, where v_U is the kinematic viscosity of the sample oil at 40 °C, while v_L and v_H are the kinematic viscosities at 40 °C of the 0 VI oil and the 100 VI oil, respectively. These v_L and v_H can be found in ASTM D2270.

Although there is a clear difference in viscosity between oils #2 and #3, the decrease with the temperature is at the same rate; signifying similar VI. However, oil #1 exhibits the sharpest variation of its viscosity indicating low VI; a common behaviour of most base oils with certain formulations. The superiority of oils #2 and #3 with respect to the gentler effect of temperature change on viscosity is attributed to additives incorporated into the base oil to enhance the VI. The hydrodynamic volume of the polymers in these oils increase with the temperature which results in the retention, to a certain degree, of the viscosity that compensates for the reduction of viscosity of the base oil [Ghosh *et al.*, 1998 ; Tanveer *et al.*, 2006]. Shear stability of the additive (polymer) is also an important property that influences its capacity to modify the viscosity of the base oil. The loss of viscosity of the lubricant under high shear rate can be of two types: temporary or permanent. The latter is more critical and is attributed to the degradation by mechanical shearing of the lubricant's molecules.

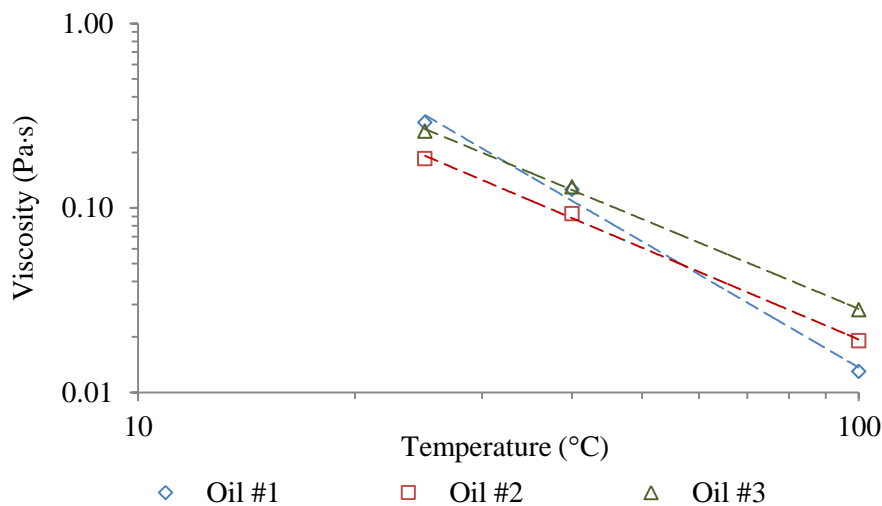


Figure 4.4 Effect of temperature on viscosity of tested oils

The viscosity is a significant parameter in the evaluation of the film thickness at the contact interface of a bearing, in accordance with the EHL lubrication theory. It also influences the behaviour of the film, specifically in starved condition as reported by the literature. This has prompted the need to precisely quantify this parameter. It is felt useful to provide a brief investigative comparison of the present results with those published by the manufacturer; shown in Table 4.2 which contains the kinematic viscosities at 40°C and 100°C as well as the respective densities at 15°C. It is worth noting that for oils #2 and #3, the average values of the kinematic viscosities range at 40 °C provided by the manufacture were considered.

Table 4.2 Tested oils specifications provided by the manufacturers

Oil #	Oil grade	Kinematic viscosity (cSt)		Density at 15°C (kg/m ³)	Applications
		40°C	100°C		
1	SAE Gear 90	192	17.8	906	Outboard and stern-drive
2	ISO 100	84–106	11.4 [†]	850–970	Air-conditioning compressor
3	ISO 150	124–139	15 [†]	850–970	Air-conditioning compressor

[†] Values according to ISO grade oil property at 100°C

To allow a complete comparison, the kinematic viscosities at 25 °C were first extrapolated, in accordance with ASTM D341 Standard, from those at 40 °C and 100 °C; available. This non-linear extrapolation involved also the estimation of the density at that temperature. The details of the extrapolation method used as well as the conversion from kinematic to dynamic viscosity are outline in Appendix E. These approximations have generated discrepancies in the predicted viscosities for the case of oil #1. However, the difference between the estimated and measured dynamic viscosity of oils #2 and #3 were found to be negligible.

4.2.3 Pressure-Viscosity Coefficient and Viscosity-Pressure Index of Tested Oils

For most liquids, the variation of viscosity due to pressure is negligible in comparison to the thermal influence because of non-compressibility. However, for oils; having initially high viscosities, there is a substantial increase with pressure due to increased flow resistance. This phenomenon is therefore particularly important in affecting the performance of lubrication of concentrated contacts found in bearings, gears etc., in which the pressure developed, rises rapidly to high levels [Stachowiak and Batchelor, 2005]. The knowledge of the adequate viscosity-pressure relationship pertinent to the used lubricant is, hence, indispensable [Hamrock and Dowson, 1981]. Although experiments are difficult to conduct for the characterisation of such relationship models presented earlier have been put forward and commonly used in this field of research. However, these semi-empirical model used in this study contains a pressure-viscosity coefficient ξ that quantifies the EHL film generating capability of a lubricant [Errichello, 2004] as well as the Moes dimensionless material parameter L (Eq. 2.9). The pressure-viscosity coefficient is a function of the molecular structure of the lubricant and its physical characteristics such as molecular interlocking, molecular packing, rigidity [Stachowiak and Batchelor, 2005]. It can be evaluated using graphical charts developed on the basis of Roeland's model with the knowledge of the viscosity and

viscosity-pressure index Z_l [Khonsari and Booser, 2008]. For most mineral oils, synthetic hydrocarbons, di-esters and polyesters, with and without additives, the viscosity-pressure index, Z_l is related to the dynamic viscosities at 40°C and 100°C according to the following equations [Fein, 1997 ; Khonsari and Booser, 2008]. The viscosity-pressure index is used in associate with the Roelands viscosity-pressure model (Eq.3.19) for lubricant viscosity under EHL pressure:

$$Z_l = \left[7.81(H_{40} - H_{100})^{1.5} (0.855 - 0.864H_{40}) \right] \quad (4.1)$$

$$H_{40} = \log(\log \eta_{40} + 1.200) \quad (4.2)$$

$$H_{100} = \log(\log \eta_{100} + 1.200) \quad (4.3)$$

where η_{40} and η_{100} ; the absolute viscosities under atmospheric pressure at 40°C and 100°C respectively, should be in cP (centipoise). It is worth noting that the viscosity-pressure index is a constant that is characteristic of the lubricant and is relatively independent of temperature [Khonsari and Booser, 2008].

Eq. (4.4) has been suggested as alternative approach for determining the pressure-viscosity coefficient ξ . It also involves the dynamic viscosity at atmospheric pressure, η , and Roelands' viscosity-pressure index, Z_l [Hamrock *et al.*, 2004].

$$\xi = Z_l \left[5.1 \times 10^{-9} (\ln \eta + 9.67) \right] \quad (4.4)$$

Eq. (4.4) is unit sensitive and is valid only applicable when η is expressed in SI unit (Pa·s). Reported values of this coefficient, for different lubricants, range from $10 \times 10^{-9} \text{ Pa}^{-1}$ to $40 \times 10^{-9} \text{ Pa}^{-1}$ [Leeuwen, 2009]. The results are shown in Table 4.3 (a). In addition, Table 4.3 (b) contains published values of this parameter for various lubricants obtained at 30 °C by different researchers [Gohar, 2001]. The comparison indicates reasonable accuracy.

Table 4.3 (a) Estimated pressure-viscosity coefficient at 25°C

Oil #	Pressure-viscosity coefficient ξ (Pa ⁻¹)
1	24.8×10^{-9}
2	14.0×10^{-9}
3	12.3×10^{-9}

Table 4.3 (b) Pressure-viscosity coefficient of various lubrication oils at 30°C [Gohar, 2001]

Oil	Pressure-viscosity coefficient (Pa ⁻¹)
Spindle mineral oil (low viscosity index)	25.7×10 ⁻⁹
Castor oil	15.9×10 ⁻⁹
Polypropylene glycol 750	17.8×10 ⁻⁹

4.3 Oil Surface Tension Measurements

Various lubricants generally show differences in the degree of wetting a surface and spreading on it. These phenomena are dependent on a property called surface tension [Stachowiak and Batchelor, 2005]. Surface tension characterises also a liquid-gas interface [Ghosh, 2014]. It arises from cohesive forces among molecules that act uniformly in all directions, resulting in equilibrium state [Kreider, 1985]. Below the surface of the liquid, they act equally in all directions. At the interface with the surrounding gas, the molecules at the free surface experience the internal cohesive forces as well as negligible balancing pull from gas molecules. As a result, a tension on the surface is created; the interface acts like a membrane under tension; the liquid is said to possess surface tension [Morrison, 2013 ; WaterCAMPWS, 2014]. Physically, the surface tension is defined as the force acting over the surface of a liquid per unit length of the surface perpendicular to the force [Kreider, 1985 ; Opoku, 2014]. The Du Noüy method is widely used for surface tension measurement of liquids due to its simplicity. It is based on measuring the force necessary to pull a platinum ring from the surface of the liquid being assessed.

In this study, the surface tensions of the tested oils were measured by means of the Du Noüy method using a surface tensiometer; Fisher Model 20, with 6 cm ring diameter. Photographs of this apparatus and a sample was being tested are shown in Figs 4.5 (a) and (b). The measurements were performed manually and at ambient temperature of 25°C. Care was taken to minimise uncertainty and all tests were repeated at least three times. The tensiometer has a measurement resolution of 0.0001 N/m (0.1 dyne/cm). The uncertainty of the measurements was estimated to be about $\pm 0.05 \times 10^{-3}$ N/m (0.05 dyne/cm). The statistical analysis of the obtained data yielded small deviations of less than $\pm 0.07 \times 10^{-3}$ N/m with respect to the average values. The surface tension measurement results are shown in Table 4.4.

They span between 0.0347 N/m and 0.0376 N/m. These are comparable to published results using typical mineral oils [Stachowiak and Batchelor, 2005]. However, the present results are 16% to 25% higher than the values considered in the starvation studies by Cann *et al.* [2004] and Berthe *et al.* [2014].

Table 4.4 Liquid-Air surface tension measurement results

Oil #	Surface tension (N/m)
1	0.0347
2	0.0353
3	0.0376



(a)



(b)

Figure 4.5 Photographs of (a) Fisher surface tensiometer Model 20 ;
(b) An oil sample under test

In addition, a brief discussion of the apparent dependence of the viscosity and surface tension of tested oils is given in Appendix F.

5. FRICTION EXPERIMENT

A ball-on-cylinder lubricity tester (BOCLT), which simulates non-conformal elliptical contact configuration between a ball and rotating cylinder, is used to perform friction experiments with the lubrication oils described in previous chapters. Different loadings, surface roughness, sliding speeds and lubricant amounts are considered in the present study. Starvation conditions were created to study the behaviour of the lubricating film in mixed lubrication regime. The precise total friction force is measured under different operating conditions. These results are used to determine the film thickness, as well as the corresponding inlet meniscus length, at the contact interface. The apparatus and procedures used for the friction experiments are described in this chapter; while the results will be presented and discussed in the subsequent chapter.

5.1 Friction Test Apparatus

The friction experiments were carried out on an InterAv Model BOC-100 ball-on-cylinder lubricity tester, conforming to ASTM International Designation D5001-08 [ASTM, 2008]. A photograph and schematic diagram of its main components are shown in Figs 5.1 and 5.2, respectively. A stationary steel ball fixed on the balance arm of the tester rubs against the rotating surface of a ring (test cylinder) driven by a motor. The technical specifications of the controller supplying the necessary voltage, as well as the circuit diagram of the voltage doubler, which was developed for these experiments, are presented in Appendix B. The rotational speed of the cylinder is monitored by a tachometer Monarch Instrument PLT200. The normal contact load is applied by dead weight attached to the free end of the balance arm. The actual friction force at the contact point is measured by an Omega LCFD-10LB load cell attached to a lever arm mechanism. The friction arm converts the tangential friction force at the contact to a compressive load captured by the load cell. The signal from the load is conditioned by an Omega DMD-465 signal conditioner, with filtering and amplifying capabilities. The USB-6003 data acquisition/control device is used to digitise the conditioned analog signals. The digitised signal is then analysed by the National Instruments LabView software sampling at high rate. All technical specifications of the test balls, cylinders and experimental setup are reported in Appendix B. The tribometer together with the measurement system chain were calibrated by performing reference test according to the manufacture's recommendations [InterAv Inc., 1989]. A maximum discrepancy of +2.6% between measured and reference friction values was observed. The detail of the verification test is described in Appendix G.

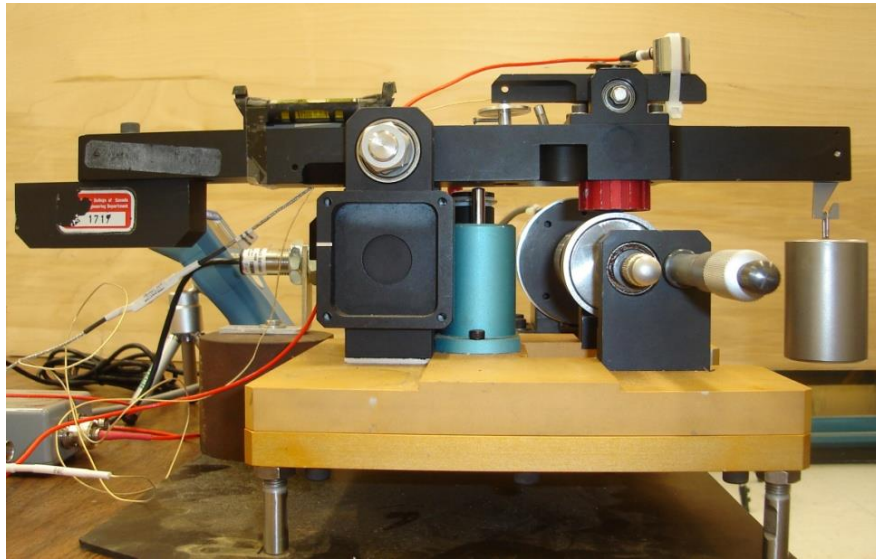


Figure 5.1 Photograph of the ball-on-cylinder tester for friction test

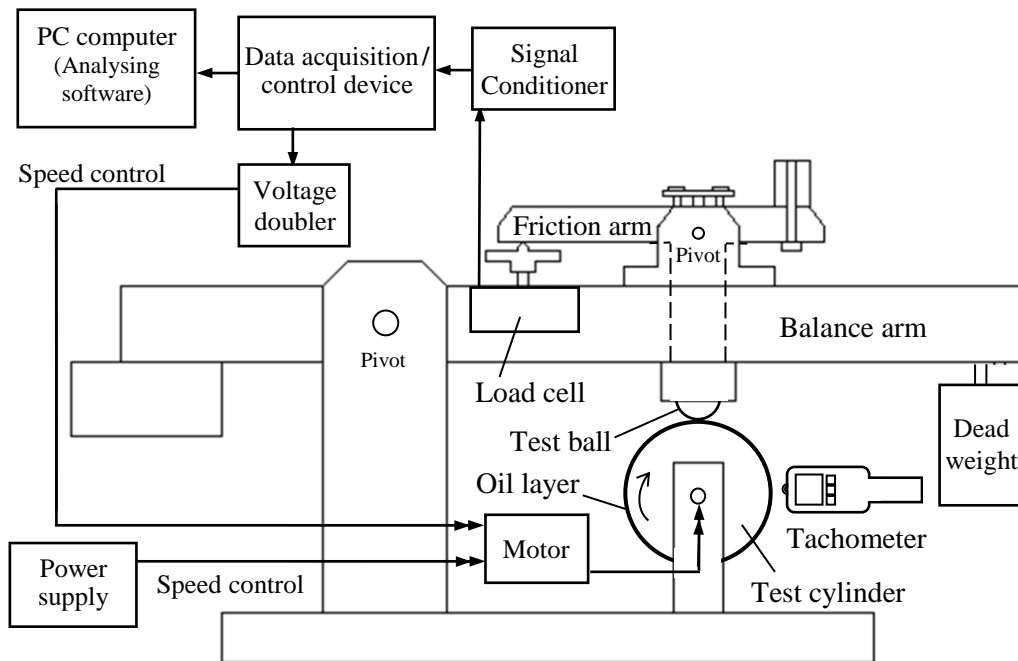


Figure 5.2 Schematic diagram of the friction tests experimental setup

5.2 Test Ball and Cylinder

There was one type of ball with the same surface roughness and three types of similar cylinders with different surface roughness used. The test balls conform to ASTM International Designation D5001-08 [ASTM, 2008] without further modification of the surface. Two different surface roughness, one satisfying the requirements specified by ASTM International Designation D5001-08 [ASTM, 2008], the second obtained by careful sanding of the surface were used for to simulate the mixed lubrication conditions under fully flooded and starved conditions. The smooth cylinders, which conform to ASTM International Designation D6078-04 [ASTM, 2010], were used to simulate EHL thick film lubrication conditions. The surface roughness generated by sanding was obtained by applying 600 grit silicon carbide abrasive paper subjected to 20 N of compression against the surface of the rough cylinder rotating at 200 rpm. This process has proven to yield reproducible surface roughness lower than that of rough cylinders. A photograph of the test cylinders and ball is shown in Fig.5.3.



Figure 5.3 Photograph of tested cylinders and ball

Prior to metrology measurements, the test cylinders and balls were cleaned according to the ASTM International Designation D5001-08 [ASTM, 2008]. The diameter and surface roughness properties were measured before testing by means of Mitutoyo caliper and Mitutoyo Surftest SJ-400 surface roughness tester. This surface roughness tester provides a skid-less detector and a curved surface compensation that offer capability for evaluating roughness on the spherical

surface of the tested balls and the cylinders. The pertinent technical information of these measurement devices is located in Appendix B. Average values of three measurements are used in this study. The surface roughness measurements of the cylinders were taken in the transverse direction; perpendicular to the rotating direction, at three locations at 120° angles apart. As for ball surface, random spots were assessed according to the process required for curved surfaces. The travelling speed of the stylus was set at 1 mm/s over 4 mm distance with a 0.8 mm cutoff; while the travelling distance was 1.25 mm with a 0.25 mm cutoff for the balls and the smooth cylinders samples. The average roughness R_a or centre line average (CLA), root mean square (RMS) roughness, R_q , and the asperity average slope derived. In addition, in order to obtain the density of the asperities on the surface, n' , the high spot counts in both transverse, HSC_t , and rolling directions, HSC_r , were also measured. As stated earlier, in this study it was not possible to perform direct measurements of the 2-D density of the asperities; therefore, approximation was made as the product of the high spot counts in the transverse and rolling direction for the 2-D density of the asperities. The method used for evaluating the apparent contact pressure p_{app} will take into account the real contact area that depends on the separation, which is according to the normal load. The actual measurement results are shown in Appendix H; average values are contained in Table 5.1.

Table 5.1 Measured surface parameters of test cylinders and balls

Component	Diameter (mm)	CLA roughness	RMS roughness	Asperity average slope	High spot count	
		R_a (μm)	R_q (μm)	m	HSC_t (cm^{-1})	HSC_r (cm^{-1})
Smooth cylinder	49.2	0.044	0.055	—	—	—
Sanded cylinder	49.2	0.489	0.607	0.095	434.8	349.8
Rough cylinder	49.2	0.530	0.664	0.092	382.3	332.2
Ball	12.7	0.028	0.034	0.020	1533.7	1533.7

The CLA and RMS roughness of the tested balls are comparatively low by comparing to those of the sanded and rough cylinders. Although the contributions of the tested ball roughness are moderate in the resulting equivalent roughness

when the test ball is paired with these cylinders, the tested ball roughness is not negligible in this study.

The surface profiles and the surface profile height amplitude distribution histogram of the smooth, sanded and rough cylinders as well as the test ball are shown in Figs 5.4 (a) to (d). In all cases, the surface roughness exhibits Gaussian distribution of its surface profile height amplitude.

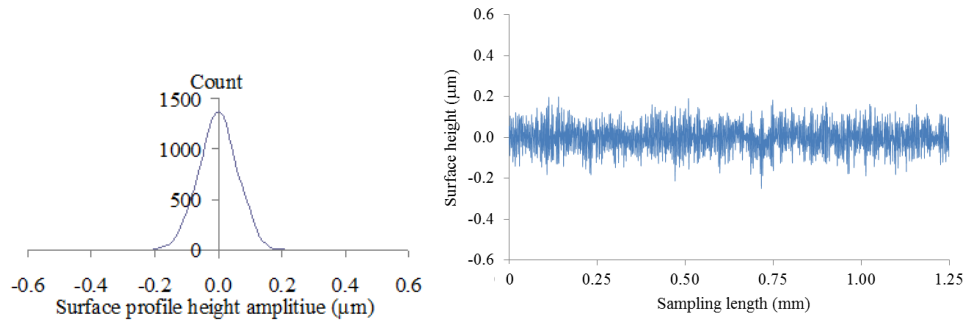


Figure 5.4 (a) Surface profile and surface profile height amplitude distribution histogram of smooth cylinder

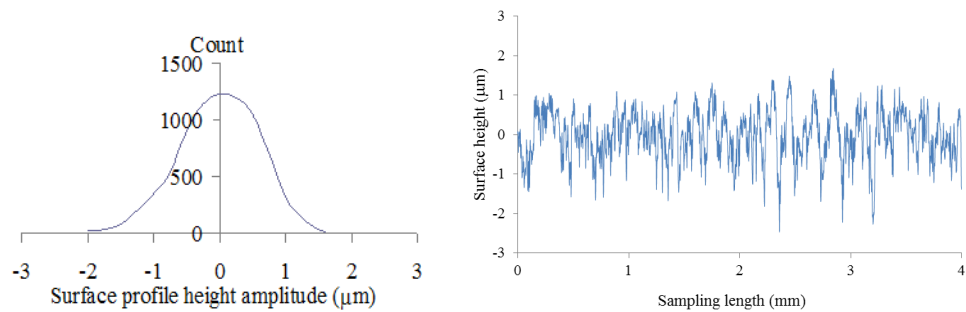


Figure 5.4 (b) Surface profile and surface profile height amplitude distribution histogram of sanded cylinder

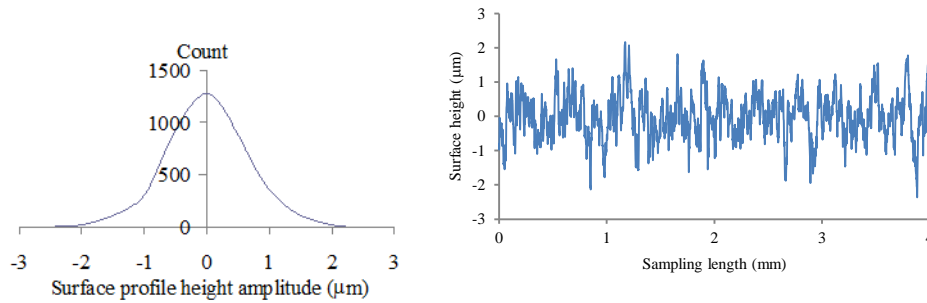


Figure 5.4 (c) Surface profile and surface profile height amplitude distribution histogram of rough cylinder

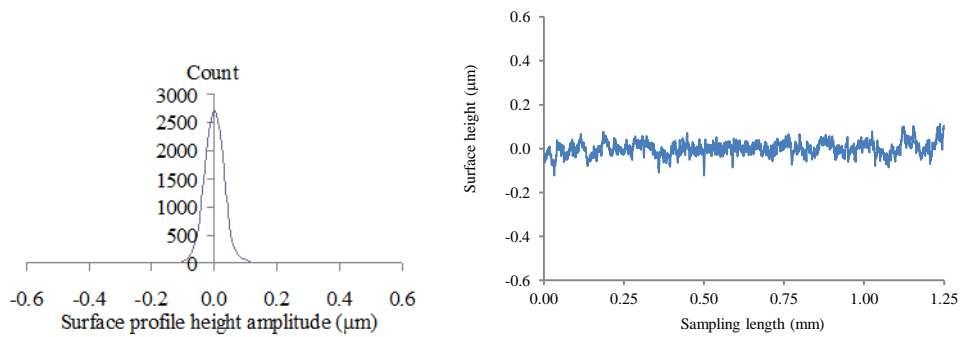


Figure 5.4 (d) Surface profile and surface profile height amplitude distribution histogram of test ball

5.3 Friction Test Procedures

The experimented applied loads were 5.88 N and 9.82 N, generating average Hertzian contact pressures (Eq. 1.5) of 0.52 GPa and 0.61 GPa, respectively. The tests simulating the conditions of hydrodynamic regime; for evaluating of the rheological behaviour of the lubricant at high shear rate, the rotational speed of the cylinder was controlled manually; ranging from 100 rpm (sliding speed of 0.26 m/s) to 1000 rpm (2.58 m/s), in 100 rpm (0.26 m/s) increments. As for the experiments in mixed lubrication fully flooded or starved, operational speeds varied from 100 rpm to 800 rpm with 100 rpm stepwise increments. Preliminary investigations revealed that 180 s duration of each step was sufficient to create steady state regime. All tests were conducted at an ambient, but well-controlled,

environmental condition of $24\text{ }^{\circ}\text{C} \pm 1\text{ }^{\circ}\text{C}$ and $40\% \pm 1\%$ relative humidity, and were repeated to ensure reproducibility. The test cylinders and balls were cleaned according to the ASTM International Designation D5001-08 [ASTM, 2008] and care was taken to prevent any contamination of the active surface prior to testing. Fresh test surfaces of both contacting elements were experimented for each condition.

Fully flooded conditions were generated by applying on the surface of the cylinder an amount of lubricant equivalent to $400\text{ }\mu\text{l}$ before starting the test. To ensure uniformity, the total amount was spread in the form of $20\text{ }\mu\text{l}$ droplets applied at intervals equivalent to 18° of the cylinder rotation. An oil distribution run-in process was then carried out with 2.94 N contact load; the cylinder spinning at 20 rpm (0.05 m/s), in an effort to distribute the oil continuously on the rolling track. A photograph of the cylinder surface with the distributed oil layer is shown in Fig. 5.5. Additional $20\text{ }\mu\text{l}$ oil droplets were applied by using a syringe, at a rate of approximately every 2 seconds per drop, to the rolling track on the cylindrical surface during the tests to ensure sufficient oil was available at the contact.

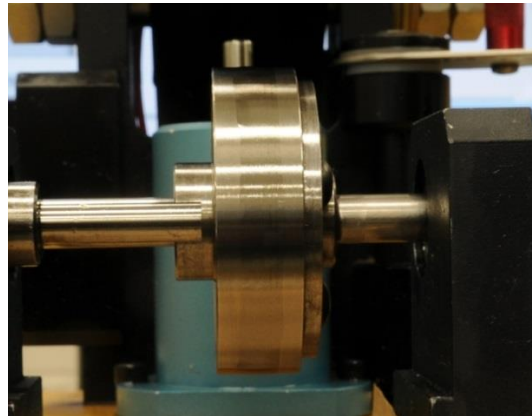


Figure 5.5 Photograph of a typical distributed oil layer on test cylinder

The starvation study was carried out by performing experiments with insufficient lubricant oil at the contact; it was achieved by limiting the volume of oil applied on the cylinder in comparison to the fully flooded case. The limited oil volumes applied to the test cylinder surface were $60\text{ }\mu\text{l}$ and $100\text{ }\mu\text{l}$. In the first situation, three $20\text{ }\mu\text{l}$ oil droplets were deposited on the track 120° apart and five $20\text{ }\mu\text{l}$ oil droplets 72° apart in the second. The oil distribution run-in process described previously was then performed. There was no re-supply of lubricant during the starvation experiment. From the continuous measurements of the

friction reaction at the interface, the friction force used in this study consisted averaging the data acquired during 30 second of steady state operation reached after 120 seconds of operation at each operating condition. The conditions for different tests are summarised in Table 5.2.

Table 5.2 Experimental conditions for friction tests

Test	Cylinder	Oil volume	Rotation speed (rpm)	Sampling interval (s)	
Eyring stress	Smooth	Continuously Supplied	100 to 1000	10	
Friction test	Fully flooded	Sanded and Rough	Continuously Supplied	100 to 800	10
	Starvation	Sanded and Rough	60 μ l and 100 μ l	100 to 800	30

In addition, an attempt was made to quantify the thermal effect by measuring the surface temperature on the test ball in proximity of the contact zone. The case of the highest applied load (9.82 N) using the rougher surface cylinder and with least amount of oil amount (60 μ l) was examined by applying a type-K thermocouple to the stationary test ball in close proximity of 1.5 mm to the centre of the contact interface at the outlet side. Schematic diagrams of the thermocouple location are shown in Figures 5.6 (a) and (b). The recorded temperature variation as function of the relative speed is shown in Fig. 5.7. This rise in temperature although perceivable was deemed insignificant to affect the behaviour of the lubricating film.

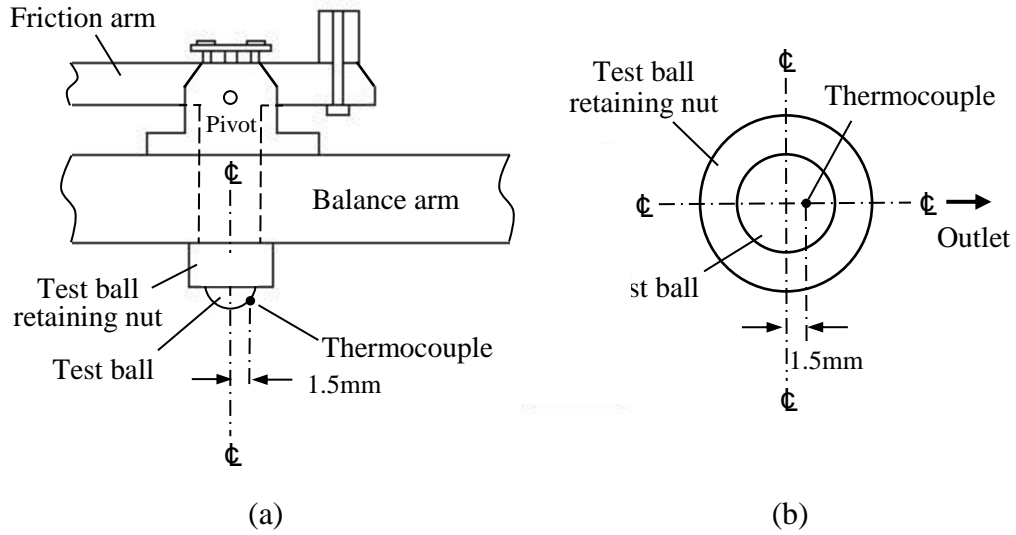


Figure 5.6 Schematic diagram of the temperature assessments with thermocouple
 (a) Side view ; (b) Bottom view

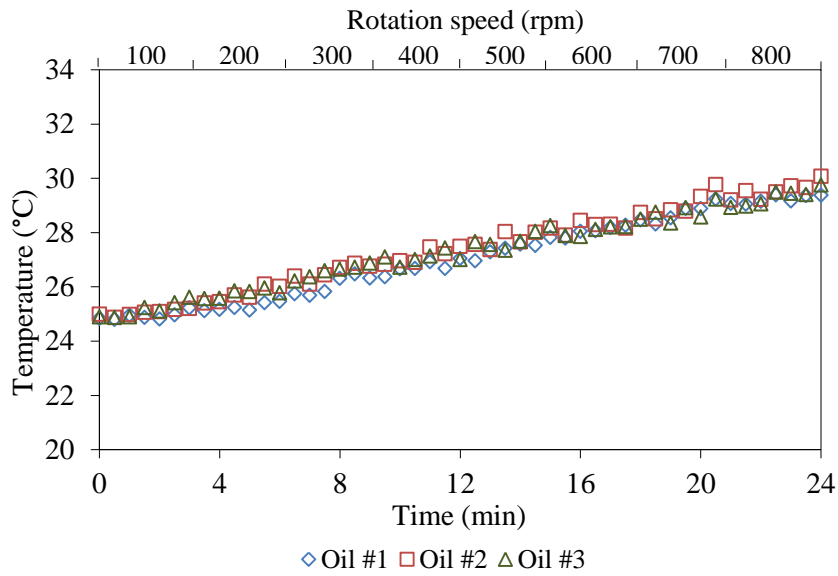


Figure 5.7 Test ball surface temperature variation in friction test (with 9.82 N applied load, rough cylinder surface and 60 μ l oil amount)

6. RESULTS AND DISCUSSION

6.1 Eyring Stress of Tested Oils

As stated earlier, the Eyring model has been retained to express the rheological behavior of the lubricants according to Eq. (3.67). This model requires the knowledge of the limiting shear stress called Eyring stress. Eyring stress τ_o depends on the lubricant, shear rate and pressure. In this study a specific experimental method has been developed to measure the traction force of the lubricant loaded and sheared under fully flooded thick film EHL regime; which yields the shear stress in the lubricant. The determination of the shear rate requires the knowledge of the film thickness which was calculated using Eqs (3.30) to (3.32). Because of the non-linearity of Eq. (3.67), the Newton-Raphson method numerical iterative process was used to find its root τ_o . Studies have predicted values varying between 3 MPa to 10 MPa for common lubrication oils [Liu, 2002]; therefore an initial guess of 1 MPa was considered in the Newton-Raphson iteration with convergence criterion set at 0.005 (0.5%). In this study a comprehensive characterisation of the lubricant properties is planned in order to be able to generate accurate insights of the film behaviour in starved mixed lubrication conditions. The tribometer was used to perform these experiments permitting the measurement of the friction force as function of the sliding speed for the case of smooth contacting surfaces (ball and cylinder). An assessment of the variation of the friction coefficient obtained by normalizing the measured friction force with respect to the normal load according to Eq. (1.18) is first conducted. This parameter is plotted in Fig. 6.1 against the Hersey number as defined by Eq. (1.19). Each data point represents an average of three consecutive measurements.

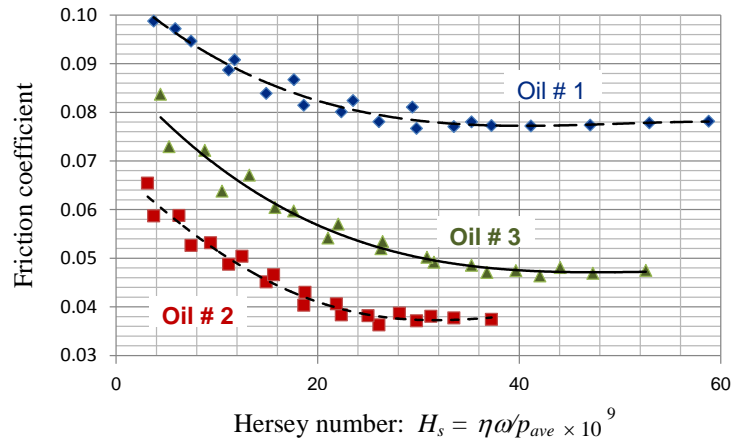


Figure 6.1 Friction coefficient versus Hersey number in thick film lubrication

Predictable trend of initially high friction decreasing with Hersey number is evident when the bearing operates in the mixed regime. Both loadings are considered simultaneously in the present case. Most important is the occurrence of a threshold speed after which the favorable conditions of the EHL are established promoting higher performance of the bearing. The observed variation of friction is consistent with typical Stribeck curve predictions. It is the lubricant film buildup and formation of fully flooded contact mechanisms that take place during the first phases. A third is characterized by the onset of friction rise generated by higher shear stress on the film, not visible in Fig. 6.1, is associated with the further increase of the shear rate. However, this phenomenon depends also on the behavior of the lubricating film specifically its thickness which affects the shear rate. The present results indicate very distinct performance when comparing the three oils. The establishment of EHL occurs at $H_s = 42 \times 10^{-9}$ for oils # 1 and #3 and at $H_s = 31 \times 10^{-9}$ for oil # 2. The results further reveal an effect of the normal loading during the mixed lubrication phase whose effect becomes less significant when the transition point is reached. High loading produces high pressure which increases the viscosity and decreases the film thickness promoting the contact between asperities. This condition produces higher solid and liquid (lubricant) friction. The above analysis has indicated that the conditions simulating the development of EHL regime were successfully achieved which validates the proposed procedure of assessing the rheological behavior of the lubricants at high pressure and shear rate. The traction force of the lubricant (this designation reflects the shearing phenomenon of the film without any solid contact at the aperture) was therefore equated to the measured friction force. Therefore, the shear stress on the film can be determined knowing its sheared area taken equivalent to the Hertzian contact area. On the other hand, from the estimation of the central film thickness (Eq. 3.30) based on Reynolds equation, the shear rate is determined. These results are depicted in Fig. 6.2 together with predictions according to the Eyring stress model and the Newton's law illustrated by dash and dotted lines, respectively. One can conclude that all tested oils in present study do not display Newtonian behaviour when operating in EHL regime. At the same time, it can be seen that the increase of the shear stress is moderate at high shear rate and loading. It appears that the developed models based on limited data points predict fairly well the rheological behaviour of the lubricant under the conditions of this study.

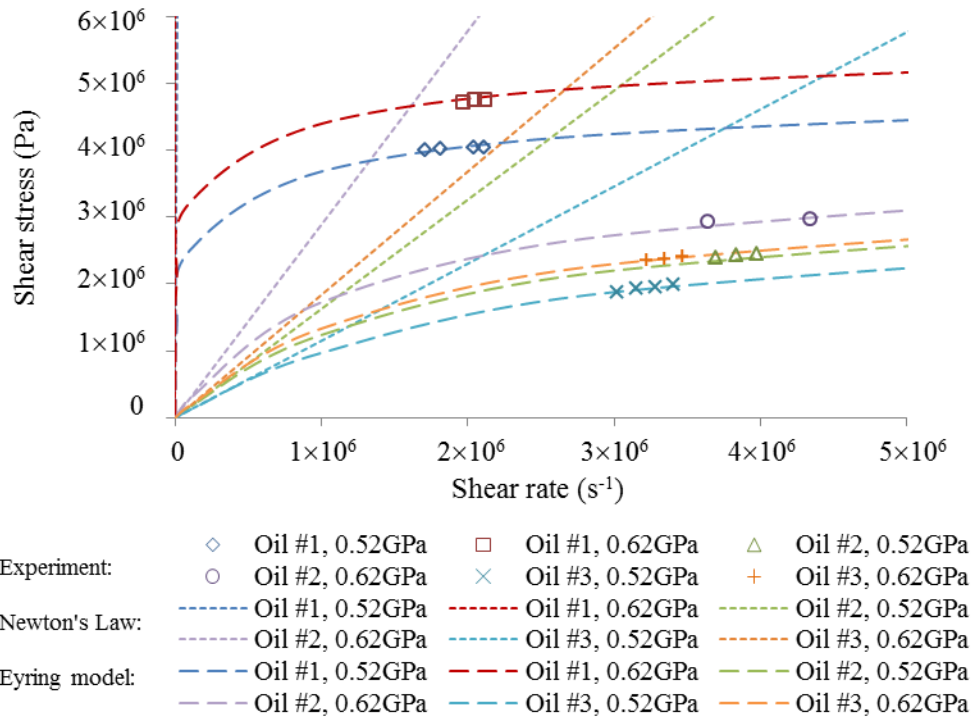


Figure 6.2 Shear stress of tested oils versus shear rate

The present results are plotted again in Fig. 6.3, together with experimental data obtained by different researchers for various lubricants using viscometers operating at high pressure and high shear rate [Bair, 1996 ; 2002 ; Kong *et al.*, 2001]. The aim of this plot is not for comparison but to emphasize the leveling trend of the shear stress at high shear rates for the case of all lubricants. It is concluded that Eyring stress model, which imposes a threshold shear stress when the lubricant is subjected to high shear rate, represents well the behaviour of the film under these conditions.

Table 6.1, summarizes the results of the estimation of the Eyring stress, which satisfies Eq. (3.67) based on the experimental data expressing the rheological behaviour of the lubricant. Only small deviations of this parameter with the experimented range of shear rate and normal loading have been observed for all oils. It was therefore decided to use an average value in the rheological model as shown in the last row of Table 6.1. Values of this coefficient ranging from 3 MPa to 10 MPa for typical lubrication oils have been reported in the literature [Liu, 2002]. It is worth noting that these full film lubrication tests with smooth contacting surfaces were designed to determine Eyring stresses but did not serve as

for independent check of other friction test results discussed in the following sections.

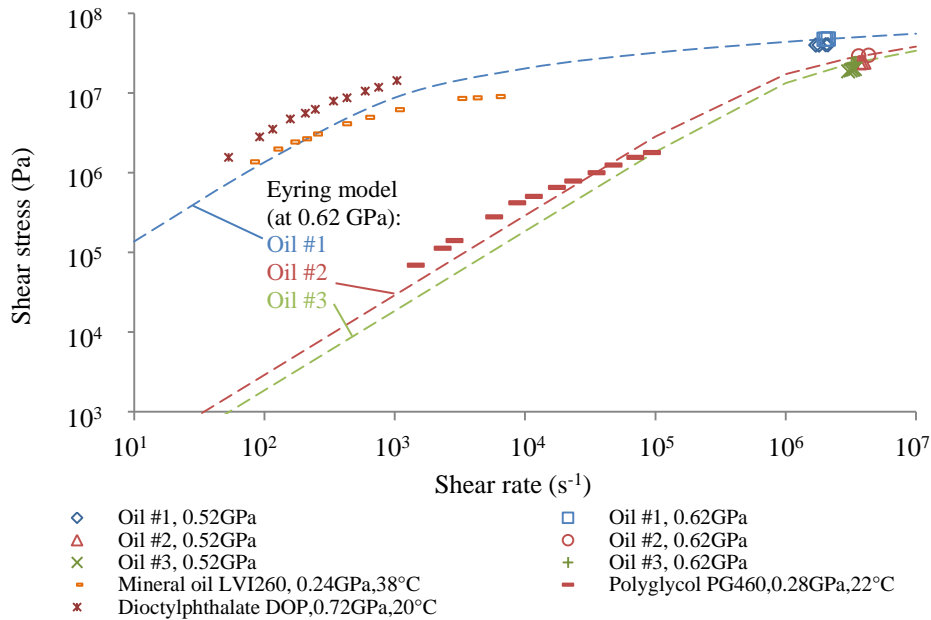


Figure 6.3 Shear stress of tested oils and various fluids versus shear rate

When contrasting the different oils, the Eyring stress is low in the case of oil #1 and higher but comparable for oils #2 and #3. In order to further investigate the significance of this parameter, which represents the onset of non-linear behaviour of the lubricating film described by monotonic increase on the shearing stress with the shear rate, its relationship with the apparent viscosity as well as surface tension of the lubricant was evaluated. These data are plotted in Fig. 6.4. The results showing an increase of the shear stress with the normal load independently of the shear rate are difficult to predict from Eyring rheological model. It is the increase of viscosity with pressure (loading), according to Roelands equation that reflects the increase. It appears that the viscosity influences the range of the developed limiting Eyring stress. At the same time, the increase of loading influences the limiting stress in a complex way. The present results show higher Eyring stress for thinner and higher surface tension oils. More data are needed to be able to draw definite conclusions. However, the rheological models shown in

the last row of Table 6.1 will be used as illustrative of the oil behaviour for the study of starvation.

Table 6.1 Eyring stress of tested oils

Entrainment speed (m/s)	Eyring stress (MPa)					
	Oil #1		Oil #2		Oil #3	
	5.88 N	9.82 N	5.88 N	9.82 N	5.88 N	9.82 N
0.90	5.14	-	-	-	9.25	-
1.03	5.12	5.13	9.38	-	9.22	9.25
1.16	5.12	5.14	9.32	9.20	9.22	9.23
1.29	5.11	5.13	9.38	9.23	9.25	9.18
Average	5.12 ± 0.010		9.31 ± 0.075		9.23 ± 0.025	
Eyring model	$\tau_L = 5.12 \sinh^{-1} \left(\frac{\eta^* \dot{\gamma}}{5.12} \right)$		$\tau_L = 9.31 \sinh^{-1} \left(\frac{\eta^* \dot{\gamma}}{9.31} \right)$		$\tau_L = 9.23 \sinh^{-1} \left(\frac{\eta^* \dot{\gamma}}{9.23} \right)$	

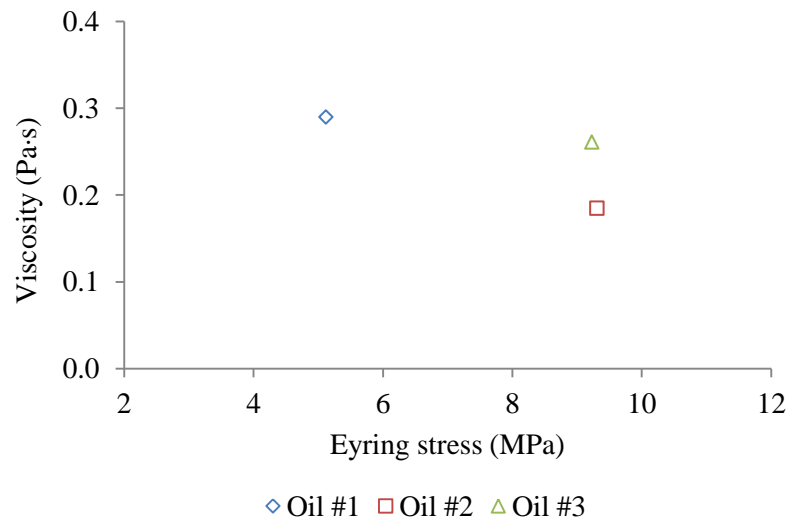


Figure 6.4 Viscosity and surface tension versus Eyring stress of tested oils at 25°C

6.2 Asperity and Lubricant Friction-Load Ratio in Fully Flooded Mixed Lubrication

As elucidated earlier, the asperity interaction, in mixed lubrication, contributes to the total friction. There are no precise models permitting the evaluation of this contribution. Researchers were rather focused on developing universal methods of prediction of the total friction force; to be used by bearing designers. It was already mentioned that these were established on approximations of the solid friction between asperities using Coulomb friction model. As well, rheological models have been developed to calculate the traction force of fluids. In the prediction of the friction due to the asperity interaction in mixed EHL lubrication, for simplicity, Coulomb friction model was commonly considered [Faraon and Schipper, 2006; 2007 ; Liu *et al.*, 2009 ; Sojoudi and Khonsari, 2010 ; Gasni, 2013]. The coulomb friction coefficient for the asperity interaction was obtained by performing friction experiment under very low speeds in which the elasto-hydrodynamic film thickness is small compared to the surface roughness and where the elasto-hydrodynamic friction component is negligible [Liu *et al.*, 2009]. This Coulomb friction coefficient was considered to be independent of the operating speed and taken as constant to predict the asperity interaction friction throughout the mixed lubrication analysis at different speeds. However, in the Coulomb friction model approach, the effect of the sliding velocity on the asperities deformation is ignored [Sojoudi and Khonsari, 2010]. The Coulomb friction coefficient provides only a rough approximation of the quotient of frictional force to the normal load [Popov, 2010]. The assumption of using the Coulomb friction model to predict asperity interaction friction in mixed lubrication is oversimplified. In the present study, however, it is proposed to determine the solid friction component from experimental measurements of the total friction force generated at a well-defined contact zone; operating in fully flooded mixed lubrication regime. It is to note that this is done to gather one of the tools necessary for the assessment of the film behaviour in starved mixed lubrication. Fig. 6.5 is a schematic modeling of the friction mechanism in mixed lubrication.

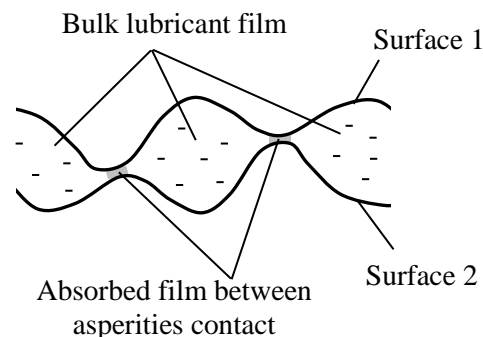


Figure 6.5 Friction contact model for mixed lubrication regime

There is only few molecules-thick lubricant layer absorbed on the contacting asperities tips, while the cavities between the two rough surfaces are filled with lubricant. The shearing resistance at the asperities contact zones depends not only on the bulk properties of the lubricant, but also on the chemical nature of its adhesive bounds to the solids [Hironaka, 1984 ; Buyanovskii, 2010]. The recorded data of the friction force, conforming the experimental procedure outlined earlier, as function of the sliding speed and normal load are depicted in Fig. 6.6 (a) for the case of the rough cylinder ($R_a = 0.530 \mu\text{m}$) and Fig.6.6 (b) for the sanded cylinder ($R_a = 0.489 \mu\text{m}$).

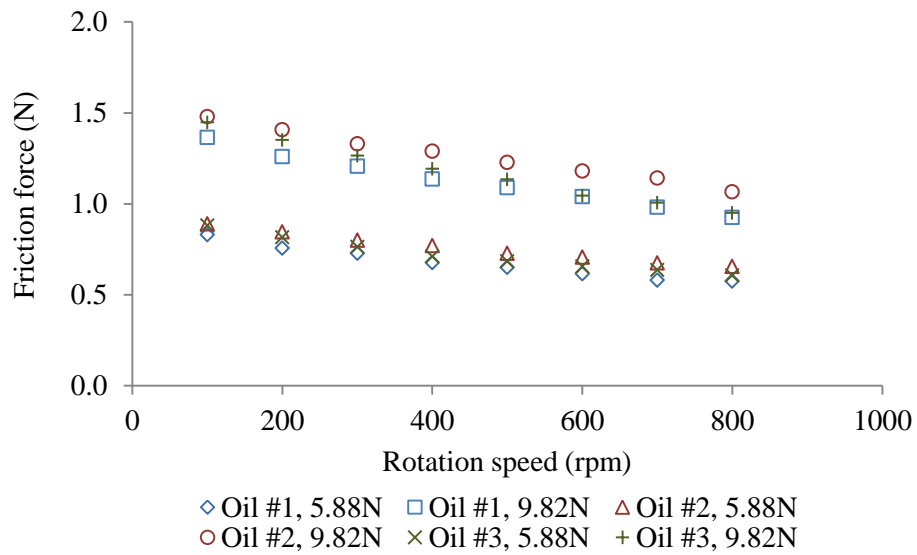


Figure 6.6 (a) Friction force versus rotation speed for mixed fully flooded lubrication using rough cylinder

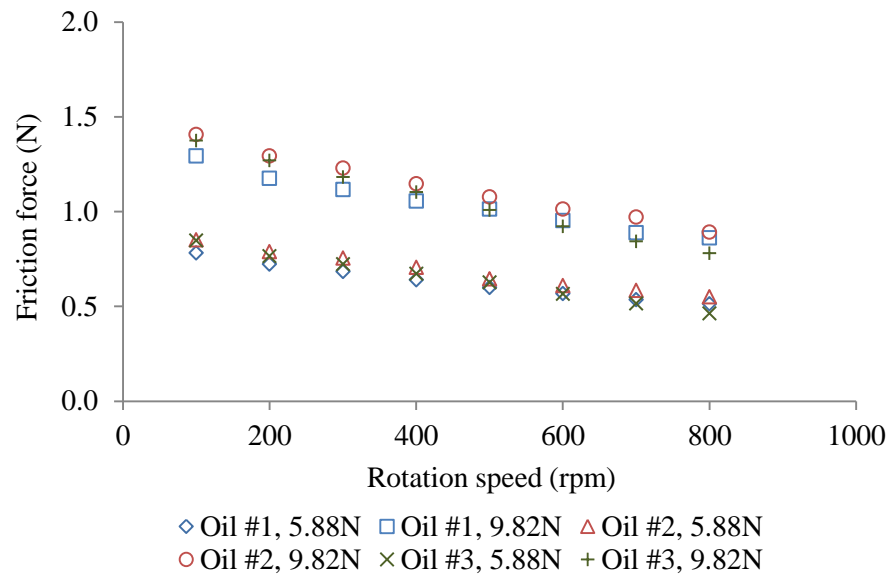


Figure 6.6 (b) Friction force versus rotation speed for mixed fully flooded lubrication using sanded cylinder

The conventional friction decrease with increasing speed independently of normal load, surface roughness and the type of lubricant is observed. This is a typical behaviour of lubricated contacts and reflects well the mixed regime. These results are in agreement with those reported in different papers [Liu *et al.*, 2009 ; Sojoudi and Khonsari, 2010 ; Gasni, 2013]. Although higher friction resistance takes place at low speed in comparison to smoother contact, pressure build-up is apparent at increasing speed as a lubricating film forms; punctured by the asperities. This result implies that a thicker film develops at high speed, reducing the contact area across the asperities. An important effect of the normal loading on the total friction is clearly demonstrated; more precisely, in the present case, an increase of 67% of applied load has generated about 60% increase in friction resistance in all cases. However, the decrease of friction with speed is more pronounced at higher load. In addition, the viscosity plays a more important role at higher load. These results demonstrate that the present experimental conditions have generated well established mixed lubrication regimes. The friction reaches lower level and stabilizes at 800 rpm. The effect of increase of viscosity with pressure becomes beneficial at higher loading. The surface roughness influences the film behaviour. Also, the friction resistance, in mixed lubrication, is heavily dependent on the loading, speed and roughness in a complex way which cannot be approximated by a linear relationship with the loading. Similar influence of surface roughness on

friction coefficient has been reported by other researchers [Wang *et al.*, 2007 ; Li, 2013].

The above interpretation of the results and observed phenomena are in agreement with published knowledge. This is considered as a validation of the present approach as there is still a lack of robust models expressing the mixed regime. In fact, recent attempts to perform such comparisons have concluded that appreciable gaps may exist between experimental and simulated results. As an example, [Akchurin *et al.* 2015] have found variances in friction up to 32%, depending on the load and surface roughness, when comparing different predicting models applicable to line contact geometry. In the present study, the measured total friction is reduced by an estimated traction force in the lubricant to obtain the friction generated by the solid contact, applicable to each surface roughness, lubricant and operating condition. The load sharing concept, introduced in section 3.2.1, is applied until convergence, which permits to evaluate the load sharing factor for the lubricant γ_l necessary for the evaluation of the film thickness from Eq. (3.36) in this regime. The shear rate is then deduced; implying the shear stress which develops in the film according to the acquired equation (Eyring model) expressing the rheological behaviour of the lubricant. The viscous resistance of the oil is obtained knowing the shear stress and sheared area. The difference between the total measured friction force and the calculated shear resistance of the film is equivalent to the portion of resistance produced by the solid contact (asperities). The ratio of the resulting reaction force contributed by the asperity interactions and the corresponding normal load (as determined from the load sharing iterative process) is called the asperity friction-load ratio and it is dimensionless; to differentiate it from the traditional coefficient of friction. This scheme is repeated for each lubricant, roughness, sliding speed and loading. These results are plotted for each lubricant in Figs 6.7 (a), (b) and (c). Very important aspects can be revealed keeping in mind the peculiarities of the approach used to generate them. This ratio is sensitive to the behaviour of the lubricating film as well as the properties of the adhesive bonds of the layer at the asperities interface, and therefore it cannot be understood as the coefficient of friction obtained at a certain loading and varying speed. The asperity friction-load ratio is sensitive to the variation of speed because an increasing speed permits the establishment of the film; affected by its capacity to support the load, which in turn decreases the area of solid contact implying a decrease of the load supported by the asperities. A new distribution of the shared load to balance the same total load applied to the bearing ensues. As for the tangential load (asperity friction), it depends on the shearing resistance of the adsorbed layer of lubricant at the solid contact.

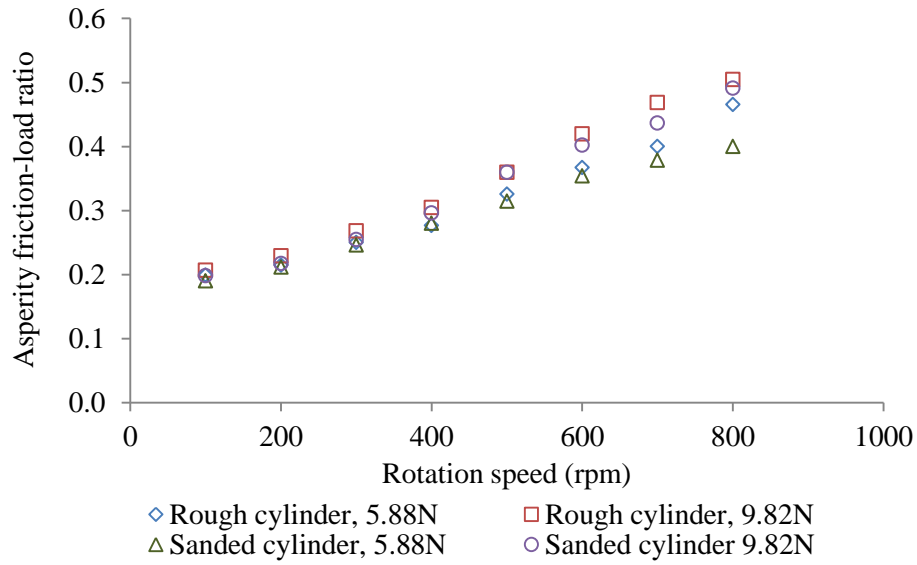


Figure 6.7 (a) Asperity friction-load ratio of oil #1

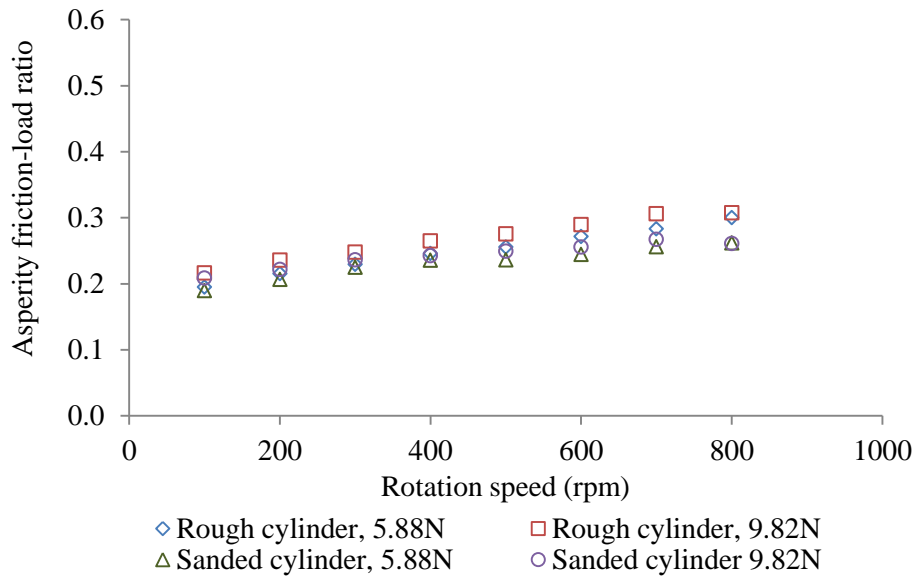


Figure 6.7 (b) Asperity friction-load ratio of oil #2

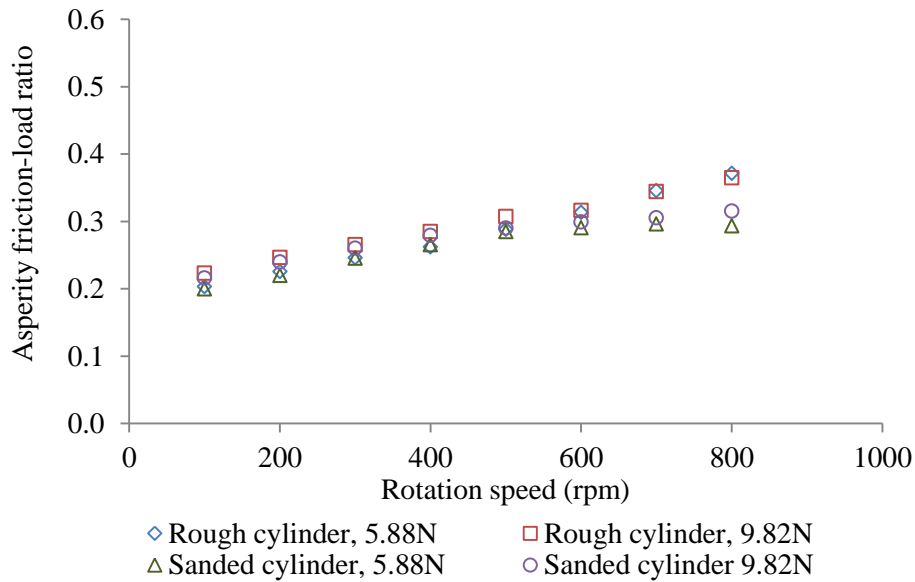


Figure 6.7 (c) Asperity friction-load ratio of oil #3

Fig. 6.8 has been plotted to illustrate the normal load and the generated friction force involved to indicate the asperities are in contact, for the case of rough contact lubricated with oil #1 and subjected to 9.82 N of total loading on the bearing. Both, the normal load on the asperities and friction force decrease with the increasing speed, but at different rates yielding an increase of their ratio. Referring back to Figs 6.7 (a), (b) and (c), the ratio between the normal load on the asperities and the friction due to asperities interaction is significantly affected by the viscosity but also the adsorption properties of the layer and to a lesser degree the applied total loading; although its effect becomes more apparent at speeds higher than 400 rpm. There is an indication that it is the strong adhesive bonds of the polymer additives long molecules in oils #2 and #3; forming a third body, that contribute to lowering this ratio.

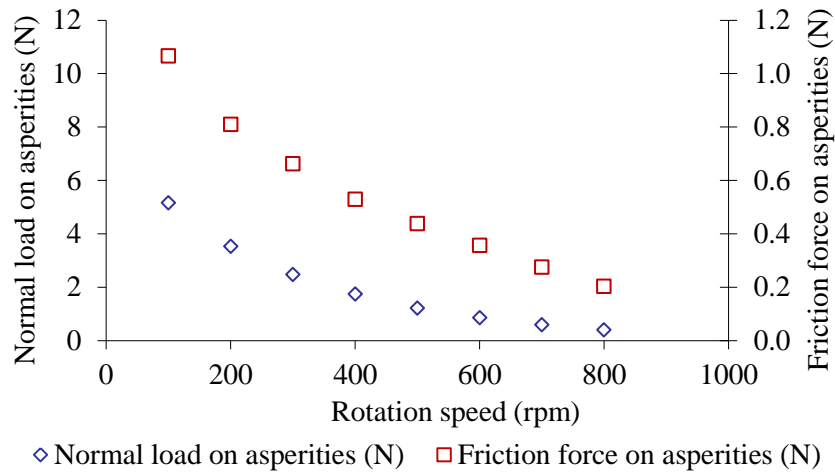


Figure 6.8 Asperity normal load and friction force components versus rotational speed for oil #1 with rough cylinder and 9.82 N applied total load

For the case of oil #1 with rough cylinder and 9.82 N applied total load, an illustration of the variation of the normal load and tangential friction force, acting on the lubricant film, with the speed is depicted in Fig. 6.9 for the case of oil #1, rough cylinder and 9.82 N loading; taken as example. Both forces increase but at different rates; the friction force on lubricant amplifying faster.

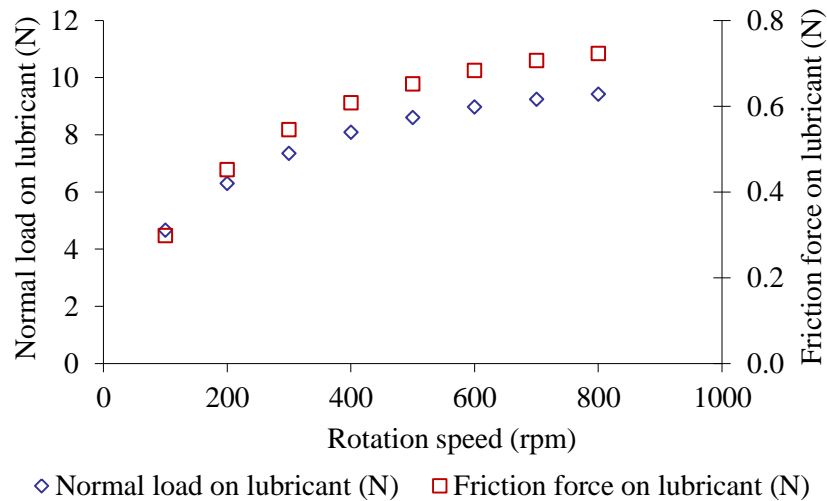


Figure 6.9 Lubricant normal load and friction force components versus rotational speed for oil #1 with rough cylinder and 9.82 N applied total load

The plots of Figs 6.10 (a), (b) and (c) illustrate the variation of the lubricant friction-load ratio with the rotational speed. As for the fluid portion of the contact zone, it was mentioned earlier that the increasing speed promotes pressure build-up at the separated regions of the contact zone and thus thicker film forms. As shown in Fig. 6.9 taken as example, during this process, there is an increase of the load portion supported by the film and at the same time a rise of the shear stress takes place due to the increasing shear rate. The results reveal the important role of the viscosity in the performance of the mixed lubrication regime. High viscosity is shown to lead to conditions of high lubricant friction-load ratio which stabilizes at relatively low rotational speed independently of the roughness.

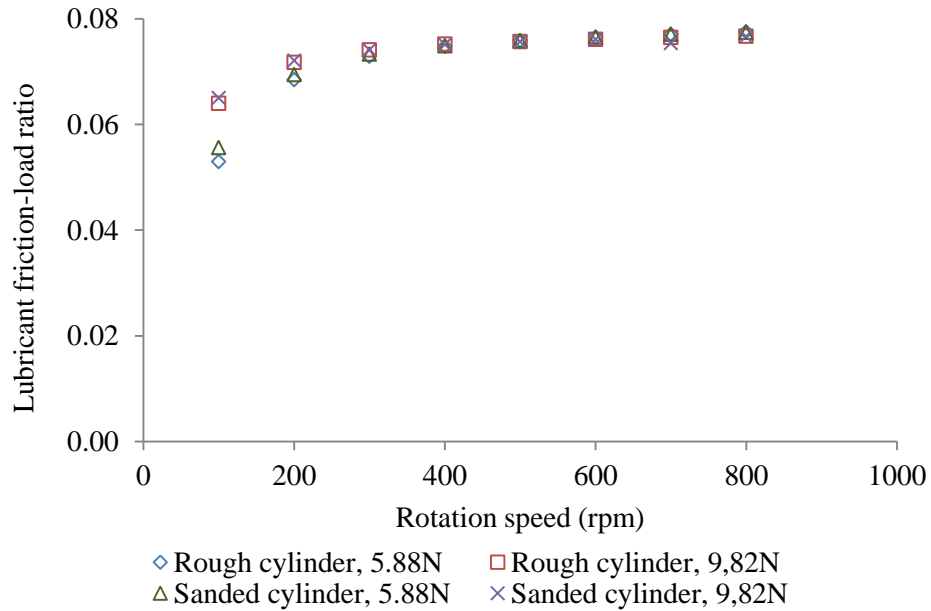


Figure 6.10 (a) Lubricant friction-load ratio of oil #1

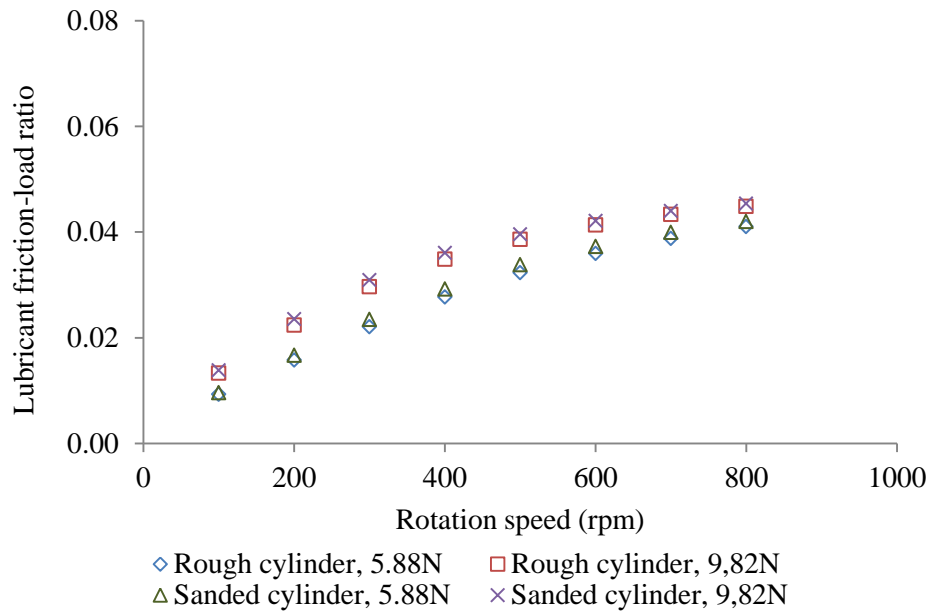


Figure 6.10 (b) Lubricant friction-load ratio of oil #2

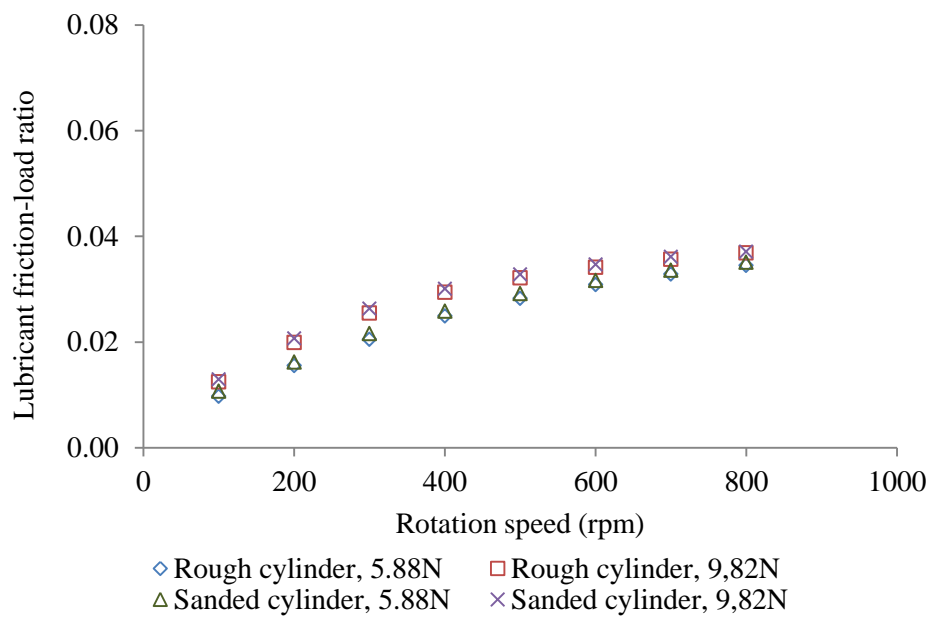


Figure 6.10 (c) Lubricant friction-load ratio of oil #3

Fig. 6.11 has been generated to exemplify the simultaneous development of both ratios with speed. The asperity friction-load ratio is higher and increases slightly then stabilizes when the EHL regime is attained. On the other hand, the second ratio although smaller increases at higher rate due to the rise of the shear stress in the film until it fully forms. These results indicate clearly that the modelling of the friction in mixed lubrication may prove to be inaccurate when the asperity friction, the most dominant parameter in the equation, is approximated by Coulomb constant.

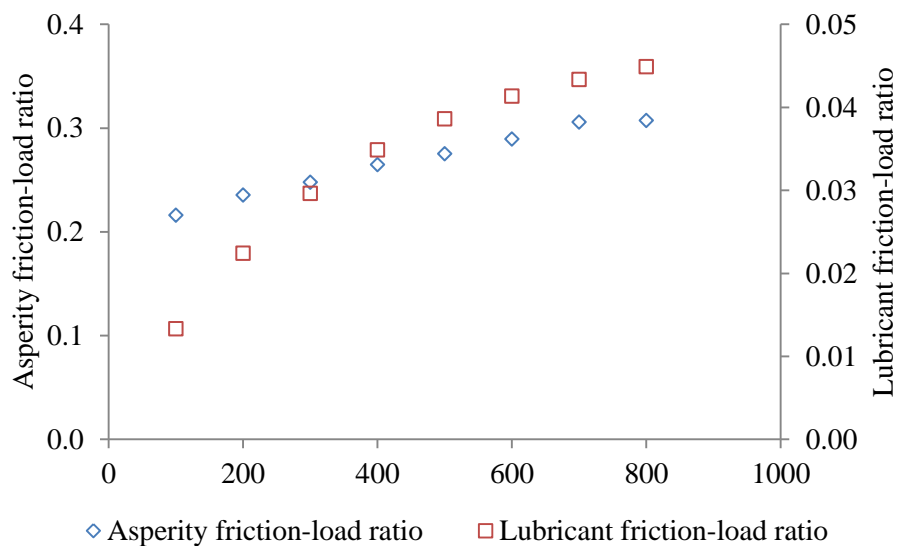


Figure 6.11 Superposition of asperity and lubricant friction-load ratios for rough contact lubricated with oil #2 and loaded at 9.82 N

6.3 Friction force in Starved Film Condition

The friction force in starved mixed lubrication regime was measured in a similar way as in the fully flooded case. However, in this study, the condition of starvation was simulated by limiting the supply of lubricant entering the active zone of the bearing. Preliminary testing has determined the adequacy of total amounts of lubricant equivalent to 60 μ l and 100 μ l to generate starved settings. The process of their application onto the cylinder surface was described earlier. All raw data, as acquired, are shown in the form of tables in Appendix I.

Averaged total friction force as function of the rotational speed is shown in Figs 6.12 to 6.17 for all experimental variables; together with the equivalent operating conditions under fully flooded mixed lubrication. Each data point shown represents an average of the triplicate measurements at identical test conditions. The maximum scatter of these measurements that deviates with respect to the average value was 7%. The comparison between the fully flooded and the limited oil amount tests with the same operating condition indicates similarities (less than 4% and attributed to measurement uncertainties) at low speeds but disparities occur at critical speeds signaling the onset of starvation. This observation demonstrates the suitability of the testing procedure to assess the behaviour of starved film. In starved condition, there is not enough lubricant to generate a robust film even at high speed. The results suggest critical speeds ranging from 200 rpm to 400 rpm depending on the operating conditions. In agreement with other findings, Cann *et al.* [2004] and Berthe *et al.* [2014], the condition of starvation is strongly linked to the viscosity; initiated at lower speed for high viscosity lubricants. It is also dependent, in the same manner, on the magnitude of the normal loading supported by the bearing. These authors [Damiens *et al.*, 2001 ; Cann *et al.*, 2004] have proposed a starvation onset parameter proportional to $N^{-0.333}$. Hence, starvation is more likely to occur at high speed, high lubricant viscosity, and high loading which induces larger nominal (Hertzian) contact area. The latter denotes that lower critical speed is triggered with higher loading.

It has been reported by Ali and Hartl [2012] that the apparent friction coefficient obtained with ball-on-plate bearing configuration lubricated with limited amount of oil, operating at very low speeds, were higher than those for the fully flooded condition; reached at high speeds. Using small amount (20 μl) of viscous oil (0.383 Pa·s at 40°C) and high loading the authors verified that starvation can occur even at very low speed. The present results confirm this conclusion as they show clearly the effect of the amount of lubricant on the onset of starvation. It is considered that the applied loading influences the film thickness at the contact zone even in the EHL regime. However, the effect of the increase of the nominal contact area due to higher loading; which affects the replenishment process by creating environments similar to limiting the lubricant amount at the inlet, leads to starvation beginning at relatively lower speeds. This finding shows that the effect of the applied load on the onset of starvation for the case of thick film lubrication [Damiens *et al.*, 2001 ; Cann *et al.*, 2004] also holds for mixed lubrication. Furthermore, the results indicate that starvation starts at higher speeds in the cases of 100 μl oil volume than in the cases of 60 μl oil, specifically for the cases of oils #1 (Figs 6.12 and 6.13) and #3 (Figs 6.16 and 6.17). Thicker oil layer across the track generates more efficient replenishment, at the same time the data show comparable friction resistance in starved condition (high speed) independently of the amount of lubricant. Therefore, it is concluded that the consequence of the

amount of oil supplied to the rolling track on the friction performance of the bearing becomes insignificant when starvation is fully developed.

In a starved situation, it is the amount of lubricant that reaches the actual contact interface that influences the lubrication process. Even if there is an abundance of lubricant supplied to the inlet of the contacting zone, the operating conditions could limit the film thickness prompting starvation. In addition, the present results show that a gradual increase in friction with speed in the starved regime before stabilizing at the high speed range, generally above 600 rpm. This implies that the amount of oil at the contact interface is not reducing continuously with speed but a certain film thickness is maintained. When focussing on the role of the asperities, the results suggest a beneficial effect on the lubrication process which may be attributed to their geometry allowing the formation of trapped bulk lubricant in reservoirs, as illustrated in Fig. 6.5. These reservoirs also supply lubricant to the solid interface. This favourable effect is demonstrated by the delayed onset of starvation for the rough cylinders.

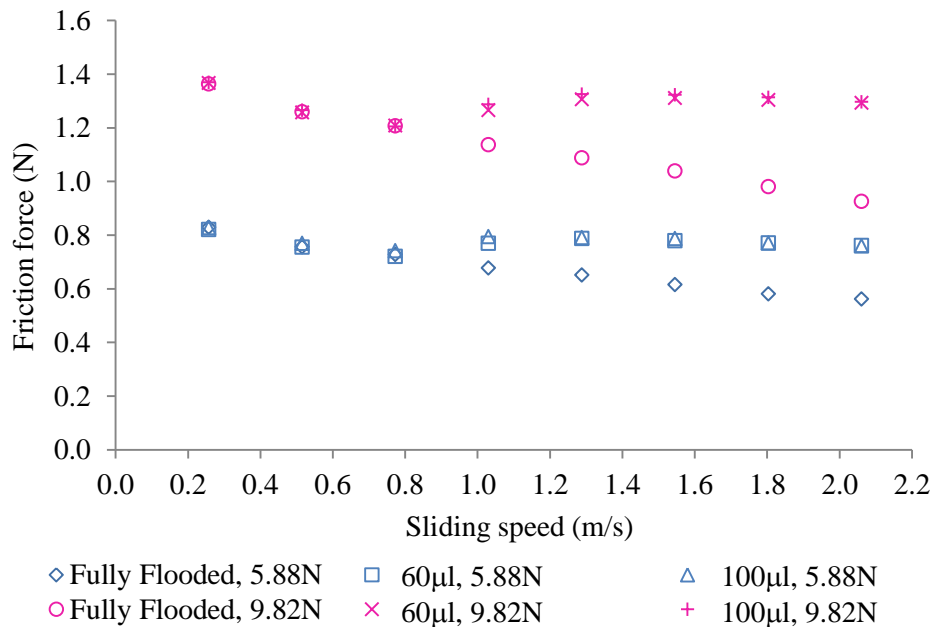


Figure 6.12 Friction force versus rotation speed of oil #1 for rough cylinder

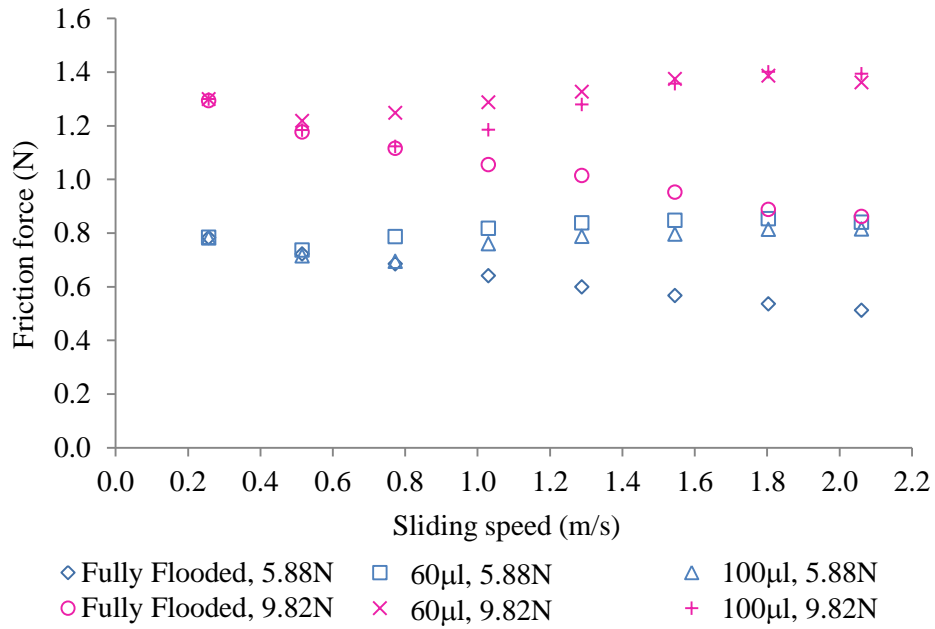


Figure 6.13 Friction force versus rotation speed of oil #1 for sanded cylinder

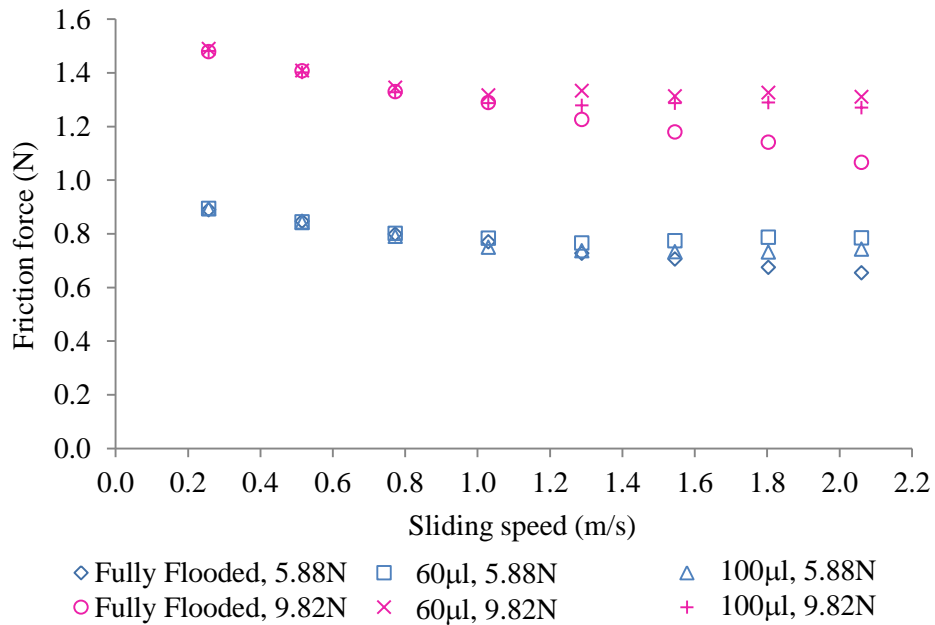


Figure 6.14 Friction force versus rotation speed of oil #2 for rough cylinder

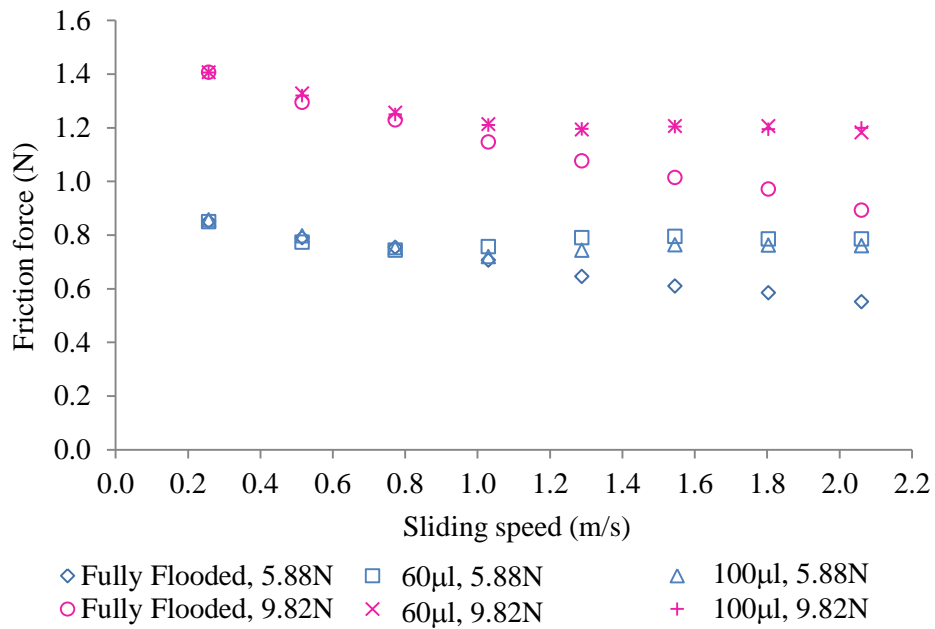


Figure 6.15 Friction force versus rotation speed of oil #2 for sanded cylinder

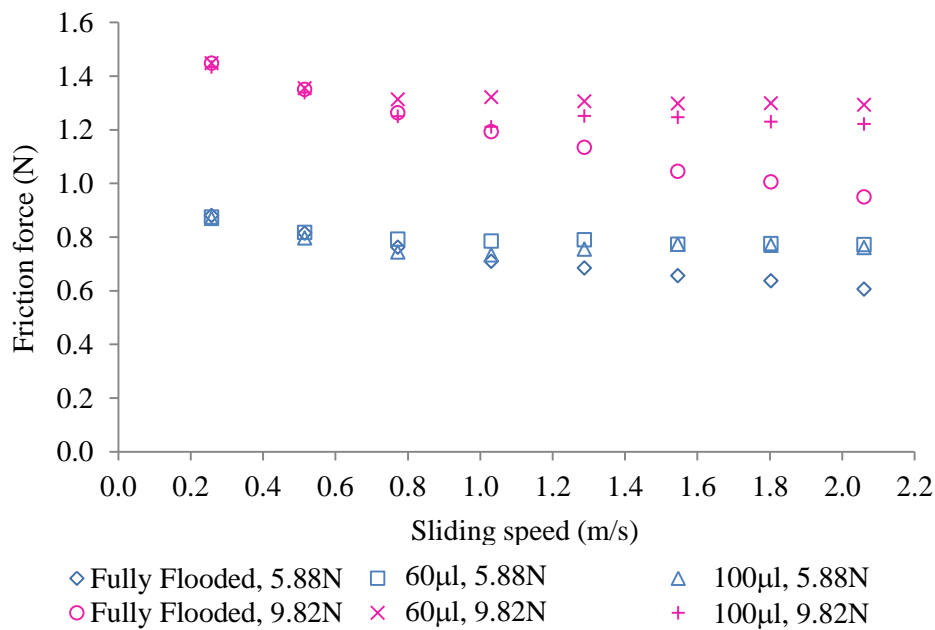


Figure 6.16 Friction force versus rotation speed of oil #3 for rough cylinder

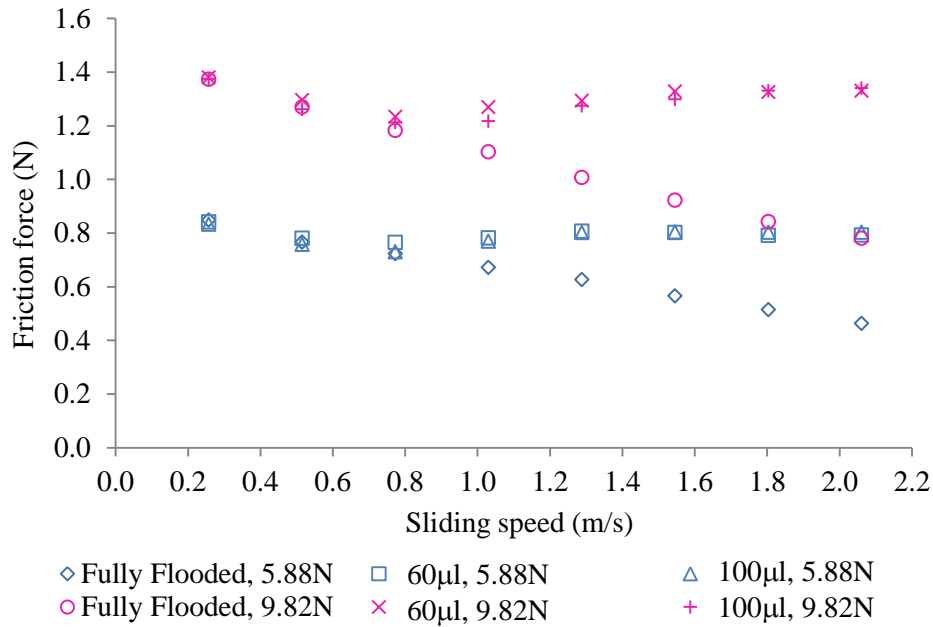


Figure 6.17 Friction force versus rotation speed of oil #3 for sanded cylinder

6.4 Central Film Thickness in Starved Mixed Lubrication

This study focuses on the assessment of the behaviour of the lubricating film when operating in the mixed lubrication regime with starved film. A model combining Reynolds theory and the well acknowledged load sharing concept, presented in Chapter 3, is available to estimate the film thickness in this regime under fully flooded state. However an iterative routine had to be developed in order to find the proper distribution of the applied normal loading among the solid (asperities) and the lubricant. This model was used for the estimation of the asperity friction-load ratio from experimental measurements of the total friction force. Starved lubrication occurs when the operating conditions do not permit the build-up of a thick film in accordance to the theory. Although research in this field for EHL regime and smooth contacts has progressed substantially; the case of starved mixed lubrication condition is still at its embryonic stage. So far, it is believed that the starved central film thickness can be estimated by applying an attenuation factor to the predictions for fully flooded contact, and a link between this correction factor and the starvation degree (SD) has been suggested. In this research, the film thickness is estimated from measurements of the total friction in starved conditions and the known asperity friction-load ratio determined earlier. Fig. 6.18 presents an example of results of the friction force on the asperities determined as the product of the normal load; obtained using the load sharing

concept, and the asperity friction-load ratio satisfying the fully flooded condition. The normal load on the asperities is also shown.

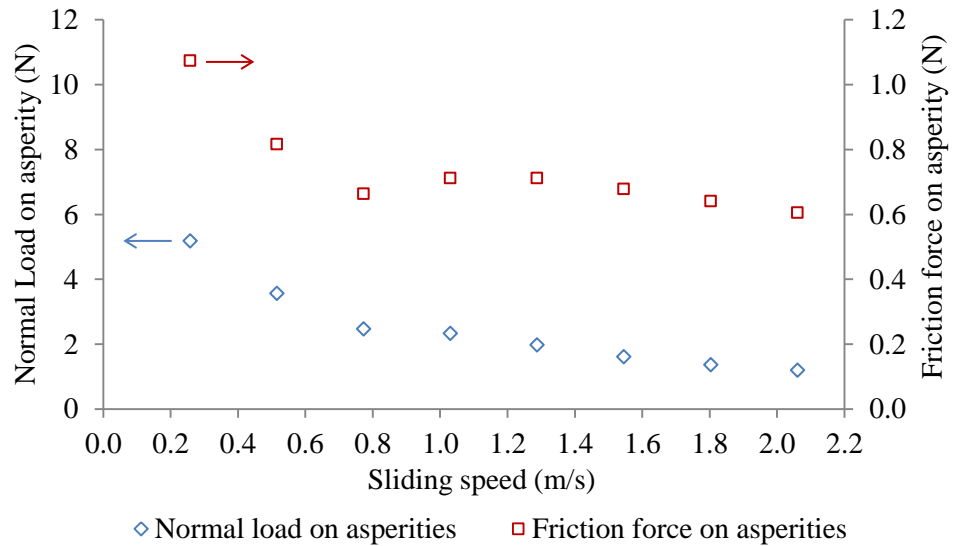


Figure 6.18 Normal and friction forces for 100 ml of oil #1, rough cylinder, total applied load 9.82 N

The effects of the operating conditions on the fully flooded central film thickness are assessed first. As expected, the fully flooded film thickness increases with speed; Fig. 6.19 exemplifies this trend. Tested oils with higher viscosity resulted thicker films. This shows that the influence of oil viscosity on film thickness, according to the classical film thickness theory, is maintained for fully flooded mixed lubrication. The surface roughness has only marginal effect. It is concluded that the central film thickness can be well correlated to the rotation speed by power laws indicated on the graph for each oil and 5.88 N total loading on the bearing; independently of the surface roughness.

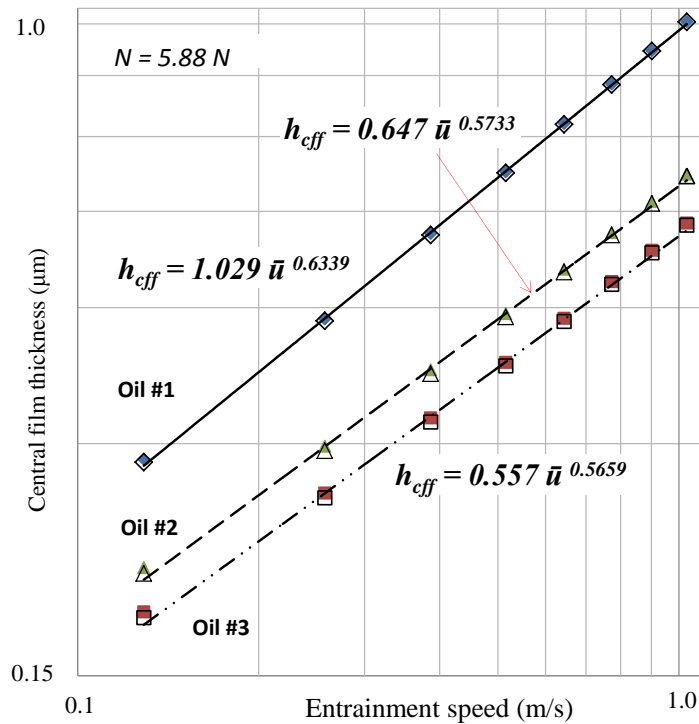


Figure 6.19 Estimated central film thickness versus rotation speed fully flooded contact for rough and sanded (empty markers) cylinders, $N = 5.88 N$

The effect of the loading, for case of the rough cylinder taken as reference, is depicted in Fig. 6.20. The anticipated decrease of the film thickness with the loading is confirmed. These variations with the rotation speed can also be expressed by powers laws. At the same time, the high performance of oil #1, generating thicker film offsets the effect of higher loading. The positive effect of the viscosity on the film thickness is also revealed when comparing oils #2 and #3. It is found that the film build-up process with increasing speed, in fully flooded mixed lubrication, is affected by the loading, however higher viscosity can compensate by fostering a thicker film at high speed. The roughness of the contacting surface does not influence the development of the film in mixed lubrication at fully flooded state. The use of the classical film thickness theory for smooth contact [Hamrock and Dowson, 1981 ; Nijenbanning *et al.*, 1994]; which also predicts power law relationship of the central film thickness with the speed [Damiens *et al.*, 2001 ; Cann *et al.*, 2004] would not be applicable for the mixed regime.

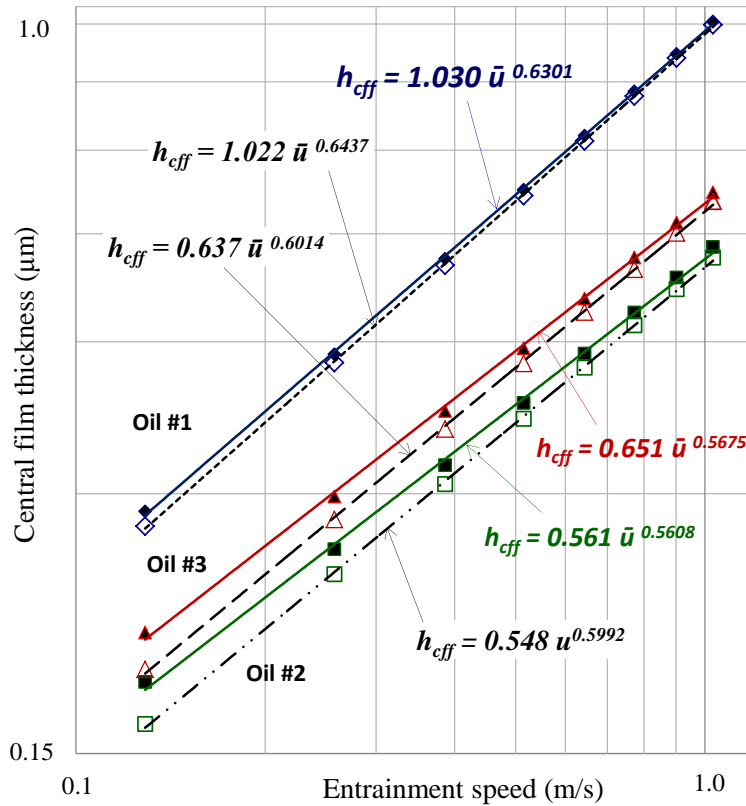


Figure 6.20 Estimated central film thickness versus rotation speed fully flooded contact for rough cylinder, $N = 5.88 \text{ N}$ and $N = 9.82 \text{ N}$ (empty markers)

The behaviour of the starved film under the experimented operating conditions is thoroughly analysed. In starved conditions, the central film thickness increases at a lower rate in comparison to the fully flooded contact; behaviour shown in Fig. 6.21 showing that evaluation for rough contact loaded at 5.88 N and lubricated with $60 \mu\text{l}$ of oil. Similar to earlier observations on the variation of the friction force, depending on the type of oil, the film build-up process tempers starting from a certain speed level. Also, higher viscosity generates a more severe drop in the film thickness with speed. However, this finding contradicts the results of optical measurement of the film thickness in starvation studies of thick film lubrication [Damiens *et al.*, 2001 ; Cann *et al.*, 2004]. This important deviation is indicative of a distinct behaviour of the film in starved mixed lubrication. Therefore, it is believed that the sole existing model proposed to define the onset of starvation cannot be generalized to encompass bearings operating under starved

mixed lubrication regime. The present results show that; similarly to the fully flooded case, the starved film thickness can be approximated by power laws or logarithmic functions of the speed.

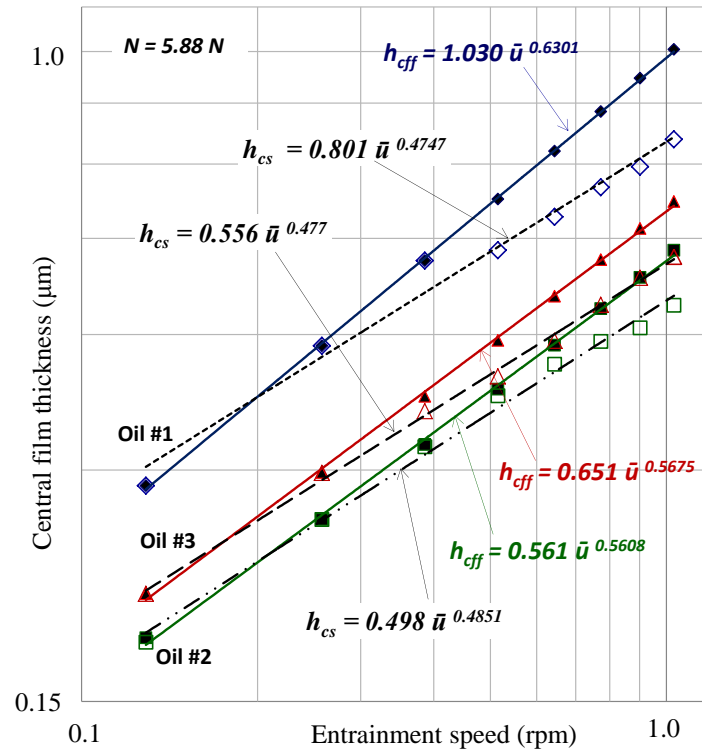


Figure 6.21 Estimated central film thickness versus rotation speed, for rough cylinder, $N = 5.88 \text{ N}$, fully flooded and starved $60 \mu\text{l}$ (empty markers)

The plots of Fig. 6.22 serve to assess the effect of the surface roughness on the build-up of the film. The beneficial influence of the roughness is demonstrated once more. For the same operating conditions and amount of lubricating oil supplied to the inlet; thicker film is generated with rougher surface of the bearing.

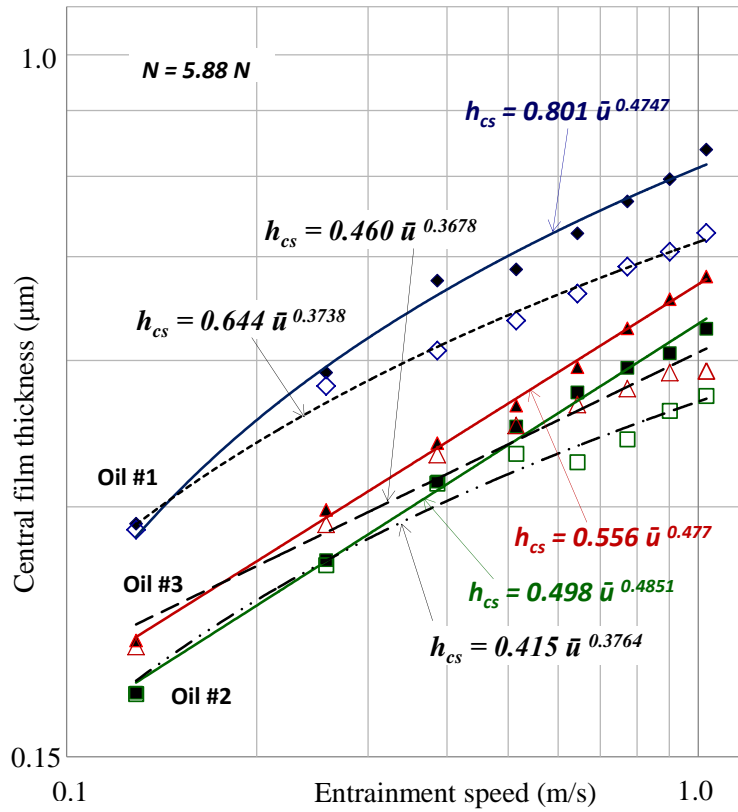


Figure 6.22 Estimated central film thickness versus rotation speed for starved contact $60 \mu\text{l}$, $N = 5.88 \text{ N}$, for rough and sanded (empty markers) cylinders

The effect of the loading exemplified in Fig. 6.23 holds for the starved film as well. The generated film is thinner at higher loading and the decrease is influenced by the viscosity.

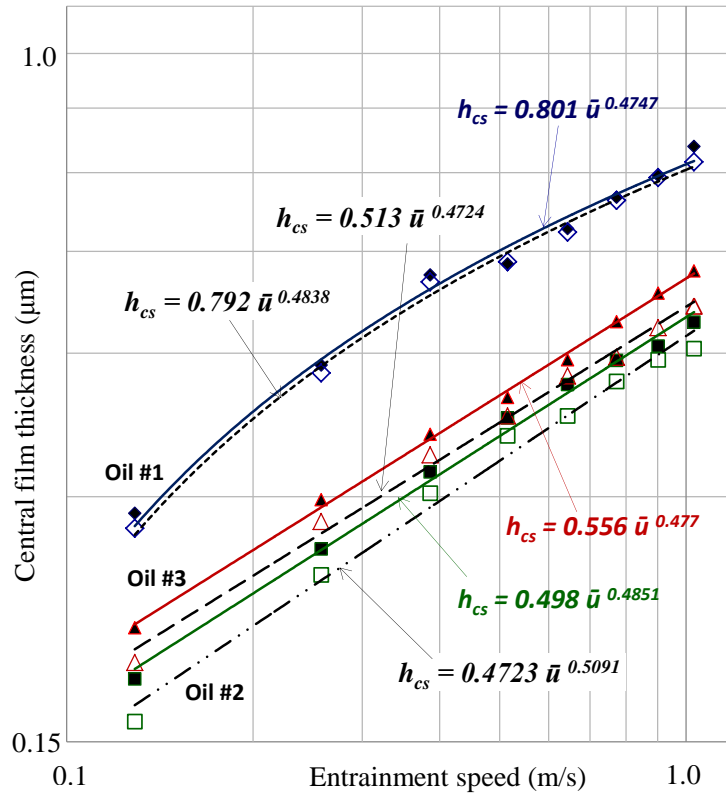


Figure 6.23 Estimated central film thickness versus rotation speed for starved contact $60 \mu\text{l}$, rough surface, $N = 5.88 \text{ N}$ and $N = 9.82 \text{ N}$ (empty markers)

The results shown in Figs 6.24 and 6.25 further demonstrate the strong influence of the roughness on the film thickness coupled with the dependence on the amount of lubricant. Smoother surfaces generate thinner films but the thickness is increased with the amount of lubricant supplied. These important findings reveal the importance of not only the operating parameters (speed and loading) and the rheological properties of the lubricant but also the surface roughness. Therefore, it is believed that the starvation degree model defining starvation in thick film lubrication without asperity contact proposed by Cann *et al.* [2004] is not suitable for bearings operating in mixed lubrication regime, where the roughness plays an important role. The present results indicate that the efficiency of the replenishment process of lubricant at the inlet controls to a large degree the condition of starvation. Because of the comparable trends and values of the central film thickness for both supplied amounts of lubricant, there is reason to believe that in

the case of rough surface, the actual volume of lubricant present at the active contact zone is independent of the total amount supplied to the inlet.

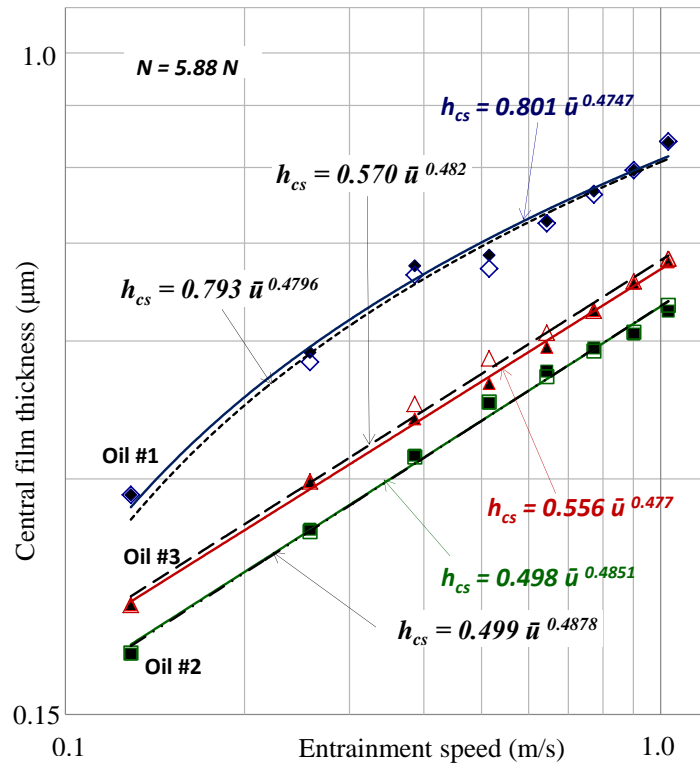


Figure 6.24 Estimated central film thickness versus rotation speed, rough surface, $N = 5.88 \text{ N}$ for starved contacts $60 \mu\text{l}$ and $100 \mu\text{l}$ (empty markers)

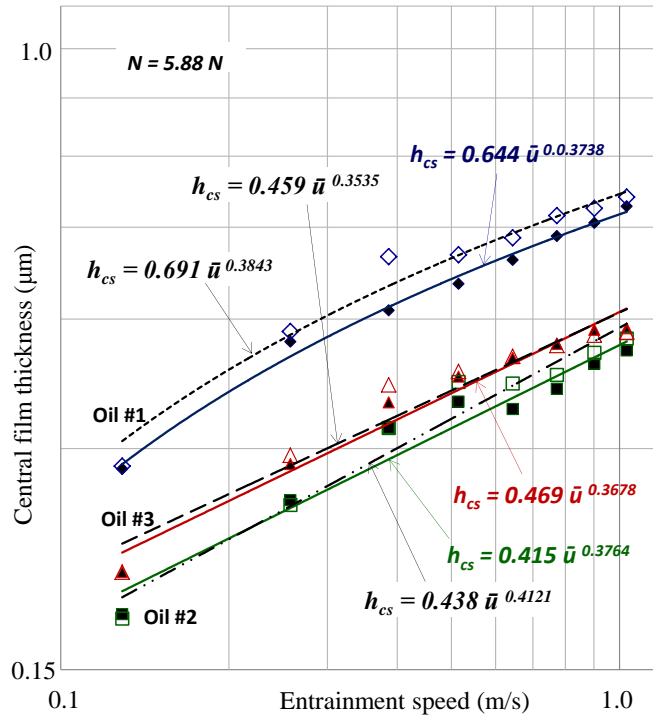


Figure 6.25 Estimated central film thickness versus rotation speed, sanded surface, $N = 5.88 N$ for starved contacts $60 \mu\text{l}$ and $100 \mu\text{l}$ (empty markers)

In this thesis, the investigation of the behaviour of the starved film is conducted by examining the effects of the lubrication parameters considered in this study on the predicted relative film thickness, the predicted meniscus length and the starvation degree parameter.

The methods of estimating the central film thickness in both the fully flooded and starved conditions were presented earlier. The normalised starved film thickness with respect to its corresponding fully flooded is called here in this study the relative film thickness. An example of the variation of the relative film thickness with the entrainment speed is shown in Figs 6.26 and 6.27. These results reveal, in a clearer way, the transition speed to the state of a starved regime; when the relative ratio experiences a first major drop. At the same times, this parameter is affected by the amount of lubricant supplied to the inlet only for low roughness surface.

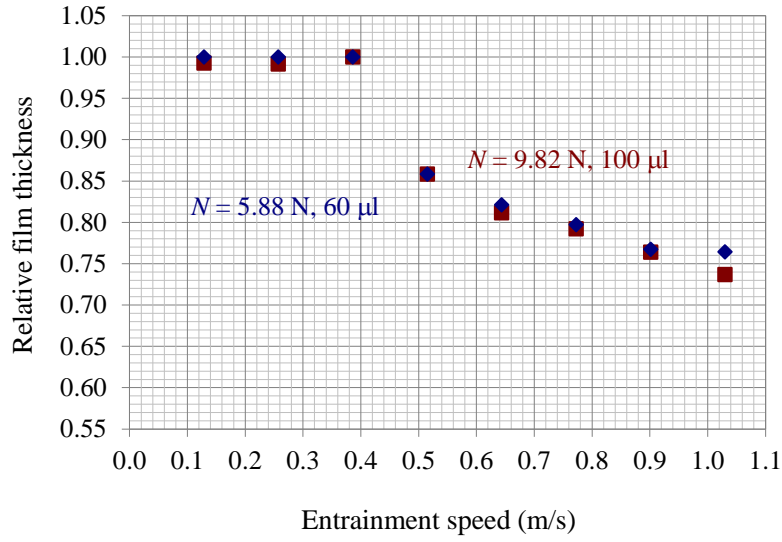


Figure 6.26 Relative film thickness for oil #1, rough surface

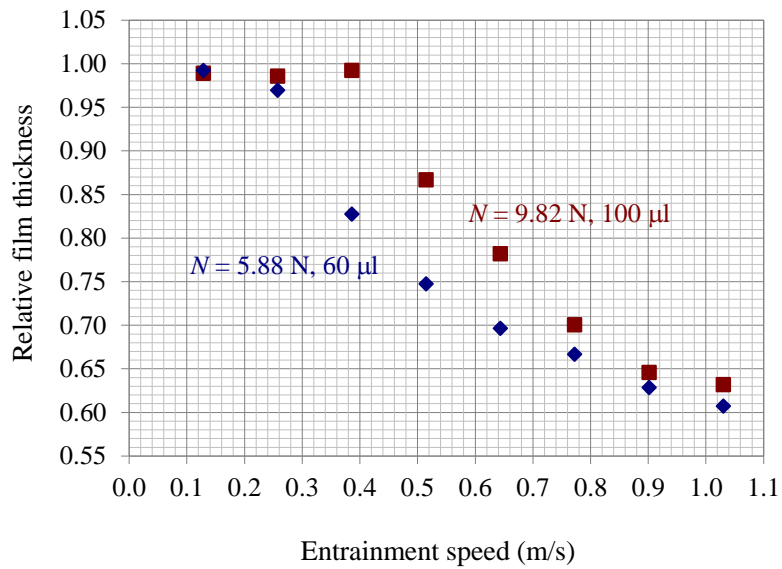


Figure 6.27 Relative film thickness for oil #1, sanded surface

The compilation of the critical speed for the onset of starvation together with the minimum value of the relative thickness is summarized in Fig. 6.28 for the rough surface. Negligible effects of the normal load and lubricant amount on these results were found. The results for the sanded surface are shown in Figs 6.29 and 6.30; emphasizing the effect of the amount of lubricant.

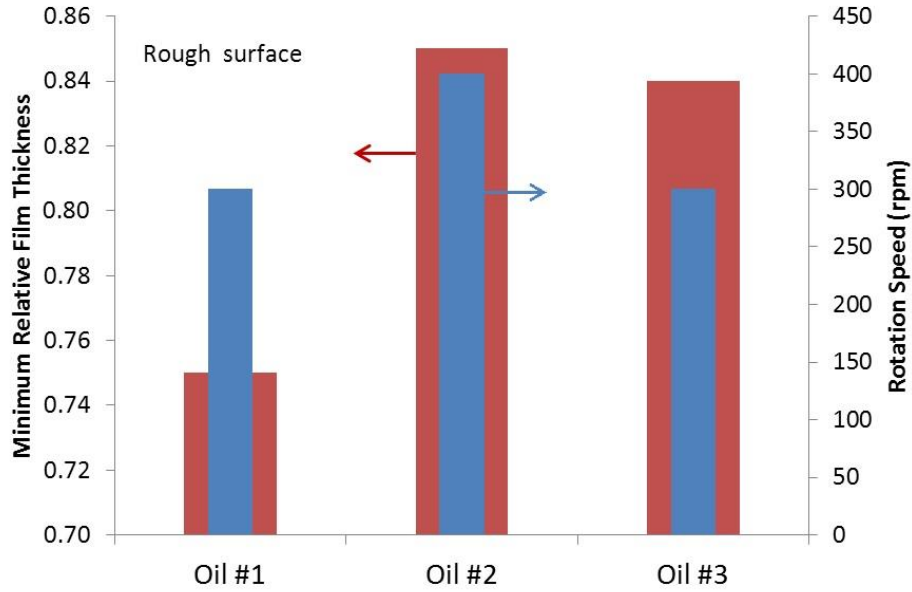


Figure 6.28 Minimum relative film thickness and critical transition speed, all loads and amounts

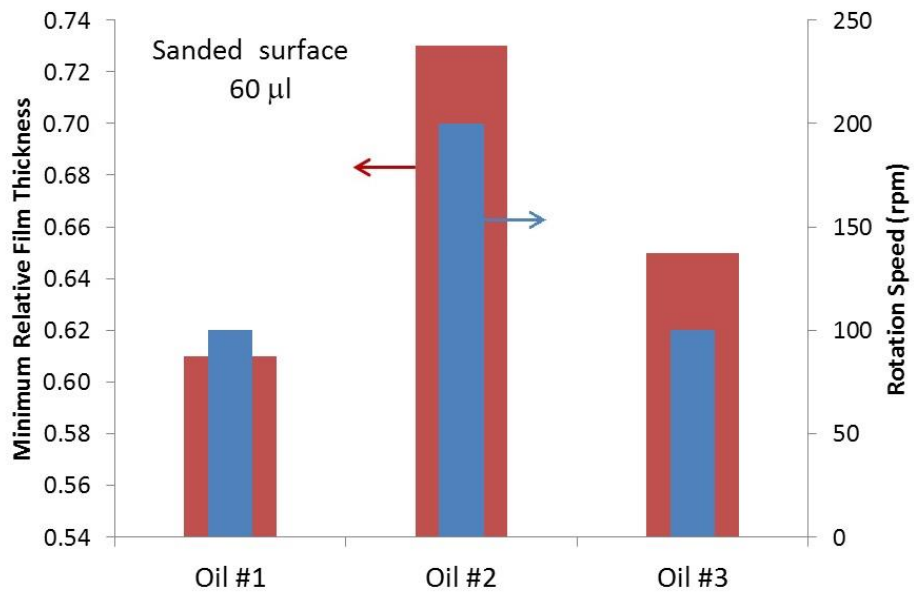


Figure 6.29 Minimum relative film thickness and critical transition speed, all loads and 60 μ l

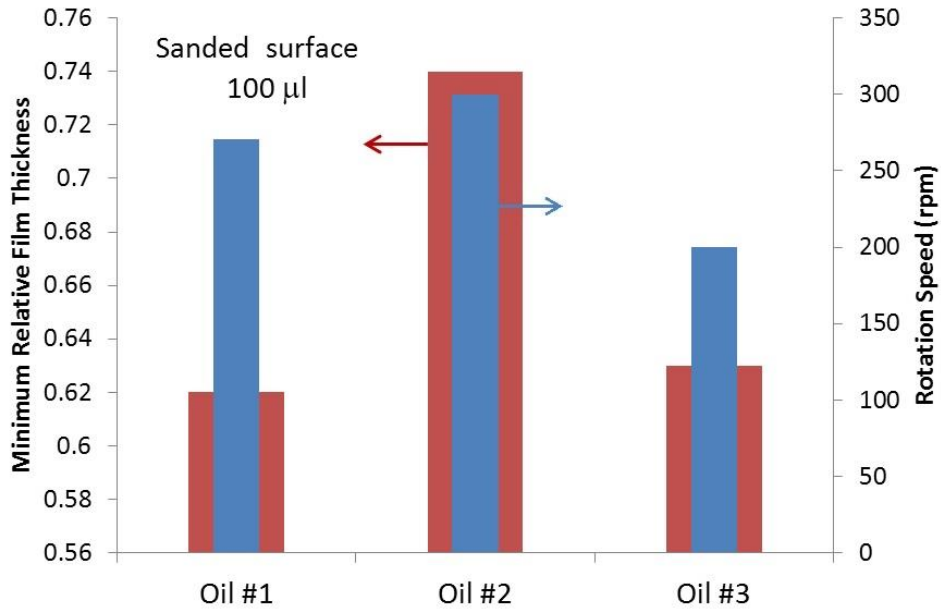


Figure 6.30 Minimum relative film thickness and critical transition speed, all loads and 100 μ l

It is concluded that the roughness of the contacting surface delays the occurrence of starvation to a higher speed and decreases its fully developed severity independently of the supplied amount of lubricant; one example can be seen by comparing Figs 6.26 and 6.27. Increasing the supply of lubricant for low surface roughness is beneficial. Although oil #2 performance in this regard is superior, the influence of the viscosity as such is complex due to its effect on the reflow mechanism of the lubricant to the inlet which in turn depends on the loading. It is to note that we consider that the conditions of this study do not create major thermal transformations. The applied loading has negligible effect specifically for rough surface.

6.5 Inlet Condition

The condition of starvation in this study in relationship to the inlet film thickness was assessed by using Chevalier *et al.* [1998] model, as described in Chapter 2:

$$h_{in} = \frac{\bar{\rho}_{max} h_{cff}}{\sqrt[\gamma]{\left(\frac{h_{cff}}{h_{cs}}\right)^\gamma - 1}} \quad (2.3)$$

This model requires the estimation of the parameter γ defined earlier. A relationship between this parameter and the operating conditions of the bearing has been sought by Damiens, *et al.* [2004]. Simulating the inlet condition in terms of film thickness to generate starved condition, they were able to develop what they called starvation plots. The starvation factor γ was derived, for the conditions of this study, according to a least-square fit procedure. In their study they developed, based on the theory predicting the film thickness, a relationship which permits to determine γ as function of $\sqrt{M/L}$ for different ellipticity parameter of the Hertzian contact k ; where M and L are the Moes dimensionless load and material parameters, respectively, as described in Chapter 2:

$$M = \frac{N}{E' r_x^2} \left(\frac{\eta u_s}{E' r_x} \right)^{-3/4} \quad (2.8)$$

$$L = \xi E' \left(\frac{\eta u_s}{E' r_x} \right)^{1/4} \quad (2.9)$$

The relationship shown in Fig. 6.31 has been developed by interpolation of the published results [Damiens *et al.*, 2004] for the case of the present study with $k = 0.864$.

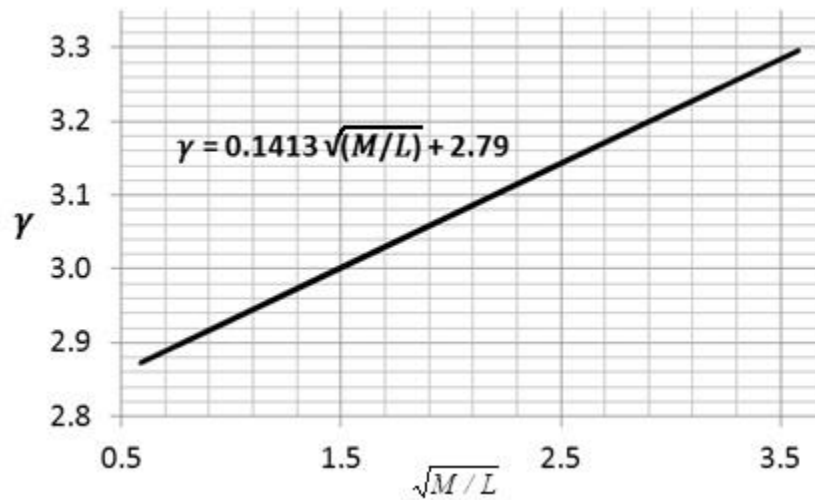


Figure 6.31 Linear variation of γ as function of $\sqrt{M/L}$

The relationship between relative central film thickness h_{cs}/h_{eff} and the h_{in} predicted analytically by using Chevalier *et al.* model in non-dimensional form: $h_{in}/(\bar{\rho}_{max} h_{eff})$ is plotted in Fig. 6.32.

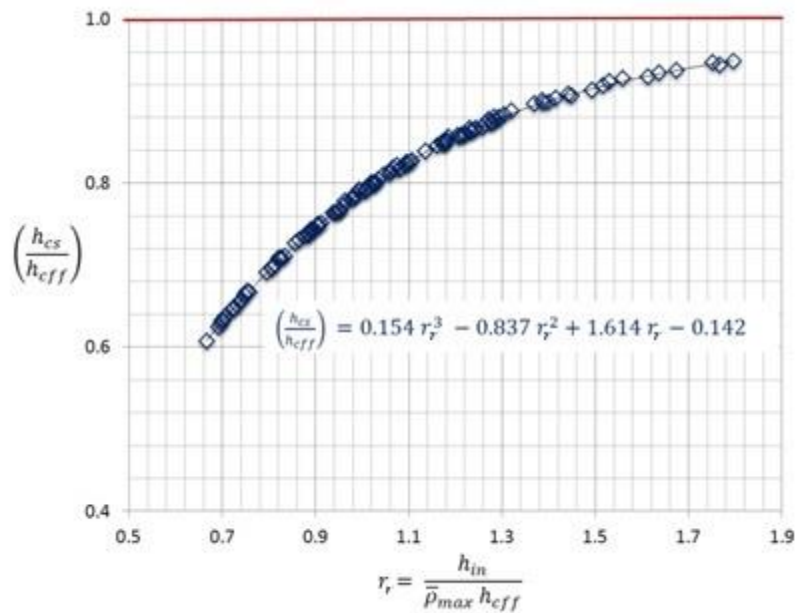


Figure 6.32 $\left(\frac{h_{cs}}{h_{eff}}\right)$ representing the condition of starvation as function of $\frac{h_{in}}{\bar{\rho}_{max} h_{eff}}$

Starvation is initiated when the relative central film thickness h_{cs}/h_{cff} is less than 1. From the results as shown in Fig. 6.32, which depicts the relationship between h_{cs}/h_{cff} and $h_{in}/(\bar{\rho}_{max} h_{cff})$, it was found that starvation is initiated when $h_{in}/(\bar{\rho}_{max} h_{cff}) < 2.2$. At the conditions of this study, $\bar{\rho}_{max}$ varies between 1.1 and 1.2, therefore we have established a general starvation criterion signaling its onset when the condition expressed by the following equation is met:

$$\frac{h_{in}}{h_{cff}} \equiv \left(\gamma \sqrt[3]{\left(\frac{h_{cff}}{h_{cs}} \right)^\gamma - 1} \right)^{-1} \leq 2.64 \quad (6.1)$$

However, the amount of lubricant supplied to the inlet is not represented by the proposed model. Further analysis of the inlet behaviour in starved conditions revealed an interesting relationship between h_{in}/h_{cff} and $\sqrt{M/L}$. At the same time the physical meaning of the important relationship between γ and M/L . This assessment has been done by researchers [Chevalier *et al.*, 1998 ; Damiens *et al.*, 2004] based on a numerical analysis imposing random variations of the parameters M and L ; which simulate the operating conditions, contact model and materials as well as lubricant viscosity. A linear relationship with positive slope was found. However this finding was not clearly related to the severity of starvation. In fact, an increase of γ implies a thicker film at the inlet which reduces the severity of starvation until reaching an ideal steady state when fully flooded regime is established; γ leveling-off to about 6. In this ideal situation, there is enough lubricant to create high performance lubrication and even some of it flowing around the active contact zone.

As for the ratio M/L , its increase decreases the severity of starvation; reflected by milder operating conditions. The effects of the amount of lubricant supplied as well as the surface roughness were assessed by examining the plots of Figs 6.33, 6.34 and 6.35. These depict the variation of the normalized inlet thickness with respect to the central fully flooded h_{in}/h_{cff} , against the operating conditions parameter M/L , for each oil. It is observed that the slope of the linear correlation of γ with the same ratio, also plotted, could be used as a good indicator of the severity of starvation generated by different operating conditions which include the viscosity. Oil #1, with the highest viscosity, is more susceptible of generating starved lubrication; followed by oil #3 and oil #2. This is in agreement with the conclusions of many studies. This research is emphasizing the implication of this parameter; at the same time, it is establishing the importance of the rate of its variation with M/L , which is affected by the viscosity, for the qualitative prediction of the severity of starvation. It is the ratio h_{in}/h_{cff} that permits to quantify it.

Coming back to the same plots, this ratio increases with $\sqrt{M/L}$ and γ . The experimented operating conditions yielded levels of $\sqrt{M/L}$ summarized in Table 6.2. It is to note that although the loading is represented by the parameter M , to be able to assess the effects of the loading and the speed independently, the first was kept constant while varying the second.

Table 6.2 Experimental conditions expressed by $\sqrt{M/L}$

Oil	N (N)	$\sqrt{M/L}$
#1	5.88	$0.59 \leq \sqrt{M/L} \leq 0.83$
	9.82	$0.76 \leq \sqrt{M/L} \leq 1.08$
#2	5.88	$1.40 \leq \sqrt{M/L} \leq 2.11$
	9.82	$1.27 \leq \sqrt{M/L} \leq 1.60$
#3	5.88	$0.88 \leq \sqrt{M/L} \leq 1.24$
	9.82	$1.14 \leq \sqrt{M/L} \leq 1.61$

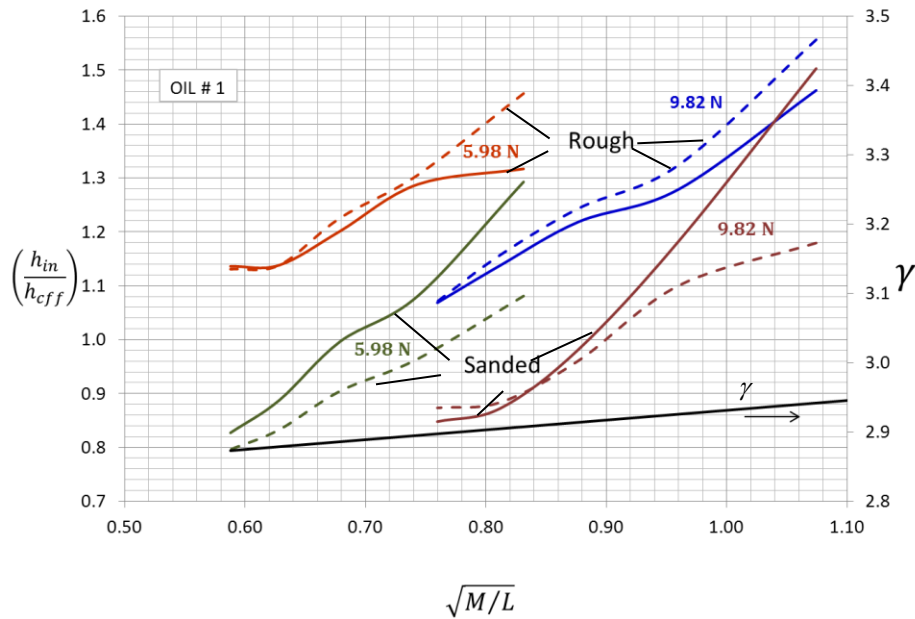


Figure 6.33 Assessment of h_{in}/h_{cff} and γ with respect to $\sqrt{M/L}$ for oil #1, dotted lines represent 60 μl supply, solid lines are for 100 μl supply

These plots serve to demonstrate the effects of the loading, surface roughness as well the supplied amount on starvation in terms of h_{in}/h_{cff} ; which were not apparent previously. It is clear that higher $\sqrt{M/L}$ creates the conditions for the increase of h_{in}/h_{cff} ; converging toward milder starvation independently of the varying conditions. The lowest h_{in}/h_{cff} indicates severe starvation state. Focusing on the loading, the plots show distinctively its important influence on the inlet behaviour. Higher loads induce both mild and severe starvation conditions at higher h_{in}/h_{cff} ; independently of the surface roughness and supply. It is to note that this comportment was not perceived earlier when the friction and film thickness were evaluated. Additionally, milder starvation occurs for smoother surfaces. At the same time, this unique way of presenting the results constitutes a powerful technique for the evaluation of starvation permitting the development of tangible conclusions. It offers complete insights of the mechanisms governing this important phenomenon in the case of mixed lubrication.

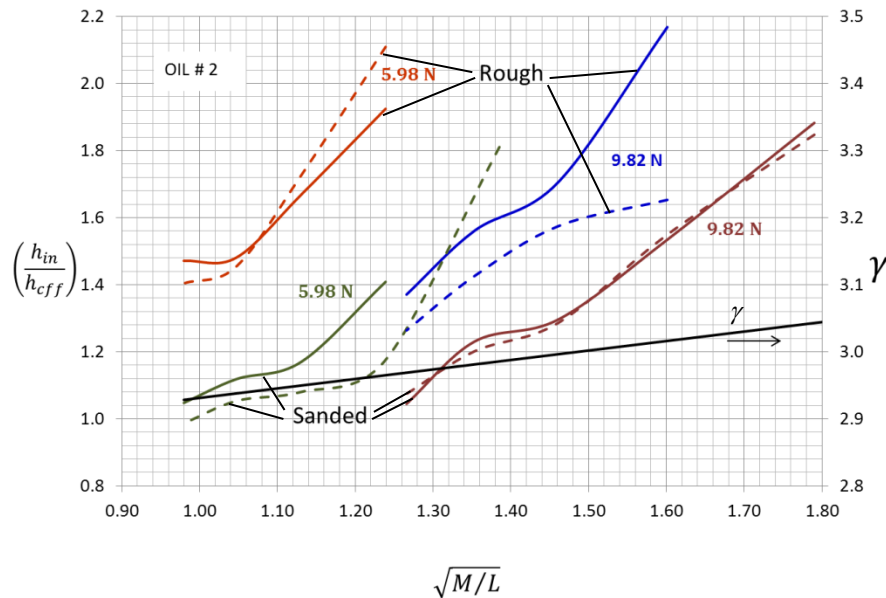


Figure 6.34 Assessment of h_{in}/h_{cff} and γ with respect to $\sqrt{M/L}$ for oil #2, dotted lines represent 60 μl supply, solid lines are for 100 μl supply

Although the conclusion with respect to the delay of the starvation level to higher speeds when roughness increases, enunciated earlier is maintained; a more aggressive starvation occurs for the same $\sqrt{M/L}$ with increasing the roughness. The

influence of the amount of lubricant is clearly confirmed in the case of the smoother surface; higher amount not only delays the same level of starvation to higher speed but also reduces its severity at any operating condition. At the same time, the plots reveal a peculiar behaviour, not clearly recognized earlier, which consist of a mild but perceptible negative effect of the increase of supply for the case of rough surface. However, the noted anomaly, more pronounced when operating at low speed, vanishes when reaching the critical level of starvation. On the other hand, independently of the supplied amount, higher level of critical starvation is generated by smoother surface.

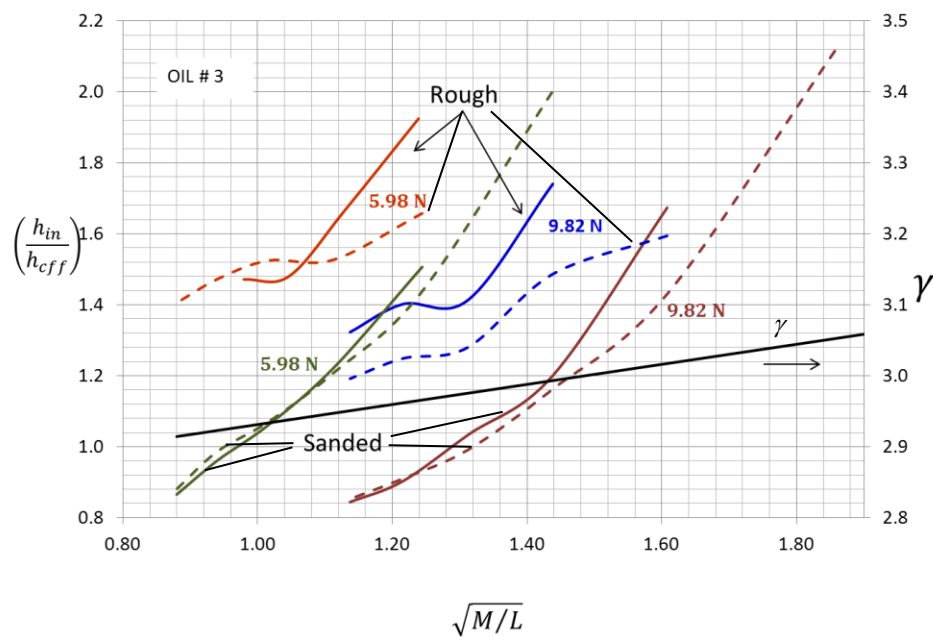


Figure 6.35 Assessment of h_{in}/h_{cff} and γ with respect to $\sqrt{M/L}$ for oil #3, dotted lines represent 60 μl supply, solid lines are for 100 μl supply

The effect of the viscosity can be assessed when comparing the three figures above. It is apparent that the viscosity accelerates the development of starvation as well as its degree for equivalent operating conditions. At the same time, the effect of the applied volume of the less viscous lubricant on starvation is more predictable for rough surface. The results identifying the critical state, which can be interpreted as the oil performance in starved condition, are summarized in Table 6.3. It is seen that oil #3 delivers the highest performance corresponding to

the lowest degree of starvation at operating conditions equivalent to $\sqrt{M/L} = 0.88$ when rough surface is used.

Table 6.3 Critical starvation conditions expressed by $\sqrt{M/L}$ and h_{in}/h_{eff}

Oil	Roughness	N (N)	$\sqrt{M/L}$	Starvation severity h_{in}/h_{eff}
#1	Rough	5.88	0.59	1.13
		9.82	0.76	1.07
	Sanded	5.88	0.59	0.80
		9.82	0.76	0.86
#2	Rough	5.88	0.98	1.40
		9.82	1.27	1.26
	Sanded	5.88	0.98	0.99
		9.82	1.27	1.04
#3	Rough	5.88	0.88	1.41
		9.82	1.14	1.19
	Sanded	5.88	0.88	0.87
		9.82	1.14	0.84

The interest in this study is the investigation of the impact of a properly controlled inlet meniscus distance from the contact zone boundary on the behaviour of the central film. The fully flooded inlet oil length model proposed by Damiens *et al.* [2004], discussed in Chapter 2, was applied to the cases of operating conditions for all tested oils in the present study. The ratio s/s_{ff} was used to express the severity of the starvation, where s is the inlet oil length (Eq. 2.5) and s_{ff} is the fully flooded inlet oil length (Eq. 2.6). The fully flooded results were first analyzed based on the plots of Fig. 6.36 which show the effect of the operating conditions encompassed in the parameter $\sqrt{M/L}$, on the normalized inlet distance with respect to the minor semi-axis of the elliptical contact. The performance of the inlet can be well correlated to the operating conditions and the loading. As the parameter $\sqrt{M/L}$ decreases the establishment of the EHL environment progresses toward an ideal phase that symbolized by an increase of the normalized inlet distance s/b , where b is the semi-minor axis of the Hertzian contact ellipse. At the same time γ decreases simulating a decrease of the ability of the active zone to resist to side-flow. The effect of the loading is represented by the shift of the curves toward higher values of $\sqrt{M/L}$ and a decrease of s/b as b increases with the loading.

The viscosity, also comprised in the parameter $\sqrt{M/L}$ improves the performance of the inlet; shifting it upstream away from the Hertzian zone. There

was no significant effect of the roughness on the inlet behaviour for fully flooded contact and all data can be collapsed on a single curve described with reasonable confidence by the following relationship:

$$\frac{s_{ff}}{b} = 3.8552(M/L)^{-0.24} \quad (6.2)$$

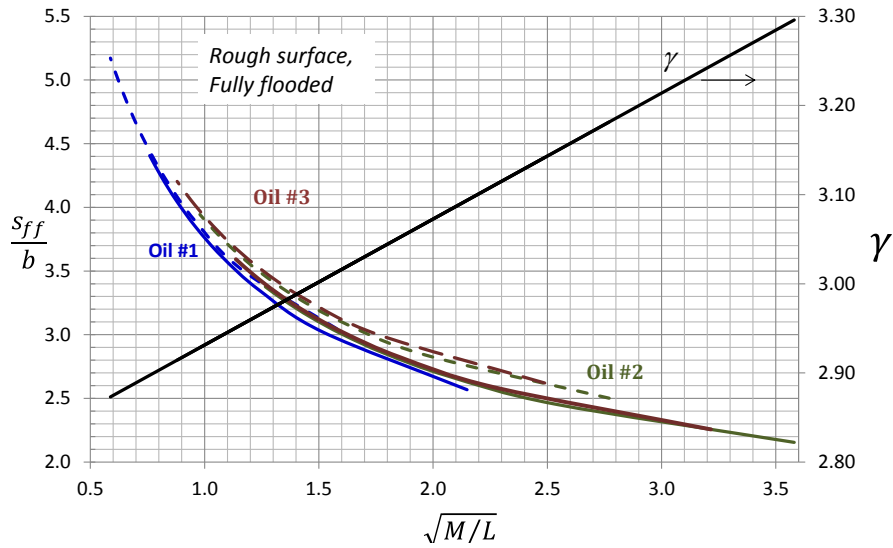


Figure 6.36 s_{ff}/b as function of $\sqrt{M/L}$ for rough surface, fully flooded contact, effect of loading dotted lines for $N = 5.88$ N

The results of starved lubrication are shown in Fig. 6.37 for the case of rough surface and $60 \mu\text{l}$ amount of oil; taken as example. The phenomenon of starvation is fully described by these plots. When focussing on oil #1 for which a line joining the data-points has been drawn to make the trend more visible, there is a sharp increase of the inlet distance with the decrease of $\sqrt{M/L}$, representing the establishment of EHL, to a maximum at which point starvation is initiated by the formation of meniscus that is vigorously pulled upstream as the speed increases. The effect of the loading is also clearly demonstrated and has a strong influence on the inlet behaviour. When comparing the oils, similarities exist between oils #2 and #3 although they have different viscosities. Starvation is initiated much earlier (at lower speeds) for both oils in contrast to oil #1, however the latter experiences a sharp increase in its severity afterwards. The assessment of the effect of the

lubricant supply has revealed its important influence of the critical operating conditions that trigger the onset of starvation but not on its severity.

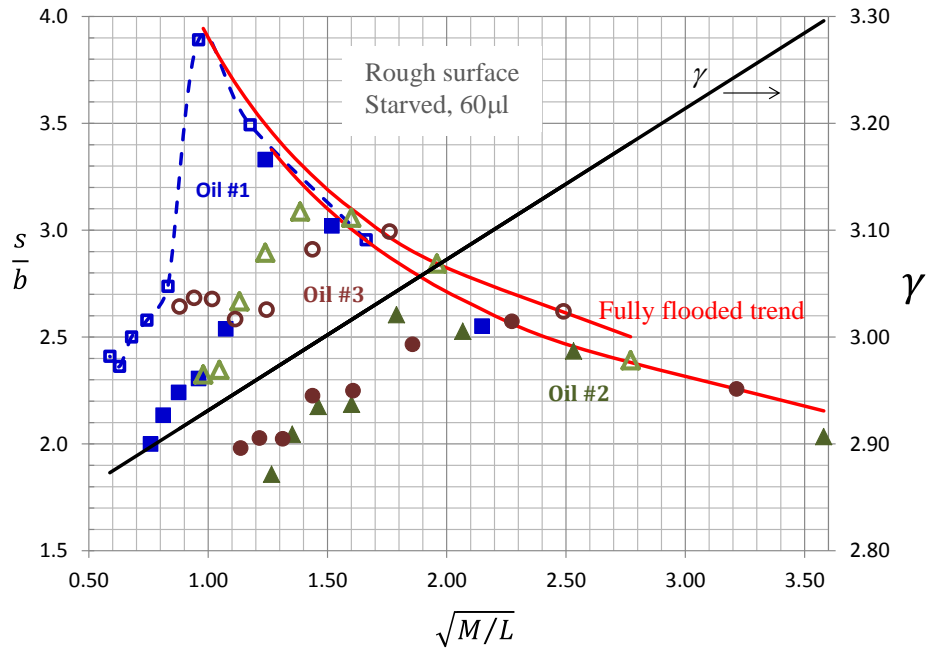


Figure 6.37 s/b as function of $\sqrt{M/L}$ for rough surface, starved contact 60 μ l, effect of loading empty markers for $N = 5.88$ N

According to the data in Fig. 6.38, for the same operating conditions, the roughness develops a mechanism by which the meniscus is held further upstream of the Hertzian contact zone.

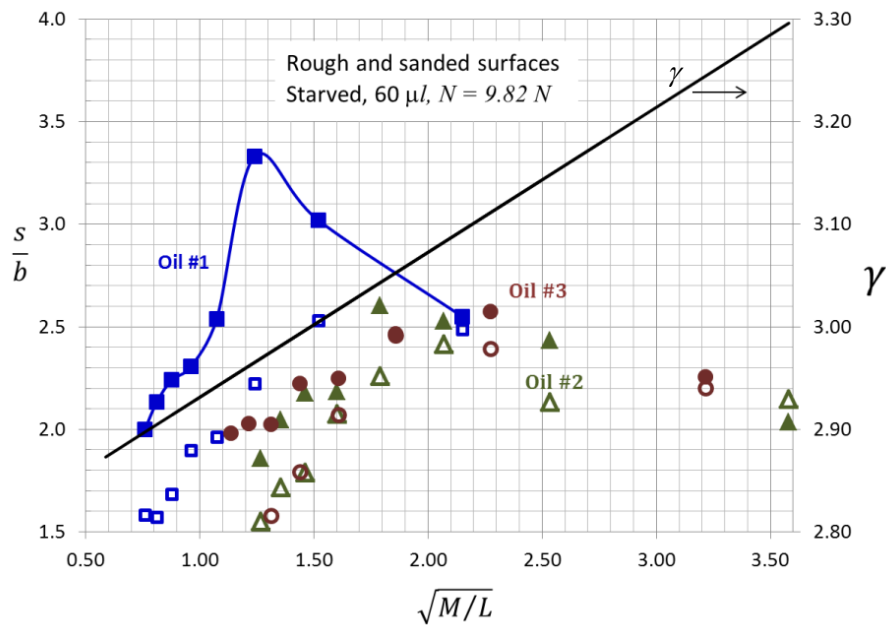


Figure 6.38 s/b as function of $\sqrt{M/L}$, $N = 9.82 \text{ N}$, starved contact $60 \mu\text{l}$, effect of roughness, solid marker for rough surface

A clear representation of the degree of starvation expressed by the ratio s/s_{ff} is demonstrated by the plots of Fig. 6.39. The case of the smallest amount supplied, rougher surface and both loading levels was chosen for illustrating this concept. It is determined that this parameter can be used as a good tool to assess the performance of lubricants starved regime. Log-log scales were found convenient to show the good correlation between the degree of starvation and the operating conditions. These were approximated by power law relationships. The slopes of these lines indicate the rate at which starvation progresses with harsher operating conditions of loading and relative velocity. There is a unique slope for each oil; believed to be related to the viscosity. Oil #1 generates the most severe starvation for comparable operating condition. The lines are equivalent to the asymptotic line simulating the starved state. It is shown that contrary to the fully flooded regime where the film thickness increases with speed; the most important parameter for the early generation of pressure to counteract the loading, in starved conditions the development of the meniscus alters the behaviour of the film at the contact zone. Starvation could therefore be defined as a phenomenon that produces particular physical properties of the inlet film making it unable to generate EHL as predicted by Reynolds equation. It was shown that deficiency in lubricant supply can be one of the symptoms. Additionally, the severity of phenomenon is directly

linked to the ratio s/s_{ff} representing the upstream distance between the meniscus and Hertzian area boundary. In the analysis of starvation as conducted in this study, the decrease of γ with the decrease of $\sqrt{M/L}$ reflects the increase of the resistance of the contact to side flow which becomes sparse to inexistent. However, the effects of lubricant supply as well as roughness have only been assessed qualitatively.

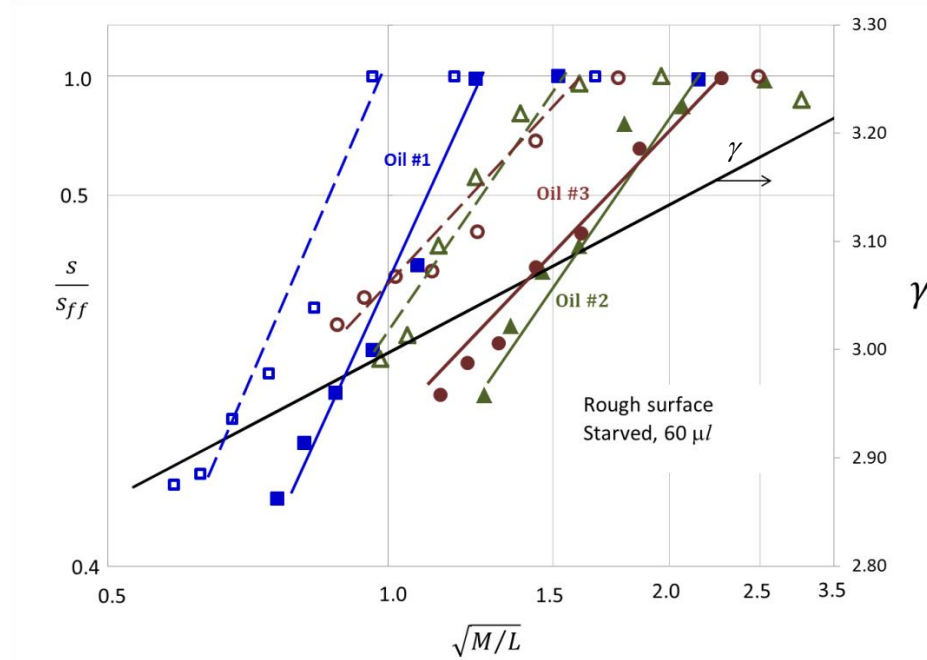


Figure 6.39 s/s_{ff} as function of $\sqrt{M/L}$, rough surface, starved contact $60 \mu l$, effect loading, solid marker $N = 9.82 \text{ N}$

6.6 Starvation Degree (SD)

Cann *et al.* [2004] have developed a criterion for the onset of starvation they called starvation degree (SD) expressing the fully flooded to starved transition for the case of oil-lubricated point contact, which has been discussed in Chapter 2. SD is a dimensionless parameter constructed with five factors, described by Equation (2.13), to predict the onset of starvation:

$$SD = \frac{\eta u a}{h_{oil\infty} \sigma_s} \quad (2.13)$$

where η = viscosity,
 u = sliding speed,
 a = transverse length of the Hertzian contact area,
 $h_{oil\infty}$ = oil reservoir height,
 σ_s = lubricant air surface tension.

From the condition of balance between loss and replenishment of the lubricant to the EHL contact, the authors proposed that, in the ideal case, starvation is triggered when SD is higher than 1, which indicates that the loss is greater than the replenishment. On the contrary, when SD is lower than 1; interpreted by reflow that exceeds the removal, fully flooded condition prevails and the central film thickness can be predicted analytically. From this concept, the minimum quantity of lubricant to adequately lubricate a contact under given operating conditions can be predicted.

In the case of the present study, care was taken in order to supply oil in the form of uniform layer of w_{oil} width, $h_{oil\infty}$ thick and evenly distributed along the track. Therefore, knowing the volume of the supply, we were able to determine $h_{oil\infty}$ with good accuracy according to the following equation:

$$h_{oil\infty} = \frac{V}{2\pi r_{x2} w_{oil}} \quad (6.3)$$

where V = volume of oil applied
 r_{x2} = radius of the cylindrical track (radius of curvature of body 2)

The width w_{oil} was determined using high definition photographs of the oil layer on the track, and an average value of three measurements was considered. The film dimensions for all tested oils, supplied volume and surface characteristics are summarized in Table 6.4.

Table 6.4 Oil layer width and reservoir height

Oil #	Cylinder	Oil volume, V (μl)	Oil layer width, w_{oil} (mm)	Reservoir height, $h_{oil\infty}$ (μm)
1	Rough	60	3.6	107.8
		100	4.0	161.7
	Sanded	60	3.5	110.9
		100	3.9	165.9
2	Rough	60	3.7	104.9
		100	4.4	147.0
	Sanded	60	3.8	102.2
		100	4.5	143.8
3	Rough	60	3.6	107.8
		100	4.1	157.8
	Sanded	60	3.6	107.8
		100	4.1	157.8

The model expressing SD was tested against our results when starvation was quantified by the ratio h_{cs}/h_{eff} to stay consistent with the literature. The totality of the data pertinent to our study was plotted as shown in Fig. 6.40. This model appears to be too conservative in predicting an early onset of starvation at $SD = 1$ when the contact is still operating in fully flooded regime. It became evident that a correction should be considered to take the particular conditions of mixed lubrication into account.

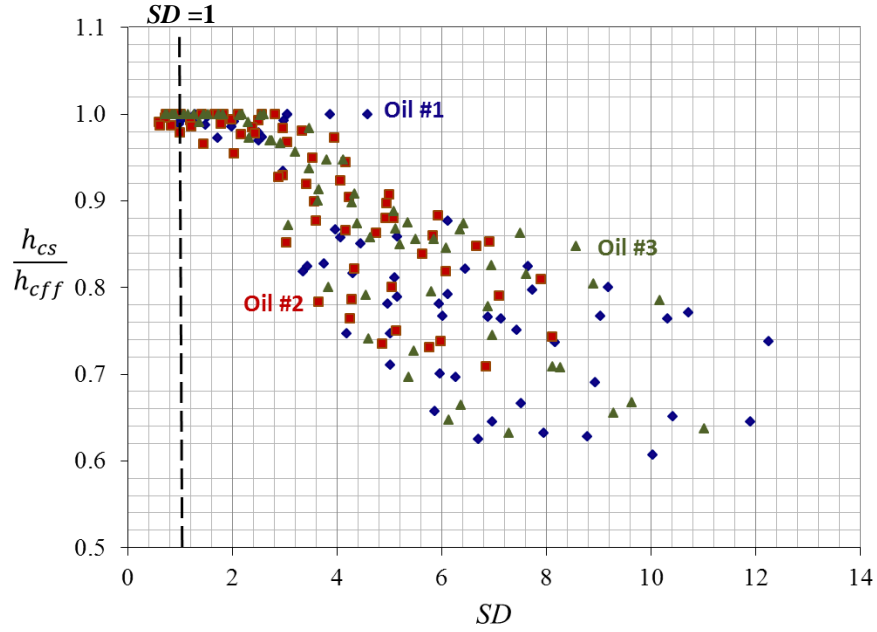


Figure 6.40 h_{cs}/h_{eff} as function of SD for all oils and conditions

A new dimensionless root mean square roughness \bar{R}_q , as well as the concept of resistance to side-flow expressed by the coefficient γ were introduced to the present study. This roughness parameter encompasses not only the equivalent roughness at the contact but also the loading and the equivalent elastic property of the materials involved as shown by Eq. 6.4.

$$\bar{R}_q = \frac{N}{R_q' E'} \quad (6.4)$$

where N = applied load,

R_q' = equivalent root mean square roughness,

E' = equivalent modulus of elasticity

The introduced slide-flow parameter is in the form $(a\gamma)^{-1}$. The amended starvation degree limit is expressed by Eq. 6.5:

$$SD' = \frac{\eta u N}{\gamma h_{oil\infty} \sigma_s R_q' E'} \quad (6.5)$$

The plot of Fig. 6.41 shows the results of the assessment of starvation using the proposed modified starvation degree SD' .

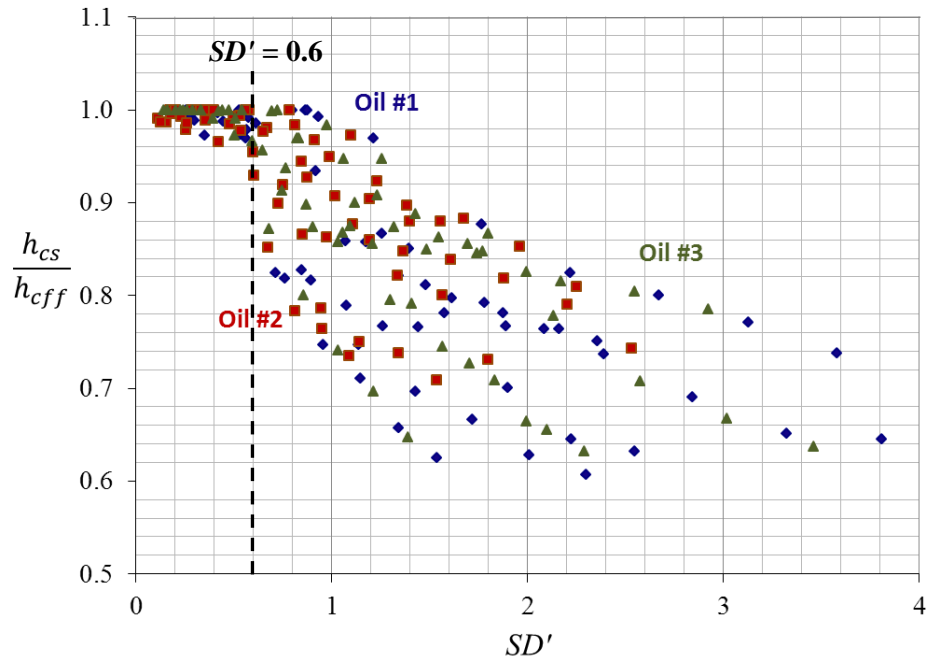


Figure 6.41 h_{cs}/h_{eff} as function of SD' for all oils and conditions

According to the present results, starvation is well established when $SD' = 1$, and is initiated at $SD' = 0.6$. To avoid starvation on mixed lubrication it is recommended to operate at conditions generating $SD' < 0.6$.

As described in Chapter 2, the starvation degree is defined according to the balancing of the cycle time t_c , the time for one over-rolling that represents the time available for replenishment, and the replenishment time t_r , the time required to replenish the contact. In the condition of no starvation (fully flooded condition) in the system, the ratio between t_c and t_r is maintained at or less than 1. Values above 1 represent the occurrence of starvation. If this concept holds for the present study in mixed lubrication, the original starvation degree SD would underestimate the possibility of the occurrence of starvation (Fig. 6.40). With the modified starvation degree SD' , although the onset of starvation begins at $SD' = 0.6$, which allows a conservative criterion for predicting lubrication failure due to starvation.

7. CONCLUSIONS AND RECOMMENDATIONS

7.1 Conclusions

This research focussed on the investigation of starvation in mixed EHL regime. While the phenomenon of starvation has been amply explored, not much attention has been paid to its effects on the well-established laws governing the fully flooded state for the case of mixed lubrication. In addition, much of the work done on starvation focussed on the determination of the film thickness and thus effort was concentrated on developing measurement methods. Optical techniques have been successfully used to assess the film thickness but on simplified experimental contact models not representative of actual bearings. In addition only circular contacts and light operating conditions of speed and loading have been experimented. A unique methodology that circumvents the mentioned restrictions was developed in order to assess the behavior of the starved lubricating film. It is based on the measurement of the total friction force generated at the contact; using a tribometer. The case of contact between a ball and rotating cylinder was investigated; which simulates the critical condition of sliding friction occurring in a seized ball bearing. The effects of loading, relative speed, surface roughness and amount of lubricant supplied on the behavior of the active film were evaluated with the aim of assessing their role on the severity of starvation. Three oils representing a variety of rheological and physical properties were evaluated. We were successful in simulating conditions that produce starvation and estimating the film thickness in the active zone with good confidence, based on the combination of experimental and computational methods. The results of this complete and meticulous study are used to draw the following main conclusions:

The proposed method, based on experimental friction force measurements can be universally used by manufacturers to determine the conditions leading to the onset of starvation as well as the progression of its severity.

Approximating the friction component at the asperities in contact by Coulomb law produces erroneous modelling of the actual behavior. The friction-load ratio concept is suggested for a more accurate representation.

The friction resistance, in mixed lubrication, is heavily dependent on the loading, speed and roughness in a complex way which cannot be approximated by a linear relationship with the loading.

This research suggests that the model for starvation in thick film lubrication is not suitable for bearings operating in mixed lubrication regime.

The well-established film thickness model developed by Hamrock and Dowson for fully flooded EHL (elastic-viscous) regime was combined with the load sharing concept to generate simple models, based on regression method, for predicting the central film thickness in mixed starved EHL as function of the operating conditions as well as roughness of the contacting surfaces.

The roughness of the contacting surface delays the occurrence of starvation to a higher speed and decreases its fully developed severity independently of the supplied amount of lubricant. Increasing the supply of lubricant for low surface roughness is beneficial.

A general criterion signaling the onset of starvation is proposed:

$$\frac{h_{in}}{h_{cff}} \equiv \left(\gamma \sqrt{\left(\frac{h_{cff}}{h_{cs}} \right)^{\gamma} - 1} \right)^{-1} \leq 2.64$$

The behavior of the starved lubricating film is very dependent on the properties of the inlet. The proposed model of the assessment of starvation expressed by (h_{in}/h_{cff}) as function of the operating conditions represented by $\sqrt{M/L}$ constitutes a powerful technique permitting the development of tangible conclusions on the mechanisms governing this important phenomenon. This model can be used by bearing designers.

The performance of the inlet in the development of ideal mixed EHL regime is intimately linked to its location with respect to the Hertzian area perimeter. Our results have permitted to develop an empirical relationship for the prediction, with reasonable confidence, of the inlet distance as function of the operating conditions which would generate fully flooded mixed EHL:

$$\frac{S_{ff}}{b} = 3.8552 (M/L)^{-0.24}$$

Contrary to the fully flooded regime where the film thickness increases with speed, in starved conditions the development of a meniscus alters the behaviour of the film at the contact zone. Starvation could therefore be defined as a phenomenon that produces particular physical properties of the inlet film making it unable to generate EHL as predicted by Reynolds equation. It was shown that deficiency in lubricant supply can be one of the symptoms.

The only model available to predict the onset of starvation taking into account the amount of lubricant supplied to the inlet was found insufficient when tested

against the present results. A modified starvation degree empirical model is proposed:

$$SD' = \frac{\eta u N}{\gamma h_{oil\infty} \sigma_s R'_q E'}$$

7.2 Recommendations

The present study has investigated several aspects of starvation in mixed lubrication. Suggestions for future work in order to enhance further the understanding and develop design tools which could be used to predict the severity of starvation are presented below.

- The influence of the geometric characteristics of the bearing elements on starvation needs to be investigated.
- The influence of the surface roughness on Hertzian contact area needs consideration. Moreover, the investigation of the influence of surface roughness on starvation can be extended to examine the configuration of surface topography, such as two-dimensional roughness and surface texture directions.
- Future studies need to examine the thermal effects on starvation.
- Future investigation in this field should consider the development of automated systems for oil supply in order to enhance the accuracy and repeatability of this experimental variable.
- This starvation study should be extended to lubrication with grease.
- The proposed starvation degree parameter needs to be generalized.
- The wear should be assessed.
- 3D roughness profiles should be considered.

REFERENCES

- Akchurin, A., Bosman, R., Lugt, P. M., van Drogen, M., 2015. "On a model for the prediction of the friction coefficient in mixed lubrication based on load-shearing concept with measured surface roughness, " Tribology Letters, vol. 59, No.19, pp. 1-11.
- Ali, F. and Hartl, M., 2012. "Friction of non-conformal contacts under starved EHD lubrication," MM Science Journal, Prague, Czech Republic, pp. 374-377.
- ANSI, 1978. "Surface Texture, "American National Standards Institute, ANSI B46.1-1978.
- Archard, J.F., 1968. "Non-dimensional parameters in isothermal theories of elastohydrodynamic lubrication," Journal of Mechanical Engineering Science, Vol. 10, No.2, pp. 165-167.
- Arnell, R.D., Davies, P.B., Halling, J. and Whomes, T.L., 1991. Tribology – Principles and Design Applications, Springer-Verlag, New York, U.S.A..
- AST Bearings LLC, 2010. Technical Information: Lubrication, Document No. ENB-04-0555 REV. A DCR14-109 004.
- ASTM, 2008. Designation: D5001-08, "Standard Test Method for Measurement of Lubricity of Aviation Turbine Fuels by the Ball-on-Cylinder Lubricity Evaluator (BOCLE)," ASTM International, U.S.A..
- ASTM, 2009. Designation: D341-09, "Standard Practice for Viscosity-Temperature Charts for Liquid Petroleum Products," ASTM International, U.S.A..
- ASTM, 2010. Designation: D6078-04, "Standard Test Method for Evaluating Lubricity of Diesel Fuels by the Scuffing Load Ball-on-Cylinder Lubricity Evaluator (SLBOCLE)," ASTM International, U.S.A..
- Åström, H., Ostenson, J.O. and Höglund, E., 1992. "Lubricating grease replenishment in an elastohydrodynamic point contact," Journal of Tribology, Vol. 115, Issue 3, pp. 501-506.
- Bair, S., 1996. "Normal stress difference in liquid lubricants sheared under high pressure," Rheologica Acta, Vol.35, pp. 13-23.

Bair, S., 2002. "The high pressure rheology of some simple model hydrocarbons," Proceedings of the Institution of Mechanical Engineers, Part J: Journal of Engineering Tribology, Vol.216, pp. 139-149.

Bair, S. and Winer, W. O., 1979, "A Rheological Model for Elastohydrodynamic Contacts Based in Primary Laboratory Data, " Transactions of ASME, Journal of Tribology, Vol. 101, pp. 258-265.

Baly, H., Poll, G., Cann, P.M. and Lubrecht, A.A., 2006. "Correlation between model test devices and full bearing tests under grease lubricated conditions," IUTAM Symposium on Elastohydrodynamics and Micro-elastohydrodynamics, Vol.40, Springer, The Netherlands, pp. 229-240.

Barus, C., 1893. "Isothermals, isopiestic and isometrics relative to viscosity," American Journal of Science, Vol. 45, pp. 87-96.

Berthe, L., Adams-Chaves, A. and Lubrecht, A.A., 2014. "Friction measurement indicating the transition between fully flooded and starved regimes in EHL lubrication," Proceedings of the Institution of Mechanical Engineers, Part J: Journal of Engineering tribology, pp. 1-7.

Bhushan, B., 2002. Introduction to Tribology, John Wiley & Sons, Inc., New York, U.S.A..

Blahey, A.G, 1985. The Elastohydrodynamic Lubrication of Elliptical Contacts with Thermal Effects, Ph.D. Thesis, Department of Mechanical Engineering, University of Waterloo, Waterloo, Ontario, Canada.

Blok, H., 1952. "Discussion of paper by E. McEwen, the effect of variation of viscosity with pressure on the load-carrying capacity of the oil film between gear teeth," Journal of the Institute of Petroleum, Vol.38, No.344, pp. 673-683.

Brewe, D.E. and Hamrock, B.J., 1977. "Simplified solution for elliptical contact deformation between two elastic solids," Journal of Lubrication Technology, Vol. 99, No. 4, pp. 485-487.

Brewe, D.E., Hamrock, B.J. and Taylor, C.M., 1979. "Effect of geometry on hydrodynamic film thickness," Journal of Lubrication Technology, Vol.101, pp. 231-239.

Buyanovskii, I.A., 2010. "Boundary lubrication by an adsorption layer," Journal of friction and wear, Vol.31, No.1, pp. 33-47.

- Cann, P.M.E., Chevalier, F., Lubrecht, A.A., 1996. "Track depletion and replenishment in a grease lubricated point contact: a quantitative analysis," Proceedings of the 23rd Leeds–Lyon Symposium on Tribology. p. 405–414.
- Cann, P.M.E., Damiens, B. and Lubrecht, A.A., 2004. "The transition between fully flooded and starved regimes in EHL," Tribology International, Vol.37, pp. 859-864.
- Cann, P.M. and Lubrecht, A.A., 1999. "Analysis of grease lubrication in rolling element bearings," Lubrication Science, Vol.11, pp. 227-245.
- Cann, P.M. and Lubrecht, A.A., 2005. "Bearing performance limits with grease lubrication," Proceedings of WTC2005, World Tribology Congress III, Washington D.C., U.S.A. pp. 35-36.
- Cann, P.M. and Lubrecht, A.A., 2007. "Bearing performance limits with grease lubrication: the interaction of bearing design, operating conditions and grease properties," Journal of Physics, Part D: Applied Physics, Vol.40, pp. 5446-5451.
- Cann, P.M. and Spikes, H.A., 1992. "Film thickness measurements of lubricating grease under normally starved conditions," NLGI Spokesman, Vol. 56, No. 2, pp. 21-26.
- Cann, P.M., Williamson, B.P., Coy, R.C. and Spikes, H.A., 1992. "The behaviour of greases in elastohydrodynamic contacts," Journal of Physics D: Applied Physics, Vol.25, pp. A124-A132.
- Castle, P. and Dowson, D., 1972. "A theoretical analysis of the starved elastohydrodynamic lubrication problem for cylinders in line contact," Proceedings of the Institution of Mechanical Engineers, Elastohydrodynamic Lubrication, pp. 131-137.
- Chevalier, F., Lubrecht, A.A., Cann, P.M.E., Colin, F. and Dalmaz, G., 1998. "Film thickness in starved EHL point contacts," ASME Transactions, Journal of Tribology, pp. 126-133.
- Chiu, Y.P., 1974. "An analysis and prediction of lubricant film starvation in rolling contact systems," ASLE Transactions, Vol.17, No.1, pp. 22-35.
- Crook, A.W., 1961. "The lubrication of rollers II. Film thickness with relation to viscosity and speed," Philosophical Transactions of the Royal Society of London. Series A, Mathematical and Physical Sciences, Vol. 254, pp. 223-236.

- Damiens, B., 2003, "Modélisation de la lubrification sous-alimentée dans les contacts élastohydrodynamiques elliptiques", PhD Thesis, I.N.S.A. de Lyon, France.
- Damiens, B., Cann, P.M.E. and Lubrecht, A.A., 2001. "Lubrication regimes in rolling element bearings," Proceedings of the 27th Leeds-Lyon Symposium on Tribology, pp. 295-301.
- Damiens, B., Venner, C.H., Cann, P.M.E. and Lubrecht, A.A., 2004. "Starved lubrication of elliptical EHD contacts," Journal of Tribology, Vol.126, pp. 105-111.
- Dowson, D. and Higginson, G.R., 1966. *Elastohydrodynamic Lubrication: The Fundamentals of Roller and Gear Lubrication*, Pergamon Press, Oxford, United Kingdom.
- Elrod, Jr.H.G., 1981. "A cavitation algorithm," Vol.103, No.2, pp. 350-354.
- Elsharkawy and Hamrock, 1996. "Subsurface Stresses in Micro-EHL Line Contacts," ASME Journal of Tribology, Vol. 113, pp. 645-657.
- Engineering Edge, 2010. "Elastohydrodynamic (EHD) Lubrication," Lubrication Knowledge Menu, retrieved from http://www.engineersedge.com/lubrication/elastohydrodynamic_lubrication.htm, visited on 14 March 2010.
- Errichello, R., 2004. "Selecting oils with high pressure-viscosity coefficient," Machinery Lubrication, Vol. 4, No. 2, 2004, pp. 48-52.
- Errichello, R., 2015. "Elastohydrodynamic Lubrication (EHL): A Review," Gear Technology, Issue: July 2015, retrieved from [http://www.geartechnology.com/articles/0715/Elastohydrodynamic_Lubrication_\(EHL\):_A_Review](http://www.geartechnology.com/articles/0715/Elastohydrodynamic_Lubrication_(EHL):_A_Review), visited on 8 June 2016.
- Evans, H. P., and Snidle, R. W., 1981. "Inverse solution of Reynolds equation of lubrication under point contact elastohydrodynamic conditions," Journal of Tribology, Vol.103, No.4, pp 539-546.
- Evans, H. P., and Snidle, R. W., 1982. "The elastohydrodynamic lubrication of point contacts at heavy loads," Proceedings of the Royal Society A, Vol.382, pp 183-199.
- Faraon, I.C. and Schipper, D.J., 2006. "Stribeck curve for starved concentrated contacts," IUTAM Symposium on Elastohydrodynamics and Micro-elastohydrodynamics, pp. 311-320.

- Faraon, I.C. and Schipper, D.J., 2007. "Stribeck curve for starved line contacts," *Journal of Tribology*, Vol.129, pp. 181-187.
- Fein, R.S., 1997. "Chapter 59. High Pressure Viscosity and EHL Pressure-Viscosity Coefficients," *Tribology Data Handbook: An Excellent Friction, Lubrication, and Wear Resource*, CRC Press.
- Gasni, D., 2013. "Transition of regime lubrication from fully flooded lubrication to starved lubrication," *TeknikA*, Vol.20, No.2 (November), pp. 1-10.
- Gecim, B. and Winer, W.O., 1981. "Lubricant limiting shear stress effect on EHD film thickness," *Transactions ASME, Journal of Lubrication Technology*, Vol. 102, pp. 213-221.
- Gelinck, E.R.M., 1999. *Mixed Lubrication of Line Contacts*, Ph.D. Thesis, Faculty of Engineering Technology, University of Twente, Enschede, The Netherlands.
- Gelinck, E.R.M. and Schipper, D.J., 2000. "Calculation of Stribeck curves for line contacts," *Wear*, Vol.21, No.1, pp. 49-101
- Gershuni, L., Larson, M.G. and Lugt, P.M., 2008. "Lubricant Replenishment in Rolling Bearing Contacts," *Tribology Transactions*, Vol.51, No.5, pp. 643-651.
- Ghosh, P., 2014. *Surface Tension, Module 2: Lecture 1*, NPTEL – Chemical Engineering – Interfacial Engineering, Department of Chemical Engineering, Joint Initiative of IITs and IISc.
- Ghosh, P., Pantar, A.V., Rao, U.S. and Sarma, A.S., 1998. "Shear stability of polymers used as viscosity modifiers in lubricating oils," *Indian Journal of Chemical Technology*, Vol.5, No.5, pp. 309-314.
- Gohar, R., 2001. *Elastohydrodynamics*, 2nd ed., Imperial Collage Pres, London, United Kingdom.
- Goodyer, C.E., 2001. *Adaptive Numerical Methods for Elastohydrodynamic Lubrication*, Ph.D. Thesis, University of Leeds, Leeds, England, United Kingdom, 2001.
- Greenwood, J.A. and Tripp, J.H., 1970-71. "The contact of two nominally flat rough surfaces," *Proceedings of Institution of Mechanical Engineers*, Vol.185, pp. 625-633.

Greenwood, J.A. and Williamson, J.B.P., 1966. "Contact of nominally flat surfaces," Proceedings of the Royal Society, series A, Vol.295, No. 1442, pp. 300-319.

Grubin, A.N., and Vinogradova, I.E., 1949. Fundamentals of the hydrodynamic theory of lubrication of heavily loaded cylindrical surfaces, Investigations of the contact of machine components, Central Scientific Research Institute for Technology and Mechanical Engineering, Book 30, Moscow. (DSIR Translation 337, Kh.F. Ketova, Ed.), pp. 115-166.

Guangteng, G., Cann, P.M. and Spikes, H.A., 1992. "A study of parched lubrication," Wear, Vol.153, pp. 91-105.

Hamrock, B.J. and Anderson, W.J., 1973. "Analysis of an arched outer-race ball bearing considering centrifugal forces," Journal of Lubrication Technology, Vol. 95, No. 3, pp. 265-276.

Hamrock, B.J. and Brewe, D., 1983. "Simplified solution for stresses and deformations," Journal of Lubrication Technology, Vol. 105, pp.171-177.

Hamrock, B.J. and Dowson, D., 1976a. "Isothermal elastohydrodynamic lubrication of point contacts, part I – theoretical formulation," Journal of Lubrication Technology, Vol.98, No.2, pp. 223-229.

Hamrock, B.J. and Dowson, D., 1976b. "Isothermal elastohydrodynamic lubrication of point contacts, part II – ellipticity parameter results," Journal of Lubrication Technology, Vol.98, No.3, pp. 375-378.

Hamrock, B.J. and Dowson, D., 1977a. "Isothermal elastohydrodynamic lubrication of point contact, part III – fully flooded results," Journal of Tribology, Vol.99, No.2, pp. 264-276.

Hamrock, B.J. and Dowson, D., 1977b. "Isothermal elastohydrodynamic lubrication of point contact, part IV – starvation results," Journal of Tribology, Vol.99, No.1, pp. 15-23.

Hamrock, B.J. and Dowson, D., 1978. "Elastohydrodynamic lubrication of elliptical contacts for materials of low elastic modulus, part I – flooded conjunction," Journal of Lubrication Technology, Vol.100, No.2, pp. 236-345.

Hamrock B.J. and Dowson, D., 1979. "Elastohydrodynamic lubrication of elliptical contacts for materials of low elastic modulus, part II – starved conjunction," Journal of Lubrication Technology, Vol.101, No.1, pp. 92-98.

Hamrock, B.J. and Dowson, D., 1981. Ball Bearing Lubrication – The Elastohydrodynamics of Elliptical Contacts, John Wiley & Sons, Inc., U.S.A..

Hamrock, B.J., Schmid, S.R. and Jacobson, B.O., 2004. Fundamentals of Fluid Film Lubrication, 2nd ed., Marcel Dekker, Inc., U.S.A..

Harris, T.A., 1966. Rolling Bearing Analysis, Wiley & Son, Inc., New York, U.S.A..

Harrison, W.J., 1913. "The hydrodynamical theory of lubrication with special reference to air as a lubricant," Transactions of the Cambridge philosophical society, pp. 6-54.

Hertz, H., 1896. Über die berührung fester elastischer Körper (On the contact of rigid elastic solids). In: Miscellaneous Papers. Jones and Schott, Editors, J. reine und angewandte Mathematik 92, Macmillan, London, p. 156 English translation: Hertz, H.

Hili, J., Olver, A., Edwards, S. and Jacobs, L., 2010. "Experimental investigation of elastohydrodynamic (EHD) film thickness behavior at high speeds," Tribology Transactions, Vol. 53, pp. 658-666.

Hironaka, S., 1984. "Boundary lubrication and lubricants," Three Bond Technical News, Issue 1 July.

Höglund, E., 1989. "The relationship between lubricant shear strength and chemical composition of the base oil," Wear, Vol. 130, pp.213-224.

Höglund, E. and Jacobson, B., 1986. "Experimental investigation of the shear strength of lubricants subjected to high pressure and temperature," Transactions of ASME, Journal of Tribology, Vol. 108, pp.571-578.

Houpert, L., 1985. "New results of traction force calculations in elastohydrodynamic contacts," Transactions ASME, Journal of Lubrication Technology, Vol. 107, pp. 241-248.

Iivonen, H. and Hamrock, B. J., 1991, "A new non-Newtonian fluid model for elastohydrodynamic lubrication of rectangular contacts," Wear, Vol. 143, pp. 297-305.

InterAv Inc., 1989. User's Manual, Friction Force measurement Capability for BOCLE Machine, InterAv Inc., San Antonio, Texas, U.S.A..

Jacobson, B.O., 1991. *Rheology and Elastohydrodynamic Lubrication*, Elsevier Science Publishing Company, Inc., New York, U.S.A..

Jacobson, B., 1985. "A high pressure-short time shear strength analyser for lubricants," *Transaction of ASME, Journal of Tribology*, Vol. 107, pp. 221-223.

Jacob, B., Pabilier, F., Cann, P.M.E. and Lubrecht, A.A., 1998. "An analysis of track replenishment mechanisms in the starved regime," *Proceedings of the 25th Leeds-Lyon Symposium on Tribology*, pp. 483-492.

Jedynak, R. and Gilewicz, J., 2013. "Approximation of the integrals of the Gaussian distribution of asperity heights in the Green-Tripp contact model of two rough surfaces revisited," *Journal of Applied Mathematics*, Vol.2013, Aritcal ID 459280.

Jeng, Y.R., Hamrock, B.J. and Brewe, D.E., 1987. "Piezoviscous effects in nonconformal contacts lubricated hydrodynamically," *ASLE Transactions*, Vol.30, No.4, pp. 452-464.

Johnson, K.L., 1970. "Regimes of elastohydrodynamic lubrication," *Journal of Mechanical Engineering Science*, Vol.12, No.1, pp. 9-16.

Johnson, K.L., 1985. *Contact Mechanics*, Cambridge University Press, United Kingdom.

Johnson, K.L., Greenwood, J.A. and Poon, S.Y., 1972. "A simple theory of asperity contact in elastohydrodynamic lubrication," *Wear*, Vol.19, pp. 91-108.

Jones, A.B., 1946. *New Development Engineering Data: Analysis of Stresses and Deflections*. Vol. I & II, General Motors, Inc., Detroit, Michigan, U.S.A..

Kapitza, P.L., 1955. "Hydrodynamic theory of lubrication during rolling," *Zh. Tekh. Fiz.*, Vol.25, pp. 747-762.

Khonsari, M.M. and Booser, E.R., 2008. *Applied Tribology – Bearing Design and Lubrication*, 2nd ed., John Wily & Sons, Ltd., West Sussex, England, United Kingdom.

Kingsbury, E., 1973. "Cross flow in a starved EHD contact," *ASLE Transactions*, Vol.16, pp. 276-280.

Kingsbury, E., 1985. "Parched elastohydrodynamic lubrication," *Journal of Tribology*, Vol.107, pp. 229-233.

- Kong, S., Sharif, K., Evans, H.P. and Snidle, R.W., 2001. "Elastohydrodynamics of a worm gear contact," Vol.23, 268-275.
- Koyo, 2009. Ball & Roller Bearings: Failures, causes and Countermeasures, Document no. B3001E, Koyo Seiko Ltd., Japan.
- Kreider, J.F., 1985. Principles of Fluid Mechanics, Allyn and Bacon, Massachusetts, U.S.A..
- Kumar, P. and Khonsari, M.M., 2008. "Combined effects of shear thinning and viscous heating on EHL characteristics of rolling/sliding line contacts," Journal of Tribology, Vol.130, No.4, pp. 041505-1 to 041505-13.
- Lee, R.T. and Hamrock, B. J., 1990, "A Circular Non-Newtonian Model: Part 1- Used in Elasto-hydrodynamic Lubrication, " Transaction of ASME, Journal of Tribology, Vol. 112, pp. 386-496.
- Leeuwen, H. van, 2009. "The determination of the pressure-viscosity coefficient of a lubricant through an accurate film thickness," Proceedings of the Institution of Mechanical Engineers, Part J: Journal of Engineering Tribology, Vol. 223, pp. 1143-1163.
- Li, D., 2013. Continuous Stribeck curve measurement using pin-on-disk tribometer, Nanovea, U.S.A..
- Liu, Q., 2002. Friction in Mixed and Elastohydrodynamic Lubricated Contacts Including Thermal Effects, Ph.D. Thesis, Faculty of Engineering Technology, University of Twente, Enschede, The Netherlands.
- Liu, Q., Ten Napel, W., Tripp, J.H., Lugt, P.T. and Meeuwenoord, R., 2009. "Friction in highly loaded mixed lubricated point contacts," tribology Transactions, Vol. 52, pp. 360-369.
- Lu, X., Khonsari, M.M. and Gelinck, E.R.M., 2006. "The Stribeck curve: experimental results and theoretical prediction," Journal of Tribology, Vol.28, pp. 789-794.
- Lu, X. and Khonasri, M.M., 2007. "An experimental investigation of grease-lubricated journal bearings", Transaction of the ASME, Vol.129, pp. 84-90.

Lubrecht, A.A., 1987. The Numerical Solution of Lubricated Line and Point Contact Problem Using Multigrid Techniques, Ph.D. Thesis, University of Twente, The Netherlands.

Masjedi, M. and Khonsari, M.M., 2015. "A study on the effect of starvation in mixed elastohydrodynamic lubrication," *Tribology International*, Vol. 85, pp. 26-36.

Mathias, S., 1996. "Ball bearing – how products are made," Gale Research Inc., retrieved from http://www.encyclopedia.com/topic/Ball_Bearing.aspx#1-1G2:2896500018-full, visited on 6 April 2011.

Moes, H., 1992. "Optimum similarity analysis with applications to elastohydrodynamic lubrication," *Wear*, Vol.159, pp. 57-66.

Moes, H., 2000. *Lubrication and Beyond*, University of Twente, Enschede, The Netherlands.

Morrison, F.A., 2013. *Fluid Mechanics*, Cambridge University Press, New York, U.S.A..

Nijenbanning, G., Venner, C.H., Moes, H., 1994. "Film thickness in elastohydrodynamically lubricated elliptic contacts," *Wear*, Vol.176, pp. 217-229.

Nogi, T., 2015. "An analysis of starved EHL point contacts with reflow," *Tribology Online*, Japanese Society Tribologists, Vol.10, No.1, pp. 64-75.

Olaru, D.N. and Gafitanu, M.D., 1993. "Starvation in ball bearings," *Wear*, Vol.170, pp. 219-234.

Opoku, E., 2014. Experiment on Surface Tension, CHEM 270: Practical Chemistry IV, Department of Chemistry, Kwame Nkruman University of Science and Technology, Ghana.

Padir, N. and Cheng, H.S., 1978. "An average flow model for determining effects of three dimensional roughness on partial hydrodynamic lubrication," *Journal of Lubrication Technology*, ASME, Vol., 100, pp. 12-17.

Padir, N. and Cheng, H.S., 1979. "Application of average flow model to lubrication between rough sliding surfaces," *Journal of Lubrication Technology*, ASME, Vol., 101, pp. 220-230.

- Panayi, A.P. and Schock, H.J., 2008. "Approximation of the integral of the asperity height distribution for the Greenwood-Tripp asperity contact model," Proceedings of Institution of Mechanical Engineers, Part J: Journal of Engineering Tribology, Vol.222, pp. 165-169.
- Pemberton, J. and Cameron, A., 1976. "A mechanism of fluid replenishment in elastohydrodynamic contacts," *Wear*, Vol.37, No.1, pp. 185-190.
- Petrusevich, A.I., 1951. Fundamental conclusions from the contact-hydrodynamic theory of lubrication. *Izv. Akad. Nauk. SSSR (OTN)*, Vol.2, pp. 209-223.
- Pepper, S.V., 2008. "Ultra starvation studied in the spiral orbit tribometer," *Tribology Transactions*, Vol.51, pp. 723-729.
- Popov, V.L., 2010. *Contact Mechanics and Friction*, Springer-Verlag Berlin Heidelberg.
- Radu, C., 2010. "The most common causes of bearing failure and the importance of bearing lubrication," *RKB Technical Review*, Issue February 2010, pp. 1-7.
- Ramezani, M. and Ripin, Z.M., 2009. "Effect of friction models on stress distribution of sheet materials during V-bending process," *International Science Index*, Vol.3, No.8, pp. 654-659.
- Roelands, C.J.A., 1966. *Correlational Aspects of the Viscosity-Temperature-Pressure Relationship of Lubricating Oils*, Ph.D. Thesis, University of Delft, The Netherlands.
- Schmitt, L., 2003. "Investigations in the rheology of stirred yoghurt," 3rd International Symposium on Food Rheology and Structure, pp. 575-576.
- Snyder, D.R., 2005. "Proper lubrication keeps bearings rolling along," *Machinery Lubrication*, Issue 5/2005, <http://www.machinerylubrication.com>.
- So, H., Kao, S.J. and Chen, C.R., 1987. "The influence of surface roughness on the starved lubrication of ball bearings," *Journal of the Chinese Institute of Engineers*, Taiwan, R.O.C., Vol.10, No.1, pp. 33-43.
- Sojoudi, H. and Khonsari, M.M., 2010. "On the behavior of friction in lubricated point contact with provision for surface roughness," *Journal of Tribology*, Vol.132, pp. 012102-1 to 012102-8.

Stachowiak, G.W. and Batchelor, A.W., 2005. *Engineering Tribology*, 3rd ed., Elsevier Butterworth-Heinemann, Burlington, Massachusetts, U.S.A..

Svoboda, P., Košťál, D., Popelka, M. and Křupka, I., 2013. "The Experimental Study of Transition Between Fully Flooded and Starved Regime in EHL Contact," *Engineering Mechanics*, Vol. 20, No. 1, pp. 13–25.

Svoboda, P., Kostal, D., Kunak, J. and Krupka, I., 2014. "Study of grease behaviour in a starved elastohydrodynamically lubricated contact," *Modern Machinery Science Journal*, June 2014 Issue, pp. 464-469.

Tanveer, S., Sharma, U.C. and Prasad, R., 2006. "Rheology of multigrade engine oils," *Indian Journal of Chemical Technology*, Vol.13, No.2, pp. 180-184.

The Engineering ToolBox, 2014. "ISO Grade Oil Properties," retrieved from http://www.engineeringtoolbox.com/iso-grade-oil-d_1207.html, visited 5 September 2014.

Timosheko, S. and Goodier, J.N., 1951. *Theory of Elasticity*, 2nd ed., McGraw-Hill, New York, U.S.A..

Venner, C.H., 1991. *Multilevel Solution of the EHL Line and Point Contact Problems*, Ph.D. Thesis, University of Twente, Enschede, The Netherlands.

Venner, C.H. and Lubrecht, A.A., 2000. *Multilevel methods in lubrication*, Tribology Series, Vol. 37.

Venner, C. H., Popovici, G., Lugt, P. M. and Organisciak, M., 2008. "Film thickness modulations in starved elastohydrodynamically lubricated contacts induced by time-varying lubricant supply," *Journal of Tribology*, Vol. 130, No.4, pp. 041501-1 to 041501-10.

Wang, W.Z., Wang, S., Shi, F., Wang, Y.C., Chen, H.B., Wang, H. and Hu, Y.Z., 2007. "Simulations and measurements of sliding friction between rough surfaces in point contacts: from EHL to boundary lubrication," *Journal of Tribology*, Vol.129, pp. 495-501.

WaterCAMPWS, 2014. "Surface Tension – Teacher’s Guide," STEM Educational Curriculum Supplement, The WaterCAMPWS Center for Advanced materials for Purification of Water with Systems, University of Illinois.

Weber, C. and Saalfeld, K., 1954. "Schmierfilm bei Walzen mit Verformung," Zeitschrift für Angewandte Mathematik und Mechanik (Journal of Applied Mathematics and Mechanics), Bd. 34, Nr. 1-2, S.54-64.

Wedeven, L.D., Evans, D. and Cameron, A., 1971. "Optical analysis of ball bearing starvation," Journal of Lubrication Technology, Vol.93, Issue 3, pp. 349-362.

Wei, R., Chen, J-H, Huizinga, J.D., 2014. "On the relationship between viscosity and surface tension," Journal of Emerging Investigators, September 2014, retrieved from <http://www.emerginginvestigators.org/2014/09/on-the-relationship-between-viscosity-and-surface-tension/>, visited 20 September 2015.

Whitehouse, D.J. and Archard, J.F., 1970. "The properties of random surfaces of significance in their contact," Proceedings of the Royal Society of London. Series A, Mathematical and Physical Sciences, Vol. 316, No. 1524, pp. 97-121.

Williams, J.A., 1994. Engineering Tribology, Oxford University Press Inc.

Wiśniewska-Weinert, H., 2011. "Experimental study and modelling of mixed particulate lubrication with MoS₂ powder solid lubricant," Journal of Achievements in Materials and Manufacturing Engineering, Vol.49, Issue 2, pp. 467-476.

Wolveridge, P.E., Baglin, K.P. and Archard, J.F., 1971. "The starved lubrication of cylinders in line contact," Proceedings of the Institution of Mechanical Engineers, Vol.185, pp. 1159-1169.

Zhao Y.W., Maietta D.M., Chang L., 2000. "An asperity microcontact model incorporating the transition from elastic deformation to fully plastic flow," Journal of Tribology, Vol.122, pp. 86-93.

APPENDIX A
DEVRIVATION OF FILM THICKNESS EQUATION
FOR MIXED LUBRICATION

In the mixed lubrication, in which contact between asperities on the surfaces take place. Johnson's load-sharing approach is applied for the mixed and boundary regimes [Johnson *et al.* 1972]. In this approach, the applied load is supported by the hydrodynamic lifting force of the lubricant and asperities interacting force at the contact. In order to apply this concept to the film thickness equation, the relevant scaling factors for the hydrodynamic part and asperity part were introduced to the film thickness equations [Nijebanning *et al.*, 1994] and, hence, the equations were modified for this case. In this section, the modification of the Nijebanning *et al* central film thickness equations, in associate with the load sharing factors, is described.

Recall Nijebanning *et al.* [1994] dimensionless central film thickness equation for thick film (fully separated) condition:

$$H_c = \left\{ \left[H_{RI}^{3/2} + (H_{EI}^{-4} + H_{00}^{-4})^{-3/8} \right]^{2s/3} + (H_{RV}^{-8} + H_{EV}^{-8})^{-s/8} \right\}^{1/s} \quad (3.24)$$

$$\text{where } H_{c,RI} = 145 \left(1 + 0.796 D^{14/15} \right)^{-15/7} D^{-1} M^{-2} \quad (3.18)$$

$$H_{c,EI} = 3.18 \left(1 + 0.006 \ln D + 0.63 D^{4/7} \right)^{-14/25} D^{-1/15} M^{-2/15} \quad (3.19)$$

$$H_{c,RV} = 1.29 \left(1 + 0.691 D \right)^{-2/3} L^{2/3} \quad (3.20)$$

$$H_{c,EV} = 1.48 \left(1 + 0.006 \ln D + 0.63 D^{4/7} \right)^{-7/20} D^{-1/24} M^{-1/12} L^{3/4} \quad (3.21)$$

$$M = \frac{N}{E' r_x^2} \left(\frac{\eta u_s}{E' r_x} \right)^{-3/4} \quad (3.22)$$

$$L = \xi E' \left(\frac{\eta u_s}{E' r_x} \right)^{1/4} \quad (3.23)$$

$$\hat{s} = 1.5 \left[1 + e^{-1.2(H_{c,EI}/H_{c,RI})} \right] \quad (3.25)$$

$$H_{00} = 1.8 D^{-1} . \quad (3.26)$$

The dimensionless central film thickness equations for mixed condition are:

$$H_{c,mix} = \left\{ \left[H_{c,RI,mix}^{3/2} + \left(H_{c,El,mix}^{-4} + H_{00}^{-4} \right)^{-3/8} \right]^{2\hat{s}_{mix}/3} + \left(H_{c,RV,mix}^{-8} + H_{c,EV,mix}^{-8} \right)^{-\hat{s}_{mix}/8} \right\}^{1/\hat{s}_{mix}} \quad (A.1)$$

$$\hat{s}_{mix} = 1.5 \left[1 + e^{-1.2(H_{c,El,mix}/H_{c,RI,mix})} \right] \quad (A.2)$$

The subscript "mix" designates the parameters those are in the condition of mixed lubrication, in which the applied load is acting on both the asperities in contact and the lubricant at the contact interface. It is worth noting that the parameter H_{00} remains unchanged since it is only a function of the geometry (D).

In the mixed lubrication, the applied load is shared by the asperities and the lubricant at the contact; the deformation of surfaces is, however, ruled by the total load. In this condition, the fraction $1/\gamma_l$ of the load is carried by the lubricant film. Johnson *et al.* [1972] further assume that the pressure at the contact zone is scaled everywhere by the same factor. This scaled pressure can only produce a contact zone of the same size as the original, according to the classical Hertzian contact theory, if the equivalent elastic modulus of the bulk material is reduced by the same factor. Substituting the reduced load (N/γ_l) and equivalent elastic modulus (E'/γ_l) into the established elastohydrodynamic film thickness formula is thus a convenient device to allow the prediction of the film thickness applicable to the load-sharing mixed lubrication situation [Liu *et al.*, 2009]. Replacing the total applied load N with N/γ_l and the equivalent elastic modulus E' with E'/γ_l in Eq. (2.8), the Moes [1992] dimensionless load parameter for mixed lubrication is:

$$M_{mix} = \frac{N/\gamma_l}{(E'/\gamma_l)r_x^2} \left(\frac{\eta u_s}{(E'/\gamma_l)r_x} \right)^{-3/4} = \frac{N}{E' r_x^2} \left(\frac{\eta u_s}{E' r_x} \right)^{-3/4} \left(\gamma_l^{-3/4} \right) = \gamma_l^{-3/4} M \quad (A.3)$$

Similarly, the same substitutions were performed to Eq. (2.9), the Moes [1992] dimensionless material parameter for mixed lubrication is:

$$L_{mix} = \xi (E'/\gamma_l) \left(\frac{\eta u_s}{(E'/\gamma_l)r_x} \right)^{1/4} = \xi E' \left(\frac{\eta u_s}{E' r_x} \right)^{1/4} \left(\gamma_l^{-3/4} \right) = \gamma_l^{-3/4} L \quad (A.4)$$

Therefore, the four asymptotic solutions for mixed lubrication are:

$$\begin{aligned}
H_{c,RI,mix} &= 145 \left(1 + 0.796D^{14/15}\right)^{-15/7} D^{-1} M_{mix}^{-2} \\
&= 145 \left(1 + 0.796D^{14/15}\right)^{-15/7} D^{-1} \left(\gamma_1^{-3/4} M\right)^{-2} \\
&= 145 \left(1 + 0.796D^{14/15}\right)^{-15/7} D^{-1} M \left(\gamma_1^{3/2}\right) = H_{c,RI} \gamma_1^{3/2}
\end{aligned} \tag{A.5}$$

$$\begin{aligned}
H_{c,EI,mix} &= 3.18 \left(1 + 0.006 \ln D + 0.63D^{4/7}\right)^{-14/25} D^{-1/15} \left(M_{mix}\right)^{-2/15} \\
&= 3.18 \left(1 + 0.006 \ln D + 0.63D^{4/7}\right)^{-14/25} D^{-1/15} \left(\gamma_1^{-3/4} M\right)^{-2/15} \\
&= 3.18 \left(1 + 0.006 \ln D + 0.63D^{4/7}\right)^{-14/25} D^{-1/15} M^{-2/15} \left(\gamma_1^{1/10}\right) = H_{c,EI} \gamma_1^{1/10} \\
&= H_{c,EI} \gamma_1^{1/10}
\end{aligned} \tag{A.6}$$

$$\begin{aligned}
H_{c,RV,mix} &= 1.29 \left(1 + 0.69ID\right)^{-2/3} \left(L_{mix}\right)^{2/3} = 1.29 \left(1 + 0.69ID\right)^{-2/3} \left(\gamma_1^{-3/4} L\right)^{2/3} \\
&= 1.29 \left(1 + 0.69ID\right) L^{2/3} \left(\gamma_1^{-1/2}\right) = H_{c,RV} \gamma_1^{-1/2}
\end{aligned} \tag{A.7}$$

$$\begin{aligned}
H_{c,EV,mix} &= 1.48 \left(1 + 0.006 \ln D + 0.63D^{4/7}\right)^{-7/20} D^{-1/24} \left(M_{mix}\right)^{-1/12} \left(L_{mix}\right)^{3/4} \\
&= 1.48 \left(1 + 0.006 \ln D + 0.63D^{4/7}\right)^{-7/20} D^{-1/24} \left(\gamma_1^{-3/4} M\right)^{-1/12} \left(\gamma_1^{-3/4} L\right)^{3/4} \\
&= 1.48 \left(1 + 0.006 \ln D + 0.63D^{4/7}\right)^{-7/20} D^{-1/24} \left(\gamma_1^{1/16}\right) M^{-1/12} \left(\gamma_1^{-9/16}\right) L^{3/4} \\
&= 1.48 \left(1 + 0.006 \ln D + 0.63D^{4/7}\right)^{-7/20} D^{-1/24} M^{-1/12} L^{3/4} \left(\gamma_1^{-1/2}\right) \\
&= H_{c,EV} \gamma_1^{-1/2}
\end{aligned} \tag{A.8}$$

Substitute Eqs (A.5) to (A.8) into Eq. (A.1) the dimensionless central film thickness for mixed lubrication is:

$$\begin{aligned}
H_{c,mix} &= \left\{ \left[\left(\gamma^{3/2} H_{c,RI} \gamma^{3/2} \right)^{3/2} + \left(\left(H_{c,EI} \gamma_1^{1/10} \right)^{-4} + H_{00}^{-4} \right)^{-3/8} \right]^{2\hat{s}_{mix}/3} \right. \\
&\quad \left. + \left(\left(H_{c,RV} \gamma_1^{-1/2} \right)^{-8} + \left(H_{c,EV} \gamma_1^{-1/2} \right)^{-8} \right)^{-\hat{s}_{mix}/8} \right\}^{1/\hat{s}_{mix}} \\
&= \left\{ \left[H_{c,RI}^{3/2} \gamma_1^{9/4} + \left(H_{c,EI}^{-4} \gamma_1^{-2/5} + H_{00}^{-4} \right)^{-3/8} \right]^{2\hat{s}_{mix}/3} + \left(H_{c,RV}^{-8} \gamma_1^4 + H_{c,EV}^{-8} \gamma_1^4 \right)^{-\hat{s}_{mix}/8} \right\}^{1/\hat{s}_{mix}}
\end{aligned} \tag{A.9}$$

Similarly, the parameter s for mixed lubrication is:

$$\hat{s}_{mix} = 1.5 \left[1 + e^{-1.2 \left[\left(\gamma_1^{1/10} H_{c,EI} \right) / \left(\gamma_1^{3/2} H_{c,RI} \right) \right]} \right] = 1.5 \left[1 + e^{-1.2 \gamma_1^{-7/5} \left(H_{c,EI} / H_{c,RI} \right)} \right] \tag{A.10}$$

Eq. (A.9) and Eq. (A.10) are Eq. (3.38) and Eq. (3.39), respectively.

Recall the dimensional central film thickness for thick film condition (Eq. (3.27)):

$$h_c = H_c r_x \left(\frac{\eta u_s}{E' r_x} \right)^{1/2} \tag{3.33}$$

Similarly, substituting the equivalent elastic modulus E' with E'/γ_1 for mixed lubrication:

$$h_{c,mix} = H_{c,mix} r_x \left[\frac{\eta u_s}{(E'/\gamma_1) r_x} \right]^{1/2} = H_{c,mix} r_x \left(\frac{\eta u_s}{E' r_x} \right)^{1/2} \gamma_1^{1/2} \tag{A.11}$$

Eq. (A.11) is Eq. (3.40).

APPENDIX B
EQUIPMENT SPECIFICATIONS

Rheometer

Manufacturer: TA Instruments, Delaware, U.S.A.
Model: AR-2000
Angular velocity range: 0 rad/s to 300 rad/s
Minimum torque: 0.03 μ N
Maximum torque: 200 mNm
Torque resolution: 1 nNm
Displacement resolution: 40 nrad
Time for step change in velocity: 25 ms
Time for step change in strain: 60 ms
Peltier plate temperature range: -40 °C to 200 °C
Temperature accuracy: ± 0.1 °C

Surface profilometer

Manufacturer: Mitutoyo Corporation, Kawasaki, Japan.
Model: Surftest SJ-401
Tip material: Diamond
Tip radius: 2 μ m
Tip angle: 60°
Measuring range: 8 μ m to 800 μ m (Vertical) ; 25 mm (Horizontal)
Measuring speed: 0.05 mm/s to 2.0 mm/s
Detector minimum resolution: 0.000125 μ m for 8 μ m vertical range

Ball on cylinder lubricity tester (BOCLT)

Manufacturer: InterAv, Inc., Texas, U.S.A.
Model: BOC-100
Ball diameter: 12.7 mm
Cylinder diameter: 49.10 mm to 49.25 mm
Test standard: ASTM D-5001 ; ASTM D-6078

Load cell

Manufacturer: Omega Engineering, Inc., Connecticut, U.S.A.
Model: LCFD-10
Capacity: 100 lbf (44.5 N)
Excitation: 5 Vdc
Output: 1.5 mV/V
Operating temperature: -54 °C to 121 °C
Safe overload: 150% of capacity
Bridge resistance: 350 Ω

Voltage doubler

Input voltage range: 0 V to 10 V

Output voltage range: 0 V to 15 V

Amplifier:

Manufacturer: Texas Instruments Incorporated, Texas, U.S.A.

Model: TL084 JFET-Input Operational Amplifiers

Supply voltage: 18 V

Equivalent input noise: 4 μ V

Rise time: 0.05 μ s

Input bias current: 30 pA (typical)

Input offset current: 5 pA (typical)

Operation temperature: 0 $^{\circ}$ C to 70 $^{\circ}$ C

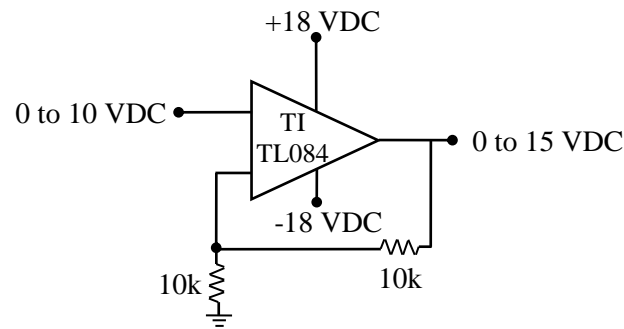


Figure B.1 Circuit diagram of the voltage doubler

Power supply (for voltage doubler)

Manufacturer: Tenma, Premier Farnell Company, Leeds, U.K.

Model: 72-6615

Output voltage: 0 VDC to 30 VDC

Ripple and noise: < 1mV RMS

Output current: 0 A to 3A

Ripple current: < 3mA RMS

Signal Conditioner

Manufacturer: Omega Engineering, Inc., Connecticut, U.S.A.

Model: DMD-465

Amplifier:

Maximum input voltage: ± 15 V

Gain range: 40 to 250

Output noise: 120 μ V at gain = 100, 1 Hz to 100 Hz

Bridge supply:

Output voltage: 4 V to 15 V

Output current: 5 mA to 150 mA

Output noise: 0.5 mV RMS

Laser Tachometer

Manufacturer: Monarch Instrument, New Hampshire, U.S.A.

Model: PLT200

Laser classification: Class 2

Laser wavelength: 650 nm

Operating range: up 7.62 m / up to 70° off

Measurement range: 5 rpm to 200000 rpm

Resolution: 1 rpm

Accuracy: $\pm 0.01\%$ of reading or resolution limit

Data acquisition module

Manufacturer: National Instruments, Texas, U.S.A.

Model: USB-6003

Analog input:

ADC resolution: 16-bit

Input range: ± 10 V

Absolution accuracy at full scale: 6 mV

System noise: 0.4mV RMS

Maximum sample rate (aggregate): 100 kSample/s

Analog output:

ADC resolution: 16-bit

Output range: ± 10 V

Maximum update rate: 5 kSample/s

Absolution accuracy at full scale: 8.6 mV

APPENDIX C
PERFORMACE TEST FOR AR2000 RHEOMETER

A performance test on an AR2000 rheometer was conducted using the reference fluid test B500 with viscosity of 0.5 Pa·s at 25 °C. The viscosities subjected to the shear rate range from 0.1 s⁻¹ to 15000 s⁻¹ were measured. It was noted that the viscosity exhibits significantly low values as a result of fluctuation at low shear rate, generally below 2.5 s⁻¹, which may be attributed to the diffusion of the acceleration in the inertia of the fluid during the startup phase of the test [Schmitt, 2003]. It was also noticed that tested oils tended to migrate off the gap between the cone and the base plate of the rheometer in high test shear rates, generally above 6310 s⁻¹, because of the centrifugal force. Therefore, the viscosity measured at the shear rate ranging between 2.5 s⁻¹ and 6310 s⁻¹ was considered. A very small standard deviation with respect to the average value, less than 0.0058 Pa·s with respect to the average values, was observed. These slight deviations demonstrate that the precision of the measurements was high. The viscosity versus shear rate of the B500 reference fluid at 25 °C was plotted and shown in Fig. C.1. Each data point shown represents the average of the triplicated measurements.

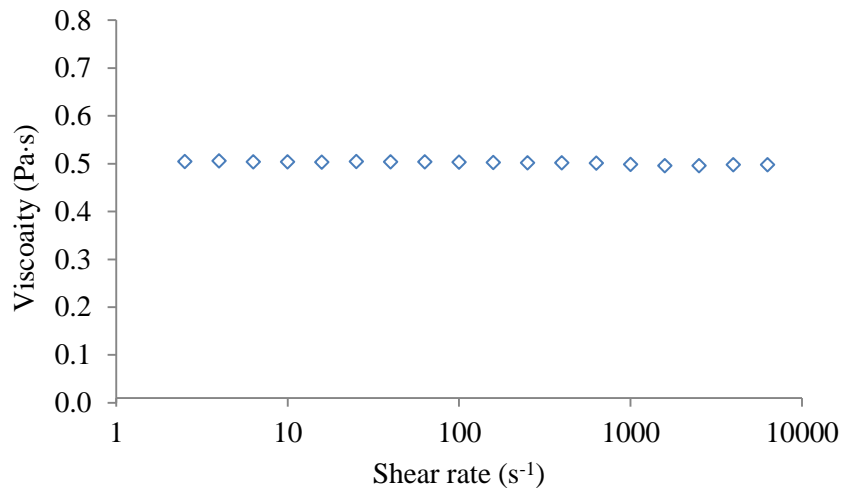


Figure C.1 Viscosity versus shear rate of reference test fluid

It can be seen that the viscosity was independent of shear rate. This indicates uniformity in viscosity. The average value of the viscosities over the considered shear rate range was obtained. It was found that the viscosity of the reference test fluid B500 at 25 °C was 0.501 Pa·s. It was only 0.001 Pa·s higher than the reference value (0.5 Pa·s). In addition, a very small standard deviation (0.0031 Pa·s) with respect to the average value was observed. It was believed that this slight difference was due to the measurement uncertainty, which is highly insignificant.

APPENDIX D
DATA FOR RHEOLOGICAL TEST AND SURFACE TENSION
MEASUREMENTS OF TEST OILS

Table D.1 Measured viscosity of oil #1 at 25°C

Shear rate (s ⁻¹)	Viscosity (Pa·s)			
	Measure 1	Measure 2	Measure 3	Average
2.512	0.2860	0.2888	0.2874	0.2874
3.981	0.2873	0.2858	0.2886	0.2872
6.309	0.2872	0.2885	0.2888	0.2882
10.00	0.2896	0.2898	0.2897	0.2897
15.85	0.2894	0.2898	0.2902	0.2898
25.12	0.2902	0.2905	0.2902	0.2903
39.81	0.2903	0.2906	0.2906	0.2905
63.10	0.2903	0.2907	0.2909	0.2906
100.0	0.2903	0.2906	0.2908	0.2906
158.5	0.2903	0.2906	0.2907	0.2905
251.2	0.2909	0.2913	0.2913	0.2912
398.1	0.2909	0.2911	0.2912	0.2911
631.0	0.2907	0.2909	0.2911	0.2909
1000	0.2903	0.2904	0.2907	0.2905
1585	0.2899	0.2899	0.2902	0.2900
2512	0.2890	0.2890	0.2894	0.2891
3981	0.2889	0.2889	0.2893	0.2890
6310	0.2842	0.2840	0.2845	0.2842

Table D.2 Measured viscosity of oil #1 at 40°C

Shear rate (s ⁻¹)	Viscosity (Pa·s)			
	Measure 1	Measure 2	Measure 3	Average
2.512	0.1208	0.1221	0.1221	0.1217
3.981	0.1234	0.1232	0.1237	0.1234
6.309	0.1242	0.1248	0.1240	0.1243
10.00	0.1251	0.1269	0.1261	0.1260
15.85	0.1251	0.1266	0.1260	0.1259
25.12	0.1251	0.1269	0.1265	0.1262
39.81	0.1257	0.1272	0.1265	0.1265
63.10	0.1257	0.1274	0.1266	0.1266
100.0	0.1253	0.1270	0.1266	0.1263
158.5	0.1251	0.1269	0.1264	0.1261
251.2	0.1250	0.1269	0.1261	0.1260
398.1	0.1255	0.1273	0.1266	0.1265
631.0	0.1253	0.1272	0.1267	0.1264
1000	0.1253	0.1273	0.1268	0.1265
1585	0.1253	0.1274	0.1265	0.1264
2512	0.1255	0.1273	0.1263	0.1264
3981	0.1262	0.1279	0.1271	0.1271
6310	0.1248	0.1267	0.1262	0.1259

Table D.3 Measured viscosity of oil #1 at 100°C

Shear rate (s ⁻¹)	Viscosity (Pa·s)			
	Measure 1	Measure 2	Measure 3	Average
2.512	0.0095	0.0101	0.0145	0.0095
3.981	0.0097	0.0147	0.0146	0.0097
6.309	0.0114	0.0129	0.0139	0.0114
10.00	0.0133	0.0134	0.0122	0.0133
15.85	0.0123	0.0131	0.0130	0.0123
25.12	0.0130	0.0132	0.0128	0.0130
39.81	0.0132	0.0136	0.0131	0.0132
63.10	0.0135	0.0140	0.0137	0.0135
100.0	0.0131	0.0135	0.0132	0.0131
158.5	0.0129	0.0132	0.0129	0.0129
251.2	0.0128	0.0131	0.0128	0.0128
398.1	0.0128	0.0130	0.0128	0.0128
631.0	0.0128	0.0130	0.0128	0.0128
1000	0.0128	0.0130	0.0128	0.0128
1585	0.0129	0.0131	0.0128	0.0129
2512	0.0130	0.0133	0.0130	0.0130
3981	0.0138	0.0140	0.0137	0.0138
6310	0.0135	0.0137	0.0134	0.0135

Table D.4 Measured viscosity of oil #2 at 25°C

Shear rate (s ⁻¹)	Viscosity (Pa·s)			
	Measure 1	Measure 2	Measure 3	Average
2.512	0.1835	0.1839	0.1827	0.1834
3.981	0.1851	0.1848	0.1837	0.1845
6.309	0.1837	0.1854	0.1845	0.1845
10.00	0.1848	0.1857	0.1847	0.1851
15.85	0.1845	0.1861	0.1852	0.1853
25.12	0.1847	0.1863	0.1855	0.1855
39.81	0.1842	0.1862	0.1852	0.1852
63.10	0.1841	0.1861	0.1852	0.1851
100.0	0.1843	0.1865	0.1855	0.1854
158.5	0.1843	0.1866	0.1857	0.1855
251.2	0.1842	0.1865	0.1856	0.1854
398.1	0.1841	0.1864	0.1855	0.1853
631.0	0.1839	0.1863	0.1853	0.1852
1000	0.1836	0.1859	0.1850	0.1848
1585	0.1844	0.1865	0.1857	0.1855
2512	0.1832	0.1853	0.1846	0.1844
3981	0.1835	0.1839	0.1827	0.1834
6310	0.1851	0.1848	0.1837	0.1845

Table D.5 Measured viscosity of oil #2 at 40°C

Shear rate (s ⁻¹)	Viscosity (Pa·s)			
	Measure 1	Measure 2	Measure 3	Average
2.512	0.0848	0.0949	0.0947	0.0915
3.981	0.0876	0.0946	0.0946	0.0923
6.309	0.0904	0.0933	0.0943	0.0927
10.00	0.0938	0.0934	0.0934	0.0935
15.85	0.0911	0.0952	0.0949	0.0937
25.12	0.0923	0.0944	0.0942	0.0936
39.81	0.0923	0.0946	0.0945	0.0938
63.10	0.0920	0.0945	0.0946	0.0937
100.0	0.0919	0.0942	0.0944	0.0935
158.5	0.0918	0.0940	0.0944	0.0934
251.2	0.0916	0.0940	0.0942	0.0932
398.1	0.0916	0.0940	0.0943	0.0933
631.0	0.0919	0.0942	0.0942	0.0934
1000	0.0919	0.0943	0.0941	0.0934
1585	0.0919	0.0942	0.0941	0.0934
2512	0.0918	0.0942	0.0941	0.0934
3981	0.0926	0.0949	0.0948	0.0941
6310	0.0919	0.0943	0.0943	0.0935

Table D.6 Measured viscosity of oil #2 at 100°C

Shear rate (s ⁻¹)	Viscosity (Pa·s)			
	Measure 1	Measure 2	Measure 3	Average
2.512	0.0148	0.0156	0.0160	0.0155
3.981	0.0160	0.0180	0.0171	0.0170
6.309	0.0174	0.0177	0.0171	0.0174
10.00	0.0182	0.0178	0.0178	0.0179
15.85	0.0180	0.0187	0.0185	0.0184
25.12	0.0189	0.0188	0.0189	0.0189
39.81	0.0194	0.0193	0.0191	0.0192
63.10	0.0194	0.0195	0.0193	0.0194
100.0	0.0191	0.0192	0.0191	0.0191
158.5	0.0190	0.0190	0.0189	0.0190
251.2	0.0189	0.0189	0.0188	0.0189
398.1	0.0190	0.0190	0.0188	0.0189
631.0	0.0189	0.0189	0.0188	0.0189
1000	0.0189	0.0190	0.0188	0.0189
1585	0.0190	0.0190	0.0189	0.0189
2512	0.0191	0.0191	0.0190	0.0191
3981	0.0201	0.0201	0.0200	0.0200
6310	0.0196	0.0196	0.0195	0.0195

Table D.7 Measured viscosity of oil #3 at 25°C

Shear rate (s ⁻¹)	Viscosity (Pa·s)			
	Measure 1	Measure 2	Measure 3	Average
2.512	0.2609	0.2609	0.2543	0.2587
3.981	0.2608	0.2608	0.2571	0.2596
6.309	0.2605	0.2605	0.2573	0.2594
10.00	0.2617	0.2617	0.2593	0.2609
15.85	0.2620	0.2620	0.2598	0.2613
25.12	0.2619	0.2619	0.2604	0.2614
39.81	0.2621	0.2621	0.2609	0.2617
63.10	0.2622	0.2622	0.2609	0.2618
100.0	0.2621	0.2621	0.2608	0.2617
158.5	0.2619	0.2619	0.2607	0.2615
251.2	0.2625	0.2625	0.2614	0.2621
398.1	0.2623	0.2623	0.2614	0.2620
631.0	0.2622	0.2622	0.2615	0.2620
1000	0.2619	0.2619	0.2613	0.2617
1585	0.2616	0.2616	0.2609	0.2614
2512	0.2610	0.2610	0.2605	0.2608
3981	0.2615	0.2615	0.2609	0.2613
6310	0.2586	0.2586	0.2581	0.2584

Table D.8 Measured viscosity of oil #3 at 40°C

Shear rate (s ⁻¹)	Viscosity (Pa·s)			
	Measure 1	Measure 2	Measure 3	Average
2.512	0.1286	0.1268	0.1298	0.1284
3.981	0.1305	0.1274	0.1294	0.1291
6.309	0.1305	0.1275	0.1294	0.1291
10.00	0.1290	0.1290	0.1287	0.1289
15.85	0.1300	0.1294	0.1305	0.1300
25.12	0.1294	0.1295	0.1296	0.1295
39.81	0.1297	0.1296	0.1297	0.1297
63.10	0.1299	0.1294	0.1299	0.1297
100.0	0.1297	0.1292	0.1295	0.1295
158.5	0.1295	0.1291	0.1294	0.1293
251.2	0.1294	0.1289	0.1295	0.1293
398.1	0.1298	0.1295	0.1298	0.1297
631.0	0.1299	0.1294	0.1298	0.1297
1000	0.1298	0.1295	0.1299	0.1297
1585	0.1297	0.1294	0.1297	0.1296
2512	0.1296	0.1292	0.1296	0.1295
3981	0.1303	0.1301	0.1305	0.1303
6310	0.1295	0.1291	0.1296	0.1294

Table D.9 Measured viscosity of oil #3 at 100°C

Shear rate (s ⁻¹)	Viscosity (Pa·s)			
	Measure 1	Measure 2	Measure 3	Average
2.512	0.0246	0.0226	0.0228	0.0234
3.981	0.0258	0.0251	0.0251	0.0253
6.309	0.0268	0.0260	0.0264	0.0264
10.00	0.0281	0.0271	0.0264	0.0272
15.85	0.0283	0.0274	0.0277	0.0278
25.12	0.0290	0.0281	0.0279	0.0283
39.81	0.0294	0.0288	0.0288	0.0290
63.10	0.0292	0.0285	0.0286	0.0288
100.0	0.0289	0.0284	0.0284	0.0286
158.5	0.0288	0.0283	0.0282	0.0284
251.2	0.0287	0.0282	0.0281	0.0283
398.1	0.0287	0.0282	0.0282	0.0284
631.0	0.0287	0.0282	0.0282	0.0284
1000	0.0287	0.0282	0.0283	0.0284
1585	0.0289	0.0283	0.0284	0.0285
2512	0.0290	0.0284	0.0284	0.0286
3981	0.0299	0.0293	0.0294	0.0295
6310	0.0294	0.0287	0.0291	0.0291

Table D.10 Measured surface tension of test oils at 25°C

Oil #	Surface tension (Nm)			
	Measure 1	Measure 2	Measure 3	Average
1	34.8	34.7	34.7	34.7
2	35.4	35.3	35.3	35.3
3	37.6	37.7	37.6	37.6

APPENDIX E

**CONVERSION OF KINEMATICS TO DYNAMIC VISCOSITY OF
TESTED OILS IN ACCORDANCE WITH OIL MANUFACTURERS
SPECIFICATIONS**

It is common that the specifications of a lubrication oil provided by its manufacturer states the kinematic viscosities at 40 °C and 100 °C instead of the engineering dynamic (absolute) viscosity. In order to compare the manufacturer-provided values with the rheological test results, which were measured in the dynamic viscosity, at 25 °C, 40 °C and 100 °C, the kinematics viscosities were converted to the dynamic viscosity. In this process, the kinematic viscosity of the tested oils at 25 °C was first evaluated according to the ASTM [2009] Standard D341 based on the specifications given by the oil manufacturers. The kinematics viscosities of the tested oils at the three temperatures were then converted to the dynamic viscosities. The procedures are described in this section.

E.1 Kinematic Viscosity of Tested Oil at 25 °C

The kinematic viscosity of tested oils at 25°C, ν_{25} , was evaluated by using Eq. (E.1), according to the ASTM Standard D341-09 [ASTM, 2009]. The calculated kinematic viscosities of tested oils at 25°C are shown in

$$\nu_{25} = 10^{10(K_A - K_B \log 298)} \quad (\text{E.1})$$

where $K_A = \log[\log(\nu_{100} + 0.7)] + K_B \log 373$

$$K_B = \frac{\log[\log(\nu_{40} + 0.7)] - \log[\log(\nu_{100} + 0.7)]}{\log 373 - \log 313}$$

Table E.1 Estimated kinematic viscosity of tested oils at 25°C

Oil #	Kinematic viscosity at 25°C (cSt)
1	494.8
2	221.1
3	308.7

It is worth noting that the average values of the kinematic viscosities range at 40 °C provided by the manufacture (Table 4.2 in Chapter 4) were used to estimate the kinematic viscosities at 25 °C of oils #2 and #3.

E.2 Conversion from Kinematics to Dynamic Viscosity

The dynamic viscosity, η , of an oil can be calculated by multiplying the kinematic viscosity, ν_k , by the density, ρ , of the oil [Hamrock and Dowson, 1981]:

$$\eta = \nu_k \rho \quad (\text{E.2})$$

The densities of tested oils at different temperatures were estimated via the density-temperature relationship expression as shown in Eq. (E.3) below [The Engineering ToolBox, 2014], with the densities at given temperatures provided by manufacturers.

$$\rho_t = \rho_{oo} / [1 + \beta(t_t - t_o)] \quad (\text{E.3})$$

where ρ_t = density at a given temperature,

ρ_{oo} = density at the reference temperature,

t_t = given temperature,

t_o = reference temperature,

β = volumetric expansion coefficient.

The common value, $0.00070 \text{ } ^\circ\text{C}^{-1}$, of volumetric expansion coefficient for oil was considered for the tested oils [The Engineering ToolBox, 2014] in this study. The estimated tested oils densities at $25 \text{ } ^\circ\text{C}$, $40 \text{ } ^\circ\text{C}$ and $100 \text{ } ^\circ\text{C}$ are shown in Table E.2.

Table E.2 Estimated tested oils density

Oil #	Density (kg/m^3)		
	25 $^\circ\text{C}$	40 $^\circ\text{C}$	100 $^\circ\text{C}$
1	899.7	890.4	855.1
2	903.7	894.3	858.9
3	903.7	894.3	858.9

It is worth noting that the average values of the kinematic viscosity range at $40 \text{ } ^\circ\text{C}$ provided by the manufacture were used in the estimation of the dynamic viscosities of oil #2 and #3 at $40 \text{ } ^\circ\text{C}$. The dynamic viscosity of the tested oils at $25 \text{ } ^\circ\text{C}$, $40 \text{ } ^\circ\text{C}$ and $100 \text{ } ^\circ\text{C}$ can be approximated by using Eq. (E.2).

APPENDIX F
APPARENT DEPENDENCE OF VISCOSITY AND SURFACE TENSION
OF TESTED OILS

From the definitions outlined earlier, both, the viscosity and the surface tension of a fluid are properties defined by their molecular interaction. Therefore attempts were made to clarify this possible apparent dependence. The results from the present study are plotted in Fig. F.1. Even though no straightforward relationship is apparent when considering all results; despite the small sampling number a clear direct correlation may exist for oils with similar formulation. Wei *et al.* [2014] has also reported non-conclusive results.

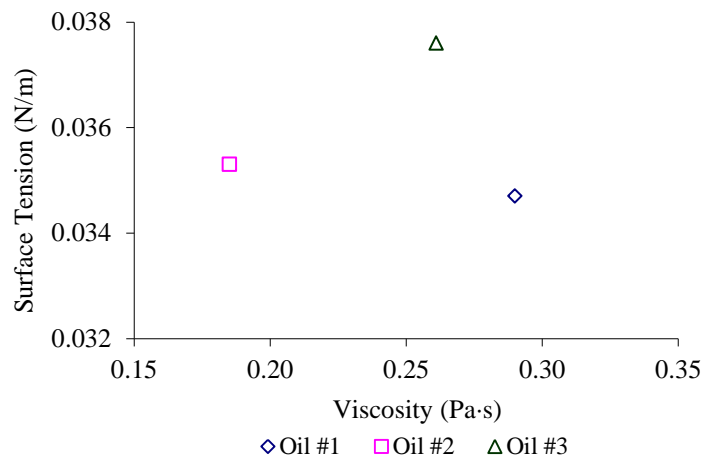


Figure F.1 Surface tension versus viscosity of tested oils at 25°C

APPENDIX G

REFERENCE TEST FOR BALL-ON-CYLINDER LUBRICITY TESTER

The friction force measurement of the ball-on-cylinder lubricity tester (BOCLT) was examined by performing reference test in accordance to the manufacture's menu [InterAv Inc., 1989]. In this test, the test ball and the rough test cylinder, as described in section 5.2, were used as the contact components. Isopar M fluid was used as the lubricant. The lower portion of the rotating test cylinder was submerged into the Isopar M fluid in a reservoir such that the fluid was continuous supplied to the cylinder surface during the test (Fig. G.1). A standard dead weight of 500.6 g, which produced 9.82 N applied load at the contact, and a constant test speed of 240 rpm were used. An Omega LCFD-10LB load cell was used to measure the friction force at the contact and the signal was conditioned by an Omega DMD-465 signal conditioner. A National Instruments USB-6003 data acquisition/control device was used to digitise the conditioned analog signals for the test. The digitised signals were then analysed by the National Instruments LabView software with 1000Hz sampling rate and recorded in 0.1 s interval in a PC computer. The constant test speed was control by direct constant voltage supplied from a power supply unit. A Monarch Instrument PLT200 tachometer was used to monitor the rotation speed of the cylinder throughout each test. It was observed that the variations of the rotation speed during tests were less than ± 0.1 rpm. All tests were conducted at an ambient, but well-controlled, environmental condition of $24\text{ }^{\circ}\text{C} \pm 1\text{ }^{\circ}\text{C}$ and $40\% \pm 1\%$ relative humidity, and were repeated 5 times to ensure reproducibility. The test cylinders and balls were cleaned prior to measurements and each test, according to the ASTM International Designation D5001-08 [ASTM, 2008]. A new contacting surface and fresh oil were used for each test at a certain loading. The friction force at the contact was obtained from averaging observed values of steady state operation took place after 2 minutes, according to the manufacture's menu, for 10 minutes.

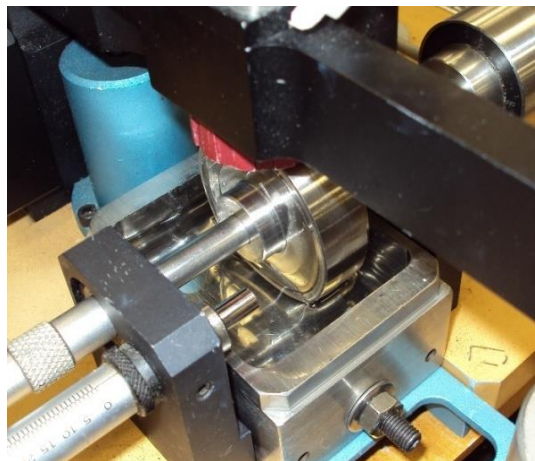


Figure G.1 Lower portion of test cylinder submerged into Isopar M fluid in BOCLT reference test

The results are shown in Table G.1 together with the percentage difference with respect to the manufacture's data. It can be seen that all 5 measured friction forces were higher than the reference value, however, they were within the allowable range. The maximum difference between the measured friction forces and the reference value was +2.6%.

Table G.1 Results of BOCTL reference test

Reference test #	Speed (rpm)	Measured Friction Force (N)	Reference Friction Force (N)	Difference (%)
1	240.02	1.456		+2.4
2	240.05	1.459		+2.6
3	240.06	1.455	1.422 ± 0.049	+2.3
4	240.02	1.447		+1.8
5	240.02	1.452		+2.1

APPENDIX H
DATA FOR TEST CYLINDER AND TEST BALL DIAMETER AND
SURFACE PARAMETERS

Table H.1 Measured smooth cylinder diameter

Cylinder #	Diameter (mm)			Average
	Measure 1	Measure 2	Measure 3	
1	49.20	49.20	49.20	49.20
2	49.20	49.20	49.18	49.19
3	49.20	49.20	49.20	49.20
4	49.20	49.18	49.20	49.19
5	49.20	49.20	49.20	49.20
6	49.20	49.18	49.20	49.19
7	49.20	49.18	49.20	49.19
8	49.20	49.20	49.20	49.20
9	49.20	49.20	49.20	49.20
10	49.20	49.20	49.20	49.20
Overall average ± standard deviation	49.20 ± 0.003			

Table H.2 Measured sanded cylinder diameter

Cylinder #	Diameter (mm)			Average
	Measure 1	Measure 2	Measure 3	
1	49.20	49.20	49.20	49.20
2	49.20	49.20	49.20	49.20
3	49.20	49.18	49.20	49.19
4	49.20	49.20	49.20	49.20
5	49.20	49.20	49.20	49.20
6	49.20	49.20	49.20	49.20
7	49.20	49.20	49.20	49.20
8	49.20	49.20	49.18	49.19
9	49.18	49.20	49.20	49.19
10	49.20	49.18	49.20	49.19
Overall average ± standard deviation	49.20 ± 0.003			

Table H.3 Measured rough cylinder diameter

Cylinder #	Diameter (mm)			Average
	Measure 1	Measure 2	Measure 3	
1	49.20	49.20	49.18	49.19
2	49.20	49.20	49.20	49.20
3	49.20	49.20	49.18	49.19
4	49.20	49.20	49.20	49.20
5	49.20	49.18	49.20	49.19
6	49.20	49.20	49.20	49.20
7	49.20	49.18	49.20	49.19
8	49.20	49.18	49.20	49.19
9	49.20	49.20	49.20	49.20
10	49.20	49.20	49.20	49.20
Overall average ± standard deviation	49.20 ± 0.004			

Table H.4 Measured test ball diameter

Ball #	Diameter (mm)			Average
	Measure 1	Measure 2	Measure 3	
1	12.70	12.70	12.70	12.70
2	12.70	12.70	12.70	12.70
3	12.70	12.70	12.70	12.70
4	12.70	12.70	12.70	12.70
5	12.70	12.70	12.70	12.70
6	12.70	12.70	12.70	12.70
7	12.70	12.70	12.70	12.70
8	12.70	12.70	12.70	12.70
9	12.70	12.70	12.70	12.70
10	12.70	12.70	12.70	12.70
Overall average	12.70			

Table H.5 Measured smooth cylinder surface centre line roughness

Cylinder #	Centre line roughness (μm)			Average
	Measure 1	Measure 2	Measure 3	
S1	0.04	0.05	0.05	0.047
S2	0.04	0.05	0.04	0.043
S3	0.05	0.05	0.05	0.050
S4	0.05	0.05	0.05	0.050
S5	0.04	0.05	0.04	0.043
S6	0.05	0.04	0.04	0.043
S7	0.04	0.04	0.04	0.040
S8	0.04	0.04	0.05	0.043
S9	0.04	0.04	0.04	0.040
S10	0.04	0.04	0.04	0.040
Overall average \pm standard deviation	0.044 \pm 0.005			

Table H.6 Measured sanded cylinder surface centre line roughness

Cylinder #	Centre line roughness (μm)			Average
	Measure 1	Measure 2	Measure 3	
D1	0.47	0.47	0.47	0.470
D2	0.48	0.49	0.50	0.490
D3	0.48	0.51	0.51	0.500
D4	0.48	0.47	0.50	0.483
D5	0.50	0.47	0.50	0.490
D6	0.49	0.50	0.50	0.497
D7	0.50	0.47	0.49	0.487
D8	0.48	0.50	0.47	0.483
D9	0.49	0.49	0.48	0.487
D10	0.51	0.51	0.49	0.503
Overall average \pm standard deviation	0.489 \pm 0.014			

Table H.7 Measured rough cylinder surface centre line roughness

Cylinder #	Root Mean Square Roughness (μm)			
	Measure 1	Measure 2	Measure 3	Average
R1	0.53	0.53	0.53	0.530
R2	0.53	0.54	0.52	0.530
R3	0.54	0.54	0.53	0.537
R4	0.53	0.54	0.52	0.530
R5	0.53	0.51	0.54	0.527
R6	0.52	0.54	0.52	0.527
R7	0.52	0.53	0.54	0.530
R8	0.52	0.52	0.54	0.527
R9	0.54	0.53	0.52	0.530
R10	0.52	0.53	0.54	0.530
Overall average \pm standard deviation	0.530 ± 0.009			

Table H.8 Measured test ball surface centre line roughness

Ball #	Centre line roughness (μm)			
	Measure 1	Measure 2	Measure 3	Average
1	0.03	0.03	0.02	0.03
2	0.02	0.02	0.03	0.02
3	0.03	0.02	0.03	0.03
4	0.03	0.03	0.03	0.03
5	0.03	0.03	0.03	0.03
6	0.03	0.03	0.03	0.03
7	0.03	0.03	0.03	0.03
8	0.03	0.03	0.02	0.03
9	0.03	0.03	0.03	0.03
10	0.03	0.03	0.03	0.03
Overall average \pm standard deviation	0.028 ± 0.004			

Table H.9 Measured smooth cylinder surface root mean square roughness

Cylinder #	Centre line roughness (μm)			Average
	Measure 1	Measure 2	Measure 3	
S1	0.05	0.06	0.06	0.057
S2	0.05	0.06	0.05	0.053
S3	0.06	0.06	0.06	0.060
S4	0.06	0.06	0.06	0.060
S5	0.05	0.06	0.05	0.053
S6	0.06	0.05	0.05	0.053
S7	0.05	0.05	0.05	0.050
S8	0.06	0.05	0.06	0.057
S9	0.05	0.05	0.05	0.050
S10	0.05	0.05	0.06	0.053
Overall average \pm standard deviation	0.055 \pm 0.005			

Table H.10 Measured sanded cylinder surface root mean square roughness

Cylinder #	Centre Line Roughness (μm)			Average
	Measure 1	Measure 2	Measure 3	
D1	0.58	0.59	0.58	0.583
D2	0.59	0.60	0.63	0.607
D3	0.59	0.62	0.63	0.613
D4	0.60	0.58	0.61	0.597
D5	0.62	0.58	0.62	0.607
D6	0.61	0.62	0.63	0.620
D7	0.62	0.59	0.62	0.610
D8	0.61	0.62	0.59	0.607
D9	0.60	0.61	0.60	0.603
D10	0.63	0.63	0.62	0.627
Overall average \pm standard deviation	0.607 \pm 0.017			

Table H.11 Measured rough cylinder surface root mean square roughness

Cylinder #	Root Mean Square Roughness (μm)			
	Measure 1	Measure 2	Measure 3	Average
R1	0.68	0.68	0.66	0.673
R2	0.66	0.69	0.64	0.663
R3	0.67	0.68	0.66	0.670
R4	0.67	0.69	0.66	0.673
R5	0.66	0.64	0.68	0.660
R6	0.65	0.68	0.64	0.657
R7	0.64	0.66	0.68	0.660
R8	0.64	0.66	0.68	0.660
R9	0.69	0.65	0.66	0.667
R10	0.65	0.66	0.67	0.660
Overall average \pm standard deviation	0.664 ± 0.016			

Table H.12 Measured test ball surface root mean square roughness

Ball #	Root Mean Square Roughness (μm)			
	Measure 1	Measure 2	Measure 3	Average
1	0.04	0.04	0.03	0.04
2	0.03	0.03	0.04	0.03
3	0.03	0.03	0.04	0.03
4	0.04	0.04	0.03	0.04
5	0.04	0.04	0.03	0.04
6	0.04	0.04	0.03	0.04
7	0.04	0.04	0.04	0.04
8	0.03	0.03	0.03	0.03
9	0.03	0.03	0.03	0.03
10	0.03	0.03	0.03	0.03
Overall average \pm standard deviation	0.034 ± 0.005			

Table H.13 Measured sanded cylinder surface asperity average slope

Cylinder #	Asperity average slope			Average
	Measure 1	Measure 2	Measure 3	
D1	0.09	0.09	0.10	0.093
D2	0.10	0.09	0.09	0.093
D3	0.10	0.09	0.09	0.093
D4	0.11	0.10	0.11	0.107
D5	0.10	0.09	0.09	0.093
D6	0.11	0.09	0.10	0.100
D7	0.09	0.09	0.10	0.093
D8	0.09	0.10	0.09	0.093
D9	0.09	0.09	0.10	0.093
D10	0.09	0.10	0.09	0.093
Overall average ± standard deviation	0.095 ± 0.007			

Table H.14 Measured rough cylinder surface asperity average slope

Cylinder #	Asperity average slope			Average
	Measure 1	Measure 2	Measure 3	
R1	0.09	0.10	0.10	0.097
R2	0.10	0.10	0.09	0.097
R3	0.10	0.10	0.10	0.100
R4	0.10	0.10	0.10	0.100
R5	0.10	0.10	0.11	0.103
R6	0.10	0.10	0.09	0.097
R7	0.09	0.09	0.09	0.090
R8	0.10	0.09	0.10	0.097
R9	0.09	0.09	0.10	0.093
R10	0.10	0.10	0.10	0.100
Overall average ± standard deviation	0.097 ± 0.005			

Table H.15 Measured test ball surface asperity average slope

Ball #	Asperity average slope			
	Measure 1	Measure 2	Measure 3	Average
1	0.02	0.02	0.02	0.02
2	0.02	0.02	0.02	0.02
3	0.03	0.02	0.02	0.02
4	0.02	0.03	0.02	0.02
5	0.02	0.02	0.01	0.02
6	0.02	0.02	0.02	0.02
7	0.02	0.02	0.02	0.02
8	0.02	0.02	0.02	0.02
9	0.02	0.02	0.02	0.02
10	0.02	0.02	0.02	0.02
Overall average ± standard deviation	0.020 ± 0.003			

Table H.16 Measured sanded cylinder surface high spot counts in transverse direction

Cylinder #	High spot counts in transverse direction			
	Measure 1	Measure 2	Measure 3	Average
D1	427.3	422.6	404.5	418.13
D2	490.0	414.3	430.5	444.93
D3	411.1	391.3	391.1	397.83
D4	468.1	500.5	442.4	470.33
D5	412.6	431.5	434.5	426.20
D6	479.8	461.5	444.1	461.80
D7	410.4	419.5	407.7	412.53
D8	456.1	429.6	446.6	444.10
D9	433.1	437.8	436.5	435.80
D10	427.2	420.5	462.1	436.60
Overall average ± standard deviation	434.8 ± 26.9			

Table H.17 Measured rough cylinder surface high spot counts in transverse direction

Cylinder #	High spot counts in transverse direction			
	Measure 1	Measure 2	Measure 3	Average
R1	392.3	371.6	399.6	387.83
R2	355.8	379.6	373.7	369.70
R3	368.7	419.1	374.6	387.47
R4	384.4	356.7	384.5	375.20
R5	404.5	375.5	385.2	388.40
R6	387.0	377.5	397.8	387.43
R7	356.9	437.2	352.8	382.30
R8	396.5	373.2	374.9	381.53
R9	357.8	385.2	379.8	374.27
R10	397.5	395.0	374.9	389.13
Overall average ± standard deviation	382.3 ± 18.9			

Table H.18 Measured sanded cylinder surface high spot counts in rolling direction

Cylinder #	High spot counts in rolling direction			
	Measure 1	Measure 2	Measure 3	Average
D1	353.7	310.6	378.8	347.70
D2	381.4	370.4	348.2	366.67
D3	318.7	332.8	396.0	349.17
D4	361.3	332.7	365.9	353.30
D5	304.3	314.9	386.3	335.17
D6	292.2	367.7	359.3	339.73
D7	318.8	305.6	315.2	313.20
D8	352.3	344.3	376.5	357.70
D9	379.7	372.5	331.2	361.13
D10	349.4	399.3	374.0	374.23
Overall average ± standard deviation	349.8 ± 29.9			

Table H.19 Measured rough cylinder surface high spot counts in rolling direction

Cylinder #	High spot counts in rolling direction			Average
	Measure 1	Measure 2	Measure 3	
R1	393.6	301.6	379.3	358.17
R2	296.1	362.7	387.3	348.70
R3	386.1	340.7	303.8	343.53
R4	376.2	326.5	368.7	357.13
R5	303.1	303.6	334.5	313.73
R6	318.4	321.7	309.1	316.40
R7	348.0	298.1	341.6	329.23
R8	346.9	305.2	321.0	324.37
R9	314.2	361.1	294.2	323.17
R10	301.0	285.1	337.2	307.77
Overall average ± standard deviation	332.2 ± 32.3			

Table H.20 Measured test ball surface high spot counts

Ball #	High spot counts			Average
	Measure 1	Measure 2	Measure 3	
1	1288.4	1237.0	1373.9	1299.77
2	1564.4	1627.0	1373.8	1521.73
3	1896.4	1965.1	1632.8	1831.43
4	1497.9	1310.0	1569.8	1459.23
5	1246.0	1686.9	1892.5	1608.47
6	1586.3	1268.1	1574.7	1476.37
7	1396.3	1652.8	1250.3	1433.13
8	1533.2	1827.7	1671.1	1677.33
9	1471.9	1545.8	1505.7	1507.80
10	1491.3	1452.2	1620.5	1521.33
Overall average ± standard deviation	1533.7 ± 198.1			

APPENDIX I
DATA FOR FRICTION TEST

Table I.1 Measured friction force and calculated friction coefficient of oil #1 with 5.88 N applied load, sanded cylinder and continuous oil supply

Rotation speed (rpm)	Friction force (N)				Friction coefficient
	Measure 1	Measure 2	Measure 3	Average	
100	0.7802	0.7739	0.7925	0.7822	0.1330
200	0.7142	0.7188	0.7332	0.7221	0.1228
300	0.6738	0.6743	0.7059	0.6847	0.1164
400	0.6321	0.6142	0.6742	0.6402	0.1089
500	0.5793	0.5838	0.6354	0.5995	0.1020
600	0.5634	0.5452	0.5916	0.5667	0.0964
700	0.5167	0.5321	0.5581	0.5356	0.0911
800	0.5091	0.4927	0.5355	0.5124	0.0872

Table I.2 Measured friction force and calculated friction coefficient of oil #1 with 5.88 N applied load, sanded cylinder and 60 μ l oil supply

Rotation speed (rpm)	Friction force (N)				Friction coefficient
	Measure 1	Measure 2	Measure 3	Average	
100	0.7733	0.7869	0.7930	0.7844	0.1334
200	0.7415	0.7264	0.7411	0.7363	0.1252
300	0.8033	0.7634	0.7903	0.7857	0.1336
400	0.8399	0.7960	0.8169	0.8176	0.1390
500	0.8454	0.8197	0.8474	0.8375	0.1424
600	0.8518	0.8278	0.8605	0.8467	0.1440
700	0.8494	0.8305	0.8800	0.8533	0.1451
800	0.8273	0.8325	0.8597	0.8398	0.1428

Table I.3 Measured friction force and calculated friction coefficient of oil #1 with 5.88 N applied load, sanded cylinder and 100 μ l oil supply

Rotation speed (rpm)	Friction force (N)				Friction coefficient
	Measure 1	Measure 2	Measure 3	Average	
100	0.7660	0.7777	0.7992	0.7810	0.1328
200	0.7088	0.7076	0.7289	0.7151	0.1216
300	0.6846	0.6895	0.7105	0.6949	0.1182
400	0.7635	0.7413	0.7756	0.7601	0.1293
500	0.8053	0.7683	0.7887	0.7874	0.1339
600	0.8086	0.7788	0.7989	0.7954	0.1353
700	0.8210	0.7937	0.8262	0.8136	0.1384
800	0.8139	0.7981	0.8311	0.8144	0.1385

Table I.4 Measured friction force and calculated friction coefficient of oil #1 with 9.82 N applied load, sanded cylinder and continuous oil supply

Rotation speed (rpm)	Friction force (N)				Friction coefficient
	Measure 1	Measure 2	Measure 3	Average	
100	1.2912	1.3126	1.2765	1.2934	0.1317
200	1.1788	1.1968	1.1516	1.1757	0.1197
300	1.1220	1.1321	1.0917	1.1153	0.1136
400	1.0657	1.0771	1.0224	1.0551	0.1074
500	1.0233	1.0320	0.9855	1.0136	0.1032
600	0.9519	0.9768	0.9271	0.9519	0.0969
700	0.8927	0.8863	0.8847	0.8879	0.0904
800	0.8596	0.8756	0.8503	0.8618	0.0878

Table I.5 Measured friction force and calculated friction coefficient of oil #1 with 9.82 N applied load, sanded cylinder and 60 μ l oil supply

Rotation speed (rpm)	Friction force (N)				Friction coefficient
	Measure 1	Measure 2	Measure 3	Average	
100	1.3093	1.2975	1.2911	1.2993	0.1323
200	1.2315	1.2099	1.2143	1.2186	0.1241
300	1.2644	1.2597	1.2196	1.2479	0.1271
400	1.2838	1.3225	1.2537	1.2867	0.1310
500	1.3237	1.3554	1.2991	1.3261	0.1350
600	1.3199	1.4104	1.3912	1.3738	0.1399
700	1.3647	1.3714	1.4243	1.3868	0.1412
800	1.3258	1.3727	1.3854	1.3613	0.1386

Table I.6 Measured friction force and calculated friction coefficient of oil #1 with 9.82 N applied load, sanded cylinder and 100 μ l oil supply

Rotation speed (rpm)	Friction force (N)				Friction coefficient
	Measure 1	Measure 2	Measure 3	Average	
100	1.3008	1.3035	1.2915	1.2986	0.1322
200	1.1793	1.1945	1.1769	1.1836	0.1205
300	1.1052	1.1399	1.1224	1.1225	0.1143
400	1.1583	1.2115	1.1853	1.1850	0.1207
500	1.2351	1.3155	1.2877	1.2794	0.1303
600	1.3094	1.3654	1.3945	1.3564	0.1381
700	1.3640	1.3906	1.4467	1.4004	0.1426
800	1.3663	1.3914	1.4224	1.3934	0.1419

Table I.7 Measured friction force and calculated friction coefficient of oil #1 with 5.88 N applied load, rough cylinder and continuous oil supply

Rotation speed (rpm)	Friction force (N)				Friction coefficient
	Measure 1	Measure 2	Measure 3	Average	
100	0.8419	0.8159	0.8314	0.8297	0.1411
200	0.7800	0.7323	0.7582	0.7568	0.1287
300	0.7491	0.7016	0.7320	0.7276	0.1237
400	0.6973	0.6620	0.6744	0.6779	0.1153
500	0.6700	0.6295	0.6551	0.6515	0.1108
600	0.6302	0.5889	0.6289	0.6160	0.1048
700	0.5850	0.5653	0.5924	0.5809	0.0988
800	0.5629	0.5501	0.5717	0.5616	0.0955

Table I.8 Measured friction force and calculated friction coefficient of oil #1 with 5.88 N applied load, rough cylinder and 60 μ l oil supply

Rotation speed (rpm)	Friction force (N)				Friction coefficient
	Measure 1	Measure 2	Measure 3	Average	
100	0.8138	0.8409	0.8080	0.8209	0.1396
200	0.7378	0.7657	0.7635	0.7557	0.1285
300	0.7102	0.7063	0.7462	0.7209	0.1226
400	0.7662	0.7453	0.7989	0.7701	0.1310
500	0.7878	0.7708	0.8026	0.7871	0.1339
600	0.7819	0.7518	0.8029	0.7789	0.1325
700	0.7753	0.7485	0.7899	0.7712	0.1312
800	0.7607	0.7440	0.7802	0.7616	0.1295

Table I.9 Measured friction force and calculated friction coefficient of oil #1 with 5.88 N applied load, rough cylinder and 100 μ l oil supply

Rotation speed (rpm)	Friction force (N)				Friction coefficient
	Measure 1	Measure 2	Measure 3	Average	
100	0.8311	0.8342	0.8175	0.8276	0.1407
200	0.7741	0.7894	0.7449	0.7695	0.1309
300	0.7482	0.7545	0.7231	0.7419	0.1262
400	0.8174	0.7909	0.7763	0.7949	0.1352
500	0.8051	0.7910	0.7785	0.7915	0.1346
600	0.8040	0.7877	0.7701	0.7873	0.1339
700	0.7939	0.7678	0.7506	0.7708	0.1311
800	0.7760	0.7557	0.7480	0.7599	0.1292

Table I.10 Measured friction force and calculated friction coefficient of oil #1 with 9.82 N applied load, rough cylinder and continuous oil supply

Rotation speed (rpm)	Friction force (N)				Friction coefficient
	Measure 1	Measure 2	Measure 3	Average	
100	1.3657	1.3455	1.3812	1.3641	0.1389
200	1.2509	1.2437	1.2857	1.2601	0.1283
300	1.2010	1.1975	1.2223	1.2069	0.1229
400	1.1347	1.1205	1.1546	1.1366	0.1157
500	1.1030	1.0546	1.1082	1.0886	0.1109
600	1.0249	1.0095	1.0814	1.0386	0.1058
700	0.9994	0.9364	1.0073	0.9810	0.0999
800	0.9363	0.8925	0.9479	0.9256	0.0943

Table I.11 Measured friction force and calculated friction coefficient of oil #1 with 9.82 N applied load, rough cylinder and 60 μ l oil supply

Rotation speed (rpm)	Friction force (N)				Friction coefficient
	Measure 1	Measure 2	Measure 3	Average	
100	1.3372	1.3886	1.3748	1.3669	0.1392
200	1.2166	1.2895	1.2642	1.2568	0.1280
300	1.1659	1.2419	1.2163	1.2080	0.1230
400	1.2396	1.2822	1.2743	1.2654	0.1289
500	1.2768	1.3267	1.3141	1.3059	0.1330
600	1.2915	1.3238	1.3174	1.3109	0.1335
700	1.2945	1.3051	1.3117	1.3038	0.1328
800	1.2683	1.3109	1.3017	1.2936	0.1317

Table I.12 Measured friction force and calculated friction coefficient of oil #1 with 9.82 N applied load, rough cylinder and 100 μ l oil supply

Rotation speed (rpm)	Friction force (N)				Friction coefficient
	Measure 1	Measure 2	Measure 3	Average	
100	1.3879	1.3526	1.3679	1.3695	0.1395
200	1.2772	1.2606	1.2607	1.2662	0.1289
300	1.2234	1.1921	1.2004	1.2053	0.1227
400	1.3048	1.2901	1.2673	1.2874	0.1311
500	1.3473	1.3226	1.3051	1.3250	0.1349
600	1.3470	1.3172	1.3043	1.3228	0.1347
700	1.3225	1.3253	1.2941	1.3140	0.1338
800	1.3078	1.3095	1.2714	1.2962	0.1320

Table I.13 Measured friction force and calculated friction coefficient of oil #2 with 5.88 N applied load, sanded cylinder and continuous oil supply

Rotation speed (rpm)	Friction force (N)				Friction coefficient
	Measure 1	Measure 2	Measure 3	Average	
100	0.8528	0.8598	0.8388	0.8505	0.1446
200	0.8072	0.7974	0.7633	0.7893	0.1342
300	0.7396	0.7629	0.7597	0.7541	0.1282
400	0.6951	0.7042	0.7202	0.7065	0.1202
500	0.6258	0.6351	0.6763	0.6457	0.1098
600	0.5887	0.6108	0.6306	0.6100	0.1037
700	0.5652	0.5859	0.6012	0.5841	0.0993
800	0.5259	0.5528	0.5741	0.5509	0.0937

Table I.14 Measured friction force and calculated friction coefficient of oil #2 with 5.88 N applied load, sanded cylinder and 60 μ l oil supply

Rotation speed (rpm)	Friction force (N)				Friction coefficient
	Measure 1	Measure 2	Measure 3	Average	
100	0.8302	0.8470	0.8701	0.8491	0.1444
200	0.7674	0.7630	0.7888	0.7731	0.1315
300	0.7323	0.7399	0.7565	0.7429	0.1263
400	0.7535	0.7816	0.7330	0.7560	0.1286
500	0.7649	0.8164	0.7883	0.7899	0.1343
600	0.7660	0.8156	0.8017	0.7944	0.1351
700	0.7547	0.7983	0.8031	0.7854	0.1336
800	0.7591	0.8077	0.7877	0.7848	0.1335

Table I.15 Measured friction force and calculated friction coefficient of oil #2 with 5.88 N applied load, sanded cylinder and 100 μ l oil supply

Rotation speed (rpm)	Friction force (N)				Friction coefficient
	Measure 1	Measure 2	Measure 3	Average	
100	0.8360	0.8782	0.8563	0.8568	0.1457
200	0.7803	0.8134	0.7988	0.7975	0.1356
300	0.7228	0.7714	0.7657	0.7533	0.1281
400	0.6933	0.7463	0.7189	0.7195	0.1224
500	0.7089	0.7694	0.7505	0.7429	0.1263
600	0.7457	0.7706	0.7734	0.7632	0.1298
700	0.7345	0.7873	0.7669	0.7629	0.1297
800	0.7366	0.7753	0.7684	0.7601	0.1293

Table I.16 Measured friction force and calculated friction coefficient of oil #2 with 9.82 N applied load, sanded cylinder and continuous oil supply

Rotation speed (rpm)	Friction force (N)				Friction coefficient
	Measure 1	Measure 2	Measure 3	Average	
100	1.4061	1.4162	1.3959	1.4061	0.1432
200	1.2886	1.3223	1.2706	1.2938	0.1318
300	1.2226	1.2425	1.2226	1.2292	0.1252
400	1.1500	1.1555	1.1327	1.1461	0.1167
500	1.0790	1.0781	1.0726	1.0766	0.1096
600	1.0122	1.0163	1.0130	1.0138	0.1032
700	0.9808	0.9721	0.9589	0.9706	0.0988
800	0.9085	0.8749	0.8924	0.8919	0.0908

Table I.17 Measured friction force and calculated friction coefficient of oil #2 with 9.82 N applied load, sanded cylinder and 60 μ l oil supply

Rotation speed (rpm)	Friction force (N)				Friction coefficient
	Measure 1	Measure 2	Measure 3	Average	
100	1.3935	1.3768	1.4479	1.4061	0.1432
200	1.3249	1.2981	1.3603	1.3278	0.1352
300	1.2573	1.2185	1.2910	1.2556	0.1279
400	1.2012	1.1693	1.2683	1.2129	0.1235
500	1.1907	1.1656	1.2210	1.1924	0.1214
600	1.2189	1.1638	1.2348	1.2058	0.1228
700	1.2078	1.1600	1.2513	1.2064	0.1228
800	1.1863	1.1357	1.2262	1.1827	0.1204

Table I.18 Measured friction force and calculated friction coefficient of oil #2 with 9.82 N applied load, sanded cylinder and 100 μ l oil supply

Rotation speed (rpm)	Friction force (N)				Friction coefficient
	Measure 1	Measure 2	Measure 3	Average	
100	1.4000	1.4269	1.3875	1.4048	0.1431
200	1.3231	1.3502	1.2868	1.3200	0.1344
300	1.2597	1.2769	1.2109	1.2492	0.1272
400	1.2263	1.2130	1.1890	1.2094	0.1232
500	1.2279	1.2040	1.1525	1.1948	0.1217
600	1.2161	1.2316	1.1622	1.2033	0.1225
700	1.1974	1.2282	1.1559	1.1938	0.1216
800	1.1964	1.2404	1.1610	1.1993	0.1221

Table I.19 Measured friction force and calculated friction coefficient of oil #2 with 5.88 N applied load, rough cylinder and continuous oil supply

Rotation speed (rpm)	Friction force (N)				Friction coefficient
	Measure 1	Measure 2	Measure 3	Average	
100	0.8777	0.9031	0.8881	0.8896	0.1513
200	0.8272	0.8578	0.8552	0.8467	0.1440
300	0.7930	0.7862	0.8203	0.7998	0.1360
400	0.7696	0.7508	0.7921	0.7708	0.1311
500	0.7289	0.7106	0.7453	0.7283	0.1239
600	0.7158	0.6806	0.7222	0.7062	0.1201
700	0.6800	0.6558	0.6915	0.6758	0.1149
800	0.6685	0.6381	0.6589	0.6552	0.1114

Table I.20 Measured friction force and calculated friction coefficient of oil #2 with 5.88 N applied load, rough cylinder and 60 μ l oil supply

Rotation speed (rpm)	Friction force (N)				Friction coefficient
	Measure 1	Measure 2	Measure 3	Average	
100	0.8939	0.9024	0.8891	0.8951	0.1522
200	0.8190	0.8645	0.8522	0.8452	0.1437
300	0.7810	0.8224	0.8018	0.8017	0.1364
400	0.7673	0.7968	0.7869	0.7837	0.1333
500	0.7443	0.7814	0.7709	0.7655	0.1302
600	0.7496	0.7982	0.7747	0.7742	0.1317
700	0.7597	0.8017	0.8011	0.7875	0.1339
800	0.7556	0.8003	0.7992	0.7850	0.1335

Table I.21 Measured friction force and calculated friction coefficient of oil #2 with 5.88 N applied load, rough cylinder and 100 μ l oil supply

Rotation speed (rpm)	Friction force (N)				Friction coefficient
	Measure 1	Measure 2	Measure 3	Average	
100	0.8886	0.8949	0.8961	0.8932	0.1519
200	0.8225	0.8441	0.8603	0.8423	0.1432
300	0.7646	0.7925	0.8172	0.7914	0.1346
400	0.7324	0.7480	0.7707	0.7504	0.1276
500	0.7163	0.7407	0.7539	0.7370	0.1253
600	0.7057	0.7375	0.7591	0.7341	0.1248
700	0.7078	0.7353	0.7540	0.7324	0.1246
800	0.7192	0.7419	0.7698	0.7436	0.1265

Table I.22 Measured friction force and calculated friction coefficient of oil #2 with 9.82 N applied load, rough cylinder and continuous oil supply

Rotation speed (rpm)	Friction force (N)				Friction coefficient
	Measure 1	Measure 2	Measure 3	Average	
100	1.4831	1.4904	1.4638	1.4791	0.1506
200	1.4107	1.4229	1.3882	1.4073	0.1433
300	1.3299	1.3333	1.3279	1.3304	0.1355
400	1.2844	1.3059	1.2770	1.2891	0.1313
500	1.2646	1.2101	1.2060	1.2269	0.1249
600	1.1975	1.1981	1.1441	1.1799	0.1202
700	1.1692	1.1570	1.0977	1.1413	0.1162
800	1.0744	1.0877	1.0369	1.0663	0.1086

Table I.23 Measured friction force and calculated friction coefficient of oil #2 with 9.82 N applied load, rough cylinder and 60 μ l oil supply

Rotation speed (rpm)	Friction force (N)				Friction coefficient
	Measure 1	Measure 2	Measure 3	Average	
100	1.4698	1.5055	1.4949	1.4901	0.1517
200	1.3919	1.4155	1.4208	1.4094	0.1435
300	1.3225	1.3625	1.3523	1.3458	0.1370
400	1.2869	1.3288	1.3349	1.3169	0.1341
500	1.3011	1.3258	1.3748	1.3339	0.1358
600	1.2951	1.2993	1.3445	1.3130	0.1337
700	1.2901	1.3145	1.3735	1.3260	0.1350
800	1.2793	1.2898	1.3651	1.3114	0.1335

Table I.24 Measured friction force and calculated friction coefficient of oil #2 with 9.82 N applied load, rough cylinder and 100 μ l oil supply

Rotation speed (rpm)	Friction force (N)				Friction coefficient
	Measure 1	Measure 2	Measure 3	Average	
100	1.5001	1.4766	1.4667	1.4811	0.1508
200	1.4263	1.4019	1.3757	1.4013	0.1427
300	1.3515	1.3173	1.3132	1.3273	0.1352
400	1.2990	1.2967	1.2645	1.2867	0.1310
500	1.2951	1.2852	1.2555	1.2786	0.1302
600	1.3219	1.2829	1.2561	1.2870	0.1311
700	1.3341	1.2803	1.2557	1.2900	0.1314
800	1.3000	1.2722	1.2411	1.2711	0.1294

Table I.25 Measured friction force and calculated friction coefficient of oil #3 with 5.88 N applied load, sanded cylinder and continuous oil supply

Rotation speed (rpm)	Friction force (N)				Friction coefficient
	Measure 1	Measure 2	Measure 3	Average	
100	0.8486	0.8359	0.8593	0.8479	0.1442
200	0.7764	0.7455	0.7750	0.7656	0.1302
300	0.7488	0.6959	0.7251	0.7233	0.1230
400	0.6821	0.6538	0.6796	0.6718	0.1143
500	0.6295	0.6034	0.6472	0.6267	0.1066
600	0.5706	0.5341	0.5924	0.5657	0.0962
700	0.5132	0.4894	0.5417	0.5148	0.0875
800	0.4528	0.4379	0.4996	0.4634	0.0788

Table I.26 Measured friction force and calculated friction coefficient of oil #3 with 5.88 N applied load, sanded cylinder and 60 μ l oil supply

Rotation speed (rpm)	Friction force (N)				Friction coefficient
	Measure 1	Measure 2	Measure 3	Average	
100	0.8399	0.8355	0.8486	0.8413	0.1431
200	0.7670	0.7830	0.7918	0.7806	0.1328
300	0.7532	0.7534	0.7876	0.7647	0.1301
400	0.7763	0.7676	0.8023	0.7821	0.1330
500	0.8097	0.7842	0.8270	0.8070	0.1372
600	0.8110	0.7739	0.8195	0.8015	0.1363
700	0.7870	0.7787	0.8067	0.7908	0.1345
800	0.7921	0.7699	0.8156	0.7925	0.1348

Table I.27 Measured friction force and calculated friction coefficient of oil #3 with 5.88 N applied load, sanded cylinder and 100 μ l oil supply

Rotation speed (rpm)	Friction force (N)				Friction coefficient
	Measure 1	Measure 2	Measure 3	Average	
100	0.8278	0.8291	0.8412	0.8327	0.1416
200	0.7466	0.7469	0.7791	0.7575	0.1288
300	0.7124	0.7425	0.7368	0.7306	0.1242
400	0.7433	0.7807	0.7861	0.7700	0.1310
500	0.7853	0.8121	0.8085	0.8020	0.1364
600	0.7955	0.8058	0.8134	0.8049	0.1369
700	0.7969	0.7985	0.8153	0.8036	0.1367
800	0.7871	0.8157	0.8056	0.8028	0.1365

Table I.28 Measured friction force and calculated friction coefficient of oil #3 with 9.82 N applied load, sanded cylinder and continuous oil supply

Rotation speed (rpm)	Friction force (N)				Friction coefficient
	Measure 1	Measure 2	Measure 3	Average	
100	1.3692	1.3882	1.3633	1.3736	0.1399
200	1.2573	1.2878	1.2629	1.2693	0.1293
300	1.1675	1.2089	1.1702	1.1822	0.1204
400	1.0811	1.1273	1.0989	1.1024	0.1123
500	1.0005	0.9960	1.0266	1.0077	0.1026
600	0.9050	0.9331	0.9295	0.9225	0.0939
700	0.8194	0.8532	0.8563	0.8430	0.0858
800	0.7551	0.7982	0.7878	0.7804	0.0795

Table I.29 Measured friction force and calculated friction coefficient of oil #3 with 9.82 N applied load, sanded cylinder and 60 μ l oil supply

Rotation speed (rpm)	Friction force (N)				Friction coefficient
	Measure 1	Measure 2	Measure 3	Average	
100	1.3841	1.3964	1.3623	1.3809	0.1406
200	1.2531	1.3197	1.3158	1.2962	0.1320
300	1.1719	1.2577	1.2723	1.2340	0.1257
400	1.2331	1.2995	1.2768	1.2698	0.1293
500	1.2586	1.3477	1.2743	1.2935	0.1317
600	1.2897	1.3565	1.3372	1.3278	0.1352
700	1.2803	1.3658	1.3292	1.3251	0.1349
800	1.2739	1.3591	1.3584	1.3305	0.1355

Table I.30 Measured friction force and calculated friction coefficient of oil #3 with 9.82 N applied load, sanded cylinder and 100 μ l oil supply

Rotation speed (rpm)	Friction force (N)				Friction coefficient
	Measure 1	Measure 2	Measure 3	Average	
100	1.3860	1.3369	1.4018	1.3749	0.1400
200	1.2611	1.2469	1.2762	1.2614	0.1285
300	1.2034	1.1836	1.2500	1.2123	0.1235
400	1.2305	1.1878	1.2322	1.2168	0.1239
500	1.2628	1.2659	1.2957	1.2748	0.1298
600	1.2907	1.2883	1.3171	1.2987	0.1322
700	1.3157	1.3443	1.3313	1.3304	0.1355
800	1.3045	1.3447	1.3715	1.3402	0.1365

Table I.31 Measured friction force and calculated friction coefficient of oil #3 with 5.88 N applied load, rough cylinder and continuous oil supply

Rotation speed (rpm)	Friction force (N)				Friction coefficient
	Measure 1	Measure 2	Measure 3	Average	
100	0.8806	0.8696	0.8926	0.8809	0.1498
200	0.8162	0.8031	0.8262	0.8152	0.1386
300	0.7595	0.7418	0.7876	0.7630	0.1298
400	0.7126	0.7043	0.7128	0.7099	0.1207
500	0.6943	0.6656	0.6938	0.6846	0.1164
600	0.6623	0.6325	0.6747	0.6565	0.1116
700	0.6559	0.6135	0.6409	0.6368	0.1083
800	0.6087	0.5852	0.6263	0.6067	0.1032

Table I.32 Measured friction force and calculated friction coefficient of oil #3 with 5.88 N applied load, rough cylinder and 60 μ l oil supply

Rotation speed (rpm)	Friction force (N)				Friction coefficient
	Measure 1	Measure 2	Measure 3	Average	
100	0.8657	0.8873	0.8703	0.8744	0.1487
200	0.7965	0.8246	0.8299	0.8170	0.1389
300	0.7700	0.7993	0.8082	0.7925	0.1348
400	0.7601	0.7908	0.8052	0.7854	0.1336
500	0.7662	0.8020	0.8015	0.7899	0.1343
600	0.7491	0.7775	0.7934	0.7733	0.1315
700	0.7575	0.7865	0.7837	0.7759	0.1320
800	0.7552	0.7727	0.7875	0.7718	0.1313

Table I.33 Measured friction force and calculated friction coefficient of oil #3 with 5.88 N applied load, rough cylinder and 100 μ l oil supply

Rotation speed (rpm)	Friction force (N)				Friction coefficient
	Measure 1	Measure 2	Measure 3	Average	
100	0.8478	0.8908	0.8709	0.8698	0.1479
200	0.7746	0.8101	0.8060	0.7969	0.1355
300	0.7205	0.7679	0.7452	0.7445	0.1266
400	0.7072	0.7540	0.7395	0.7336	0.1248
500	0.7427	0.7629	0.7606	0.7554	0.1285
600	0.7540	0.7949	0.7702	0.7730	0.1315
700	0.7527	0.7882	0.7697	0.7702	0.1310
800	0.7386	0.7863	0.7609	0.7619	0.1296

Table I.34 Measured friction force and calculated friction coefficient of oil #3 with 9.82 N applied load, rough cylinder and continuous oil supply

Rotation speed (rpm)	Friction force (N)				Friction coefficient
	Measure 1	Measure 2	Measure 3	Average	
100	1.4577	1.4216	1.4647	1.4480	0.1475
200	1.3433	1.3419	1.3672	1.3508	0.1376
300	1.2512	1.2467	1.2934	1.2638	0.1287
400	1.1894	1.1833	1.2070	1.1932	0.1215
500	1.1383	1.1273	1.1401	1.1352	0.1156
600	1.0144	1.0508	1.0693	1.0448	0.1064
700	0.9749	1.0010	1.0408	1.0056	0.1024
800	0.9584	0.9073	0.9836	0.9498	0.0967

Table I.35 Measured friction force and calculated friction coefficient of oil #3 with 9.82 N applied load, rough cylinder and 60 μ l oil supply

Rotation speed (rpm)	Friction force (N)				Friction coefficient
	Measure 1	Measure 2	Measure 3	Average	
100	1.4275	1.4340	1.4843	1.4486	0.1475
200	1.3260	1.3525	1.3876	1.3554	0.1380
300	1.2924	1.3013	1.3469	1.3135	0.1338
400	1.2930	1.3207	1.3521	1.3219	0.1346
500	1.2801	1.2938	1.3457	1.3065	0.1330
600	1.2557	1.2859	1.3519	1.2978	0.1322
700	1.2687	1.2998	1.3286	1.2990	0.1323
800	1.2562	1.2897	1.3334	1.2931	0.1317

Table I.36 Measured friction force and calculated friction coefficient of oil #3 with 9.82 N applied load, rough cylinder and 100 μ l oil supply

Rotation speed (rpm)	Friction force (N)				Friction coefficient
	Measure 1	Measure 2	Measure 3	Average	
100	1.3974	1.4559	1.4486	1.4340	0.1460
200	1.3053	1.3650	1.3462	1.3388	0.1363
300	1.2094	1.2887	1.2547	1.2509	0.1274
400	1.1879	1.2356	1.2114	1.2116	0.1234
500	1.2157	1.2690	1.2685	1.2511	0.1274
600	1.2089	1.2501	1.2813	1.2468	0.1270
700	1.1944	1.2332	1.2636	1.2304	0.1253
800	1.1936	1.2204	1.2509	1.2216	0.1244

